Development of the Barrel Calorimeter Reconstruction and Measurement of the Beam Asymmetry (Σ) for Photoproduced π^0 and η Mesons with the GlueX Experiment

William Edmund McGinley

September 19, 2019

Abstract

The GlueX experiment is located in Hall D at Jefferson Lab with the primary goal of mapping out the spectrum of hybrid mesons. GlueX features a nearly-4π hermetic detector capable of measuring neutral and charged particles produced by a 9 GeV linearly polarized photon beam incident on a liquid hydrogen target. A description of the detector is presented to give an overview of the experiment. A lot of effort has been put forth into analyzing the data recorded by the detector. Here I discuss improving the performance of the Barrel Calorimeter subdetector by calibrating the gains and improving the reconstruction software. The immediate physics goal of GlueX is to measure observables of known particles, especially those that are expected to be decay particles of hybrid mesons, such as π^0 and η. To understand the photoproduction mechanism of these two particles the beam asymmetry (Σ) observable is measured. The measurements of Σ are obtained as a function of the four-momentum transfer squared, -t, in the photon energy range of 8.2 GeV to 8.8 GeV in the three dominant decay modes of the η meson and in the dominant decay mode of the π^0 meson. These are the first results for the η meson at this beam energy in multiple decay modes. The results agree with previously published GlueX results for η and π^0 and are made with significantly higher statistical precision. There is also agreement between theory predictions and the results which indicates that the resonance production mechanisms of the π^0 and η mesons are dominated by natural parity exchange.

Acknowledgements

Each contribution that I've made has been with a lot of help of others in the GlueX collaboration. I would like to start by thanking my advisor, Curtis Meyer, who has given me a tremendous amount of support and guidance on how to carry out a physics analysis from start to finish. I'd also like to thank Reinhard Schumacher for always being available to explain physics concepts to me.

I need to thank the entire JLAB staff who are among the smartest and most helpful people that I've ever been around. In particular I was beyond fortunate to have the pleasure to work closely with Elton Smith and Mark Dalton on a variety of BCAL projects. They both sacrificed some of the more interesting projects and allowed me to work on them, I really had so much fun working on the calibrations and reconstruction code. Elton is the most patient and kind man I've ever met and well, he had to be in order to train me from a point where I literally knew nothing to where now I still don't know much but at least it's maybe something. Mark also trained me from my first day in the collaboration and gave me an undeserving amount of support to the point where he shared his office with me for a year to help teach me the technical skills required to produce results. Mark also showed me how to work within a collaboration. The entire Calorimetry Working Group has been helpful and deserves my gratitude. One final JLAB staff to thank was Dave Mack, who took on the challenge of looking in gory detail at my physics analysis and provided very useful guidance on hammering down the many fits and error analysis.

I would also like to thank my friends in Canada, Zisis Papandreou and Tegan Beattie. Zisis, provided help with my understanding of the BCAL and pushed my physics analysis along. Tegan, provided many valuable discussions and cross-checks between our analyses.

Many people within the CMU group were a big help as well. Paul Mattione, who took much of his time to help me get started and learning the GlueX software. Naomi Jarvis and Will Levine, who were great officemates to share many work, social and snack experiences with. Of course a really big thanks to my good friend Michael Staib, who spent a truly astonishing amount of time aiding me at all levels of my work, especially at the beginning. The most important thing that I have to thank him for is introducing me to the Birch Bar in Norfolk.

Sean Dobbs who helped me on various topics, most importantly on understanding the Simulation software and calibration techniques. Justin Stevens, who provided very valuable guidance on performing a physics analysis.

To all of my fellow CMU physics friends who made grad school enjoyable. I could never give a comprehensive list of these people but they include Li Jun, Sanxi Yao, Xianglin Liu, Zach McDargh, Larisa Thorne, Juan-Carlos Cornejo and Abel Sun.

The group at JLAB who somehow made Newport News social life enjoyable during my 16 month tenure living there: Alex, Eric, Jenn, Paul, Mike and the staff at Sushi Yama.

Giovanni and Lily, for always being such positive people and cooking together, going to shows and much more. The beautiful, Shuya Li, for all the many different dinners and various adventures together.

The overwhelming support of my entire family most immediately my two brothers, Sean and Chris. My sister-in-law Kristine and my wonderful nieces and nephews: Emma, John, Fionn and Cecily. Of course, my dedicated parents Pat and Carol who have been there for me since I can remember.

Contents

Chapter 1

Introduction

The atomic nucleus is composed of protons and neutrons, which themselves are made up of quarks. A quark is an elementary particle that is a fundamental constitute of matter. Quarks are now known to be half-integer particles called fermions with fractional charge of +2/3 or -1/3 depending on the type of quark. Bosons are particles with integer spin; all particles are either fermions or bosons. The proton and neutron are two examples of states of quarks, otherwise known as hadrons (protons and neutrons are also fermions). Since hadrons aren't elementary particles, a scheme of assigning quantum numbers to them has been useful for classifying them in terms of their quark contributions. As quarks were first being discovered in the 1950's, the quark model was proposed by George Zweig [1] and Murray Gell-Man [2] as a classification scheme of hadrons. In the quark model hadronic states consisting of three quarks are called baryons, such as the proton and neutron, and states of a quark and antiquark pair are called mesons. An antiquark is an example of an antiparticle, which is a particle that has the same mass as a given particle but opposite charge. The quark states are bound together by the strong force.

The strong force is one of the four fundamental forces, along with the gravitational, electromagnetic and weak forces. The observed interactions of the fundamental forces may be thought of as the exchange of a gauge boson, called a force carrier. An observed interaction between two particles is described by one of the particles emitting an exchange boson and the other absorbing it. An exchange boson can only be produced or absorbed in an interaction by a particle that is sensitive to the mediators force. For example, the electrically neutral photon is the exchange boson for the electromagnetic interaction, which is the force that governs interactions between electrically charged particles. An electrically neutral fundamental particle cannot produce or absorb a photon. The strong force is a short-range force (it can be ignored for any system of particles separated by tens of femtometers) that is stronger than the electromagnetic force. The strong force is responsible for confining quarks to form hadronic states and also the binding of protons and neutrons to form atomic nuclei despite the Coulomb repulsion.

The scheme to categorize states of quarks using the Eightfold way based on SU(3) flavor symmetry, as shown in Fig. 1.1, was introduced by Murray Gell-Mann [3] and Yuval Ne'eman [4]. SU(3) flavor symmetry was considered because only three of the six types of quarks had been observed at that time (the up, down and strange quarks). It relies on symmetry between the three quarks. The strange quark turns out to be more massive than the up and down quarks which breaks SU(3) symmetry. Isospin symmetry was adopted to better describe the system of quarks. The up quark is assigned isospin, I = 1/2, the down quark has I = -1/2 while the strange quark has I = 0. This leads to a $\mathbf{3} \otimes \overline{\mathbf{3}} = \mathbf{8} \oplus \mathbf{1}$ representation. Due to the SU(3) symmetry breaking the mass of the isospin = 0 hadronic states may not be at the physical mass however the representation of SU(3) symmetry still explains the pattern of hadrons being grouped into the observed multiplets.

There are some limitations to the quark model's description of the strong interaction that are ex-

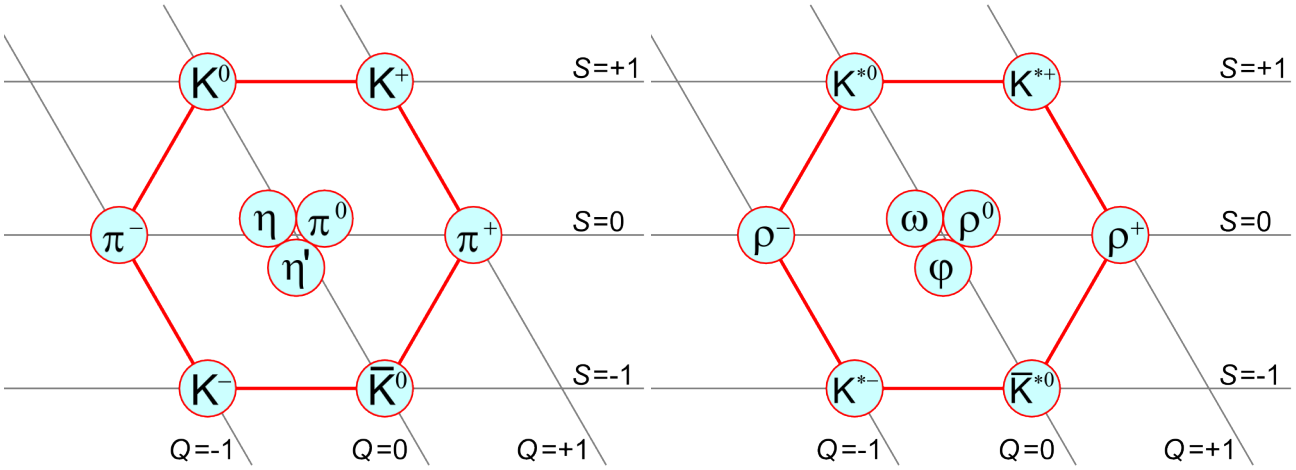

(a) Spin 0 nonet. (b) Spin 1 nonet.

Figure 1.1: Ground state nonets of light mesons governed by SU(3) flavor symmetry, similar diagrams can be produced for baryons.

plained by Quantum Chromodynamics (QCD). The quark model did not forbid free quarks, since there is no lighter particle with fractional charge for a quark to decay to the quark model would allow for stable free quark to exist. QCD introduces an SU(3) color symmetry, which assigns a color charge to each quark. For example, the quark and antiquark that make up a meson state will have a color and corresponding anticolor assigned to each, respectively. The meson state is then considered to be color-neutral. Similarly to the very successful theory of QED, the interaction between charged particles in QCD is mediated by an exchange boson. In QED the interaction of two electrically charged particles is described by the exchange of a photon, in QCD the interaction of two color charged particles is described by the exchange of a gluon to form bound states of quarks. Due to this gluonic interaction between quarks, if one were to try to separate two quarks then the energy of the gluonic field would spontaneously create a new quark-antiquark pair forbidding the existence of free quarks. One of the reasons that QED is simpler to solve than QCD is because the photon is electrically neutral and thus won't interact with itself. However, the gluon carries color charge and can interact with a quark or another gluon. The gluon-gluon interaction permits more complex states to exist including a color-neutral meson with an additional contribution from the gluon-gluon interaction. Such a state is called a hybrid meson and is further discussed later in this chapter.

The coupling (α_s), or interaction strength, of the QCD interaction has been modeled and measured as a function of the 4-momentum transfer, Q, as shown in Fig. 1.2. The coupling strength is small and close to linear at high energies which corresponds to short distance interactions between the quarks. At higher energies the coupling is small enough that the theory of QCD can be calculated using perturbative methods. There is good agreement between theory and experiment in this regime. GlueX is run at the lower energy regime which corresponds to larger distances of interactions. At these lower energies the coupling strength is large and nonlinear. The perturbative methods fail in this regime because the coupling strength is too large for a pertubative expansion to be possible. This makes it challenging to understand hadrons and nuclei using the QCD framework. Non-pertubative methods have been developed to understand QCD at these low energies, lattice QCD being one such method that has made predictions relevant to the GlueX physics program [5], Fig. 1.3.

In LQCD quarks are represented by fields placed at lattice points while gluons are represented by fields connecting adjacent lattice points. This means that LQCD is calculated in a discretized

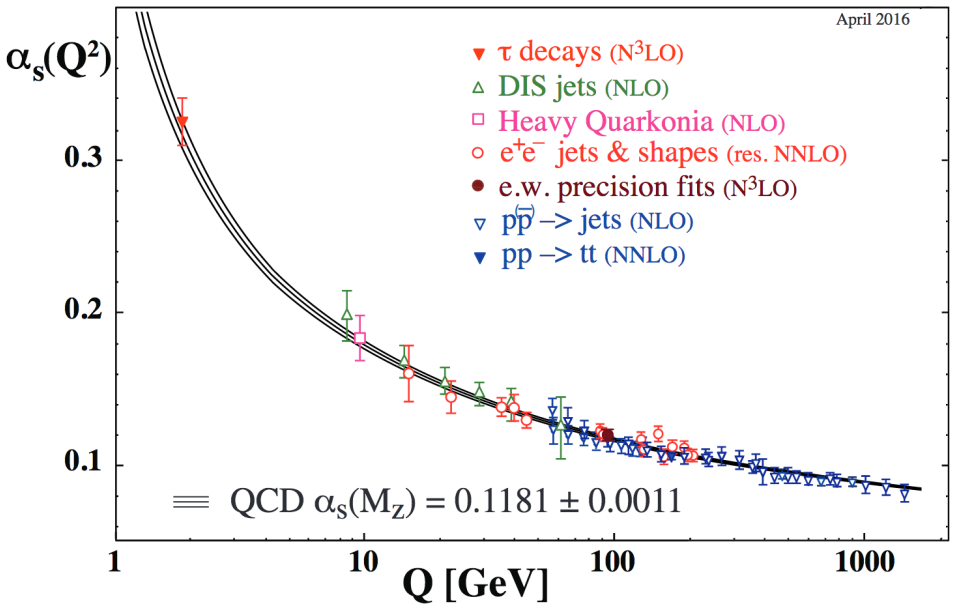

Figure 1.2: QCD coupling, α, as a function of 4-momentum transfer, Q [6].

spacetime, as the lattice spacing goes to zero the continuum QCD nature is reached. However, this is a major computational challenge and so results are often extrapolated to the limit of the continuum QCD. In order to make the calculations feasible the vacuum polarization quenching effects have been neglected, large lattice spacing with fewer points are used and unphysically large quark masses and other approximations have been made. Over the past several years LQCD has made rapid progress to reduce these limitations with the advent of modern computing power, these improvements have led to LQCD making predictions of the mass and quantum numbers of meson states forbidden by the quark model including hybrid mesons [5], tetraquarks [7] and pentaquarks [8].

The bound states of baryons and mesons are identified by their J^{PC} quantum numbers, where J is the total angular momentum, P is the parity and C is the charge conjugation. The quark-antiquark pair that make up a meson will either have their spins aligned or anti-aligned giving the meson a spin of S = 0, 1. There can also be a relative angular momentum of the two quarks, L. The total angular momentum is then given as J = S $\oplus$ L. The parity operator acting on a wavefunction flips the sign of its spatial coordinates such that $P\psi(\vec{r}) = \psi(-\vec{r}) = P_a\psi(\vec{r})$, where P_a is the eigenvalue of the parity operator, P. The wavefunction of a quark can be decomposed into its radial and angular components and the parity operator will only act on the angular component such as $P\psi(r,\theta,\phi) = PR(r)Y^l_m(\theta,\phi) = (-1)^l R(r)Y(\theta,\phi)$. Since parity is a multiplicative quantum number the parity of a meson is given as $P(q\bar{q}) = (-1)^{L+1}$. The charge conjugation operator, C, acts to change all particles into their anti-particle partners and vice versa as $C\psi = \bar{\psi}$. The charge conjugation reverses the sign of all intrinsic quantum numbers of a particle or system. In the meson system the quark becomes the antiquark and the antiquark becomes the quark. This can be thought of as the $\vec{r}$ that points to the quark as becoming $-\vec{r}$ so that it still points to the quark under charge conjugation. This mimics the parity operation and will introduce a factor of $(-1)^{L+1}$ under charge conjugation. The spins of the wavefunctions will also be flipped under this operation, this leads to an additional factor of -1 for S = 0 states and a factor of +1 for S = 1 states. Therefore the operation of charge conjugation on mesons is $C(q\bar{q}) = (-1)^{L+S}$ [9]. If only the quantum numbers of the quark-antiquark pair are considered, as is the case in the quark

model, the complete set of J^{PC} quantum numbers and their associated physics states can be seen in Tab. 1.1.

L	S	J	P	C	Meson State
0	0	0	-	+	π, η, η' K
0	1	1	-	-	ρ, ω, ϕ, K*
1	0	1	+	-	b_1, h_1, h_1', K_1
1	1	0	+	+	a_0, f_0, f_0', K_0*
1	1	1	+	+	a_1, f_1, f_1', K_1*
1	1	2	+	+	a_2, f_2, f_2', K_2*

Table 1.1: J^{PC} quantum numbers constructed from the complete set of combinations of L and S from the quark-antiquark pair for L < 2.

LQCD predicts the meson spectrum in Fig. 1.3 and states with J^{PC} quantum numbers that weren't allowed in the quark model are allowed to exist [5].Lattice QCD (LQCD) allows for additional states to exist by considering a contribution from the gluon with a nonzero L to the J^{PC} quantum numbers. These states are known as hybrid mesons and are interpreted to contain quantum number contributions from an excited gluon. These states include $J^{PC} = 0^{--}, 0^{+-}, 1^{-+}, 2^{+-}, 3^{-+}$ and so on.

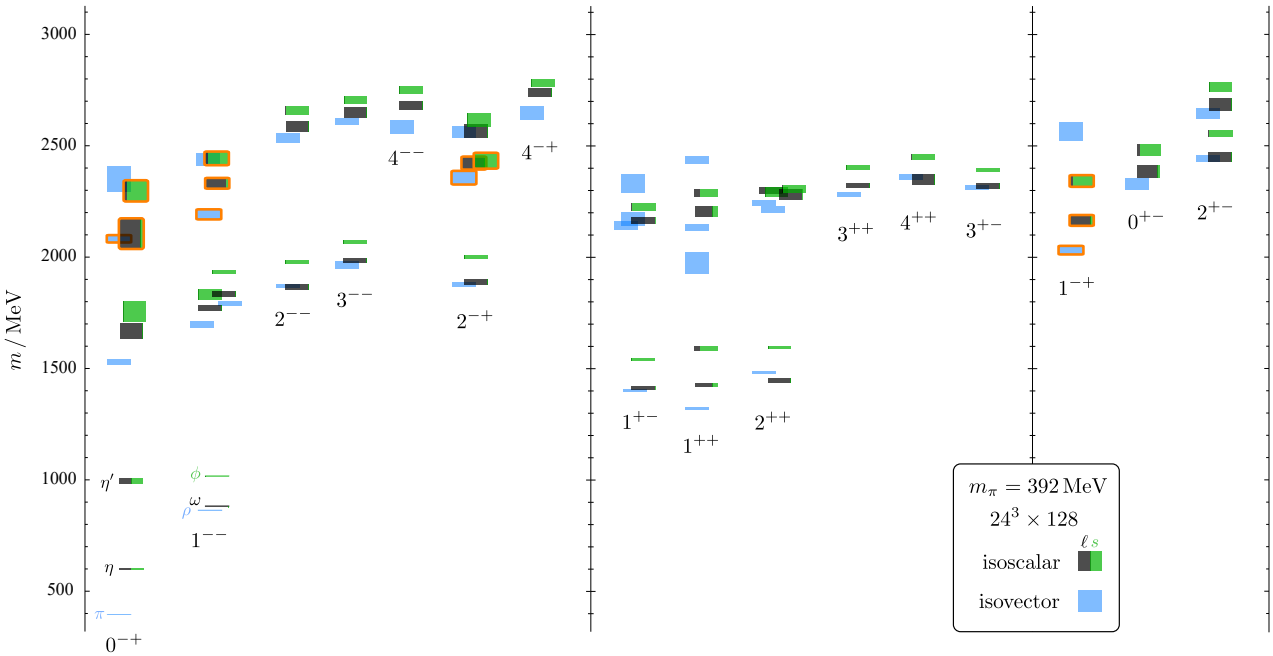

Figure 1.3: Light mesonic mass spectrum as a function of quantum numbers, J^{PC} predicted by LQCD. The height of the boxes indicates their error and states highlighted in orange correspond to the lightest hybrid meson supermultiplet [5].

1.1 Experimental Evidence for Hybrid Mesons

Hints of experimental evidence for mesons with exotic quantum numbers have been observed, most prominently for $J^{PC} = 1^{-+}$. For these states a partial wave analysis is needed to disentangle the the contributions from each resonance. The different signals are extracted by fitting the mass spectra with a set of partial waves each with a particular J^{PC}. The ensemble of partial waves relative to the cross-section of the reaction can be fit to various angular distributions of the final-state particles in order to extract the amplitudes for each partial wave [10]. To identify an exotic state, the PWA can be done with and without the exotic partial wave included. If the analysis with the exotic partial wave included fits the data significantly better than the analysis with the exotic partial wave excluded it would imply a contribution from the exotic wave.

The $\pi_1(1400)$ has been observed to to have a resonant-like structure in the $J^{PC} = 1^{-+}$ wave by a few experiments [11] [12]. This state has only been observed in the $\eta\pi$ final state but would be expected to be observed in multiple other final states. The measured mass is also consistently lower than the lowest predicted exotic meson mass. These inconsistencies with the predicted results cause some skepticism that the experimental observations are of a true resonance.

There have been many robust measurements of the $\pi_1(1600)$ in different decay modes, leading to stronger evidence for a true exotic meson resonance observation. This state was observed by the VES [13], E852 [14] and COMPASS [15] collaborations using a charged pion beam, CLEO [16] via $c\bar{c}$ decay and the Crystal Barrel experiment [17] using $p\bar{p}$ annihilation. The VES collaboration has seen signatures of the exotic wave in multiple analyses for the decay modes of $b_1\pi$, $f_1\pi$ and $\eta'\pi$. The VES results for the $\eta'\pi$ decay mode are shown in Fig. 1.4 where the intensity of the exotic wave ($J^{PC} = 1^{-+}$) is shown. There is good agreement between these experiments for each these decay modes but the $\rho\pi$ mode is inconsistent with the other decay modes [18]. It can be argued that the results for the $\rho\pi$ mode are less robust than the other modes and so there is still reasonable evidence that the observed $\pi_1(1600)$ state is a true resonance. In order to unambiguously classify this state as a hybrid meson the predicted hybrid meson nonet will need to be observed.

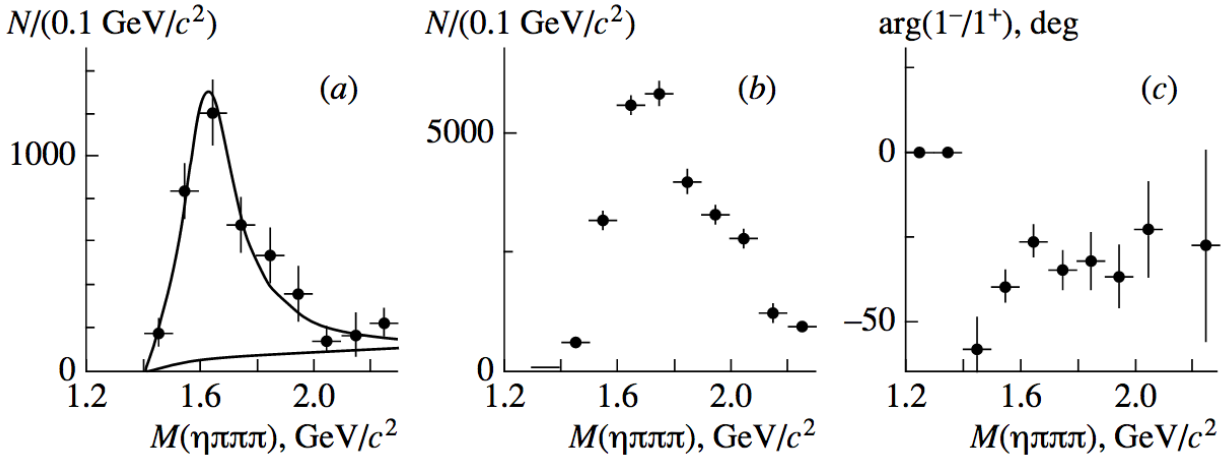

Figure 1.4: PWA results for the $\eta'\pi, \eta' \to \pi^+\pi^-\eta$ final state from VES [19]. (a) Intensity from the $J^{PC} = 1^{++}$ wave. (b) Intensity from the $J^{PC} = 1^{-+}$ wave. (c) The phase difference between the two waves.

The E852 experiment has observed evidence for the predicted exotic meson, $\pi_1(2015)$. Measurements

have been made for two decay modes, $b_1\pi$ and $f_1\pi$ [11]. This state is currently being searched for by other experiments.

1.2 GlueX hybrid exotic program

The primary goal of the GlueX experiment is to map the spectrum of exotic hybrid mesons unambiguously. GlueX is a photoproduction experiment with a linearly polarized 9 GeV photon beam incident on a fixed liquid Hydrogen target. Using a photon beam gives GlueX several advantages over previous experiments looking for exotics because the exotic states are predicted to have spin of 1. The photon beam carries the same spin quantum numbers as a vector meson, total spin of 1, which allows for exotic mesons to be produced directly. The previous evidence for exotic states was observed using a pion beam, total spin of 0, which requires a spin-flip transition of one quark to produce a hybrid meson [20]. The quark model suggests that this spin-flip will lead to a cross-section suppression by the inverse quark mass. Since the production of hybrids with a photon beam doesn't require a spin-flip there is no such suppression, leading to large exotic cross-section predictions for photoproduction at GlueX. The production of mesons at GlueX energies involves the t-channel natural and unnatural exchange of virtual mesons. The naturality of the exchange is determined by how it acts under the parity transformation, natural exchange behave as $\eta = P(-1)^J = 1$ and unnatural exchanges behave as $\eta = P(-1)^J = -1$. The linearly polarized beam is useful for filtering out possible J^{PC} quantum numbers. In the case where the production mechanism is already known then the linear polarization can be used to filter the exotic resonances by their naturality.

At this early stage of the GlueX experiment it is important to demonstrate that the detector is understood and that simple photoproduction processes can be measured before gaining confidence in measuring more complicated states such as the exotic hybrids. GlueX is sensitive to measuring polarization observables of well-known mesons as an important early step. For the pseudoscalar mesons the most interesting polarization observable that GlueX is sensitive to is the beam asymmetry, Σ. For the vector mesons, Gluex is sensitive to measuring the spin density matrix elements. A topic of this thesis will be measuring the beam asymmetry, Σ, for the pseudoscalar meson, η. Measuring Σ will provide insight into the production mechanism for the reaction $\gamma p \to \eta p$. As can be seen in Tab. 1.2, there are many predicted hybrid meson states that are expected to decay into η making it a relevant meson to understand going forward.

Predicted Hybrid	J^{PC}	Allowed Decays
π_1	1^{-+}	$\pi\eta$, ηa_1
η_1	1^{-+}	ηf_1, ηf_2, $\eta\eta'$,
η_1'	1^{-+}	$\eta\eta'$
b_0	0^{+-}	ηb_1
h_0	0^{+-}	ηh_1
h_0'	0^{+-}	ηh_1
b_2	2^{+-}	$\eta\rho$, ηb_1
h_2	2^{+-}	$\eta\omega$
h_2'	2^{+-}	ηh_1

Table 1.2: Predicted hybrid mesons and their decay modes that contain η [21]. These hybrid states have other decay modes that don't include η.

The η meson is charge-neutral and measured to have a mass of $M = 547.862 \pm 0.017$ MeV and width of $\Gamma = 1.31 \pm 0.05$ MeV [22]. This meson has zero isospin and belongs to the pseudoscalar nonet with quantum numbers $J^{PC} = 0^{-+}$. The three largest branching ratios are $\eta \to \gamma\gamma$ (39.4%), $\eta \to \pi^0\pi^+\pi^-$ (22.9%) and $\eta \to \pi^0\pi^0\pi^0$ (32.7%).

Measuring Σ is of particular interest to GlueX for two reasons. Hybrid mesons are expected to decay into the same final states as normal mesons, a full partial wave analysis will be required to determine their J^{PC} quantum numbers. The diffractive photopoduction of a meson is done via the exchange of an intermediate meson. Pseudoscalars such as η are expected to be the dominant exchange meson in the photoproduction of multiple hybrid mesons. The Σ measurement determines the naturality of the exchange particle to photoproduce a pseudoscalar meson. The natural exchange maps to an exchange meson with $J^P = 0^+, 1^-, 2^+, ...$ while the unnatural exchange maps to an exchange meson with $J^P = 0^-, 1^+, 2^-, ...$. By understanding the naturality of the exchange intermediate meson allows the naturality, or J^{PC}, of the produced meson to be filtered. This helps to identify if the produced meson has exotic quantum numbers, J^{PC}.

There have been several experiments to make high precision measurements of Σ at beam energies of less than 2 GeV [23, 24] as can be seen in Fig. 1.5. In this energy regime Σ provides insight into the nucleon resonance. Experiments have measured Σ and some of the other 15 pseudoscalar meson polarization observables to apply constraints to the models of the helicity amplitudes of the excited nucleon states. These measurements have led to a better understanding of the nucleon resonance spectrum. GlueX runs with a beam energy of 9 GeV and is therefore insensitive to the nucleon resonance spectrum. However, the t-channel component of the model extends from the low energy regime up to the GlueX energy [25, 26]. The production mechanism at the GlueX energy is only sensitive to the t-channel exchange and so Gluex is able to isolate the t-channel component of the model. A precise measurement of Σ by GlueX could apply new constraints to the t-channel of the model, these constraints could then be extrapolated back to the low energy regime to help understand the nucleon resonance spectrum.

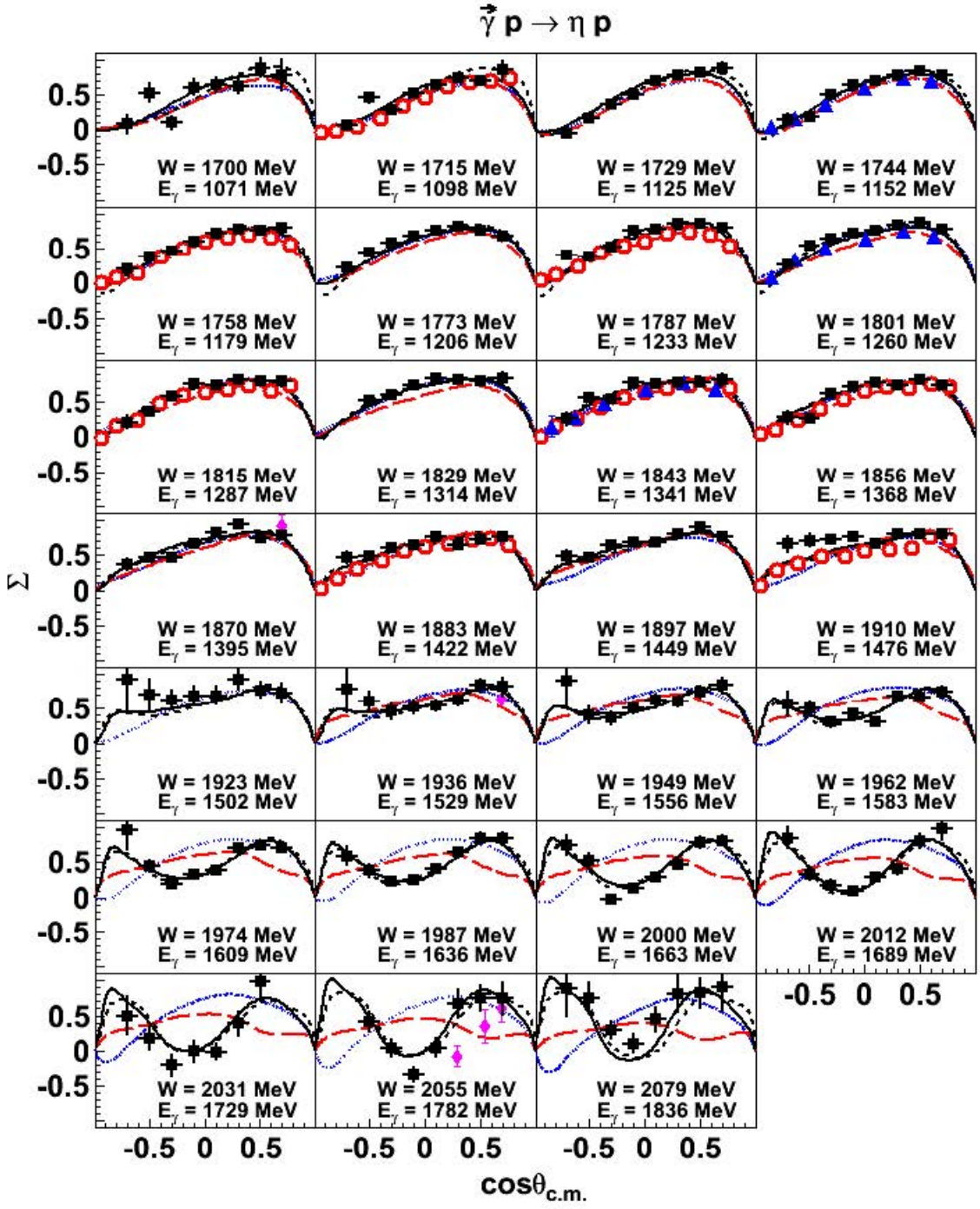

Figure 1.5: The measured Σ vs $\cos(\theta_{CM})$ for the reaction $\gamma p \to \eta p$ at incident photon energies from E = 1.071 to E = 1.836 GeV. The black filled squares and this picture come from [23]. The other data points displayed as blue filled triangles, red open circles and pink filled diamonds are previous measurements [27, 28, 29], respectively. The Blue dotted-lines come from predictions made by SAID [30], the red dashed-lines come from predictions made by the ETA-MAID model [31] and the black lines come from predictions made by the Jülich-Bonn model [32].

1.3 Polarization Observables

The beam asymmetry Σ is one of 16 polarization observables and is accessible with a linearly polarized beam. The other single-polarization observables are the target asymmetry, T, and the recoil asymmetry, P. With a linearly-polarized beam and an unpolarized target GlueX is sensitive to measuring the beam asymmetry, Σ. There are then four double-asymmetries for each of the three pairs of single-polarization asymmetries. The unpolarized cross-section constitutes the 16^{th} observable. The polarized cross-section can be written in terms of these 16 polarization observables. The polarization vectors associated with the target and target recoil are null in GlueX, so by determining the beam polarization, Σ and the unpolarized cross-section the polarized cross-section can be determined. The reactions with the polarization plane perpendicular to the reaction plane is dominated by natural exchanges whereas the reactions with the polarization plane parallel to the reaction plane is dominated by unnatural exchanges [33], more details are found in Sec. 4.5. Linear polarization enables the measurement of Σ to provide insight into the naturality of the exchange in the production mechanism.

Linearly polarized photon states can be written as a sum of longitudinal polarization states in its helicity basis [34],

$$|\gamma\rangle = -\frac{1}{\sqrt{2}}(e^{-i\Phi}\,|\lambda_\gamma = +1\rangle - e^{i\Phi}\,|\lambda_\gamma = -1\rangle). \tag{1.1}$$

where Φ is angle between the polarization pland and the reaction plane. The density matrix for pure photon states with linear polarization is given as

$$\rho^{pure}(\Phi) = |\gamma\rangle\,\langle\gamma| = \frac{1}{2}\begin{pmatrix} 1 & -e^{-2i\Phi} \\ -e^{2i\Phi} & 1 \end{pmatrix} \tag{1.2}$$

The photon beam at GlueX is partially polarized, the density matrix for a partially polarized photon beam can be written as a linear combination of the pure density matrix and longitudinal states such as

$$\rho(\Phi) = \frac{1-P_\gamma}{2}(|1+\rangle\,\langle 1+| + |1-\rangle\,\langle 1-|) + P_\gamma\rho^{pure}(\Phi) = \frac{1}{2}I + \frac{1}{2}\vec{P_\gamma}\cdot\vec{\sigma}, \tag{1.3}$$

where P_γ is the magnitude of the polarization, $\vec{\sigma_i}$ are the Pauli matrices and $\vec{P\gamma}$ is the polarization vector. For linear polarization

$$\vec{P_\gamma} = P_\gamma(\cos(2\Phi), \sin(2\Phi), 0). \tag{1.4}$$

The azimuthal angle Φ is defined as the difference between the angle of the reaction plane, ϕ, and the polarization angle of the beam, ϕ_γ. The polarized cross-section can be written out as [35]

$$\begin{aligned}
\sigma_{pol} = \sigma_0[&(1 + P_x^S P_y^i P_y^b) + P(P_y^b + P_x^S P_y^i) + \Sigma(P_x^S + P_y^i P_y^b) \\
&+T(P_y^i + P_x^S P_y^b) + T_x(P_x^i P_x^b + P_x^S P_z^i P_z^b) + T_z(P_x^i P_z^b - P_x^S P_z^i P_x^b) \\
&+E(P_z^S P_z^i + P_y^S P_x^i P_y^b) + F(P_z^S P_x^i - P_y^S P_z^i P_y^b) + G(-P_y^S P_z^i + P_z^S P_x^i P_y^b) + H(-P_y^S P_x^i - P_z^S P_z^i P_y^b) \\
&+C_x(P_z^S P_x^b + P_y^S P_y^i P_z^b) + C_z(P_z^S P_z^b - P_y^S P_y^i P_x^b) \\
&+O_x(-P_y^S P_x^b + P_z^S P_y^i P_z^b) + O_z(-P_y^S P_z^b - P_z^S P_y^i P_x^b) \\
&+L_x(P_z^i P_x^b - P_x^S P_x^i P_z^b) + L_z(P_z^i P_z^b + P_x^S P_x^i P_x^b)].
\end{aligned}$$

Since only the beam is polarized (P^S) in GlueX the contributions from the target polarization and recoil baryon polarization ($P^i = 0$ and $P^b = 0$) vanish. This leaves the observable cross-section as

$$\sigma_{pol} = \sigma_0(1 + P_x^S \Sigma) = \sigma_0(1 - P_\gamma \Sigma \cos(2\Phi)). \tag{1.5}$$

The beam asymmetry Σ can be defined as

$$\Sigma = \frac{\sigma_{natural} - \sigma_{unnatural}}{\sigma_{natural} + \sigma_{unnatural}} = \frac{\sigma_\perp - \sigma_\parallel}{\sigma_\perp + \sigma_\parallel}. \tag{1.6}$$

Σ is extracted experimentally by measuring the angle of the reaction plane, ϕ, while keeping the polarization angle, ϕ_γ fixed. When the reaction plane is perpindicular to the polarization plane the natural parity exchange will contribute positively to Σ. When the reaction plane is parallel to the polarization plane the unnatural parity exchange will contribute negatively to Σ. Therefore, the relative strength of the natural and unnatural exchange in the production mechanism can be understood by measuring Σ. If the pseudoscalar meson production mechanism is dominated by the natural exchange then Σ will be consistent with +1, if the production mechanism is dominated by the unnatural exchange then Σ will be consistent with -1.

1.3.1 Models of Σ in Photoproduction

There have been several predictions of the beam asymmetry, Σ, at high energies based on Regge models [36]. The Regge models describe the production mechanism of pseudoscalar mesons by the exchange of a quasi-particle called a Reggeon in the t-channel. Reggeons have well-defined quantum numbers, J^{PC}. For the case of the π^0 and η, the two lightest quantum numbers that are expected to contribute to the production mechanism are the Reggeon exchange with quantum numbers $J^{PC} = 1^{--}$ (natural exchange) and $J^{PC} = 1^{-+}$ (unnatural exchange). The dominant natural exchange particles are the ρ and ω vector mesons while the dominant unnatural exchange particles are the b and h axial-vector mesons. In the Regge model full trajectories of allowed quantum numbers are exchanged, not single particles. Since the Reggeons that could be involved in the exchange have different masses, Σ is predicted to be a function of the squared 4-momentum transfer to the target, $t = (p_{target} - p_{recoil})^2$, which is known as the Mandelstam variable, t. Therefore, the theoretical models of Σ at the GlueX energies all make their predictions as a function of $-t$. The currently-published world data for Σ measured for π^0 and η photoproduction in the GlueX energy regime along with the theory predictions are shown in Fig. 1.6. These models concentrate on the dynamics of the entire hadron because the quark and gluon details are not particularly important for measuring Σ at the GlueX energy. The more general approach is to describe the interaction using more general principles such as unitarity, analyticity, and crossing-symmetry. These phenomonological models are derived from the general principles while making as few assumptions as possible. The formalism used in these models to understand the production of a single pseudoscalar meson is in terms of amplitudes.

A summary of the components of the Regge theory that are common to all of the models that predict the beam asymmetry, Σ, will be presented and followed by a discussion of what makes each model unique. The commonality between the models is based on a single Regge pole contribution to the exchange. The amplitudes describe the full set of incoming and outgoing helicity states in a reaction such as $\gamma(k, \lambda)N(p_2) \rightarrow \pi^0/\eta(q)N(p_4)$. This describes the reaction of a photon with momentum, k and helicity λ, a π^0 or η with momentum q and a pair of nucleons with momentum p_2 and p_4 given in terms of four invariant amplitudes, A_i. The invariant amplitudes are a function of two independent Mandelstam variables, $s = (k + p_2)^2$ and $t = (k - q)^2$. The amplitudes multiply four independent

tensor operators (M_i) constructed from the photon polarization vector, two Dirac spinors and particle momenta that are constrained to satisfy gauge invariance. The tensors are conveniently chosen in the Chew-Goldberger-Low-Nambu (CGLN) basis [43] and the helicity amplitudes can be written as [37]

$$A^s_{\mu_4\mu_2\mu_1} = \bar{u}_{\mu_4}(p_4)\left(\sum_{i=1}^{4} A_i M_i\right) u_{\mu_2}(p_2), \tag{1.7}$$

$$A^t_{\lambda_4\lambda_2\lambda_1} = \bar{u}_{\lambda_4}(p_4)\left(\sum_{i=1}^{4} A_i M_i\right) v_{\lambda_2}(-p_2). \tag{1.8}$$

The full derivation to obtain the invariant amplitudes can be seen in Appendix A and B of Ref. [37]. The results of the invariant amplitudes are shown here to describe how they relate to the measurement of the beam asymmetry, Σ. For t-channel exchanges the invariant amplitudes for vector and axial-vector poles can be written as [44]

$$A_1(t) = \frac{e\lambda_V g^t_V}{2m_\eta M_N}\frac{t}{t - M_V^2}, \tag{1.9}$$

$$A'_2(t) = \frac{-e\lambda_A g^t_A}{2m_\eta M_N}\frac{t}{t - M_A^2}, \tag{1.10}$$

$$A_3(t) = \frac{e\lambda_A g^v_A}{m_\eta}\frac{1}{t - M_A^2}, \tag{1.11}$$

$$A_4(t) = \frac{-e\lambda_V g^v_V}{m_\eta}\frac{1}{t - M_V^2}. \tag{1.12}$$

In this definition $\lambda_{V(A)}$ denotes the electromagnetic coupling of the vector (V) and axial-vector (A) mesons with masses $M_{V(A)}$. The constants $g^{v(t)}_{V(A)}$ denote their vector (v) and tensor (t) couplings to the nucleon. $A'_2(t)$ is used to separate the vector and tensor contributions giving it good quantum numbers in the t-channel [37]

$$A'_2(t) = A_1(t) + tA_2(t), \tag{1.13}$$

The differential cross-section and the beam asymmetry can be expressed in terms of these invariant amplitudes at leading order in s as [26]

$$\frac{d\sigma}{dt} = \frac{1}{32\pi^2}\left(|A_1|^2 - t|A_4|^2 + |A'_2|^2 - t|A_3|^2\right) \tag{1.14}$$

$$\Sigma\frac{d\sigma}{dt} = \frac{1}{32\pi^2}\left(|A_1|^2 - t|A_4|^2 - |A'_2|^2 + t|A_3|^2\right) \tag{1.15}$$

The t-channel quantum numbers of the invariant amplitudes can be identified by projecting onto the t-channel parity-conserving helicity amplitudes [37] (and the references therein). The invariant amplitudes and their associated quantum numbers and possible t-channel exchanges are listed in Tab. 1.3. There hasn't been compelling evidence of the existence of a meson with quantum numbers $J^{PC} = (2, 4, ...)^{--}$ and so A_3 is ignored. Each of the models builds off of a single Regge pole ansatz. A single Regge pole contribution can be factorized into a product of couplings/residues and propagators. This property allows Regge poles to be classified similar to that of elementary particles [45]. The t-channel exchange that is encoded in the propagators for Eq. 1.9-1.12 describes the exchange of a single particle, however

A_i	J^{PC}	η	Leading exchanges
A_1	(1,3,5...)$^{--}$	+1	$\rho(770), \omega(782)$
A_2'	(1,3,5...)$^{+-}$	-1	$h_1(1170), b_1(1235)$
A_3	(2,4,...)$^{--}$	-1	$\rho_2(?), \omega_2(?)$
A_4	(1,3,5...)$^{--}$	+1	$\rho(770), \omega(782)$

Table 1.3: Relation between the invariant amplitudes, A_i and their exchange quantum numbers. This table is reproduced from Ref. [26].

in Regge theory the exchange is mediated by Regge trajectories. Therefore the propagator with the form $\frac{1}{1-M^2}$ is replaced by the Regge propagators $R(\alpha)$, given as [37]

$$R(\alpha) = \frac{\pi}{\Gamma(\alpha)} \frac{1 - e^{-i\pi\alpha}}{2\sin\pi\alpha} \left(\frac{s}{s_0}\right)^{\alpha-1}, \tag{1.16}$$

where s_0 is a mass scale factor that is commonly set to 1 GeV^2. A parameterization of the Regge trajectories are assumed to be linear in each of the relevant models and are defined as

$$\alpha_V(t) = \alpha_{V0} + t\alpha_V', \tag{1.17}$$

$$\alpha_A(t) = \alpha_{A0} + t\alpha_A'. \tag{1.18}$$

The trajectory parameters (α_{V0}, α_V', α_{A0}, α_A') are constrained by the meson-spin relations and are expected to be approximately given by [46]

$$\alpha_V(t) = 1 + 0.9(t - m_V^2), \tag{1.19}$$

$$\alpha_A(t) = 1 + 0.7(t - m_A^2). \tag{1.20}$$

The invariant amplitudes from Eq. 1.9- 1.12 can be written as the factorized product of coupling and propagator contributions [26]

$$A_1 = g_1^V t R(\alpha_V), \tag{1.21}$$

$$A_2' = g_2^A t R(\alpha_A), \tag{1.22}$$

$$A_3 = 0, \tag{1.23}$$

$$A_4 = g_4^V R(\alpha_V). \tag{1.24}$$

The coupling constants g_1, g_2 amd g_4 are the product of the electromagnetic and nucleon coupling. The method to obtain the coupling constants and trajectory parameters is model-dependent and will be discussed in the upcoming paragraphs. Before discussing the model-dependent features the cross-section measurement for $\gamma p \to \pi^0(\eta)p$ at a beam energy of $E_\gamma = 6$ GeV as shown in Fig. 1.7 demonstrates why contributions beyond the single Regge pole model are being considered by the models.

The model [44] only contains the vector contributions to the exchange (ω and ρ), shown in Fig 1.7. The large dips that exist in the model are not reproduced in data. These dips originate from $\alpha_V(t) = 0$

in Eq. 1.17, this occurs whenever $t \approx -0.5$ GeV^2 because the imaginary and real components of the propagator in Eq.1.16 vanish when $\alpha_V(t \approx -0.5) = 0$. If the axial-vector contribution to the exchange contributed significantly then the dip seen in the cross-sections could be filled in, this motivates the measurement of Σ because Σ is a measurement of the relevant strength between the vector and axial-vector contributions to the exchange. However, Fig. 1.6 shows that Σ is near unity (vector meson dominating the exchange). The measured Σ results presented later in this thesis will further support vector exchange dominance as shown in Ch. 6. To address the discrepancy of the dip between theory and experiment while predicting a Σ to be near unity different theoretical approaches beyond the single Regge pole model have been developed.

This exploration beyond the single Regge pole model is the primary reason why the models are significantly different from each other. The significant differences in the models come from differences in the Regge trajectory parameters, coupling constants, form of the Regge propagators and the implementation of Regge cuts. Regge cuts can be understood as a rescattering effect at high energies. For example the first step of a π^0 or η being produced is via a vector or axial-vector exchange and then subsequently rescattered via a Pomeron ($\mathbb{P}$) or tensor exchange. A Regge cut looks like a contracted box diagram where two trajectories are exchanged as shown in Fig. 1.8 [49].

The JPAC model for the π^0 photoproduction [37] is a combination of the single Regge pole model described above combined with Regge cut contributions. The JPAC group considers a vector-Pomeron exchange with a Regge cut propagator of the form

$$R_C(\alpha) = \frac{1}{\log(s/s_0)} \frac{\pi}{\Gamma(\alpha_C)} \frac{1 - e^{-i\pi\alpha_C}}{2\sin\pi\alpha_C} \left(\frac{s}{s_0}\right)^{\alpha_C - 1}. \tag{1.25}$$

Based on a simple model for Pomeron exchange [46] the Regge cut trajectory has a slope close to that of the Pomeron and intercept close to a vector meson such that

$$\alpha_c(t) \approx 0.5 + 0.2t \tag{1.26}$$

Regge Cut contributions to the axial-vector amplitude (A_2') were not considered in this model. The vector Regge trajectories are degenerate, meaning that $\alpha_\omega(t) = \alpha_\rho(t)$. This leaves 11 parameters to be fit, 5 coupling constants and 6 Regge trajectory parameters. The fit is performed by extracting the vector Regge pole and Regge cut parameters by fitting cross-section data at $E_\gamma > 4$ GeV [47, 50, 51, 52]. Once the parameters associated with vector exchange are fixed the axial vector parameters are fit from the beam asymmetry measurement [47]. The full results of the fits can be seen in Ref. [37], the Regge trajectories are listed in Tab. 1.4. In this model the zero from the Reggeon-Pomeron cut will not be at

intercept parameter	intercept	intercept error	slope parameter	slope [GeV^{-2}]	slope error [GeV^{-2}]
α_{V0}	0.44	0.01	α'_V	1.10	0.05
α_{c0}	0.46	0.04	α'_c	0.17	0.01
α_{A0}	-0.19	0.30	α'_A	1.02	0.18

Table 1.4: Regge trajectory parameters obtained from the fit by the JPAC π^0 model [37].

$t \approx -0.5$ GeV^2 allowing its contribution to fill in the cross-section while keeping the beam asymmetry Σ near unity.

The Donnachie model [40] uses nondegenerate vector Regge trajectories for ω and ρ

$$\alpha_\omega = 0.44 + 0.9t, \tag{1.27}$$

$$\alpha_\rho = 0.55 + 0.8t. \tag{1.28}$$

The axial-vector contribution is expected to only come from the b_1, the model uses a trajectory of

$$\alpha_b(t) \approx 0.013 + 0.664t. \tag{1.29}$$

Regge Cuts are also used in this model that contribute to both the vector and axial-vector exchange. The vector coupling constants used in this model are taken from Ref. [53] and the axial-vector coupling constants are taken from Ref. [54]. The only parameters that are used in the fit are the Regge cut trajectory parameters. These parameters are fit to cross-section data at $E_\gamma = 4, 5, 5.8$ GeV [52] and $E_\gamma = 6, 9, 12$ GeV [47] and beam asymmetry data at $E_\gamma = 4, 6, 10$ GeV [40]. This simpler fitting approach was used because the authors were only looking for qualitative description π^0 photoproduction and their primary interest is in the photoproduction of $a_0(980)$ and $f_0(980)$.

The model for π^0 photoproduction from Laget [39] makes use of degenerate vector Regge trajectories and vector-Pomeron Regge cuts in the same fashion as the above two models. The coupling constants and Regge trajectory parameters come from a previous Laget model [55] in which no Regge cut was considered. In this single Regge pole model the vector coupling and trajectories were assumed to be $g_V = 15$ and $\alpha_V(t) = 0.44 + 0.9t$. The beam asymmetry, Σ, data at $E_\gamma = 6$ GeV [47] is fit to obtain the only free parameter of this model, $g_A = g_{b_1} = 16.44$. The axial-vector coupling constant from this fit is about twice as large as the JPAC model for π^0 photoproduction and is reflected as a deeper dip in the prediction for Σ. The current Laget result that is shown uses this axial-vector coupling constant and includes the Regge cut contributions. Once the Regge cut contributions are included only the vector coupling (g_V) is fit to the beam asymmetry, Σ, at $E_\gamma = 6$ GeV data [47]. The Laget model also makes a prediction for the beam asymmetry, Σ, for η photoproduction by ignoring the axial-vector contribution to the exchange, $g_A = g_{b_1} = 0$.

The JPAC model for η photoproduction [26] takes a different approach than using Regge cuts. This model uses finite-energy sum rules (FESR) to relate the low-energy nucleon spectrum to the high-energy Reggeon exchanges. The JPAC group uses the Eta-MAID 2001 model [56] to evaluate the low-energy terms of the FESR. Interestingly, for this calculation the residue component of the Regge propagator from Eq. 1.16 will now vary for each invariant amplitude such that

$$A_1 = g_1^V t \frac{-\pi\alpha'_V}{\Gamma(\alpha_V + 1)} \frac{1 - e^{-i\pi\alpha_V}}{2\sin\pi\alpha_V} (r_1 s)^{\alpha_V - 1}, \tag{1.30}$$

$$A'_2 = g_2^A t \frac{-\pi\alpha'_A}{\Gamma(\alpha_A + 1)} \frac{1 - e^{-i\pi\alpha_A}}{2\sin\pi\alpha_A} (r_2 s)^{\alpha_A - 1}, \tag{1.31}$$

$$A_4 = g_4^V \frac{-\pi\alpha'_V}{\Gamma(\alpha_V)} \frac{1 - e^{-i\pi\alpha_V}}{2\sin\pi\alpha_V} (r_4 s)^{\alpha_V - 1}, \tag{1.32}$$

where scaling parameters, r_1, r_2, r_4 were introduced and are fit to data. The amplitude A_1 does not have a zero at $\alpha_V = 0$ because the $\frac{1}{\Gamma(\alpha_V)}$ term now goes as $\frac{1}{\Gamma(\alpha_V+1)}$. The data is fit to high-energy unpolarized cross-sections of η photoproduction [48, 57] to obtain the coupling constants and the scaling parameters. The Regge trajectories from Eq. 1.19 and 1.20 were used, it should be noted that this calculation was performed before GlueX made the only high-energy measurement of Σ for η photoproduction. It is found that the A_1 term dominates the η cross-section which agrees with the cross-section data since A_1 lacks a zero at $t \approx -0.5$ GeV^2, as shown in Fig. 1.7. This mechanism uses natural-parity exchange to fill the dip seen in the π^0 cross-section data which allows agreement with the beam asymmetry

measurement, Σ, to be near unity. The JPAC π^0 model suggests that A_1 does not dominate the production and therefore based on the FESR approach for η photoproduction it is expected that as the A_4 vanishes at $t \approx -0.5$ GeV^2 A_1 will fill the gap in the π^0 cross-section while keeping Σ positive. However, the fit to the π^0 data using the FESR approach has not yet been performed.

The Eta-MAID group also has made a prediction [44] after the data in Fig 1.6 were published. The predictions of this model for π^0 and η photoproduction can be found in Sec. 6. This model is very comprehensive, it uses the residues in the propagator from the JPAC FESR model [26] shown in Eq. 1.30- 1.32 and is the only model to include the contribution from A_3 as

$$A_3 = g_3^T \frac{-\pi\alpha'_T}{\Gamma(\alpha_T)} \frac{1 - e^{-i\pi\alpha_T}}{2\sin\pi\alpha_T} (r_3 s)^{\alpha_T - 1}, \tag{1.33}$$

where T corresponds to tensor meson exchange of ρ_2 or ω_2 in this model. Each of the Regge trajectories are non-degenerate. The Reggeon and Regge cut contributions that were used in the model can be seen in Tab. 1.5. This model uses a slightly different formalism to represent the Regge propagator, the vector

A_i	J^{PC}	η	Exchanges
A_1	(1,3,5...)$^{--}$	natural	$\rho, \omega, \rho\mathbb{P}$, $\omega\mathbb{P}$, $\rho f_2, \omega f_2$
A'_2	(1,3,5...)$^{+-}$	unnatural	$h_1, b1, \rho f_2, \omega f_2$
A_3	(2,4,...)$^{--}$	unnatural	ρ_2, ω_2, ρf_2, ωf_2
A_4	(1,3,5...)$^{--}$	natural	$\rho, \omega, \rho\mathbb{P}$, $\omega\mathbb{P}$, $\rho f_2, \omega f_2$

Table 1.5: Relation between the invariant amplitudes, A_i, their exchange quantum numbers and the Reggeon and Regge Cut exchanges that were used in the Eta-MAID model. The Pomeron is denoted as $\mathbb{P}$. This table is reproduced from Ref. [44].

exchange propagator, D_V is given as an example

$$D_V = D_V + c_{V\mathbb{P}} D_{V\mathbb{P}} + c_{Vf_2} D_{Vf_2}, \tag{1.34}$$

Where $c_{V\mathbb{P}}$ and c_{Vf_2} are coeffecients for each Regge cut with $V = \rho, \omega$. The Regge trajectory parameters are fixed according to the approach in Ref. [36]. The coupling constants are also fixed leaving the coefficients, c, as the only free parameters. The creators of this model claim to have fit all available cross-section, beam asymmetry (Σ), Target asymmetry (T) and recoil polarization (P) data for π^0 and η photoproduction in the beam energy from of 4 GeV $< E_\gamma <$ 11 GeV. It is also important to note that this is the only model that fits the GlueX beam asymmetry, Σ, data for π^0 and η photoproduction [42].

The beam asymmetry for η photoproduction can also be used in a ratio with the beam asymmetry of η' photoproduction to gain insight on a possible a hidden strangeness exchange (ϕ) in the production of η or η' [58]. According to this model by JPAC, the contribution of the exchange of the ϕ meson is expected to be antisymmetric for η and η'. Therefore, any deviation from unity for the ratio between the two could be explained by a contribution from the ϕ Regge pole. GlueX is sensitive to measuring the beam asymmetry Σ for η' photoproduction and could make this ratio measurement.

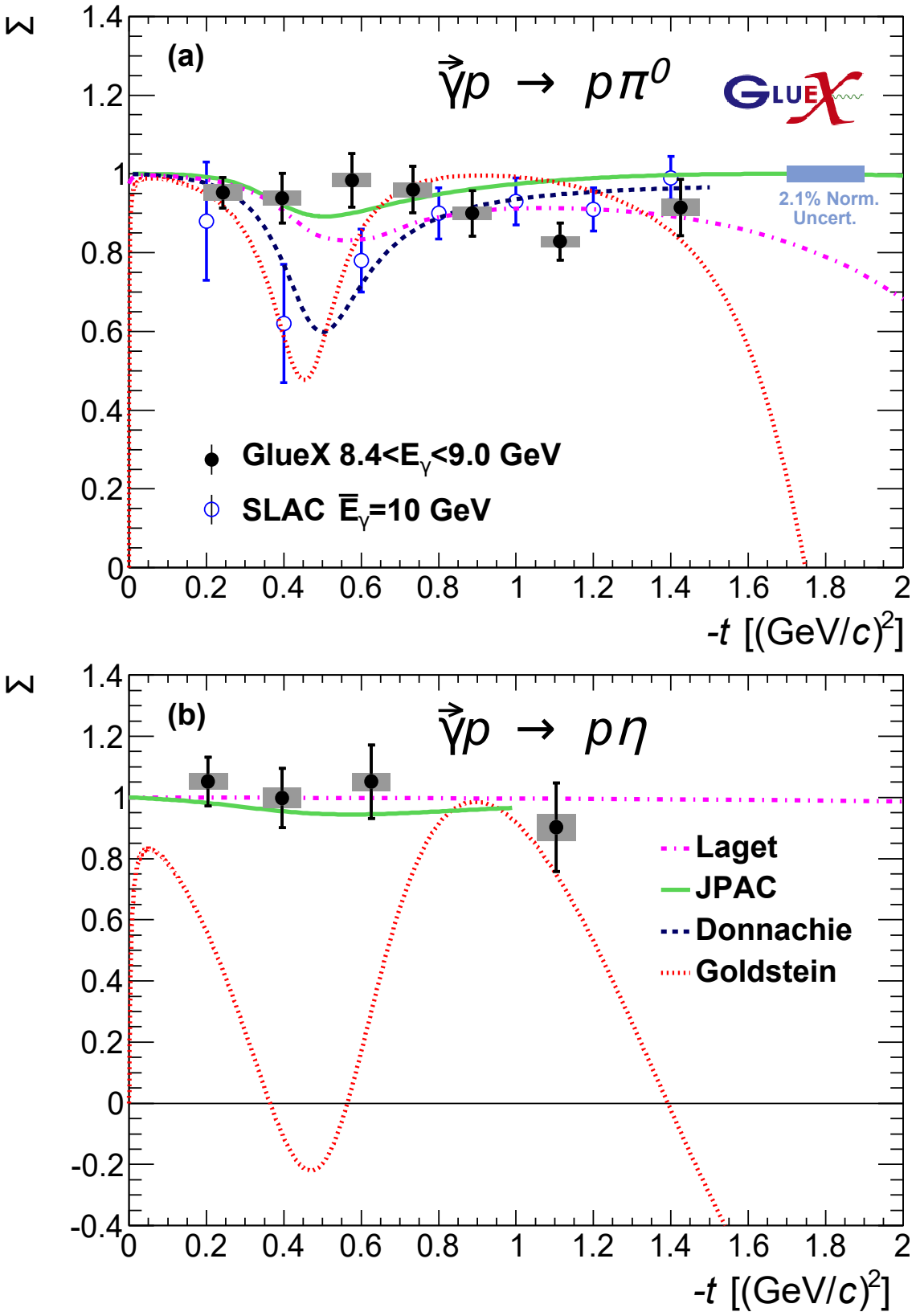

Figure 1.6: (a) Shows Σ as a function of t for π^0 photoproduction and (b) shows Σ as a function of t for η photoproduction. The published GlueX results are shown as black filled circles, the SLAC results are shows as blue open circles using an average beam energy of 10 GeV. The Green curve is the prediction by JPAC [37, 26], the dashed pink curve is a prediction by Laget [38, 39], the dashed black curve is a prediction by Donnachie [40] and the red dotted-line is a prediction made by Goldstein [41]. These plots are taken from Ref. [42].

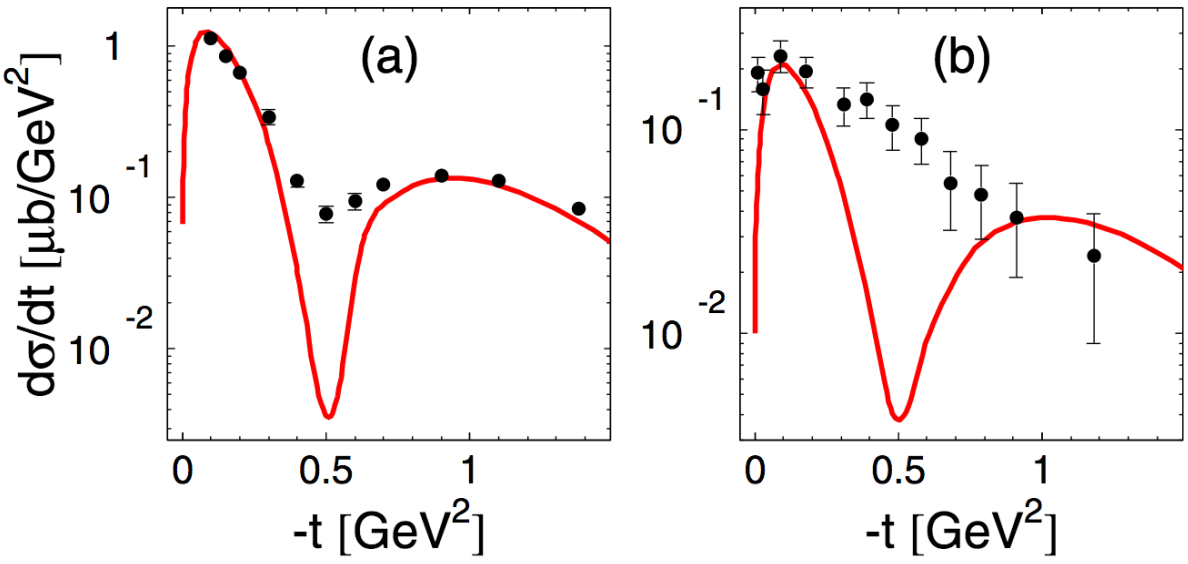

Figure 1.7: (a) shows the differential cross-section for $\gamma p \to \pi^0 p$ at $E_\gamma = 6$ GeV. The black points are data [47]. (b) shows the differential cross-section for $\gamma p \to \eta p$ at $E_\gamma = 6$ GeV. The black points are data [48]. The red line in both panels corresponds to a calculation using ω and ρ exchange contributions in the t-channel [49]. These plots are taken from Ref. [44].

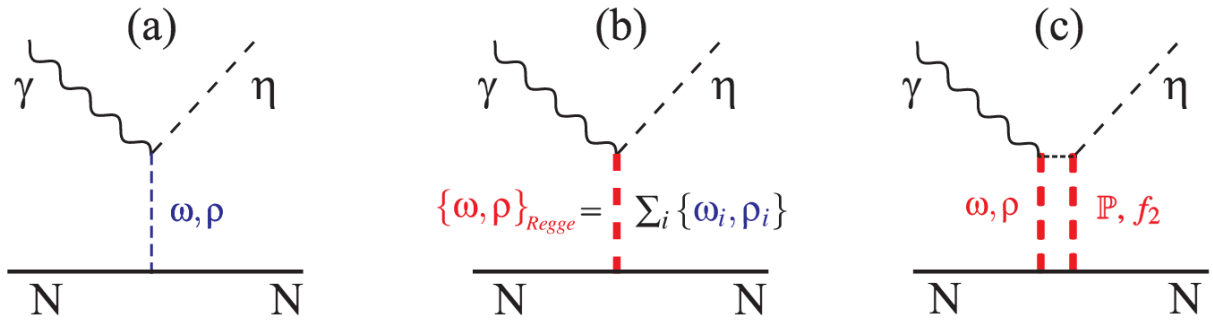

Figure 1.8: (a) shows the t-channel exchange contribution from a single pole in η photoproduction. (b) shows the t-channel exchange contribution from a Regge pole in η photoproduction. (c) shows the t-channel exchange contribution from a Regge cut with a ρ and ω exchange and Pomeron and f_2 meson rescattering in η photoproduction. Diagram is taken from Ref. [49].

Chapter 2

GlueX Detector

The GlueX experiment is located in Hall D at Thomas Jefferson Laboratory (JLab) in Newport News, Virginia. The main goal of GlueX is to map out the spectrum of hybrid exotic mesons that are predicted to exist by Lattice QCD [5]. JLAB hosts the Continuous Electron Beam Accelerator Facility (CEBAF) which provides a continuous wave 12 GeV electron beam to Hall D, as shown in Fig 2.1. CEBAF produces electron bursts using a high frequency laser incident on a strained superlattice gallium arsenide photocathode. The electron bursts are distributed into evenly-spaced beam bunches which are accelerated by cryomodules containing superconducting radiofrequency cavities [59]. Each RF cavity is divided into 7 cells each with standing RF waves set to match the phase and frequency of the electron bunch. This induces a gradient that causes the electrons to accelerate, one pass corresponds to about a 2.2 GeV energy increase to the electron beam. Three of experimental halls (A,B and C) can receive the electron beam after 1-5 passes through the accelerator. GlueX is designed to run at 5.5 passes in order to reach high-enough energy to produce mesons of mass near 3.5 GeV. In order for all 4 halls to run simultaneously and Hall D to run at 5.5 passes, a 249.5 MHz electron beam must be delivered to Hall D.

The GlueX spectrometer is a nearly 4π hermetic detector that is capable of detecting neutral and charged particles along with performing robust particle identification. The electron beam is used to produce to a photon beam that has its energy tagged to allow for exclusive reconstruction of events. The general organization of the many components of the GlueX detector is as follows: the photon beam is produced, tagged, collimated and steered on target in the beamline. There are 2 electromagnetic calorimeters responsible for detecting neutral particles, 2 tracking gas chambers to detect charged particles and various detectors that contribute to particle identification as illustrated in Fig. 2.2 and Fig. 2.3.

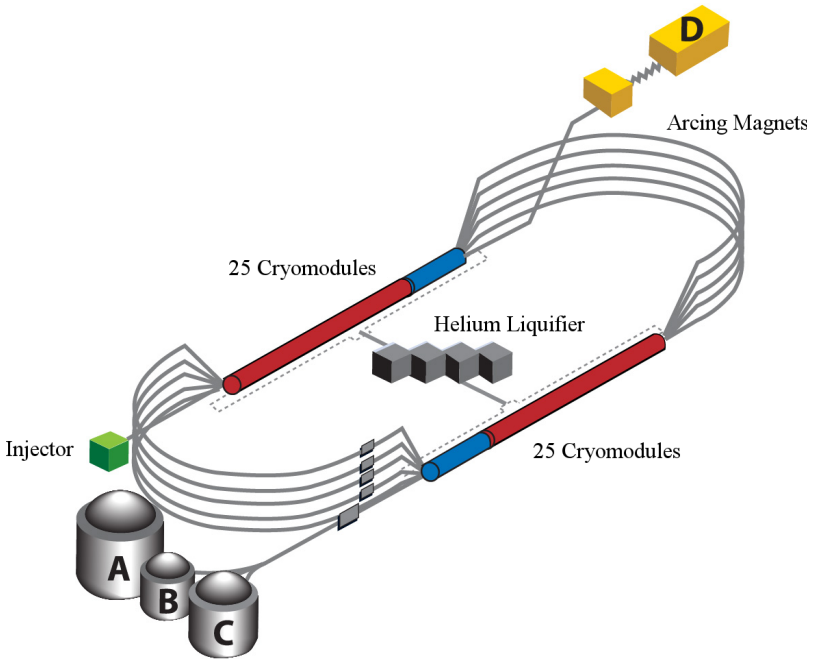

Figure 2.1: Overview of CEBAF. Image taken from Ref. [60].

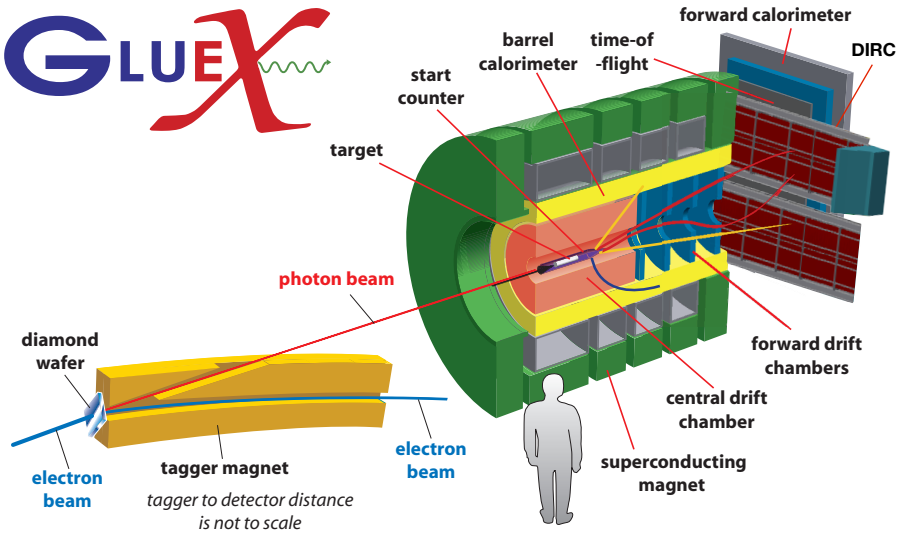

Figure 2.2: Sliced-view of the main GlueX spectrometer and some beamline components [61].

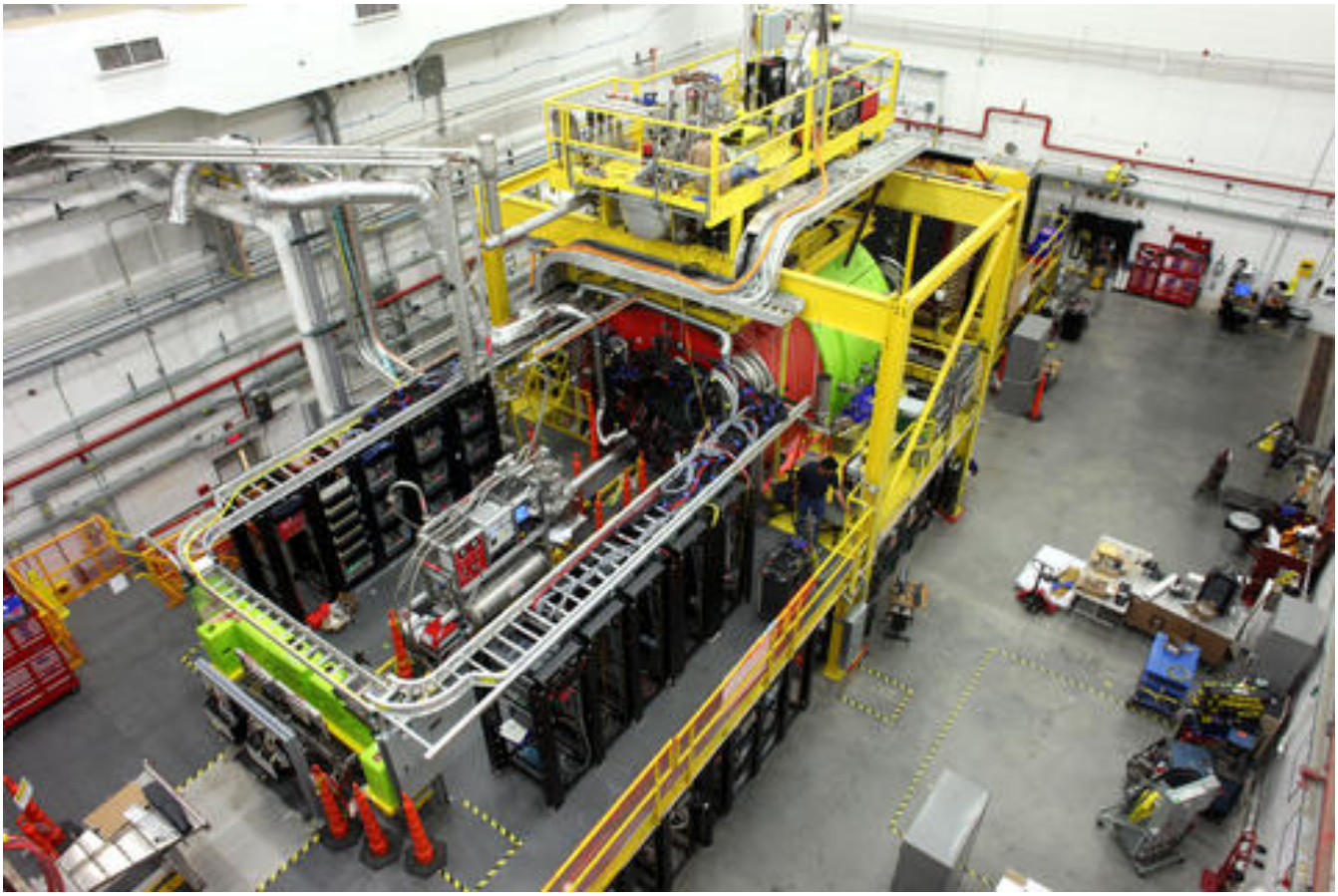

Figure 2.3: Aerial photo of Hall D taken in August, 2014 [61],

2.1 Beamline

The primary responsibility of the beamline components is to create a linearly polarized photon beam incident on the target, measure the energy of the incident photon, its degree of polarization and its flux.

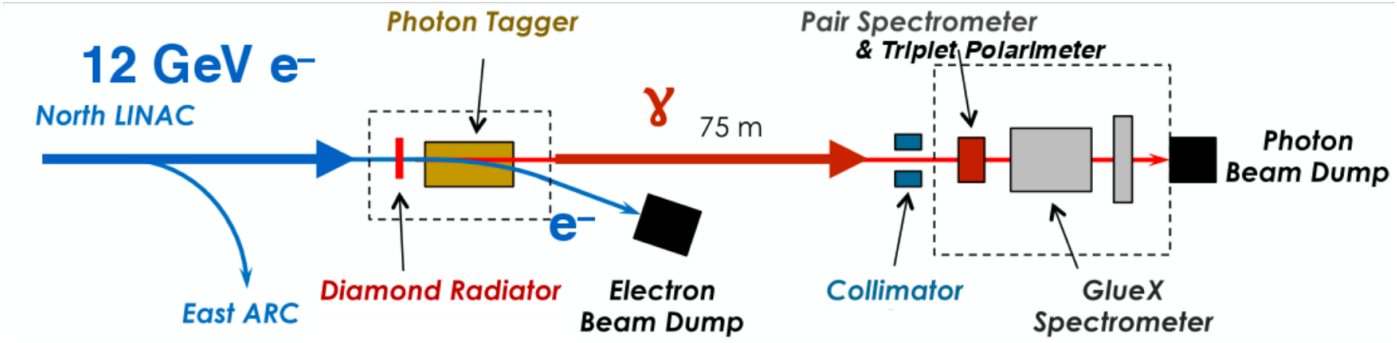

Figure 2.4: Schematic illustration of the primary beamline components and the GlueX spectrometer [62].

2.1.1 Diamond Radiator

The 12 GeV electron beam provided by CEBAF is incident on a thin diamond wafer (58 μm for the data presented in this thesis) to produce a 9 GeV photon beam via the Bremsstrahlung process. The energy of the outgoing photon is determined by the momentum transfer of the incident electron to the struck nucleus. This comes in the form of a continuum of momentum transfer to the nucleus and are averaged to give the incoherent component of the Bremsstrahlung process. When the momentum transfer matches a reciprocal lattice vector of the diamond the coherent component will be enhanced. By choosing the lowest-order lattice vectors to be positioned where the cross-section is large the coherent component will be large compared to the incoherent component [63]. Therefore the diamond is positioned to align its lattice with the electron beam to produce an enhancement in the photon spectrum as shown in Fig. 2.6a. There are also higher energy coherent Bremsstrahlung enhancements due to higher-order integer multiple lattice vectors. The coherent Bremsstrahlung process also produces a partially polarized photon beam as shown in Fig. 2.6b. Since the precise position and angular orientation of the diamond is crucial it is mounted on a goniometer. The position of the coherent peak enhancement and the direction of beam polarization can be tuned by rotating the diamond.

2.1.2 Photon Tagging

Whenever the electron interacts with the diamond radiator to produce the photon it is assumed that all of the energy that was lost was via Bremsstrahlung radiation. Due to conservation of energy and the energy of the incoming electron being very precisely known, the energy of the photon can be determined by measuring the energy of the scattered electron. The scattered electron is bent by a dipole magnet into the tagging spectrometer, as shown in Fig. 2.5. The radius of curvature determines the energy of the photon radiated by the incoming electron. The tagging spectrometer is composed of two tagging scintillation detectors that are designed to measure, or "tag", the energy of the photon based on the position that the electron interacts with the detectors. The hodoscope (TAGH) detector measures the energy of photons in the incoherent energy region and is a coarse detector with counters spanning 10-30

MeV. The microscope (TAGM) detector is positioned to measure the coherent portion of the photon beam with 5 MeV wide counters, corresponding to a photon beam energy resolution of 0.1%. The electrons that don't interact with the diamond are stopped in the beam dump.

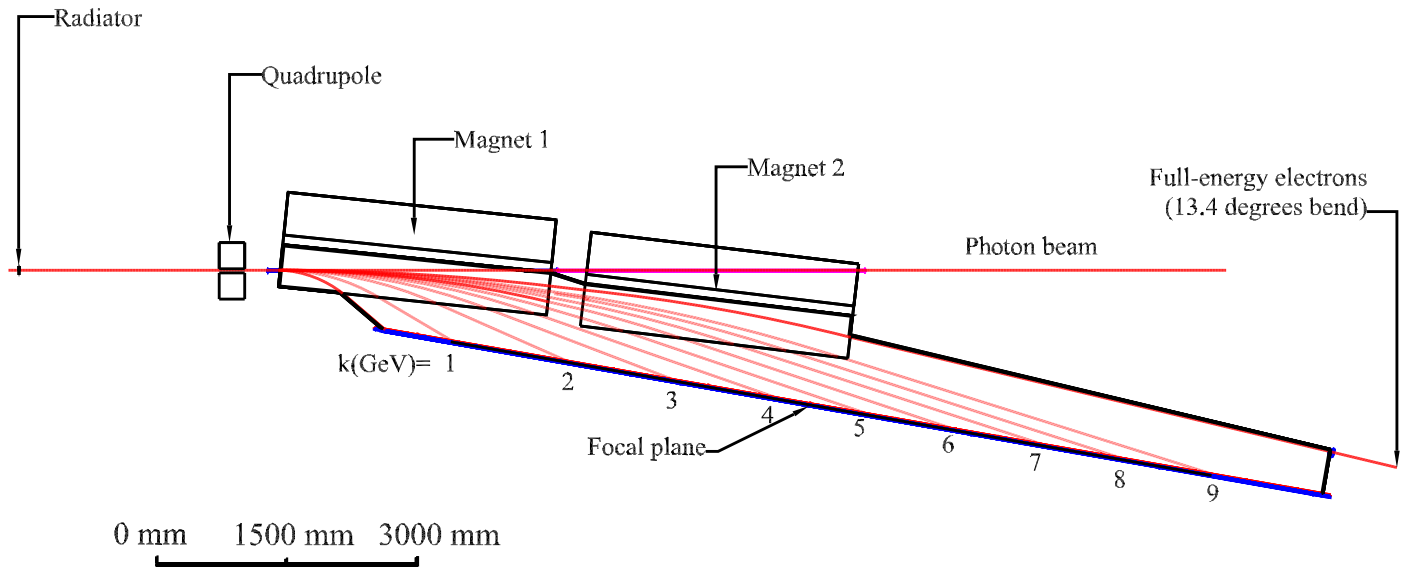

Figure 2.5: The scattered electrons are bent through dipole magnets and their paths are sketched in red lines. They are detected by the tagging detectors [62].

2.1.3 Active Collimator

Once the photon beam is produced it travels 75m and passes through a 3.4mm or 5.0mm lead-block collimator to suppress the incoherent component of the beam. The collimator is effective because the incoherent component of the beam has a wider angular spread than the coherent component does. The effect of collimation on the beam spectrum and polarization is shown in Fig. 2.6. In front of the lead-block collimator there is a Tungsten active collimator. Whenever the beam is incident on the active collimator an electrical signal is produced that provides feedback to the accelerator group to help steer the beam through the center of the collimator.

2.1.4 Triplet Polarimeter

The triplet polarimeter is a Silicon Strip Detector (SSD) split into 32 azimuthal components and 24 concentric circles. The TPOL has the granularity to achieve high precision measurements in both angular directions (azimuthal and polar). A thin Be foil is placed in front of the SSD. An incoming beam photon may interact with an atomic electron of the Be atom to produce an e^+e^- pair and also the atomic e^- recoils. The recoiled e^- is detected by the SSD and it's angular distribution contains information about the degree of polarization of the incident beam photon. The cross-section for triplet photoproduction is

$$\sigma(\phi) = \sigma_0[1 - P\Sigma\cos(2\phi)], \tag{2.1}$$

where σ_0 is the unpolarized cross-section, P is the polarization value, Σ is the beam asymmetry for triplet photoproduction and ϕ is the measured azimuthal angle of the recoil e^- by the azimuthal component

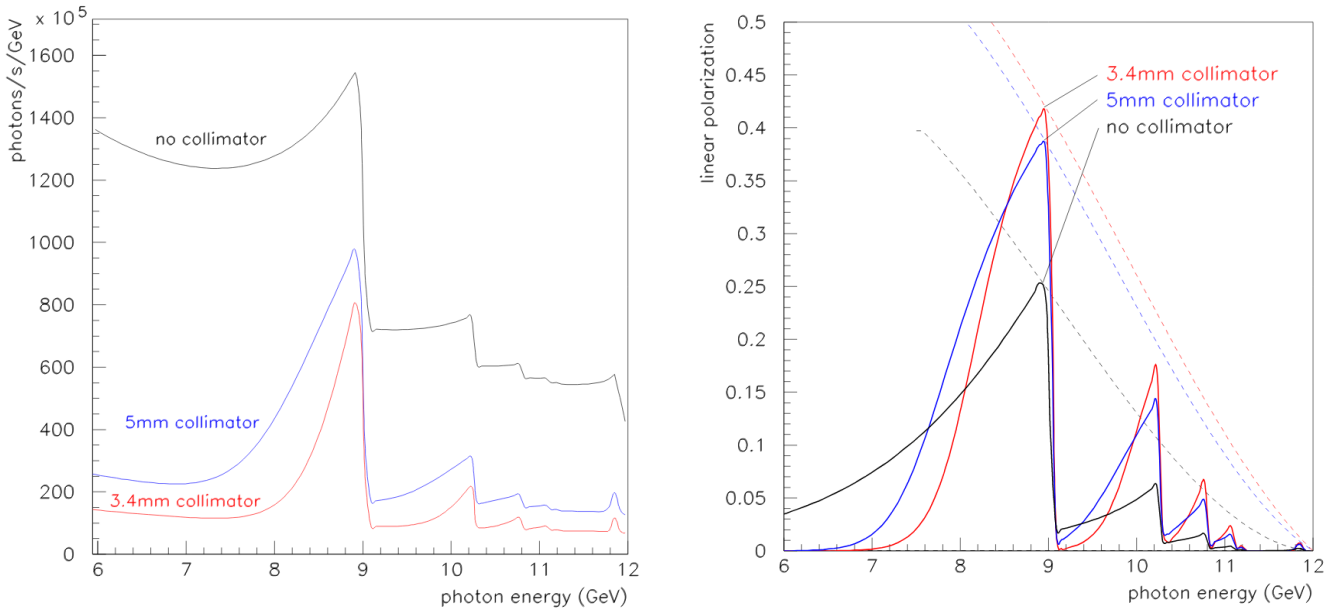

(a) Beam flux as a function of energy

(b) Beam polarization as a function of energy

Figure 2.6: Effect of collimation on beam flux and polarization. Calculations performed assuming a $1\mu Ae^-$ beam current and a diamond with a thickness of 15 μm [62].

of the polarimeter. Since this is a pure QED process the value of Σ is calculated and well-known via perturbative methods [64]. The value of Σ depends on the polar angle of the recoil electron, which is detected by the concentric circle component of the TPOL. Therefore P may be extracted by fitting the ϕ distribution of the recoil electron using the fit function

$$f(\phi) = A[1 - B\cos(2\phi)]. \tag{2.2}$$

In this definition the fit parameter B = PΣ and A normalizes the yields. The measured polarization as a function of beam energy can be seen in Fig. 2.7 and the values of polarization in the coherent peak are recorded in Tab. 2.1. The polarization value is a vital measurement to extract the Σ beam asymmetry for hadronic photoproduction where P is an input parameter and Σ extracted from a fit of an azimuthal distribution as will be discussed in Sec. 4.5.

Polarization Orientation	Average polarization	δ_p
0	0.352	0.0098
90	0.347	0.010
45	0.346	0.010
135	0.350	0.010

Table 2.1: Beam-energy weighted polarization values for different polarization directions in the coherent peak region from 8.2 to 8.8 GeV for the full 2017 dataset.

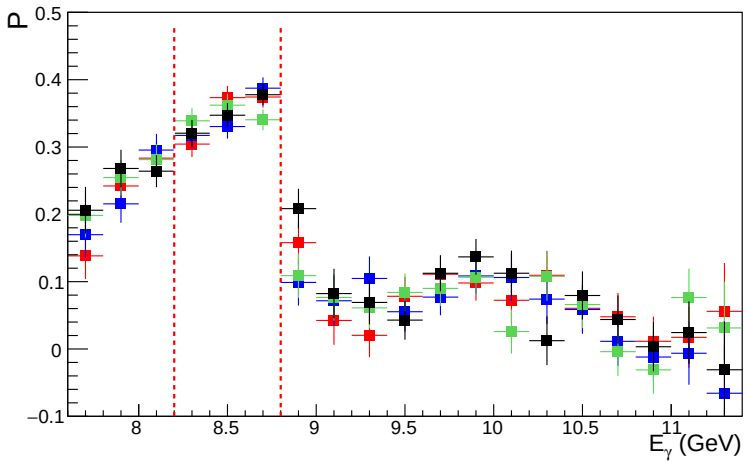

Figure 2.7: Photon beam polarization as a function of beam energy, as measured by the triplet polarimeter. Red points correspond to data taken with the polarization direction set to 0°, Blue points correspond to data taken with the photon polarization direction set to 45°, Green points correspond to data taken with the polarization direction set to 90°, Black points correspond to data taken with the polarization direction set to 135°. This plot is generated based on a script sent via e-mail [65].

2.1.5 Pair Spectrometer

The PS is designed to measure the flux of the incoming beam photons as a function of energy by detecting e^+e^- pairs produced in the Be foil placed in front of the TPol detector. The PS consists of a dipole magnet that bends the e^+ and e^- into two scintillating detector arms, as shown in Fig. 2.8. Similarly to the tagging hodoscopes the energy is determined by how much the electrons were bent by the magnetic field. The high resolution hodoscope is used to measure the leptons energy and time using Silicon Photo Multiplier (SiPM) readout. Behind the high-resolution hodoscope is a course hodoscope that is used in a coincidence trigger to reduce backgrounds due to lepton interactions near the magnetic edge regions by constraining the lepton trajectories [66]. The energy and time of each particle is measured with a 30 MeV energy resolution from photon energies of 6 to 12.5 GeV and 150 ns timing resolution.

2.2 Main Spectrometer

Once a linearly polarized beam has been produced, tagged, collimated and the beam flux and polarization measured it is sent into the main GlueX spectrometer. The main spectrometer is shown in Fig. 2.9. The photon beam is incident on a liquid hydrogen target. The target is surrounded by a Start Counter (ST) detector used for particle identification. After the ST there are two gas chamber detectors used for detecting the tracks of charged particles. the Central Drift Chamber (CDC) which measures particles at larger polar angles and the Forward Drift Chamber (FDC) which measures particles at smaller polar angles. Surrounding both of the tracking detectors is the Barrel Calorimeter (BCAL) which measures neutral particles at larger polar angles. In conjunction with the BCAL, the Forward Calorimater (FCAL) is used to detect neutrals particles in the forward direction. Surrounding the BCAL is a solenoid magnet which applies a magnetic field along the direction of the incoming beam photon. In front of the FCAL is a Time-of-Flight (TOF) detector used for particle identification.

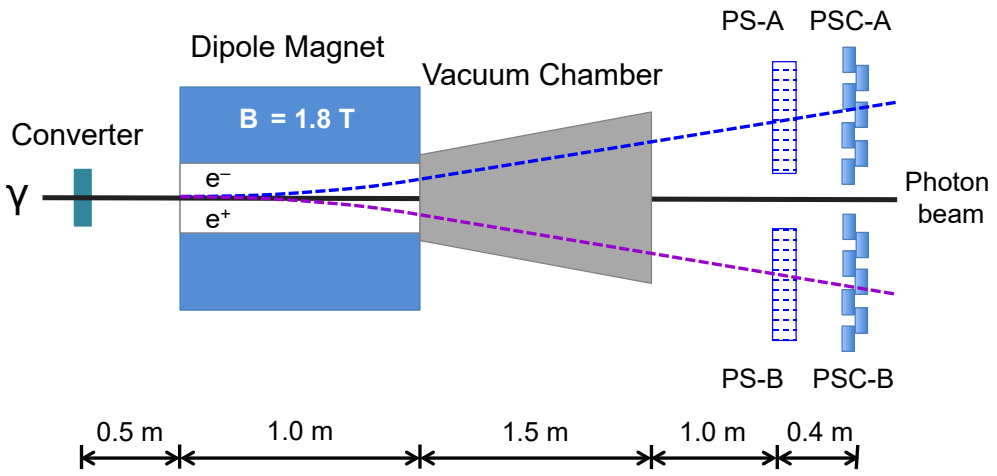

Figure 2.8: Pair spectrometer schematic showing the dipole magnet that separates the electron-positron pair [66]. The momenta of the electron and positron are measured by hodoscopes. The labeled 'PS' is the high-resolution hodoscope and the 'PSC' is the course hodoscope.

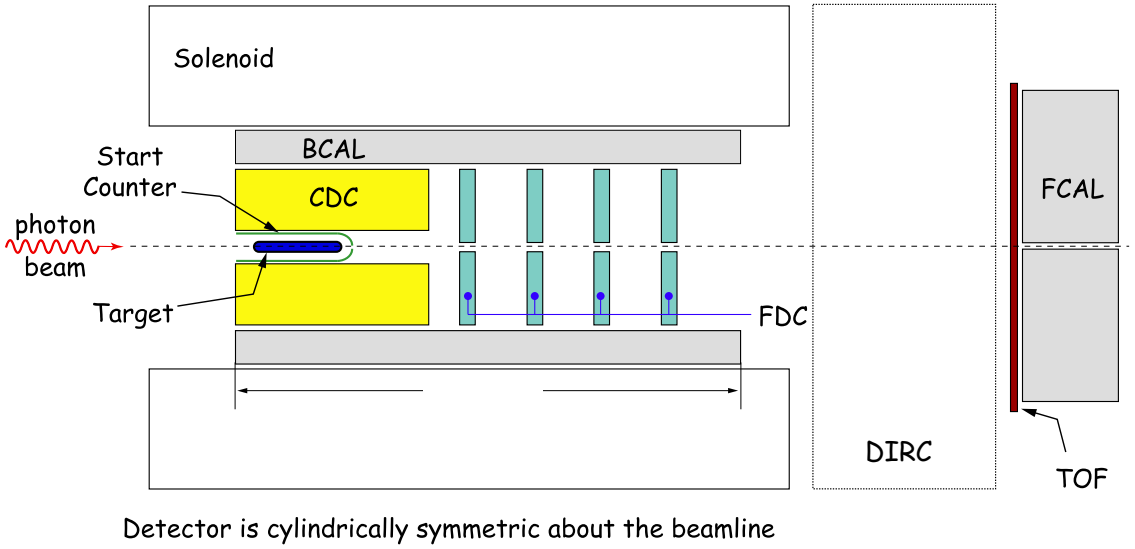

Figure 2.9: Cut-away schematic of the main GlueX spectrometer [67]. The DIRC was installed in Hall D during Winter 2019 and is not used in this analysis.

2.2.1 Liquid Hydrogen Target

The liquid hydrogen target is surrounded by the Start Counter and kept at 18K and 18 psi. The target is 30 cm long with an inner radius of 2.42 cm at the upstream end that slopes down to a radius of 1.56 cm at the downstream end. For the photon beam the 30cm thickness corresponds to 0.03 X_0.

2.3 Particle Identification Detectors

A wide variety of subdetectors contribute to particle identification but there are two detectors with the sole purpose of explicitly doing particle identification: the Start Counter (ST) and the Time-of-

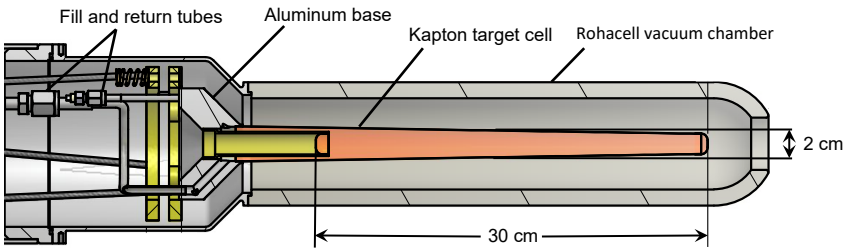

Figure 2.10: Target used by GlueX in Hall D, the liquid hydrogen is colored in orange [68].

Flight detector (TOF). A third PID detector, a DIRC detector, has been installed into Hall D and is being commissioned currently. The ST and TOF detectors are scintillator detectors while the DIRC uses quartz bars obtained from the BaBar experiment.

2.3.1 Start Counter

The Start Counter is made up of 30 scintillator paddles enveloping the liquid hydrogen target. The ST provides angular coverage of $7.5° < \theta < 149°$, Fig. 2.11. The scintillator paddles are read out by SIPMs due to their insensitivity to the magnetic field they're placed in. The primary responsibility of the ST is to identify the electron beam bunch associated with the primary interaction of the final state particles in each event at rates of 10^8 γ/s. The timing information from charged tracks are combined to determine which electron beam bunch is most likely matched to the primary interaction time in the target. A timing resolution of 550 ps has been demonstrated, surpassing the design resolution of 825 ps which allows the distinction between different RF beam bunches. The RF beam bunches are separated from each other by 4.008 ns. More information on the ST can be found in Ref. [69].

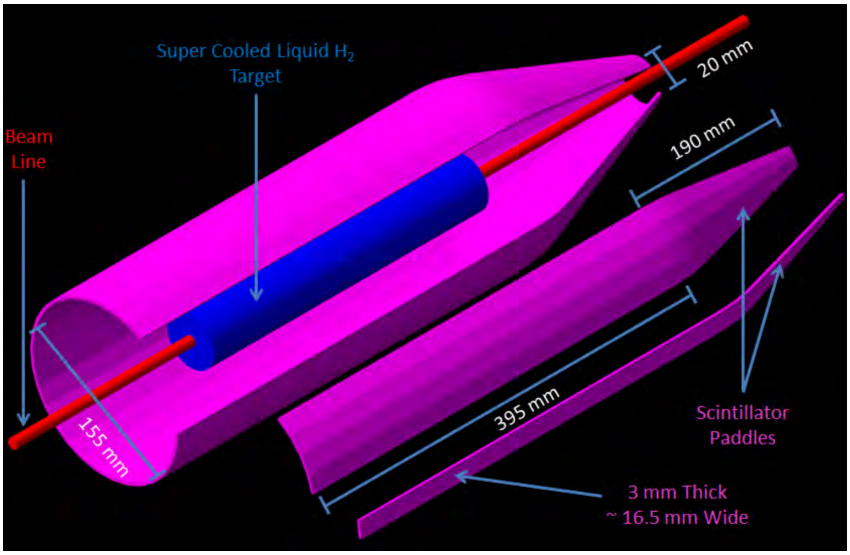

Figure 2.11: CAD rendering of the Start Counter enveloping the target [62].

2.3.2 Time of Flight Detector

The TOF detector is an array of horizontal scintillator paddles stacked in front of vertical scintillator paddles, Fig. 2.12. Each paddle is 252 cm long and 6 cm wide. A two-dimensional measurement of the track position is possible due to the crossing scintillator paddles. Hits in The TOF have their energy and time read out by photomultipler tubes (PMT). The TOF is placed downstream of the solenoid magnet with the purpose of measuring the time-of-flight of forward-going charged particles with an angular coverage of $1^\circ < \theta < 11^\circ$. The flight time of a particle is the difference between the arrival time measured in the TOF and the time of the associated RF beam bunch. The TOF has a timing resolution of around 100 ps and the RF timing resolution is negligible. The flight time measured by the TOF combined with the path measured by the tracking chambers allows the measurement of β vs momentum, Fig. 2.13. The measured β vs momentum is then compared with the analytical curves for known particle species, based on their mass. This allows the rejection of particle species hypotheses as a function of momentum. More details about the TOF can be found in Ref. [70]. The DIRC detector has been installed in front of the TOF and will provide better π-K separation for future run periods.

Figure 2.12: Time-of-Flight detector mounted in Hall D [61].

2.4 Charged Particle Detectors

The detection of the tracks of charged particles is performed by two detectors that both reside inside the solenoid magnet, the central drift chamber (CDC) and the forward drift chamber (FDC). These detectors measure the position and time of charged particles the reconstruct the particles momentum. Both of the detectors are ionization gas chambers filled with a mix of CO_2 and Ar gas. They are comprised of high voltage electrodes that create an electric field between a cathode and anode. If charged particles that enter the gas mixture are high enough energy they will ionze the gas and the ion pairs will drift towards the cathode while the free electrons drift towards the anode at a well-defined

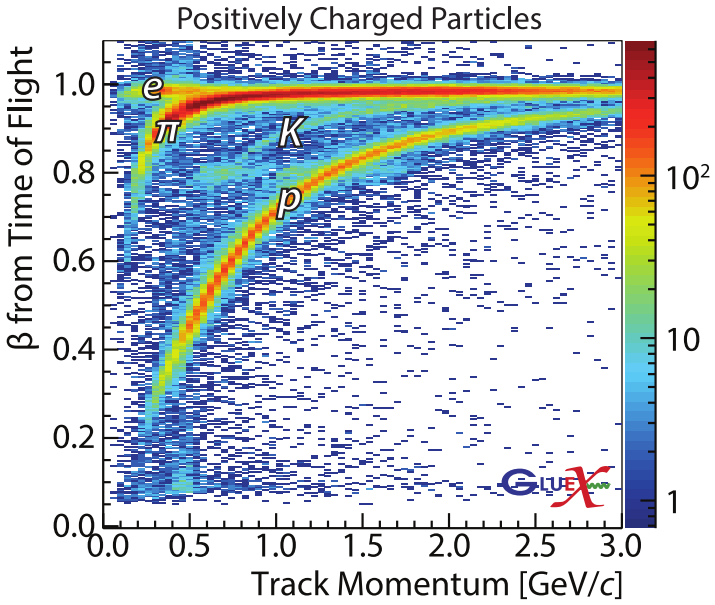

Figure 2.13: Relativistic velocity, β vs particle momenta for positively-charged particles to demonstrate the Particle identification in the TOF detector [71]. The band at $\beta \approx 0.8$ corresponds to a misidentified beam bucket and will be discussed further in Sec. 4.2.4.

velocity in the gas mixture. The high field gradient near the anode causes an amplification of the initial free electron, this avalanche of electrons is converted to an electrical signal and used to detect the position of the charged particle track. Since the radius of curvature of a track in the magnetic field is related to the particles momentum, by mapping out the track's position its momentum can be determined. The CDC uses straw tubes and the FDC uses planes of wire packages to serve as their anodes. The CDC provides polar angle coverage from 6° to 128° and the FDC covers angles shallower than 20°.

2.4.1 Central Drift Chamber

The CDC is cylindrical and surrounds the ST and consists of 12 layers of axial and 16 layers stereo straw tubes, a total of 3522 straws that are 1.5m long and 15.6mm in diameter. The chamber is filled with a 50:50 CO_2 and Ar gas mixture. The axial straw tubes go along the beam direction while the stereo straws are offset by 6° in both directions relative to the axial straws, as displayed in Fig. 2.14. The offset of the stereo straws improves the reconstruction of the z-position of tracks. Inside each straw is a 20μm diameter wire that is kept at a positive voltage relative to the straw to produce a uniform electric field inside the straw. The CDC measures the shortest drift time of the ionized electron to reach the wire using flash ADCs. The drift time in each straw is converted into a distance of closest approach to the wire and then combined with the same information from other straws to reconstruct the full track in the CDC. The position resolution of measured tracks is a function of various kinematic variables but exceeds the design resolution of 150 μm. The CDC also plays a role in PID by identifying protons for momentum up to 1 GeV. This is done by measuring the energy lost per unit length using flash ADCs. A clear proton band separated from all other particles can be seed in Fig 2.15. Even though the momentum range to separate protons is limited this is important for reconstructing the recoil proton which is typically low-momentum and have a large angle that is outside of the TOF coverage.

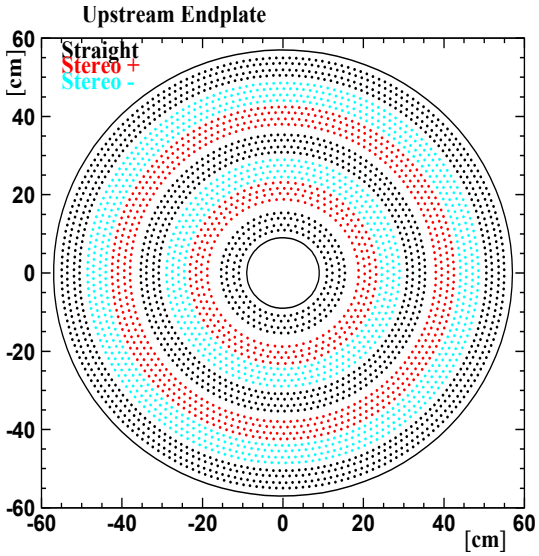

(a) Schematic slice of the CDC. Black circles represent axial straws, red and blue circles represent stereo straws offset by ± 6°, respectively [62].

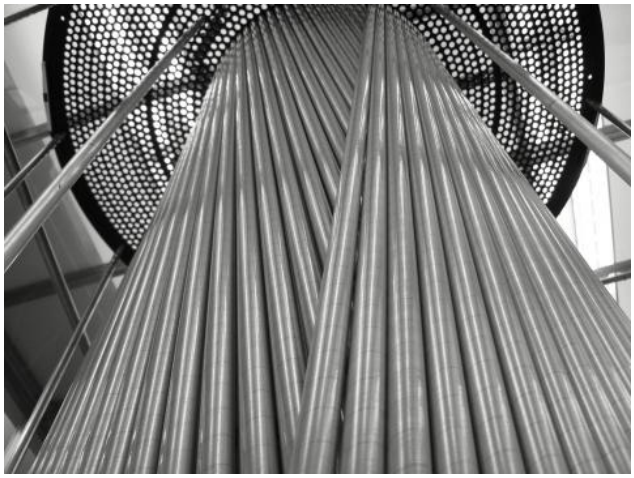

(b) Picture showing parts of layer of opposite-direction stereo straws before the rest of the straws were strung [61].

Figure 2.14: Central Drift Chamber detector visualization.

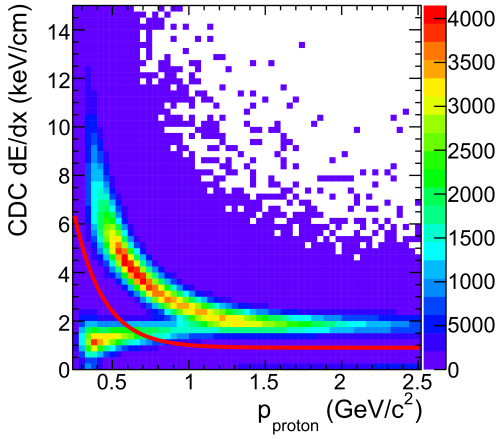

Figure 2.15: energy deposited per unit distance (dE/dx) as a function of proton momentum in the CDC. The curved band represents proton candidates. The horizontal band represents lighter charged particles such as π, e^+ and K candidates. The red curve corresponds to a loose cut to preserve all of the proton candidates up to momentum of 1 GeV.

2.4.2 Forward Drift Chamber

Downstream of the CDC is the FDC, Fig. 2.16, used to detect the forward-angled charged particles. The FDC is another ionization gas chamber with a geometry that is more suitable for detecting forward-going tracks. The FDC consists of 4 packages each containing 6 cells, where each cell is 1m in diameter and consists of 1 "U" and 1 "V" layer of cathode wire strips and 1 layer of anode wires is placed between the 2 cathode layers, Fig. 2.18. The "U" and "V" cathode layers are offset by ± 75° with respect to the anode wire. The anode wires are maintained at positive voltage with respect to the cathode. Each cell

records 3 hits, the two cathode strips measure the drift time along the wire while the anode wire measures the drift time perpendicular to itself. This allows for a three-dimensional position to be reconstructed in each cell. Each cell within a package is offset by 60° with respect to the one in front of it and is filled with a 40:60 CO_2 and Ar gas mixture. This allows the reconstruction of tracks at high density close to the beamline. By combining the information of the cells and packages the track position is reconstructed. The FDC has demonstrated a position resolution that exceeds the design resolution of 200 μm and is also capable of providing proton separation by measuring the dE/dx of forward-going charged particles. More details about the FDC can be found at Ref. [72].

Figure 2.16: View of the FDC before being inserted into the solenoid magnet bore. The 4 FDC packages are visible as the thick bands of readout cables [61].

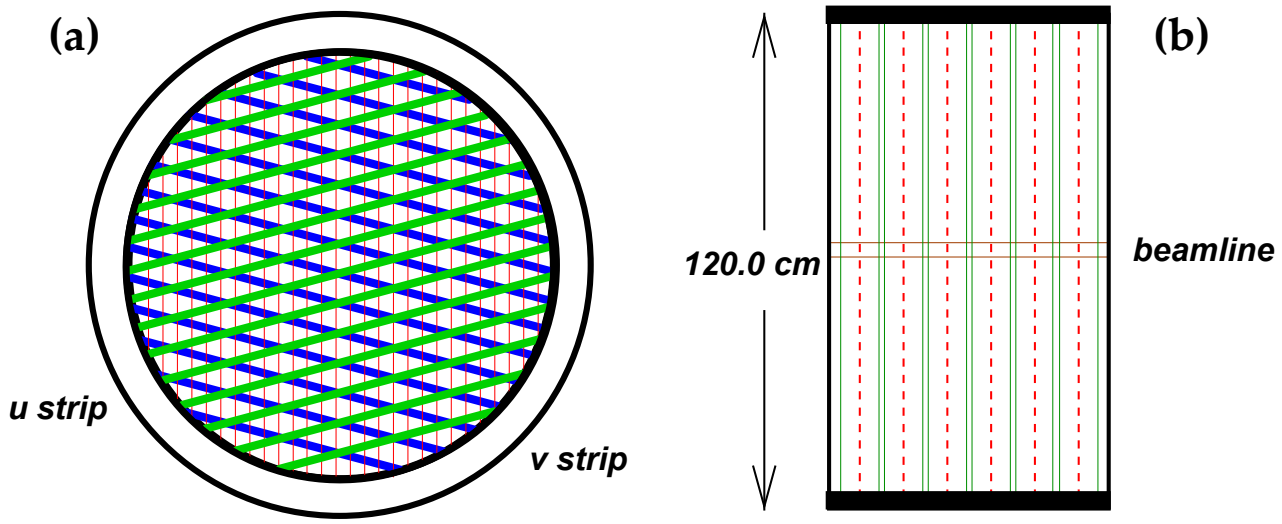

Figure 2.17: (a) Cross-section slice of the front of the FDC. The wires are shown as vertical red lines. The solid-green lines represent the u-strips and the solid-blue lines represent the v-strips. The Packages are oriented at ± 75° with respect to the wires. (b) Shows a side view of one FDC package. The red-dashed lines represent the wires and the green-solid lines represent the cathod planes. Each cathode plane is offset by 60° from the plane in front of it [73].

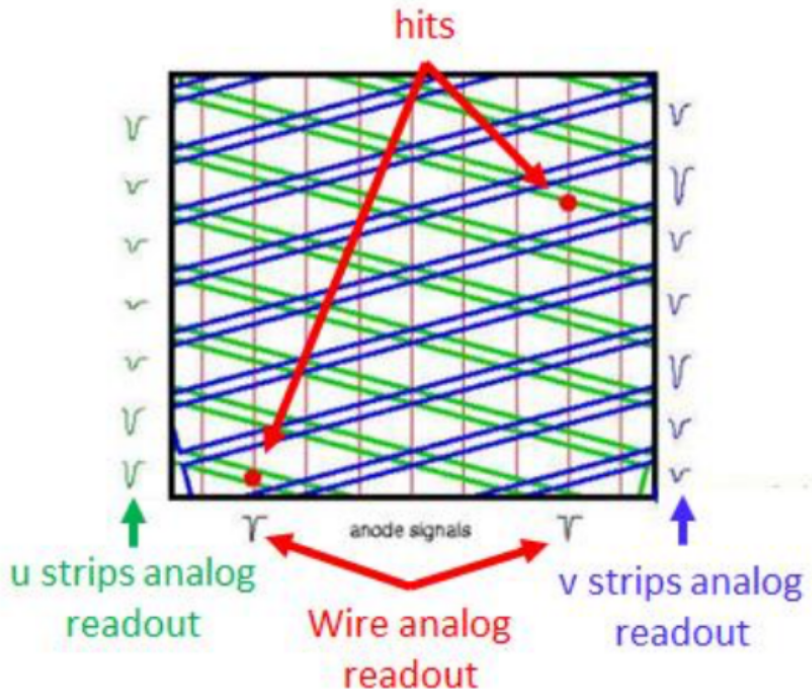

Figure 2.18: An illustration of how the FDC readout is designed to work [73].

2.5 Calorimetry

There are two electromagnetic calorimeters responsible for measuring the energy, position and arrival time of neutral particles: The Barrel Calorimeter (BCAL) and the Forward Calorimeter (FCAL). Both of these detectors are designed for the detection of photons, which will interact with the detectors to produce electromagnetic showers inside the detectors. An incoming photon will interact with the material in the calorimeter and electromagnetically shower, as sketch in Fig. 2.19. A photon converts into an electron-positron pair while the electron and positron emit photons via the Bremsstrahlung process. These two processes continue on until there is not sufficient energy or the shower leaks out of the calorimeter. The FCAL has an acceptance for polar angles less than 11.5° and the BCAL covers polar angles spanning from 11° to 126°.

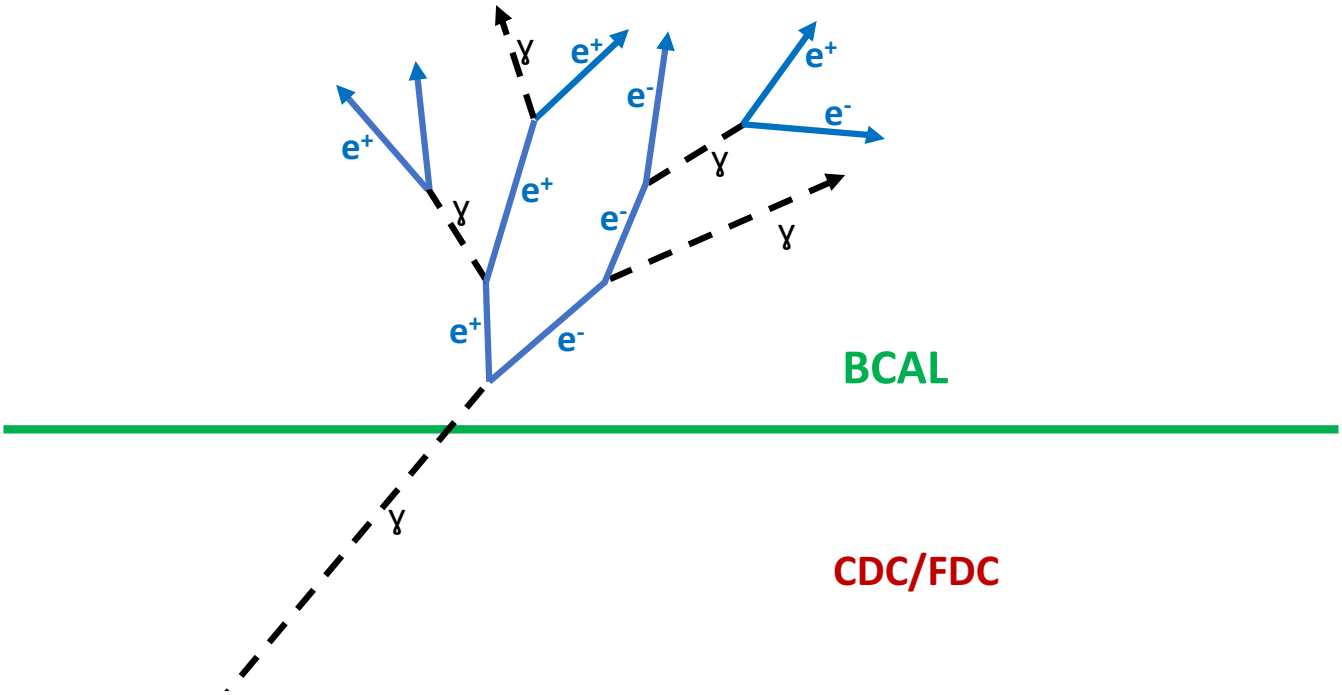

Figure 2.19: Simple illustration of the start of an electromagnetic shower in the BCAL.

2.5.1 Forward Calorimeter

The FCAL is a planar detector with radiation length of 3.1cm placed 5m downstream of the target and orthogonal to the beam axis, behind the TOF detector. It is comprised of 2800 lead-glass blocks that have photomultiplier tubes attached to their downstream ends, as shown in Fig. 2.20. The lead-glass blocks are stacked to make up an approximately circular detector with a radius of about 1.2m. Forward going particles from meson decays can be spatially close to each other so having a large-faced calorimeter placed far downstream helps to resolve particles. The PMTs are able to detect the Cherenkov light that's produced from the leptons in the electromagnetic showers inside of the blocks. By measuring the amount of light produced in each block the energy deposited can be determined. A typical shower will deposit energy in multiple blocks and they are grouped together to form clusters. The cluster information will

contain the energy, position and time associated with the incident particle. The mass resolution of a $\pi^0 \to 2\gamma$ and the single photon energy resolution have been measured and shown in Fig. 2.21. The resulting photon energy resolution is $\sigma_E/E = 5.931\%/\sqrt{E(GeV)} \oplus 3.656\%$ [74]. While the primary responsibility of the FCAL is to reconstruct electromagnetic showers it also plays a role in separating electrons from charged hadrons by taking the ratio of the energy deposited in the calorimeter and the momentum of the charged track matched to the shower. Since electrons and positrons have very small mass they are separated from charged hadrons. Since electrons are much lighter than charged hadrons the FCAL can separate electrons by considering the reconstructed energy of the shower in the FCAL divided by the momentum of the track. More details about the FCAL can be found in Ref. [62].

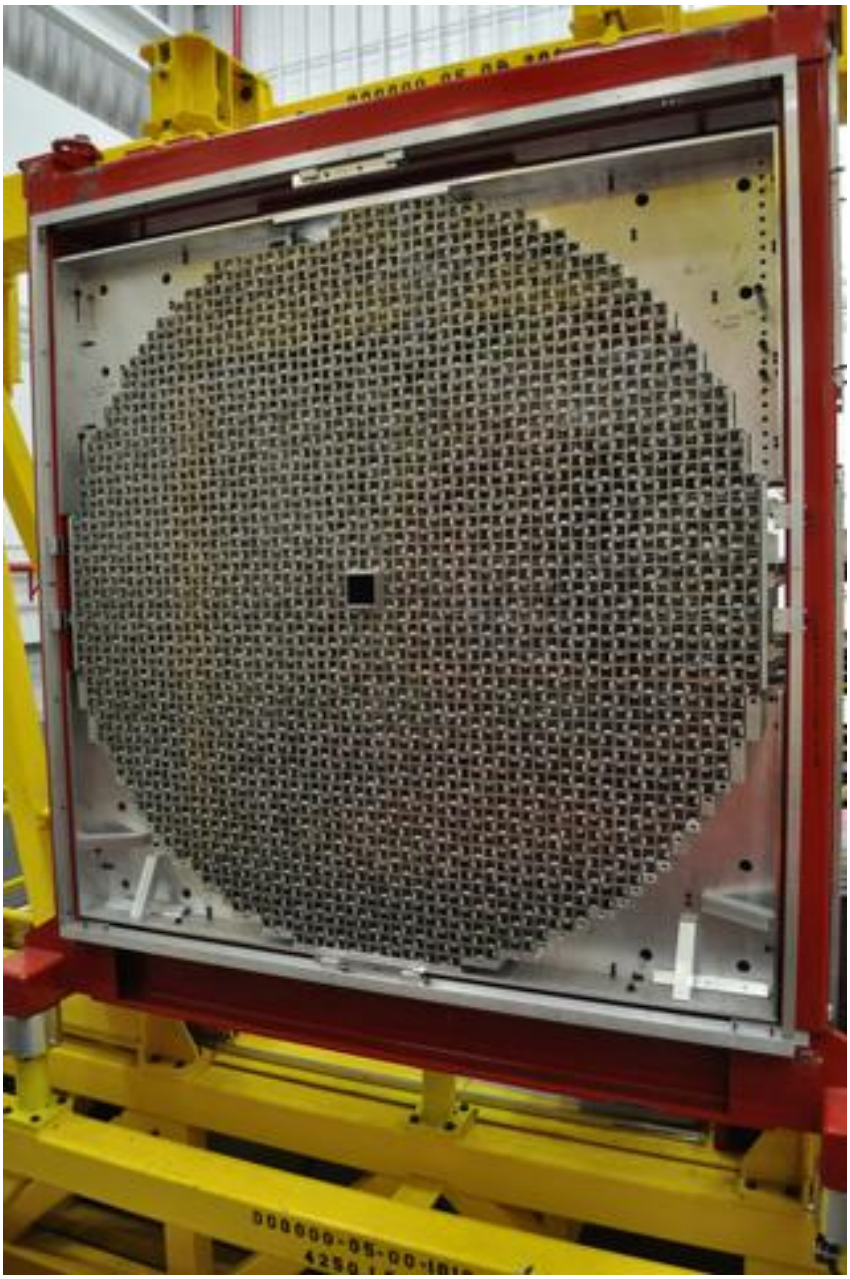

Figure 2.20: View of the front face of the FCAL before the dark room enclosure has been installed behind it [61].

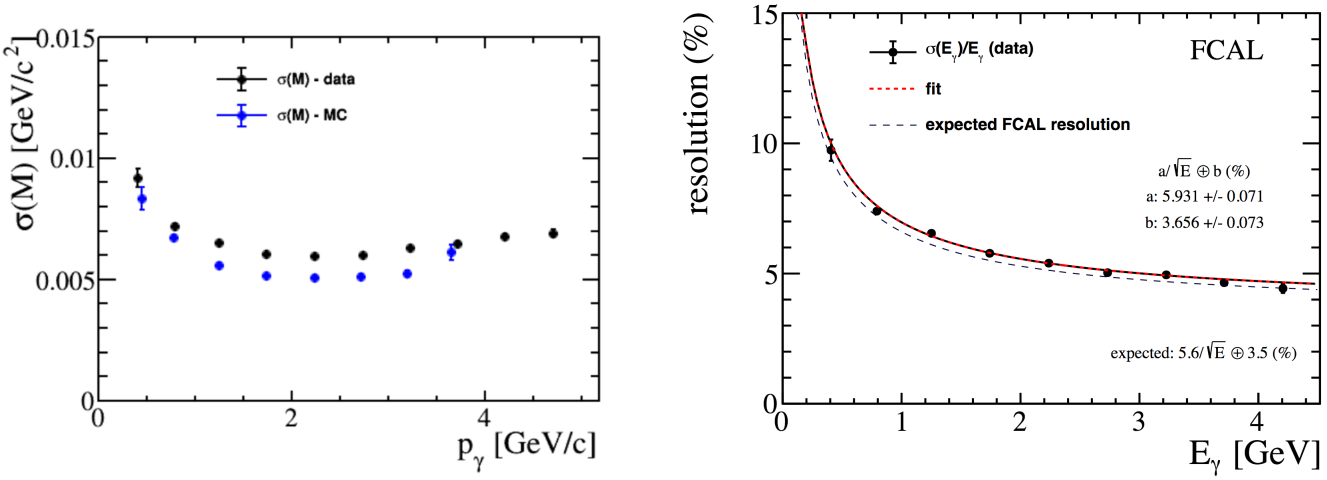

(a) π^0 mass resolution in the FCAL.

(b) Single photon energy resolution FCAL.

Figure 2.21: Distributions to extract the single photon energy resolution in the FCAL [75].

2.5.2 Barrel Calorimeter

The BCAL is a cylindrical detector that envelops the CDC and FDC with an inner radius of 65cm, an outer radius of 90cm and length of 390cm as shown in Fig. 2.24. The shower containment is a function of angle, there are 15.3 radiation lengths for particles normal to the BCAL and 67 radiation lengths for particles incident at $\theta = 14°$. The BCAL is comprised of a lead-scintillating fiber matrix. The 0.5mm thick sheets of lead produce electromagnetic showers and are interleaved with 1.0mm in diameter scintillating fibers to collect the light. Light guides are placed on the ends of the BCAL to collect the light from the fibers and guide it to the light sensors. The detector is segmented azimuthally and radially with silicon photomultiplier arrays (SIPM) chosen as light sensors on both ends for double-ended readout, resulting in 1536 total readout channels as shown in Fig. 2.22. The SiPMs convert the light into an electronic signal delivered to a custom JLab 250 MHz fADC readout in each channel [77]. Each fADC samples every 4ns to generate waveforms as shown in Fig. 2.23. The firmware computes several derived features of the pulse: the pedestal, peak value, integral over a selected window and time of the half-way point on the leading edge. The full waveforms aren't read out during physics production data-taking due to both processing speed and data size limitations. The BCAL also utilizes TDC readout to record timing information that is more precise than the fADC timing. Calibrations are applied the raw ADC and TDC data to produce energy, time and position values for reconstructed particle showers. The calibration that converts the ADC integral into a physical energy will be discussed in further detail in Sec. 3.1.

The BCAL readout is segmented into 192 azimuthal parts, called sectors, and 4 radial parts, called layers. The double-ended readout allows us to measure the position along the beam-axis by taking the time difference on both ends of the barrel. The channel in the inner most layer corresponds to one SiPM array while each radially-increasing layer is a sum of one more SiPM array than the previous layer. SIPMs are chosen for readout because they are insensitive to magnetic fields. The disadvantage of using SiPMs instead of PMTs is the higher dark rate, to mitigate the dark rate the SiPMs are cooled to 7°C. Light guides are placed at the ends of the BCAL to collect light which is sent to the SiPMs. The clustering of all these different cells to reconstruct the properties of a shower is explained in Sec. 3.2.

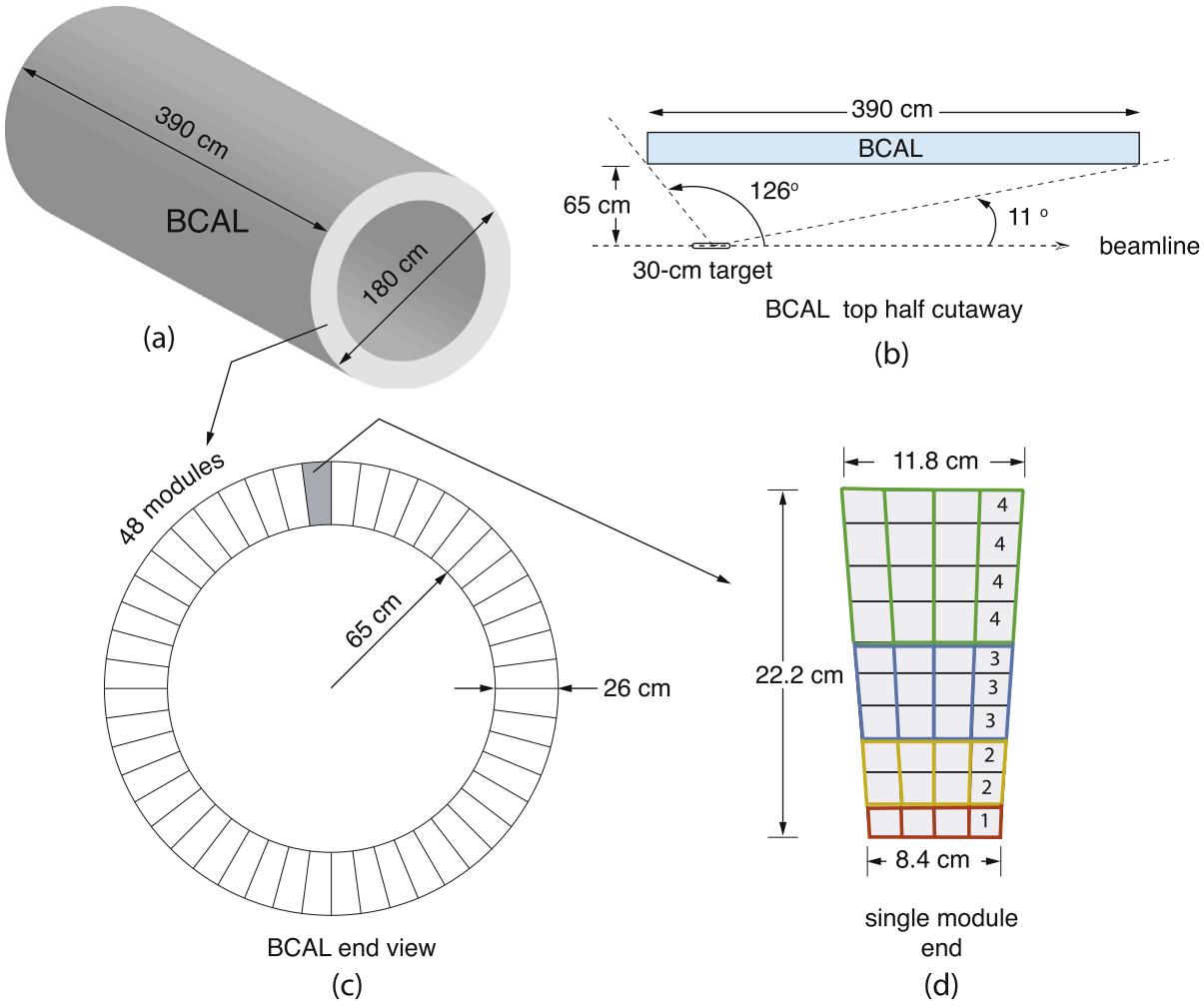

Figure 2.22: Schematic view of the BCAL. The different colors in the bottom right panel indicate a different BCAL layer [76].

The response of the calorimeter has been measured and performs as expected for electromagnetic showers. The performance of the BCAL is characterized using the energy resolution integrated over typical angular distributions for π^0 and η production yielding $\sigma_E/E = 5.2\%/\sqrt{E(GeV)} \oplus 3.6\%$. The mass distribution and mass resolution of $\pi^0 \to 2\gamma$ decays where both photons hit the BCAL is shown in Fig. 2.25. The mass resolution depends on both the energy and position resolutions of the detector. The mass resolution of the π^0 sample has significant contributions from the position resolution because it has a small opening decay angle but the η mass resolution is dominated by the energy resolution. The mass resolution as a function of the average photon energy for π^0 and η samples can be seen in Fig. 2.26 and Fig. 2.27. The position resolution is matched between data and simulation, therefore the energy resolution in simulation is tuned until the π^0 mass resolution is matched between data and simulation. The resulting energy resolution input into the simulation is quoted as the single photon energy resolution corresponding to π^0 decays in the BCAL. Since the mass resolution of η is expected to be dominated by the energy resolution, the single photon energy resolution can be extracted directly from data by ignoring the position resolution. A more sophisticated study of the energy resolution in the BCAL is underway. The timing information output from the BCAL is used in PID with a timing resolution of $\sigma = 150$ ps at 1 GeV which is particularly useful for identifying high momentum protons

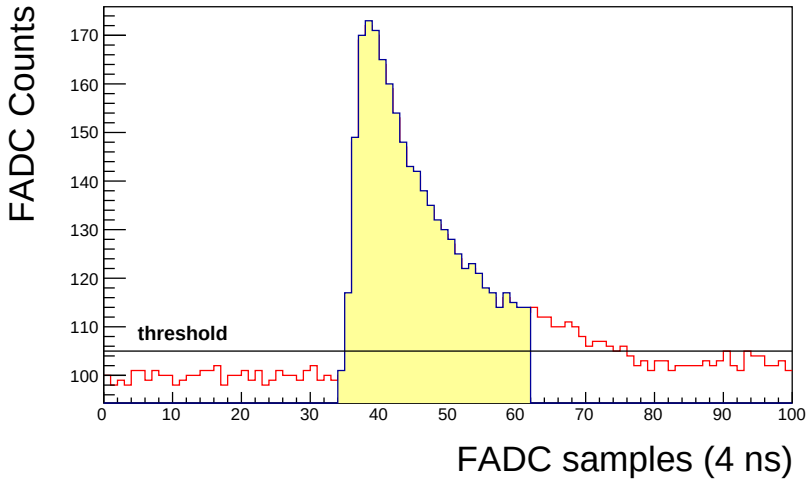

Figure 2.23: Typical FADC waveform corresponding to 20 MeV energy deposition. The readout threshold was set to 105 counts, where each counts corresponds to 0.4882 mV. The filled area in the histogram corresponds to the integration window [76].

that the CDC can't discriminate. The BCAL is also capable of recording the energy, time and position of charged particles which is useful for separating electrons from pions by looking at E/p distributions. More details about the BCAL can be found in Ref. [76].

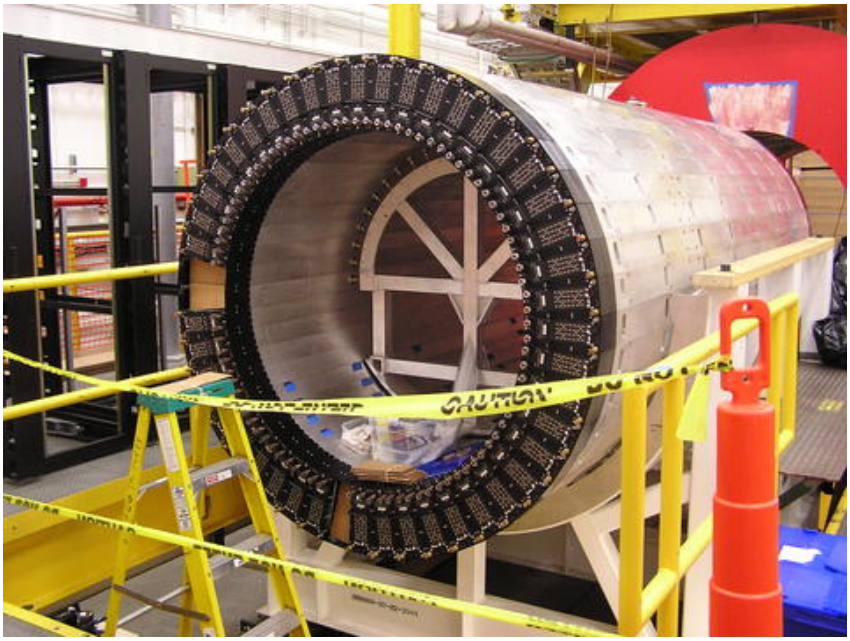

Figure 2.24: View of the upstream face of the BCAL before being inserted into the solenoid bore [76].

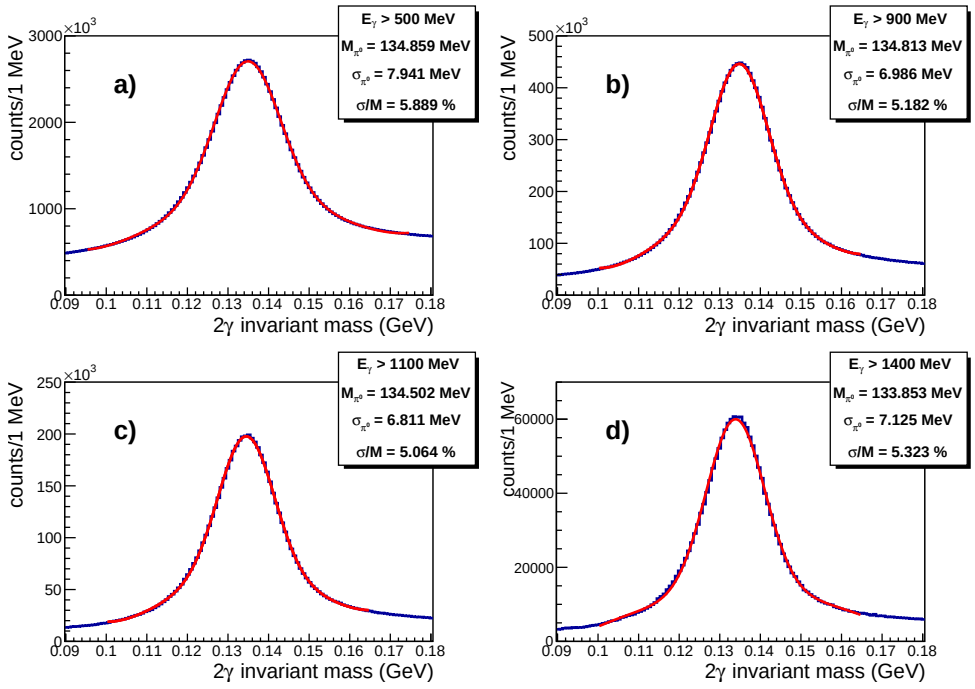

Figure 2.25: Inclusive π^0 samples after BCAL calibrations were complete for 4 varied shower energy cuts. The disitributions are fit with a double gaussian + an order order-2 polynomial.

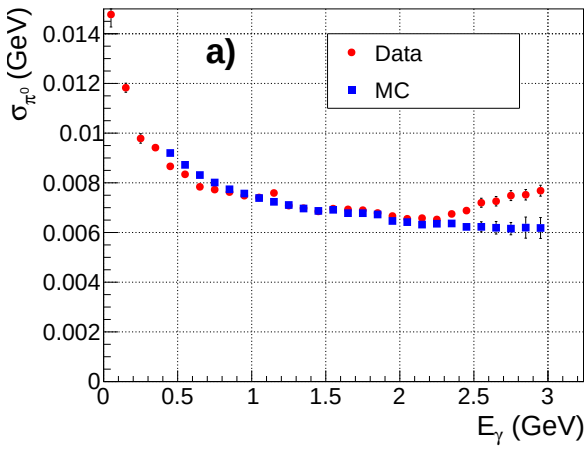

(a) π^0 mass resolution in the BCAL.

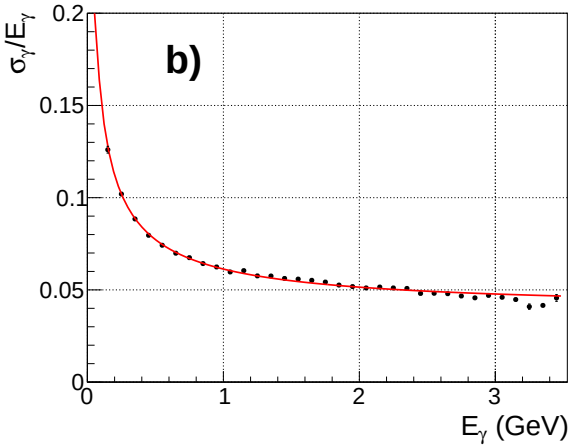

(b) Energy resolution input into the simulation to match π^0 width distributions in the BCAL.

Figure 2.26: The MC data points are fit yielding a = 4.70±0.03$\sqrt{GeV}$ and b = 3.93±0.03, which is shown as a continuous curve. The simulation contained position smearing based on an independent position resolution measurement that matched data and simulation resolutionst6y7.

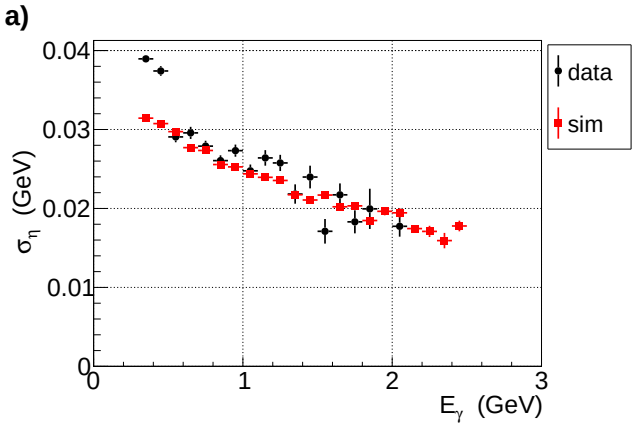

(a) η mass resolution in the BCAL.

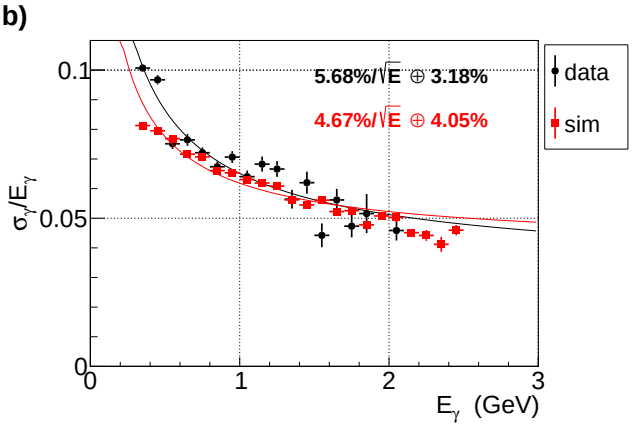

(b) Energy resolution in the BCAL assuming that the η mass resolution only depends on the energy resolution.

Figure 2.27

Chapter 3

BCAL Calibrations and Reconstruction Software

Before Gluex was in a position to make physics measurements we had to demonstrate that we understood our detectors. A substantial amount of effort was put into calibrating the entire GlueX detector and improving the analysis software to get to that point. This chapter will give some highlights on my efforts put forth towards calibrating and commissioning the BCAL.

3.1 Gain Calibration

The gains of the flash ADC readout are used to set the energy scale of the BCAL. The absolute energy scale of all channels are set to match the energy of well-known physics samples. A typical shower will deposit energy in many BCAL channels making it important to balance the gains of each channel relative to each other. By balancing the gains the energy resolution associated with an incident photon shower will be minimized when many channels are combined to reconstruct a cluster.

Two different techniques using a high-statistic inclusive $\pi^0 \to 2\gamma$ sample have been used to calibrate the gains for each channel in the BCAL. Since a sample of photons with known energy is not available a π^0 sample is used as reference for calibration because its mass is precisely known. The energy deposited in each channel by the 2 photon decays can be used to calibrate the gains of each channel by constraining the reconstructed π^0 mass to the literature value of the π^0 mass. Both techniques rely on extracting a relatively clean and high statistic sample of $\pi^0 \to \gamma\gamma$ using the full range of incident beam photons between 3 and 12 GeV to perform the calibration. Events that have at least two charged particles and two photons that reconstruct close to the π^0 mass were selected. The charged particle tracks were required to better determine the event vertex position. Since the BCAL has an angular coverage from $11^\circ < \theta < 126^\circ$ with respect to the target position, the π^0 mass distribution peak and width depend significantly on the location of the primary event interaction. The vertex position is most accuratly determined when 2 or more tracks are reconstructed in the event because the position-of-closest-approach between the 2 tracks can be used to determine the vertex instead of the position-of-closest-approach between 1 track and the beamline position. The four-momentum vectors of the photons are reconstructed by fixing the event vertex position as their point of origin. The minimum shower energy that was included into the calibration sample was set to be 300 MeV in order to produce a clean π^0 sample. This resulted in a signal-to-background ratio of greater than 4 to 1, which was determined to be the minimum signal-to-background ratio for both techniques to reliably converge. The gain constants were determined for run periods that had uniform experimental conditions and collected sufficient statistics to determine the

gain constants for every channel. These calibration data-taking periods typically lasted several weeks. Typical distributions of the two-photon invariant mass spectrum after the calibration converged are shown in Fig. 2.25.

The first technique that was applied was derived from the RADPHI experiment and is described in detail in Ref. [78]. In this technique the extremum to a global fit function is found by adjusting the gain factors of individual channels. The fit function that is minimized is given by

$$F = \sum_{i=1}^{N}(m_i^2 - m_0^2)^2 + 2\lambda\sum_{i=1}^{N}(m_i^2 - m_0^2). \tag{3.1}$$

In this equation m_i is the reconstructed π^0 invariant mass and m_0 is the known mass of the π^0 meson. The index i denotes the event number in the π^0 sample and N is the total number of π^0 events in the data sample. The constraint that $< m_i^2 > = m_0^2$ is expressed in the second term with the Lagrange multiplier, λ. Since the π^0 mass is known, the kinematics are overdetermined and the extra information can be used to iteratively adjust the gain factors for each BCAL channel in order to minimize the difference between the reconstructed mass and the known mass. Assuming that the two detected photons come from the decay of a single particle, then the decaying particle's invariant mass squared comes from the energy-momentum relation:

$$m^2 = E^2 - |\vec{p}|^2. \tag{3.2}$$

This can be rewritten in a form that contains only the reconstructed shower quantities and used to reconstruct the π^0 sample,

$$m^2 = 2E_{cluster,1}E_{cluster,2}(1 - \cos\psi). \tag{3.3}$$

For the $\pi^0 \to \gamma\gamma$ decay. The E_1 and E_2 are the energies of two photon showers and ψ is the angle between them on the plane defined by their momentum vectors.

The cluster energy is calculated as the sum of the BCAL point energy over each channel included in the cluster, namely

$$E_{cluster,j} = \sum_k E^k_{point,j} \tag{3.4}$$

where j is the π^0 photon index, which can be 1 or 2. The index k is the BCAL readout channel, spanning from 1 to 768. The point energy corresponds to the energy deposited inside the volume of the BCAL. The energy deposited in the fibers of the BCAL is propagated and attenuated to both ends of the BCAL to the readout channels. The attenuation lengths of the fibers are measured independently allowing for the conversion of energy measured at the readout ends to the point of interaction inside the barrel, which is reported as the BCAL point energy. The BCAL has 1536 readout channels in total, when both upstream and downstream ends are considered. The gain calibration technique is used to find the gains for all 1536 readout channels. The calibration is an iterative process, where each iteration introduces channel-dependent gain correction factors:

$$E'_{point,k} = c_k E_{point,k} = (1 + \epsilon_k)E_{point,k} \tag{3.5}$$

where $E_{point,k}$ is the measured energy, c_k is the gain factor for each channel and ϵ_k is another expression for the same gain factor. Primed notation is used to denote that a gain factor is applied to the measured $E_{point,k}$. Minimizing Eq. 3.1 with respect to ϵ_k we see that:

$$\frac{\partial F'}{\partial \epsilon_k} = 2\sum_{i=1}^{N}\left(m_i^2 - m_0^2 + \lambda + \sum_{k'}\epsilon_{k'}\frac{\partial m_i'^2}{\partial \epsilon'_k}\right)\frac{\partial m_i'^2}{\partial \epsilon_k} = 0 \tag{3.6}$$

The solution is given by:

$$\epsilon_k = [C^{-1}]_{kk'}(D - \lambda L)_{k'} \tag{3.7}$$

where:

$$C_{kk'} = \sum_{i=1}^{N} \left(\frac{\partial m_i'^2}{\partial \epsilon_k} \frac{\partial m_i'^2}{\partial \epsilon_k} \right) \tag{3.8}$$

$$D_k = -\sum_{i=1}^{N} \left((m_i^2 - m_0^2) \frac{\partial m_i'^2}{\partial \epsilon_k} \right) \tag{3.9}$$

$$L_k = \sum_{i=1}^{N} \frac{\partial m_i'^2}{\partial \epsilon_k} \tag{3.10}$$

$$\lambda = \frac{B + L^T C^{-1} D}{L^T C^{-1} L} \tag{3.11}$$

$$B = \sum_{i=1}^{N} (m_i^2 - m_0^2) \tag{3.12}$$

In order to solve the gain factors in Eq. 7 the 768 x 768 matrix, $C_{kk'}$, must be inverted. The elements of matrix C are statistically obtained by sampling a finite number of π^0 events. When taking the inverse of C there will inevitably be instabilities which require careful treatment. In order to properly handle these instabilities C^{-1} is expressed in terms of its eigendecomposition, namely

$$[C^{-1}]_{kk'} = \sum_{\alpha} \frac{1}{c(\alpha)} e_k(\alpha) e_{k'}(\alpha), \tag{3.13}$$

where $c(\alpha)$ are the eigenvalues and $e(\alpha)$ are the orthonormalized eigenvectors of C. There will be some eigenvalues of C whose values are statistically low, these values will dominate when taking C^{-1}. In order to deal with these instabilities, Eq. 3.13 gets truncated to include eigenvectors of C whose eigenvalues are statistically well determined by the sample. Once C^{-1} is calculated, the new gain factors can be calculated directly.

An alternative method of using a π^0 sample to calibrate the gains was developed to be complimentary. In this method the gain of a channel is adjusted only if it contributes a significant amount of energy to the total energy of a shower that results from a π^0 candidate. If a channel that belongs to the first 2 layers contributes more than half of the total energy of a shower that resulted from a π^0 candidate then the two photon invariant mass is plotted. This method is more challenging for the third layer of the BCAL because showers don't tend to deposit half of their energy in a single channel that deep into the calorimeter. A channel in layer 3 only needs to contribute 40% or more of the total shower energy to produce distributions with a prominent enough mass peak to perform the calibration. All such events are histogrammed for each dominant channel and the distribution for each channel is fit with a Gaussian. The ratio of the known π^0 mass and the fit π^0 peak position is computed and applied

as a modification to the gain on each channel. This is a brute force attempt to move reconstructed π^0 mass peak position closer to the known π^0 mass. This procedure is iterated until the reconstructed π^0 peak position is aligned with the known π^0 mass for each channel. This method does not work for the fourth layer where π^0 decays don't tend to deposit enough energy into a single channel. Following the final iteration, the calibrated π^0 mass peaks are less than 1 MeV away from their true value. The fitted peaks of the π^0 masses after making the cut that a channel in the shower contains at least 40% of the total shower energy for layer 3 and at least 50% of the total shower energy for layers 1 and 2 are shown in Fig. 3.1 before and after the calibration procedure.

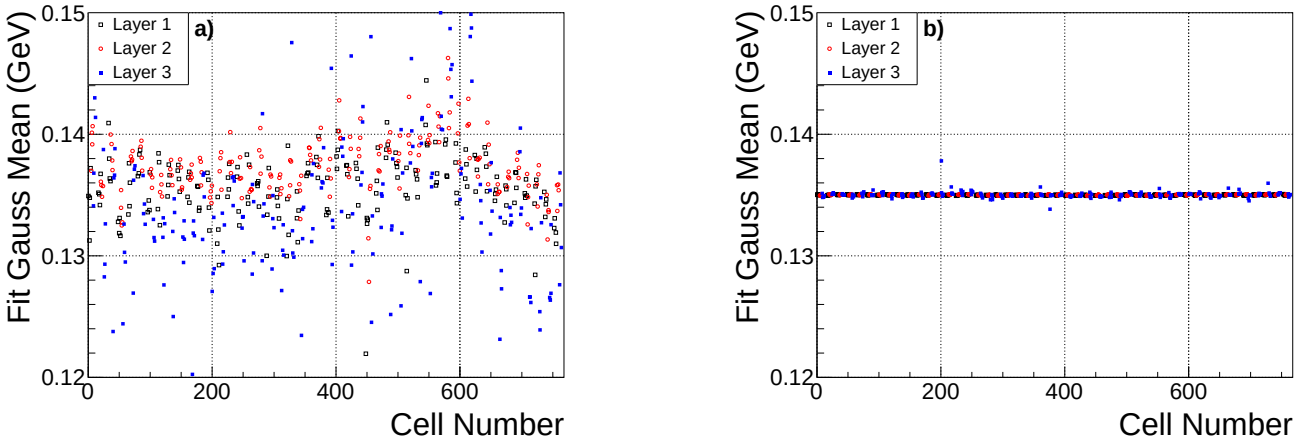

(a) Before the gain calibration.

(b) After the gain calibration.

Figure 3.1: Fitted peak of the π^0 mass distribution as a function of BCAL channel ID.

This second technique of fitting each channel and adjusting the gains directly requires an order of magnitude more data than using the global fit function method because showers tend to be spread out over many channels in the BCAL. However, the brute force method of fitting each channel directly has provided us with more closely aligned gains throughout the detector and significantly improved π^0 mass resolutions than using the global function minimization technique. These two techniques are complimentary to each other. For the cells in the fourth layer the calibration technique requiring matrix inversion. For the first three layers the fitting and adjusting technique is used because it results in a better energy resolution.

3.1.1 Nonlinear Correction

After the gain calibration is complete a walk of the π^0 mean as a function of energy is observed. At low energy the mean-walk is suspected arise from threshold effects and at high energies the mean-walk is suspected to arise from saturation of the fADCs and SiPMs. Once again a π^0 sample is used to make a non-linear correction. Since a $\pi^0 \to \gamma\gamma$ decay sample is used to make the correction to each single photon shower energy symmetric decays are required in order to place a correction on single shower energy. This allows the measured mass of the π^0 to serve as a proxy for the energy of a single photon. More specifically, both showers are required to be within 100 MeV of each other. This allows the $\pi^0 \to 2\gamma$ decay to serve as an approximate for a single shower. Therefore the mean-walk as a function of energy can be seen in Fig. 3.2. This method is limited to reach up to energies of around 3 GeV. Higher energy π^0 rarely decay both photons into the BCAL and also have very small opening angles which makes it technically challenging to resolve both photons. An alternative approach is needed to

study the nonlinear dependence above 3 GeV. The function that is used to correct the shower energies is given by Eq. 3.14.

$$f(E) = p_0 - p_1 e^{(-p_2 E + p_3)} - \frac{p_4}{(p_5 + p_6 e^{(-p_7 E + p_8)})} \tag{3.14}$$

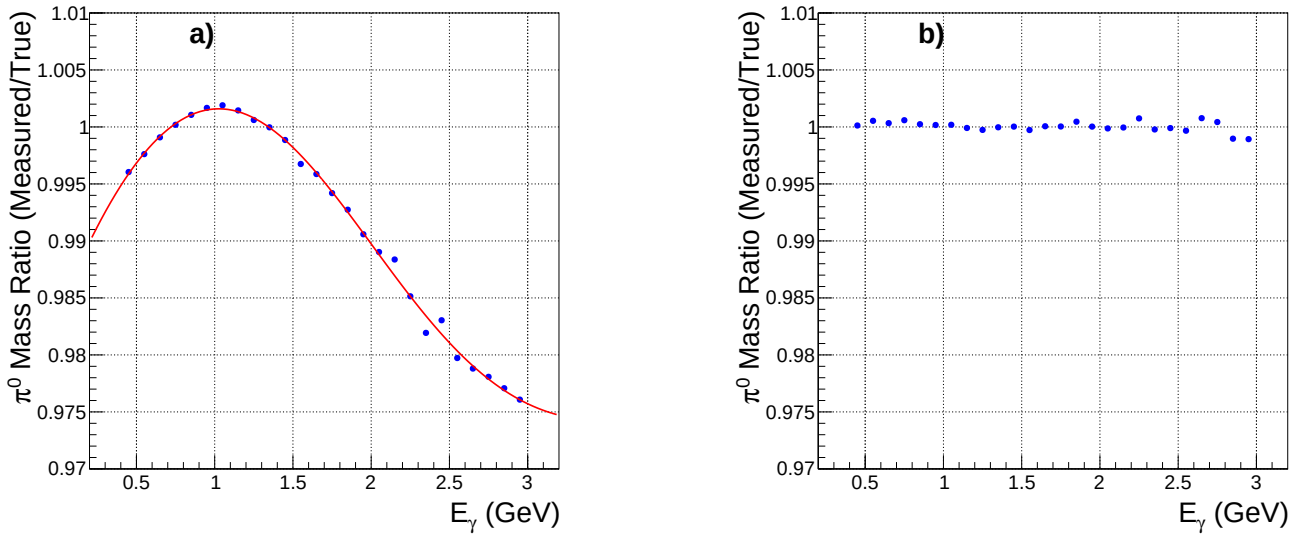

(a) Before the nonlinear correction.

(b) After the nonlinear correction.

Figure 3.2: The Gaussian mean fit to the π^0 mass distribution peak divided by the known π^0 mass value as a function of the 2γ average energy when both showers are within 100 MeV of each other. The red line represents the function that we use to correct the reconstructed single photon shower energy in Eq. 3.14.

3.2 Clustering Algorithm

Detecting photons is the primary goal of the BCAL but the BCAL is not limited to only detecting photons. A clustering algorithm has been developed to identify which channels share the energy deposited by a single particle incident on the BCAL and groups them into a single cluster. The first step of the clustering algorithm is to search through all of the channels that contain energy deposition and find the highest energy BCAL point. The BCAL point contains information of how much energy was deposited inside each cell, when the energy was deposited with respect to the beam bunch time and where the energy was deposited in cylindrical coordinates (r, ϕ, z). The point information is extracted from 1 readout channel on one end of the detector and a parallel channel on the other end. The highest energy point is used to seed the first cluster if it is above the cluster threshold of 15 MeV. The noise level is below the channel readout threshold of 2.2 MeV. Points that are in geometrical proximity to the cluster seed are added to the cluster based on how close and how much energy was deposited relative to the total cluster energy as described in Sec. 3.2.1. Each time a point is added to the cluster, the cluster's centroid position, time and energy are updated and that point is removed from the available pool of points. This procedure is repeated until all of the remaining points in the event are exhausted. In the next step, the clustering algorithm searches for the highest energy point in the event that hasn't been included into a cluster already. If the highest energy point remaining is above the cluster seed threshold then it will form a new cluster and the procedure is iterated. This will continue on until there are no more points in the event that are above the cluster seed threshold. The challenge of clustering is that there are various ways for two different particles to deposit energy nearby each other. A good clusterizer will be an optimization of clustering the energy deposited that is associated with a single particle while resolving two particles from one another. The energy, position and time of the cluster are computed based on the same quantities of the included points. Most of the cluster energy is contained in the points (double-ended hits), although single-ended hits are added to the total energy sum but are not used to compute the position or time of the cluster. The BCAL has two separate clustering routines for neutral and charged particles as described in Sec. 3.2.3.

3.2.1 Neutral Clusterizer

The neutral clustering is done in spherical coordinates to maintain symmetry with the physics processes. The clustering algorithm looks at points nearby the newly formed cluster and determines if they should be included in the cluster based on three parameters: the clusters energy, the amount of energy deposited in the cell and the distance of separation between the point and cluster centroid position. If a cluster is large in energy then it is allowed to reach out further to include points into itself. If the energy deposited in the cell is large then it should be closer to the cluster centroid position. To determine if a point is close to the cluster centroid the distance of separation along the surface of a sphere is considered, given by

$$\vec{d} = \rho\Delta\theta\hat{\theta} + \rho sin\theta\Delta\phi\hat{\phi}, \tag{3.15}$$

$$|\vec{d}| = \sqrt{\Big(\rho\Delta\theta\Big)^2 + \Big(\rho sin\theta\Delta\phi\Big)^2}. \tag{3.16}$$

The radius of the sphere is denoted as ρ, the polar angle is θ, the azimuthal angle is given as ϕ and Δ indicates difference between the cluster centroid-position and the point-position. This algorithm can be visualized by inclusion cones whose vertex is at the center of the target and projected into the

BCAL. The size of the cone varies for each point based on the fraction of energy deposited in the point over the total energy of the cluster, the distance between the cluster and point and the angle that the cluster impinges on the calorimeter. If a point falls inside the volume of an inclusion cone then it will be added to the cluster. The cones are not constrained to have a circular base. Particles that impinge the BCAL at larger polar angles will have a larger shower spread in the $\hat{\theta}$-direction than showers impinging at lower angles. The bases of the cones are allowed to stretch in the $\hat{\theta}$-direction as a function of θ.

In order to tune the sizes of the inclusion cones a sample of single-photon Monte Carlo was thrown where the noise in the BCAL was turned off and events where pair production occurred were rejected. This provided a sample where all of the energy deposited in the BCAL should be grouped into a single cluster. The MC sample covered the full length of the BCAL with photons from 0.1 to 3 GeV. By looking at the fractional energy of the point over the cluster as a function of the distance of separation between the point and cluster an appropriate cone size can be determined for a single photon as shown in Fig. 3.3. The plots in this chapter will be displayed showing the difference between using the previous clustering algorithm with what is currently being used by the BCAL. The previous clustering routine was ported from the KLOE experiment and modified according to the GlueX detector. The intent was to get the software running reasonably well at the time without spending much effort. The first look for physics signals with neutral particles in the final state made it clear that improvements were needed. The red lines were the previous clustering routine, the magenta curves correspond to the current clustering. All the points beneath the curves would be included into the cluster. The points above the curves would result in energy lost from the cluster and, if they have sufficient energy, then they will seed a new cluster leading to split-off clusters. The distance between points and the cluster centroid tends to be larger along the $\hat{\theta}$-direction than the $\hat{\phi}$-direction, to accommodate the shower shape cones with elliptical bases are used. Fig. 3.4 shows the fractional energy as a function of distance of separation in the azimuthal and polar directions independently.

In the $\hat{\theta}$-direction the shape of the shower depends on where in the BCAL it is reconstructed as shown in Fig. 3.5. The further downstream the shower is detected the tighter the distribution looks because the clustering is done in spherical coordinates. The same shower spread in z will have a narrower $\Delta\theta$ on the downstream end of the BCAL than if it were normal to the target position. An inclusion cone size is determined for each z-bin by using the function

$$f(\rho\Delta\theta, z) = e^{-\frac{\rho\Delta\theta - 0.1}{C_1(z)}} - C_2(z), \tag{3.17}$$

which is shown as the cyan curves in Fig. 3.5.

The magenta curves would be the curves to use if the cone size were set as a constant in the $\hat{\theta}$-direction for all z-positions. The two parameters, $C_1(z)$ and $C_2(z)$, that were used to fit the distributions in Fig. 3.5 are then fit as a function of z to extract a continuous family of curves in $\hat{\theta}$. These parameters are shown in Fig. 3.6 and are both fit using

$$C_{1,2}(z) = a_0 + a_1 \tanh(a_2(z - a_3)). \tag{3.18}$$

To further tune the size of the cones to prevent the merging of two clusters that are associated with two particles into one cluster, a sample of $\pi^0 \to \gamma\gamma$ Monte Carlo was generated. In this sample the only energy deposited in the BCAL was due to the two photons decaying from the generated π^0. In order to evaluate the performance of the clusterizer an event visualization tool (Fig. 3.7) was developed to quickly look at events one by one and classify various failure modes of the clusterizer. It is easy to determine which cells belong in which cluster by looking on an event-by-event basis and comparing the MC truth information with what was reconstructed. This lead to the various failure modes being addressed. An example event that was corrected by the new clustering approach can be seen in Fig. 3.7.

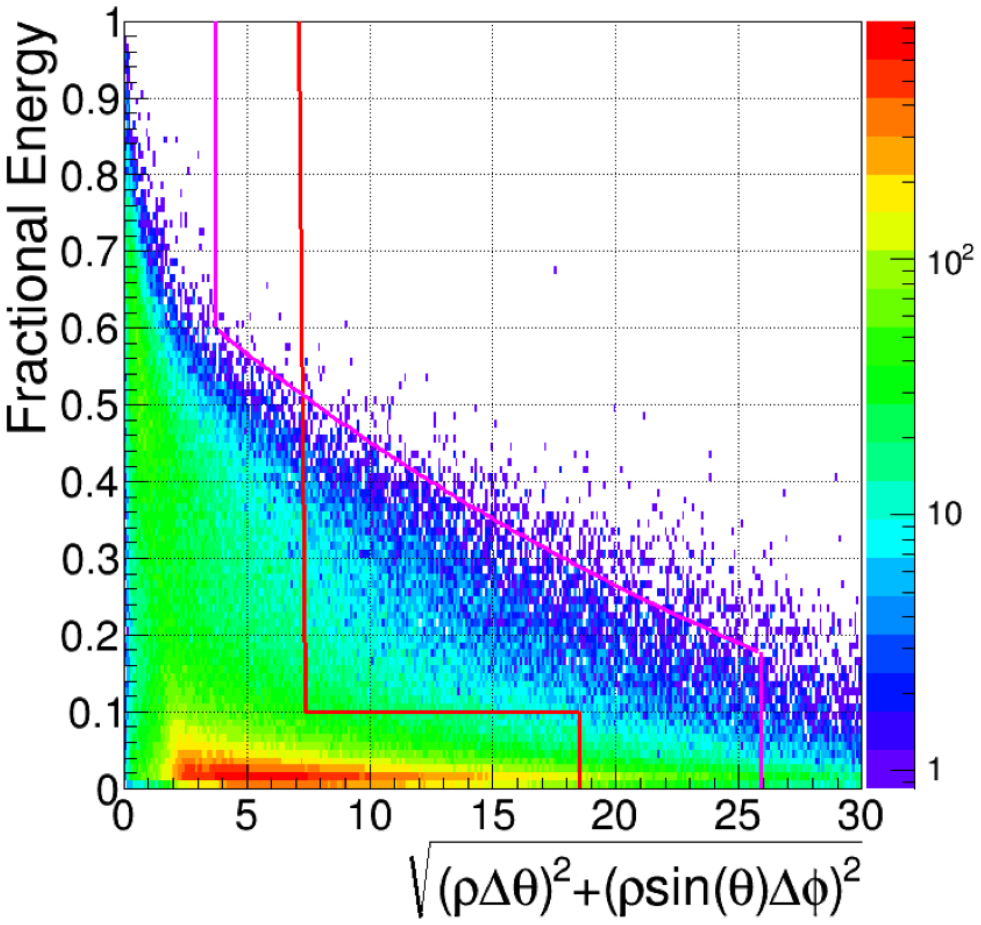

Figure 3.3: Fractional energy of a point's contribution to the cluster energy as a function of the distance between the point and the cluster before the point is added to the cluster. The red line corresponds to the previous clustering cone size and the magenta line corresponds to the current BCAL clustering cone size.

The size of the cones were tuned such that the number of merged clusters didn't increase while reducing the number of split-off clusters. This was checked by counting the number of reconstructed clusters in each event for the MC sample as shown in Fig. 3.8 along with comparing the simulated truth information with the reconstructed information. One benefit to this event-by-event approach is that a sample of π^0 candidates from real beam data can be studied as well. The Monte Carlo events are important to develop the algorithm but it needs to be evaluated on beam data before it is useful to the collaboration, as shown in Fig. 3.9. The effect of the current clustering routine was quantified by plotting the invariant mass of the same beam-on 2γ data sample using the previous and current clusterizer. The mean of the π^0 peak increases by 8 MeV and the width decreased by 7% after the energy scale was recalibrated. The signal increases by a factor of 1.2 without a significant increase in the background.

Two additional routines are performed before the clustering algorithm is finished, recycling of points and cluster merging routines. Since the clustering algorithm makes seeds out of the highest energy points and iterates through all of the points in an event, a point will be added to the first cluster that it

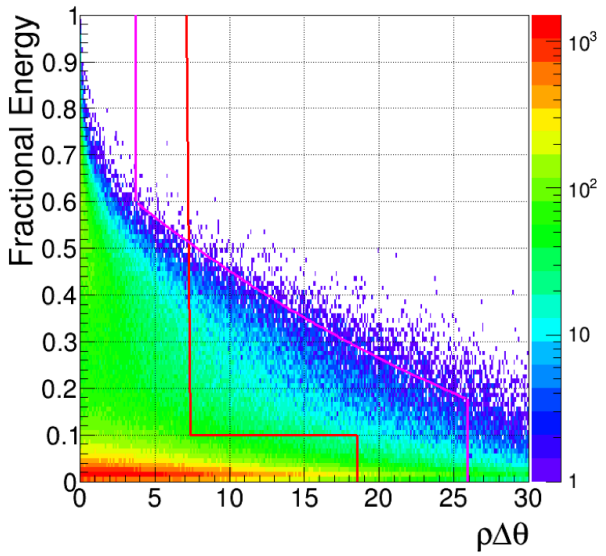

(a) Distance between the cluster centroid and the cell along $\hat{\theta}$.

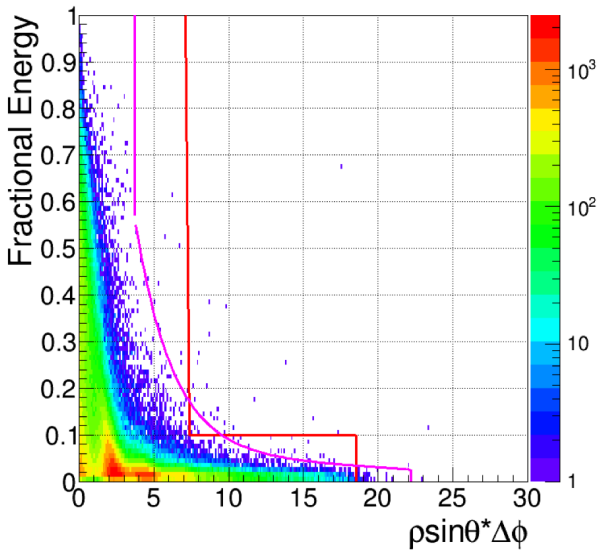

(b) Distance between the cluster centroid and the cell along $\hat{\phi}$.

Figure 3.4: Fractional energy of a cell to cluster energy as a function of the distance between the cell and the cluster before the cell is added to the cluster, decomposed into the $\hat{\theta}$ and $\hat{\phi}$ directions. The red line corresponds to the previous clustering cone size and the magenta line corresponds to the current BCAL clustering cone size.

can be added to and then removed from the available pool of points so it is not also added to any other clusters that are seeded later on. It sometimes happens that the first cluster to which a point can be added to isn't the closest cluster to which it would have been added. In the recycling routine, the closest cluster is defined as the cluster with the shortest distance between itself and a point using Eq. 3.16. There is a strict condition that recycling a point doesn't cause two clusters to have any bleed-through in the ϕ-coordinate. Once all of the clusters in an event are formed, each point that is associated with a cluster is checked to determine whether it belongs to the closest cluster, if not then it will be removed from its initial cluster and added to its closest cluster. Cluster merging is performed to combine two nearby clusters into a single cluster. The merging is tuned to merge a low energy cluster into a nearby large energy cluster whenever it looks like a split-off cluster using similar methodology as a point being included into a cluster.

3.2.2 Neutral Clustering Summary

The neutral clustering algorithm was updated and implemented into the GlueX analysis software. Using the photon MC sample described above the number of splitoff showers was decreased by a factor of 7.5. The fraction of merged showers in the MC sample of π^0 events was not significantly increased as payment for reducing the splitoff showers. Looking at real data the π^0 signal increased by a factor of 1.2 without significantly increasing the background strength. The peak of the π^0 increased by 8 MeV and the width of the π^0 sample decreased by 7% after recalibrating the energy scale.

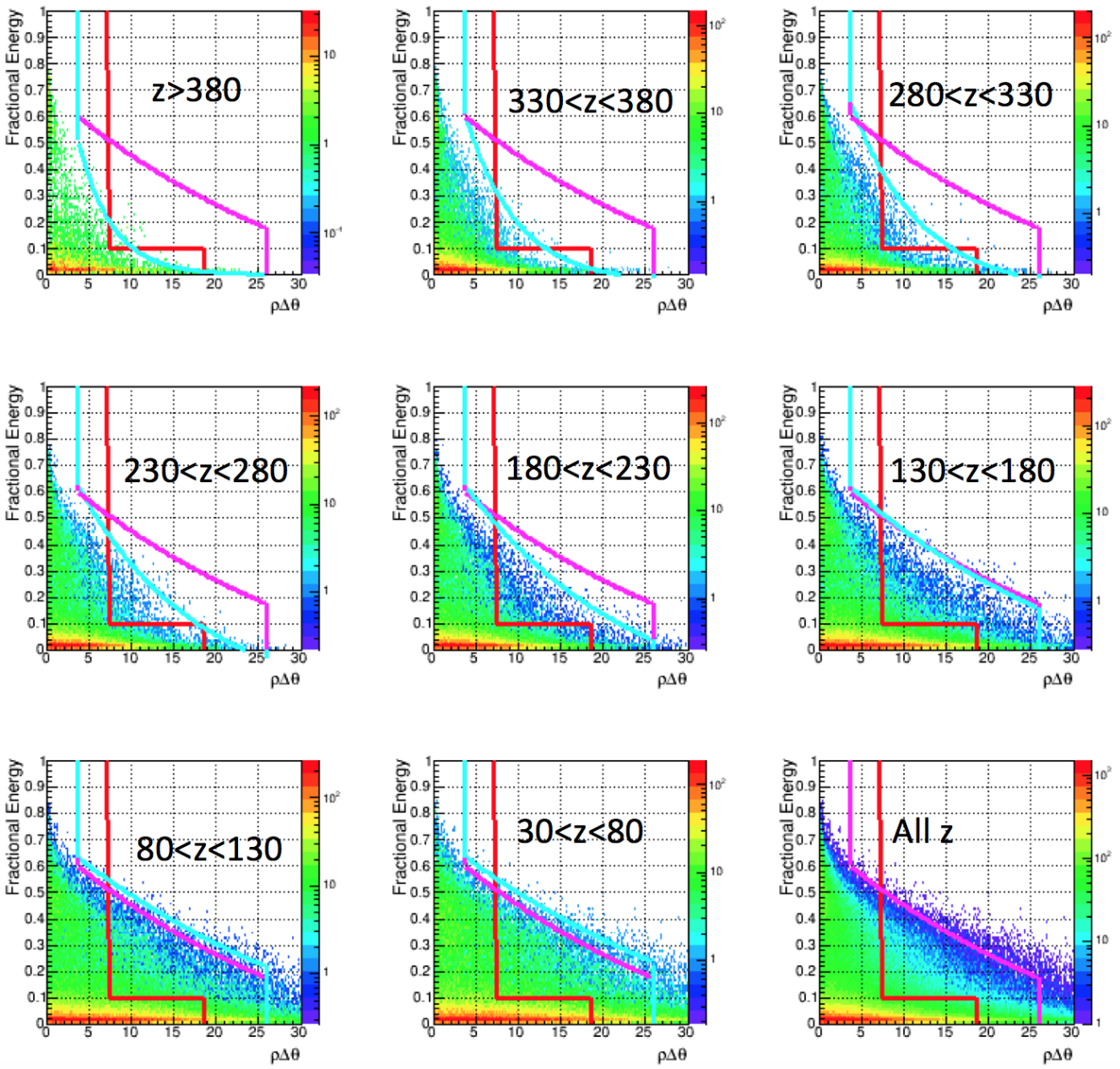

Figure 3.5: Fractional energy of a cell to cluster energy as a function of the distance between the cell and the cluster along $\hat{\theta}$ before the cell is added to the cluster. The magenta line corresponds to using an integrated clustering cone size and the cyan line corresponds to the current BCAL clustering cone size to account for z-dependence. Note that the high-z bins correspond to the downstream region of the detector and the low-z bing correspond to the upstream region.

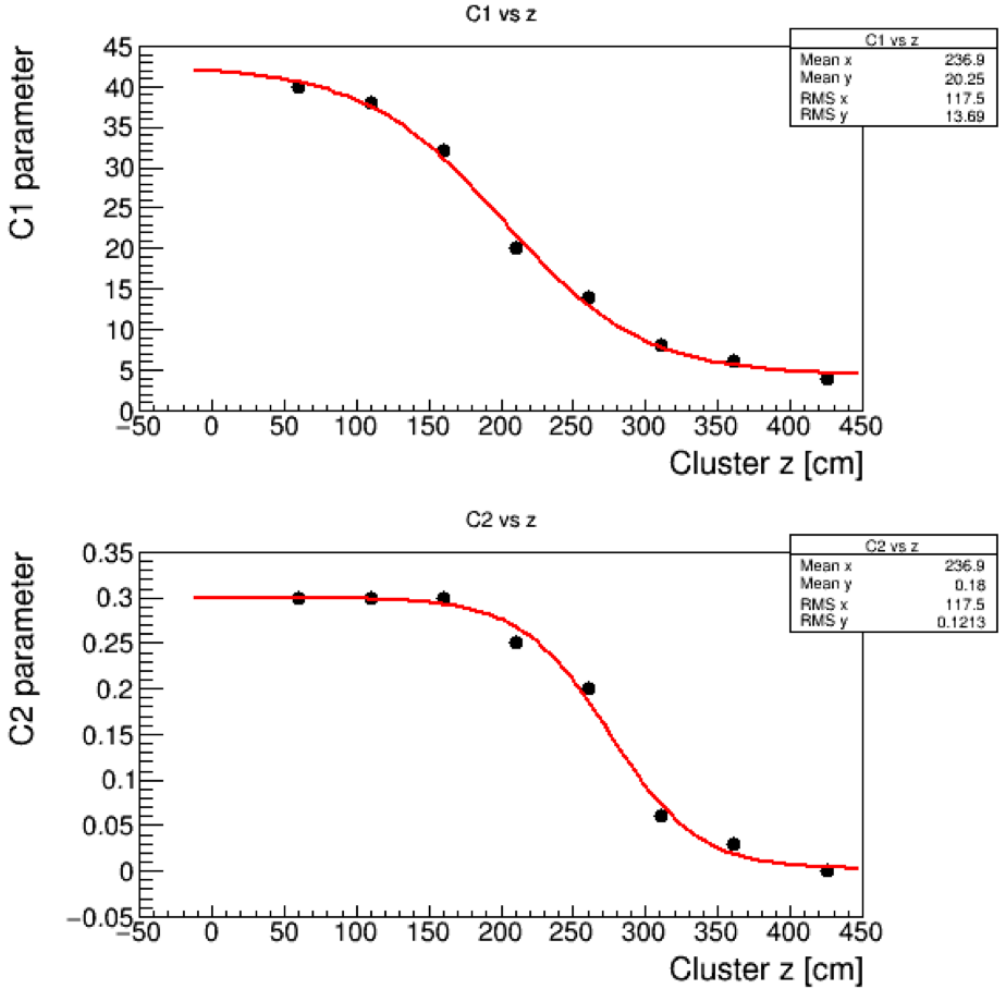

Figure 3.6: The black points are the parameters in each z-bin to set the size of the clustering cone in the $\hat{\theta}$ direction. The red curve is a fit to these points to extract a continuous cone size dependence.

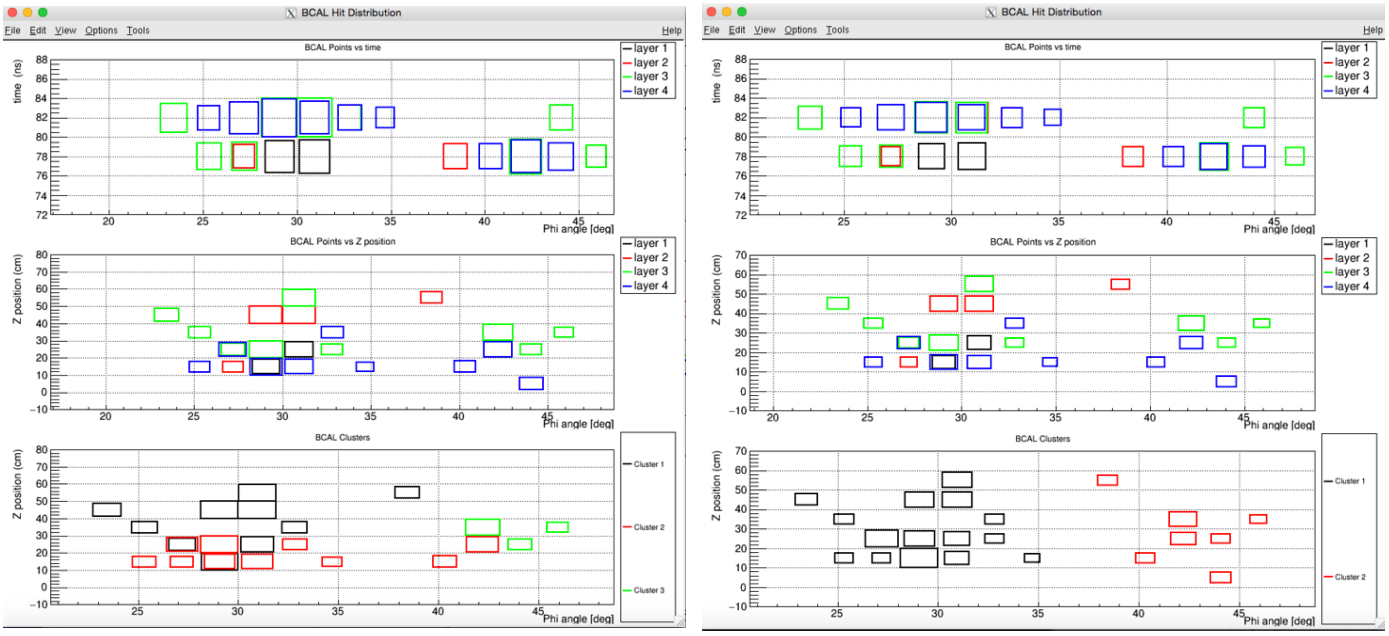

(a) Previous clusterizer.

(b) Current Clusterizer

Figure 3.7: The time and z-position of BCAL points vs their ϕ-positions. The bottom panel displays the points color-coded based on which cluster they belong to.

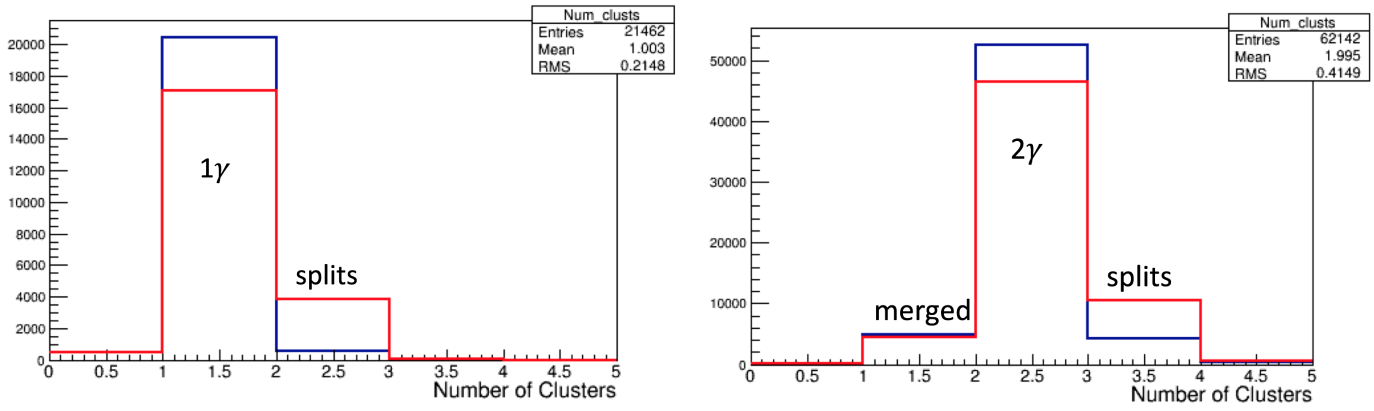

(a) single photon MC sample.

(b) $\pi^0 \to 2\gamma$ MC sample.

Figure 3.8: Number of reconstructed clusters for each event used as a performance check of the clusterizer. Red corresponds to the previous clusterizer and blue corresponds to the current clusterizer.

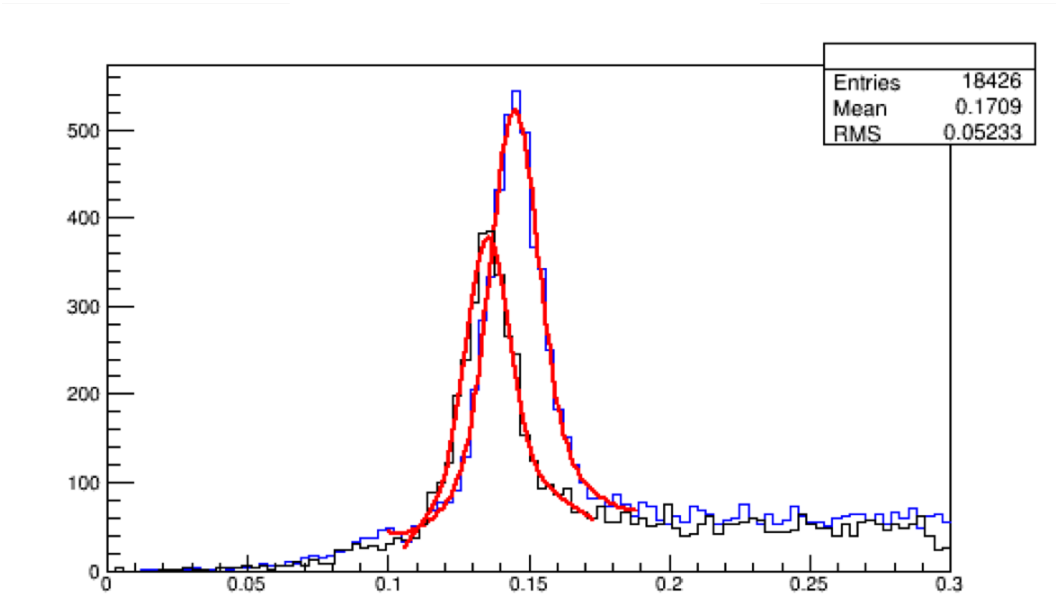

Figure 3.9: Invariant mass of 2γ comparing the previous and current clusterizer using the same sample of events from beam-on data. The black histogram corresponds to the previous clusterizer while the blue histogram corresponds to the current clusterizer.

3.2.3 Charged Particle Clustering

Hadrons have a different shower shape than photons in the BCAL, they tend to be wider and more scattered in their transverse profile while they project further and tighter in their longitudinal profile. Charged particles can have a significant deviation from a straight line projected from the target as is done in the neutral clusterizer due to their curvature in a magnetic field. A simple sketch to motivate the need for a separate clustering algorithm can be seen in Fig. 3.10. The track curvature leads to split-off showers being reconstructed when using the neutral clusterizer on charged particle showers, a charged clustering routine was developed to address this. The first step is to identify whether the neutral or charged clustering algorithm should be used. This is done by projecting a track from the drift chambers into the BCAL. If the track is matched to the cluster seed in θ- and ϕ-coordinates then the charged clustering algorithm is used, if not then the neutral clustering algorithm starts. If a point in the first layer of the BCAL is added to a neutral cluster and it is matched to a track then the charged clustering algorithm is imposed on the fly. This is because the projection of the track becomes less accurate as it is projected further distances outside of the tracking chambers.

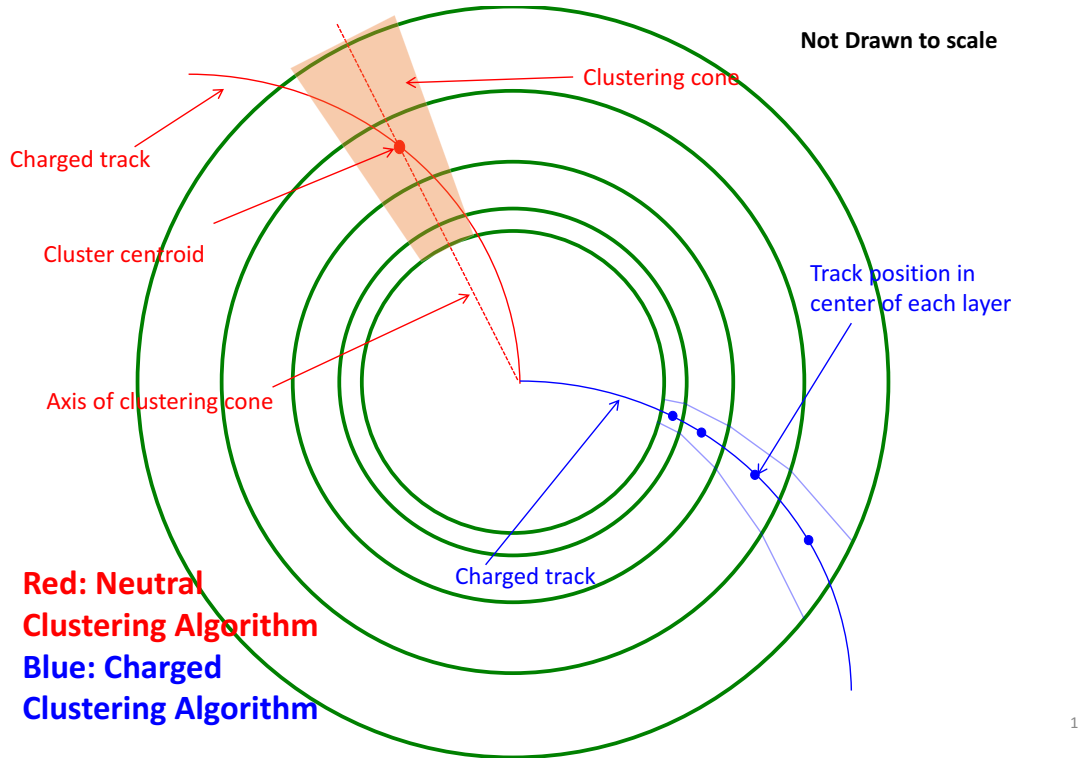

Figure 3.10: Sketch to illustrate the issue with reconstructing the energy deposited by charged tracks using the neutral clusterizer and what we want the charged clusterizer to look like. Green circles correspond to the different BCAL layers.

The clustering in the θ-direction is unchanged between the neutral and charged clustering. The initial direction of the charged cluster is defined as a straight line that passes through the cluster seed and the track projected to the inner surface of the BCAL in the ϕ vs z coordinate. This contains information about the direction of the shower in its longitudinal and transverse profiles. Each time a point is added to a cluster a linear fit of the distribution of points in the ϕ vs z coordinate is performed to obtain the azimuthal direction of the clustering cone. Similarly to the neutral clustering, inclusion cones are used

to determine if a point should be added to the cluster. For the charged clustering $\Delta\phi$ is determined by the difference between the ϕ-position of the point and the ϕ-position of the fit line evaluated at the z-position of the point, as shown in Fig. 3.11. The points used in the fit are weighted by their energy. Each time a point is added to the cluster a new linear fit is performed in ϕ vs z, as points are being added to the cluster the direction of the cluster becomes better-defined. Each time a new fit is performed each point that has already been added to the cluster is checked if it still belongs in the cluster, if not then it is returned to the available pool of points to be added to a cluster. This allows the inclusion cone to continuously develop itself in the ϕ-direction each time a point is added to align itself with the direction that the cluster is developing in the BCAL.

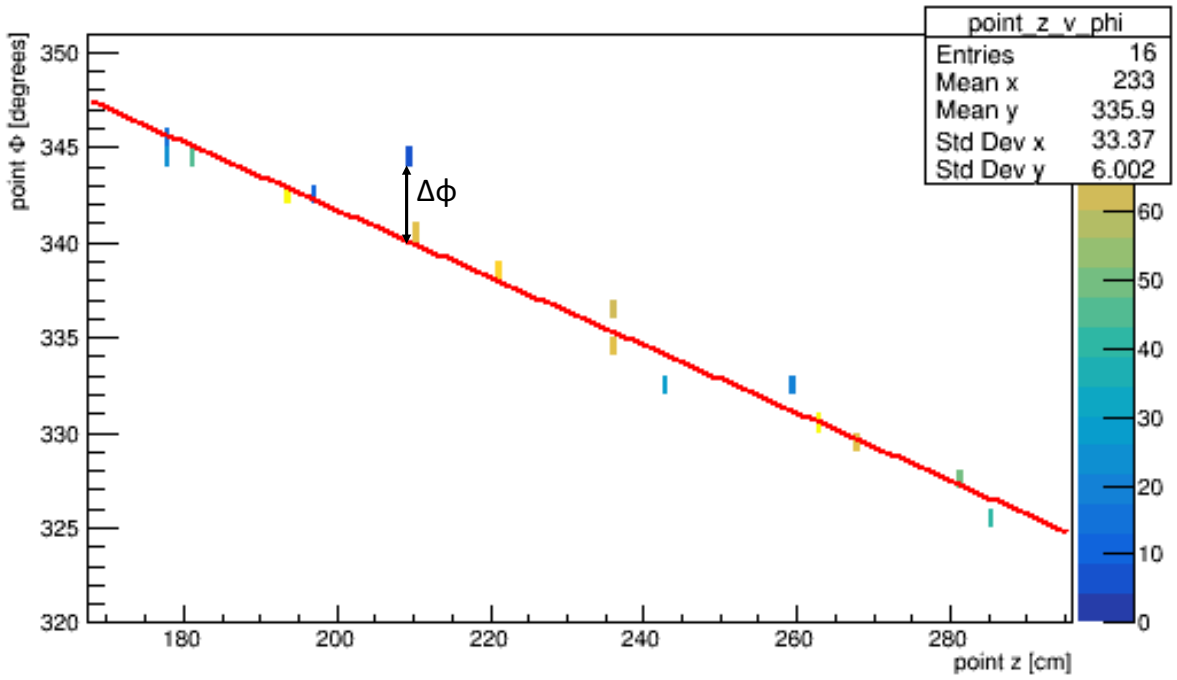

Figure 3.11: Single event illustrating the linear fit (red line) the the energy-weighted BCAL points (rectangles whose color is based on their energy in MeV) to determine the direction of the charged cluster in the BCAL.

In order to develop this technique MC samples of μ^- and μ^+ were generated with momentum from 0.5 to 1.0 GeV and θ spanning from 15°to 20°. Higher energy and angle samples were also looked at but weren't as useful to develop the algorithm. Muons at low energy and low angle have a small radius of curvature and traverse a long distance in the BCAL which makes them a difficult sample to cluster and thus a good development sample. A muon is a lepton that will minimally ionize as it passes through the BCAL making its direction easier to determine compared to a hadron that can easily shower. A similar sample of π^+ and π^- were also studied but the muon sample was more useful in the development stage.

The tuning of the inclusion cone sizes used the same variables as the neutral clustering. Specifically fractional energy of the point divided by the cluster energy is plotted as a function of the distance of separation between the point and cluster. The only difference between using the neutral and charged cluster is in the definition of $\Delta\phi$, as shown in Fig. 3.12. This distribution was produced using the

sample of generated μ^- events. The distribution is narrower whenever the charged clustering algorithm is used because the $\Delta\phi$ is tighter. This allows the use of smaller inclusion cones to capture the full energy deposited making it easier to resolve two nearby particles. The cluster seed is typically found in a radially center portion of the BCAL, which corresponds to layers 2 and 3. Fig. 3.13 shows the same distribution binned by layer to show the expected behavior that layers 1 and 4 demonstrate the largest improvement when implementing the charged clusterizer because they are further from the cluster seed. It is also observed that layer-dependent inclusion cone sizes aren't needed, one size fits all layers. After implementing these changes it was useful to view single events where more than one shower was being reconstructed for the single thrown μ^- sample. Doing so resulted in three major failure modes being classified:

- The cluster merging used for neutral particles wasn't doing a good job because, if a single charged particle shower was reconstructed as two clusters, their separation in the ϕ-coordinate was typically too large to satisfy merging criteria.
- Clusters that exhibit extreme curling in the ϕ-direction direction fail, the track typically stops in the BCAL in these events. When this happens the last cell containing the shower has a large amount of energy deposited in it and the cluster cones are designed to miss higher energy points near the periphery of the shower.
- Clusters that actually curl their way back towards the drift chambers fail because of our fitting approach in the ϕ vs z coordinate. These events are very rare and remain unadressed.

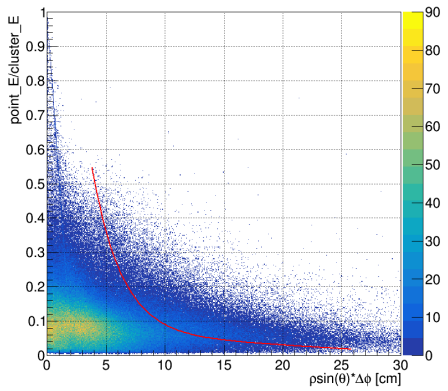

(a) Distance between the cluster's ϕ-position and the cell's ϕ-position along $\hat{\phi}$ (neutral clusterizer). Red line corresponds to the cluster cone size using the neutral clustering.

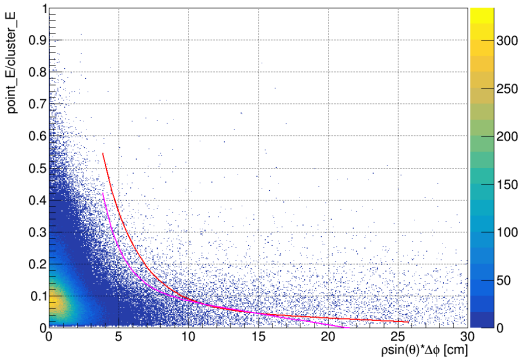

(b) Distance between the ϕ-position evaluated of the fit line evaluated at the cell's z-position and the cell's ϕ-position along $\hat{\phi}$ (charged clusterizer). Red line corresponds to the cluster cone size using the neutral clustering. Magenta line corresponds to the cluster cone size using the charged clustering.

Figure 3.12: Fractional energy of a cell to cluster energy as a function of the distance between the cell and the cluster in the $\hat{\phi}$ direction before the cell is added to the cluster. The red line corresponds to the neutral clustering cone size and the magenta line corresponds to the charged clustering cone size.

To address the cluster merging the conditions that the ϕ and θ-positions of the two clusters match is relaxed but matching criteria between the slope and intercept of the fit performed to each cluster is introduced. This fit to find the direction of the cluster for the cluster merging only considers the points associated with each cluster. The idea is that charged clusters should only be merged if their directions

match each other. An example event is shown in Fig. 3.14, if the same merging criteria for neutral and charged particles were used then these two cluster wouldn't be merged together. The merging criteria were quantified by looking at the distributions that are obtained from single μ^- MC sample that were mis-reconstructred as two clusters. These are only signal events where two or more reconstructed clusters should be reconstructed as only one cluster, without any background. The charged clustering merging criteria are used whenever at least one of the clusters was clustered using the charged clusterizer, if both clusters were clustered using the neutral clusterizer then the neutral cluster merging criteria is used. This is because whenever a charged cluster splits into two reconstructed clusters the split-off cluster typically won't follow the track projection and is thus unmatched to a track and clustered using the neutral clustering. Therefore, the points comprising neutral clusters must also be fit to obtain the neutral clusters direction so they can be considered to be merged with a charged cluster.

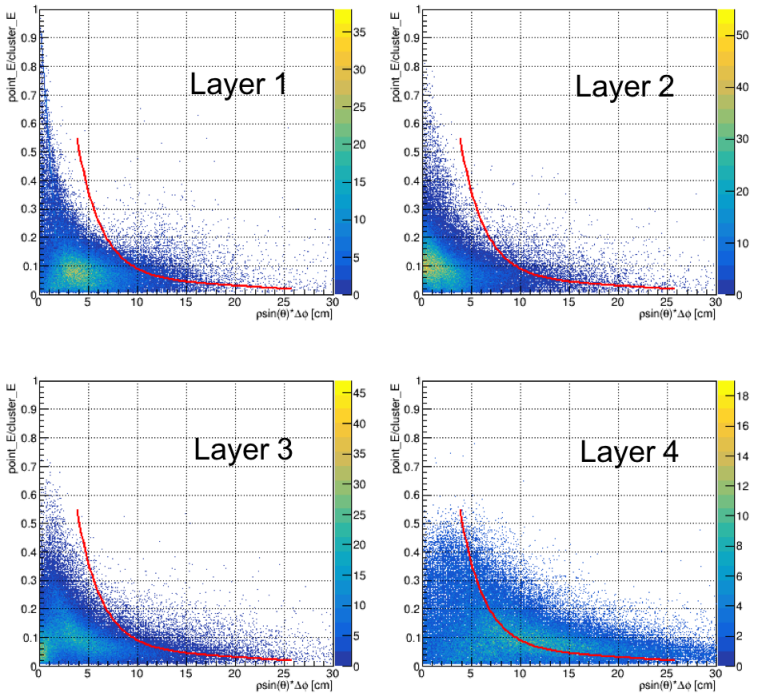

(a) Distance between the cluster centroid and the cell along $\hat{\phi}$ (neutral clusterizer).

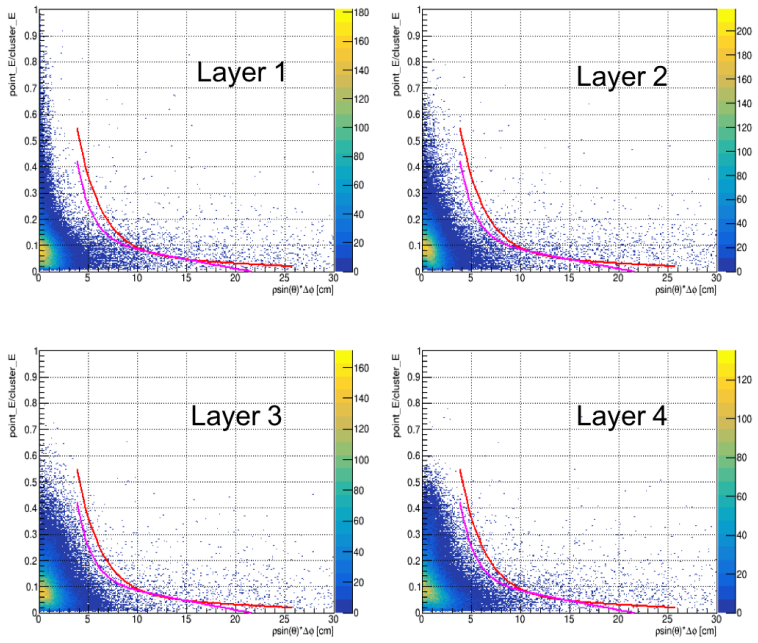

(b) Distance between the ϕ-position evaluated of the fit line evaluated at the cell's z-position and the cell's ϕ-position along $\hat{\phi}$ (charged clusterizer).

Figure 3.13: Fractional energy of a cell to cluster energy as a function of the distance between the cell and the cluster before the cell is added to the cluster in the $\hat{\phi}$ direction. The red line corresponds to the neutral clustering cone size and the magenta line corresponds to the charged clustering cone size.

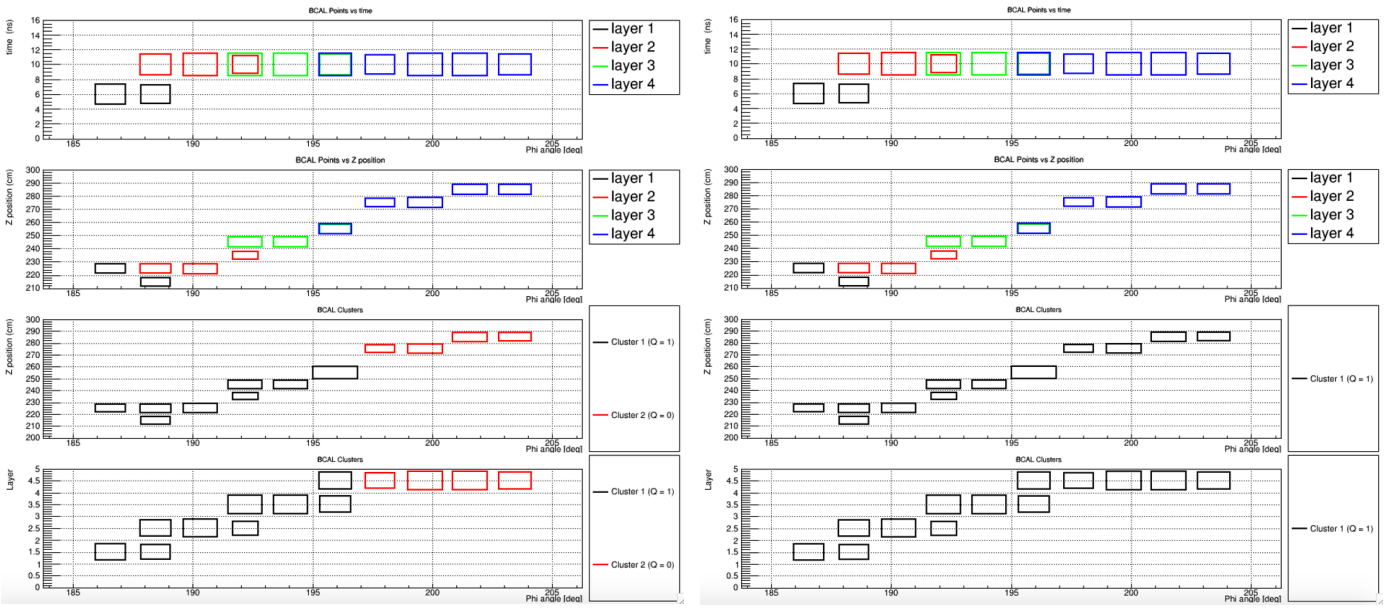

(a) Using neutral clusterizer merging criteria.

(b) Using charged clusterizer merging criteria.

Figure 3.14: Single μ^- MC sample. The second from the bottom panel shows the z-position of BCAL points vs their ϕ-positions, they are color-coded based on which cluster they belong to.

Clusters that curl very far in the ϕ-direction fail for two reasons: they can be nonlinear in ϕ vs z and a cell at the periphery of the shower tends to have a lot of energy deposited in it. The large energy being deposited in a cell near the periphery of the cluster is a difficult circumstance to include into the inclusion cone because that cell would have a high fraction of the total clusters energy deposited in it. These clusters typically correspond to a track that stops in the BCAL, an example event is shown in Fig. 3.15. A conservative approach is taken to deal with these types of events, if a single cell is sector adjacent to a cell already existing in a cluster and there are no layer adjacent cells that have energy deposited in them then the single cell will be merged into the cluster. The charged cluster merging is effective for merging two clusters when they both have multiple cells included in them, but if there's a cluster comprised of only one cell then a fit cannot be performed to obtain its direction. Since the charged cluster merging routine requires a match of fit parameters between both clusters it cannot merge a cluster with a single cell, these events require special care. This operation is intended to be performed whenever a cluster is obviously continuing on its path but doesn't include the final cell and is performed after the cluster merging routine.

A sample event where the single charged track curls it way back towards the drift chambers is shown in Fig. 3.16. This type of failure event is very rare and nothing is done to correct it. It is ambiguous with two separate charged tracks entering the BCAL from two different angles and requires a more sophisticated approach to correct. It was determined that such an effort was not worthwhile at the time.

After implementing the charged clustering as described above tuned on the single μ^- sample there is an improvement from using the neutral clustering. Since one μ^- was thrown we expect to reconstruct one cluster, Fig. 3.17 compares using the neutral and charged clusterizers. Fig. 3.17b shows that whenever a track is matched to the cluster there is a 99.1% success rate. The biggest improvement to be made at this point is to improve the track matching to the BCAL.

In order to test how greedy the charged clusterizer is a sample of events with two muons was generated. Each muon was thrown with $p = 1$ GeV and uniformly from $\theta = [15°, 25°]$, one muon was

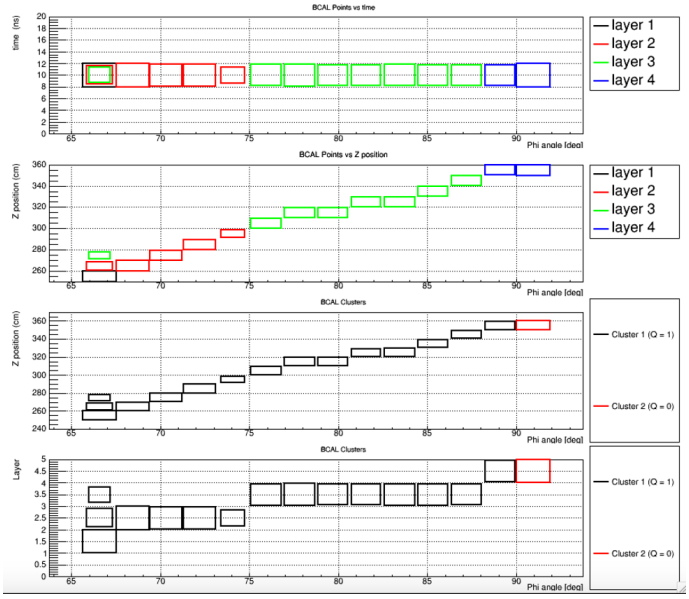

(a) Using neutral clusterizer merging criteria.

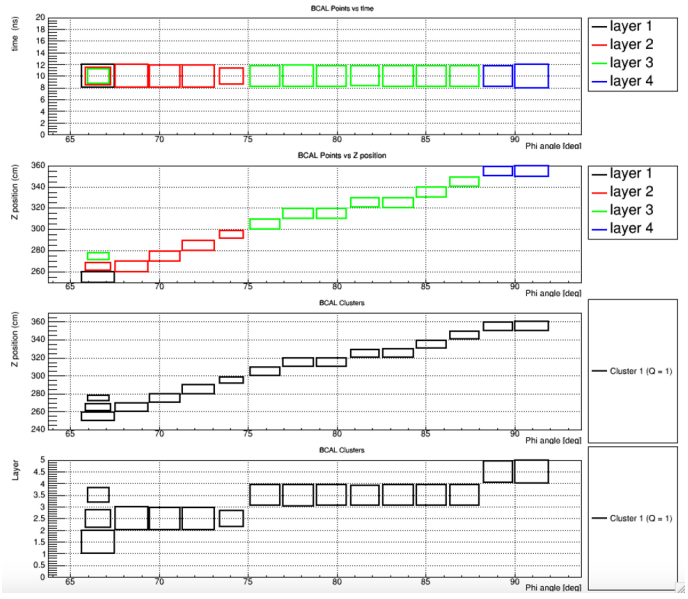

(b) Using charged clusterizer merging criteria.

Figure 3.15: The time and z-position of BCAL cells vs their ϕ-positions. They are color-coded based on what layer or cluster they belong to.

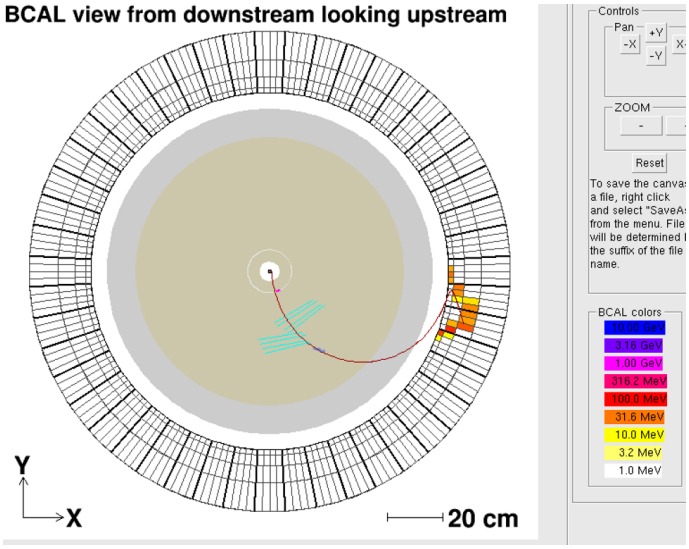

(a) burgundy line shows the reconstructed track associated with the particle and the BCAL cells are colored based on how much energy was deposited in them.

(b) The time and z-position of BCAL cells vs their ϕ-positions. They are color-coded based on what layer or cluster they belong to. In the previous clustering, there is a large energy point at the edge of the cluster that doesn't get included in the cluster when it should.

Figure 3.16: Illustration of an outstanding reconstruction issue where the charged particle enters the BCAL and curls back towards the tracking detectors.

thrown at $\phi = 180°$ and the other muon was thrown at $\phi = 170° \pm 5°$. These kinematics were chosen to reduce overlapping hits in the drift chambers in order to cleanly reconstruct two tracks while keeping

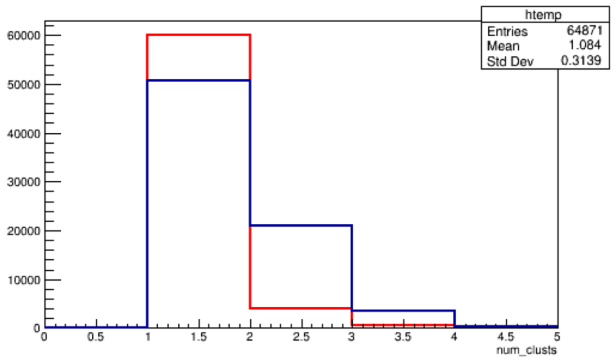

(a) Red histogram corresponds to using the charged clusterizer while the blue histogram corresponds to using the neutral clusterizer.

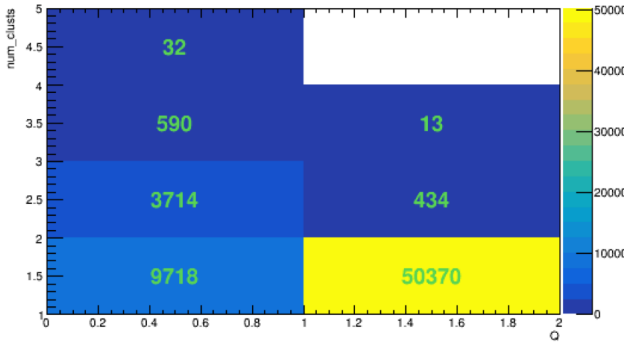

(b) Q = 0 corresponds to events where the track was not matched to the cluster and so the neutral clusterizer was used, Q = 1 corresponds to events where the track was matched to the cluster and so the charged clusterizer was used.

Figure 3.17: Number of reconstructed clusters per event for a single μ^+ MC sample.

the clusters in the BCAL close enough together that the test had meaning. Similarly to the neutral clusterizer the charged clusterizer was tuned to hold the number of cluster mergers to stay the same while reducing the number of split-offs as much as possible. The number of clusters reconstructed in each event is shown in Fig. 3.18. A complimentary sample was generated with a thrown 1 GeV photon and μ^- thrown uniformly with $\theta = [15°, 25°]$ for both particles. The photon is thrown at $\phi = 160°$ while the μ^- is thrown at $\phi = 170° \pm 5°$. This sample is useful to test the track matching criteria and the merging of a neutral and charged cluster. The cone sizes didn't need to be tuned to obtain satisfactory results. The final MC sample that was used to test the charged clusterizer was a sample of π^+ thrown from 0.5 GeV to 1 GeV at a θ spanning from 15° to 20°. Because of the messier nature of hadronic interactions in the detector it's harder to tune the inclusion cones using hadrons, but it's important to reduce hadronic splitoffs in the BCAL because much of the interesting physics GlueX involves hadronic final states. The Fig. 3.19 shows how the inclusion cones map onto the shower distribution for the π^+ MC events.

To evaluate the effect that the charged clusterizer has on beam-on data a sample of single π^+, π^- and recoil protons was selected using the production of exclusive ω candidates in their hadronic decay mode, $\omega \to \pi^+\pi^-\pi^0, \pi^0 \to 2\gamma$ decay. After placing several event selection cuts a clean sample of exclusive ω candidates was obtained, Fig. 3.21. Among the event selection requirements, no extra tracks are allowed in the event, the track of interest must be well separated from the other two tracks and the two photon showers that reconstruct to form the π^0 are well-separated from the track of interest. Then, if the track of interest is matched to a cluster in the BCAL, the number of clusters that were matched to the track is shown in Fig. 3.20. The biggest impact that the charged clusterizer has had on varying physics analyses isn't measuring the energy, position and time of charged clusters but it's in the reduction of background due to hadronic split-offs. This effect can be seen in Fig. 3.21 where the invariant mass for the $\omega \to \pi^+\pi^-\pi^0$ is plotted with the charged clusterizer toggled on and off, there is an increase in signal yield without increasing the background.

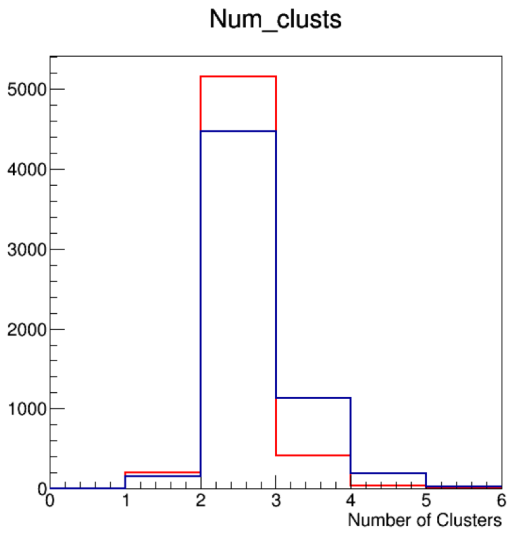

Figure 3.18: Number of reconstructed clusters for the sample of 2 muons thrown per event. The Red histogram corresponds to using the charged clusterizer while the blue histogram corresponds to using the neutral clusterizer.

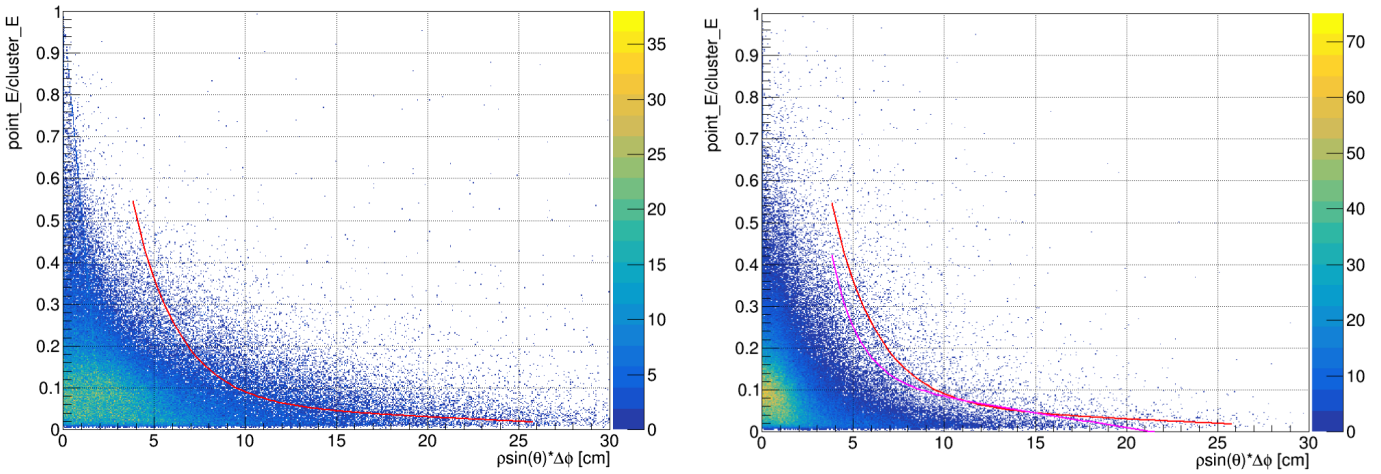

(a) Fractional energy versus the distance between the cluster fit-position and the cell along $\hat{\phi}$ using a π^+ MC sample (neutral clusterizer).

(b) Fractional energy versus the distance between the cluster fit-position and the cell along $\hat{\phi}$ using a π^+ MC sample (charged clusterizer).

Figure 3.19: For the π^+ MC sample, fractional energy of a cell to cluster energy as a function of the distance in the $\hat{\phi}$ direction between the cell and the cluster fitted ϕ-position before the cell is added to the cluster. The red line corresponds to the neutral clustering cone size and the magenta line corresponds to the charged clustering cone size.

3.2.4 Charged Clustering Summary

The improvements that the charged clustering algorithm had on reconstructing the MC samples of single μ^- and π^+ can be seen in Tab. 3.1. The reduction of split off clusters did not come at the cost of a

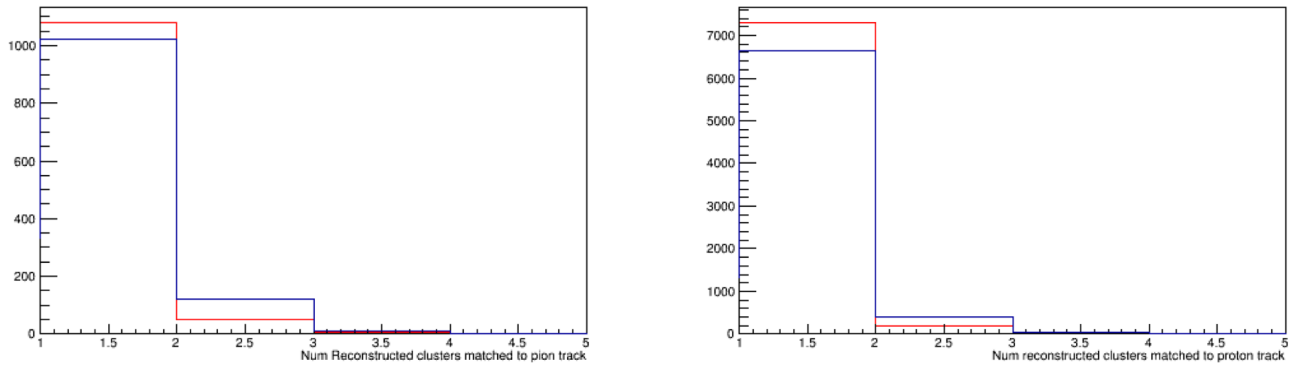

(a) Number of clusters matched to a π^+ or π^- track. (b) Number of clusters matched to the proton track.

Figure 3.20: Number of reconstructed clusters matched to a track based on standard GlueX track-to-shower matching criteria for each event used a performance check of the clusterizer. Red corresponds to the neutral clusterizer and blue corresponds to the charged clusterizer.

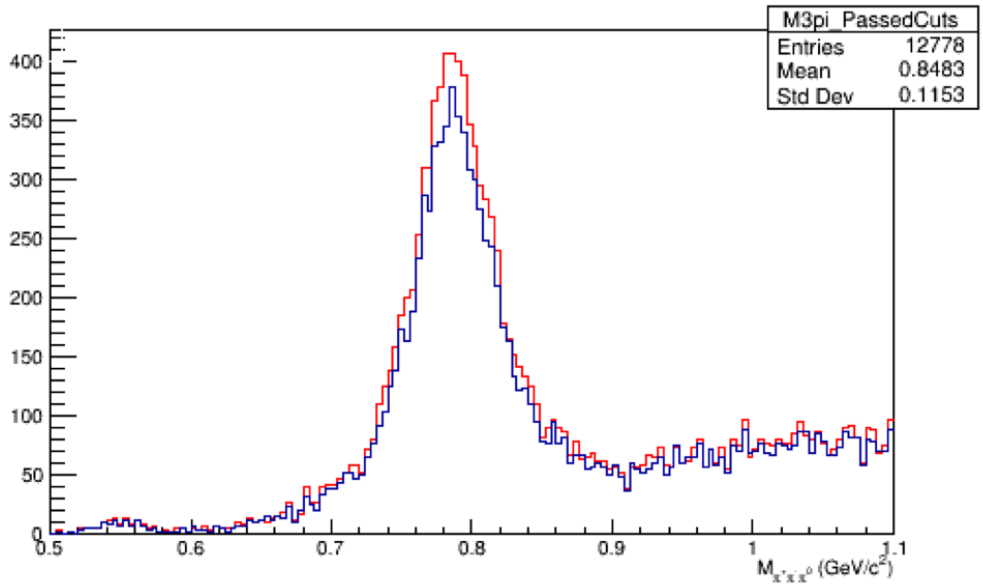

Figure 3.21: reconstructed mass of the $\omega \to \pi^+\pi^-\gamma\gamma$ sample. The red histogram was produced using the charged clusterizer when the track matching criteria was satisfied and the blue histogram was produced using only the neutral clusterizer.

significant increase in merged clusters.

Improvements were also observed using a sample of exclusive $\gamma p \to \omega p, \omega \to \pi^+\pi^-\pi^0$ events in beam-on data. The number of clusters matched to the π and proton tracks was reduced by a factor of 2.5. There was also an observed increase in signal for the $\gamma p \to \omega p$ reaction without a significant increase in background.

MC sample	Clusterizer	Success rate
μ^-	Neutral	69%
μ^-	Charged	93%
π^+	Neutral	75%
π^+	Charged	95%

Table 3.1: Comparison of success rates of reconstructing a single charged particle using MC samples.

Chapter 4

Beam Asymmetry Measurement

4.1 Data Selection

In Spring of 2017 CEBAF provided a $\sim$ 11.6 GeV electron beam under varying conditions as the accelerator completed its commissioning program. In the same period, GlueX entered its first run period of physics production data taking. There was a small amount of commissioning of the beamline and detector systems at the start of the run [79]. A brief overview of the run conditions are displayed in Figure 4.1. This report documents the analysis of GlueX data from a stable portion of the Spring 2017 run period for which a single diamond radiator (JD70-100 $\sim$ 58 μm thickness) and a single amorphous radiator ($\sim$ 30 μm thick aluminum) were used. A dataset was also taken in 2016 during a commissioning run period and opportunistic physics was extracted but that dataset is statistically limited, especially when considering multiple η decay modes.

The diamond data were collected using four different settings for the photon beams. First with the linear polarization plane parallel and perpendicular to the lab floor ($x - z$ plane), referred to as PARA and PERP, respectively. Each set of PARA and PERP data is comprised of two sets of data with a ϕ_0 offset of +45°, the PARA orientation dataset contains offsets $\phi_0 = 0°$ and $\phi_0 = 135°$ and the PERP orientation dataset contains offsets $\phi_0 = 90°$ and $\phi_0 = 45°$. The PERP dataset with $\phi_0 = 90°$ is orthogonal to the PARA dataset with $\phi_0 = 0°$ (0/90) and they are used together to construct one asymmetry measurement. The PERP dataset with $\phi_0 = 45°$ and $\phi_0 = 135°$ (45/135) are orthogonal and are used to make an independent asymmetry measurement. These two measurements of the asymmetry are used as a systematic check with each other. The amorphous data is referred to as AMO throughout the text. The range of runs considered for this analysis for each radiator setting is given in Appendix A, the data taken with the diamond radiator corresponds to a total of 20.8 pb^{-1} of data in the coherent peak region.

The data for the asymmetry analysis were collected with the standard GlueX FCAL-BCAL energy sum trigger [80]. The two innermost rings of the FCAL were masked from the tigger during this run period. The data analyzed were from the third reconstruction production, which started in September 2018 and is the most current version of the dataset. The GlueX subsystems included in the analysis are the Pair Spectrometer (PS), Triplet Polarimeter (TPOL), Central Drift Camber (CDC), Forward Drift Chamber (FDC), Forward Calorimeter (FCAL), Barrel Calorimeter (BCAL), Start Counter (ST) and Time-of-Flight (TOF).

The electron beam was delivered in 2 different average intensities of 100 nA and 150 nA. These two different intensity periods are referred to as Low Intensity and High Intensity periods, respectively. The full analysis is carried out independently for these two intensities to check for agreement before continuing. The Low Intensity and High Intensity datasets ended up agreeing well with each other and

were then combined together. The two sets of polarization direction data sets of (0/90) and (45/135) were observed to agree with each other and subsequently were combined together. Since these are all independent datasets they are combined by performing the analysis on each dataset and then computing the error-weighted mean to give a final result. In a separate analysis flow the PERP data are added together and the PARA data are added together before the analysis was carried out. These different approaches to combine the data and carry out the analysis give consistent results with each other. The Low and High intensity data were combined together before performing the analysis and the error-weighted mean between the (0/90) and (45/135) datasets were computed as the final result that is presented below.

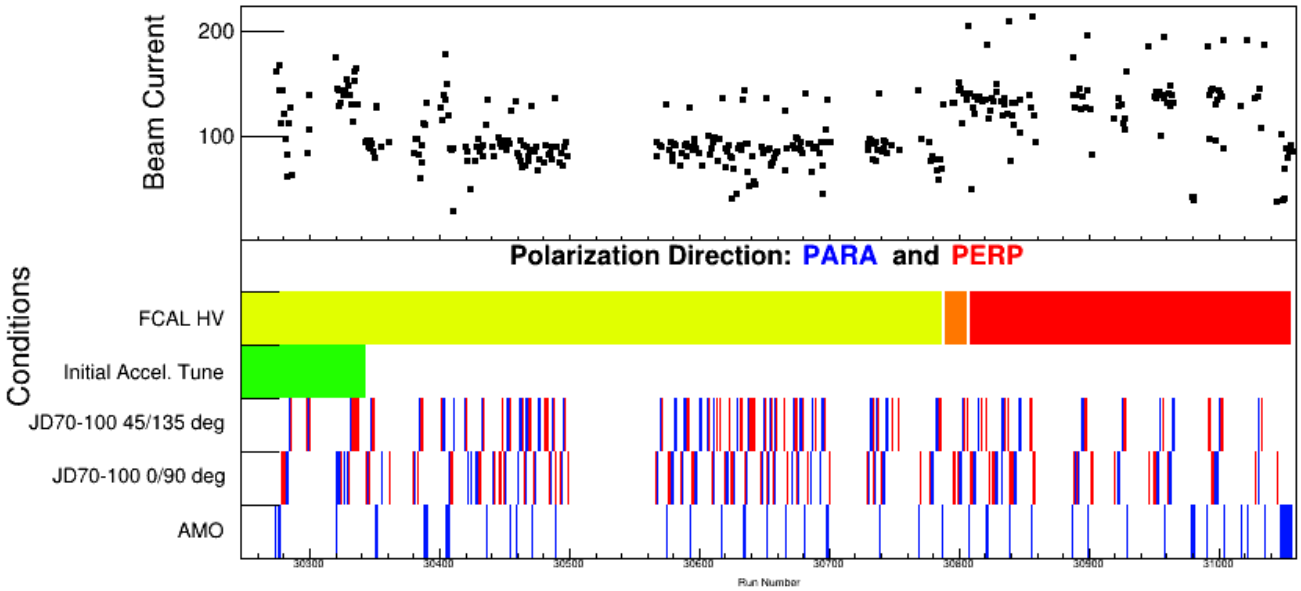

Figure 4.1: Summary of beam and detector conditions for Spring 2017 GlueX data as a function of run number. The production-quality approved data were selected throughout the full run range to be used in this analysis. The name of the diamond used in this run perdiod was JD70-100.

4.1.1 Beam Polarization

The beam polarization was determined using the triplet polarimeter (TPOL) [81], Figure 2.7 shows the polarization measured as a function of beam energy for each orientation. The coherent edge is clearly observed at $E_\gamma = 8.8$ GeV, with the polarization peaking in this range, as expected. The coherent peak region of $8.2 < E_\gamma < 8.8$ GeV is selected for this analysis because it has the highest degree of polarization while containing enough statistics for the analysis. The polarization is noticeably different between different orientations. Since the polarization and beam flux are not flat in the coherent peak region the polarization value is weighted by the beam energy spectrum to obtain an average polarization value, as shown in Tab 4.1. The beam energy spectrum is used as the only weight because the cross-section at this energy isn't well-known. The beam energy after all analysis cuts is used which is why it is chosen instead of the flux. The beam energy-weighted average polarization value is used in the fit of the ϕ distributions to extract the beam asymmetry, Σ.

Polarization Orientation	Beam Intensity	Average polarization	δ_p
0	Low Intensity	0.360	0.013
90	Low Intensity	0.357	0.013
45	Low Intensity	0.357	0.013
135	Low Intensity	0.338	0.013
0	High Intensity	0.341	0.016
90	High Intensity	0.337	0.015
45	High Intensity	0.332	0.016
135	High Intensity	0.351	0.016
0	Full Run	0.352	0.0098
90	Full Run	0.347	0.010
45	Full Run	0.346	0.010
135	Full Run	0.350	0.010

Table 4.1: Beam-energy weighted polarization values for different polarization directions and beam intensities using the beam spectrum in the $\eta \to 2\gamma$ sample. Similar weighed-polarization values are obtained for each event sample and are consistent.

4.1.2 Relative flux normalization

The pair spectrometer yields can be used to study the photon beam energy distribution. For this measurement, the integrated photon flux for a given set of runs is determined using the PS hits in coincidence with a hit in the TAGM or TAGH. The tagged flux is referred to as the integrated flux that requires the tagger coincidence, after subtractino of accidentals and correction for PS acceptance. The tagged flux integrated over all runs used in this analysis is shown in Fig 4.2. The yield ratio, F_R, between the PERP and corresponding PARA dataset in the beam energy range $8.2 < E_\gamma < 8.8$ GeV provides a measure of the flux ratios in Table. 4.2. The ratio is used to extract Σ as shown in Eq 4.10 and has negligible statistical uncertainties due to the high PS counting rate. The flux was obtained from a standardized tool [82] used by the entire collaboration.

Polarization Orientation	Beam Intensity	F_R
0/90	Low Intensity	0.962789
45/135	Low Intensity	1.000127
0/90	High Intensity	1.133984
45/135	High Intensity	0.989131
0/90	Full Run	1.0373219
45/135	Full Run	0.995373

Table 4.2: Flux normalization ratios for different polarization directions and beam intensities.

4.1.3 Phase Offset

The phase offset, ϕ_0, allows for the PARA (PERP) polarization plane orientation to vary from being parallel to the $x - z$ ($x - y$) plane in the LAB frame. The phase offsets were extracted by fitting the ϕ-distributions of a high-statistics sample of $\gamma p \to \rho p, \rho \to \pi^+\pi^-$ events [83]. Since there is an

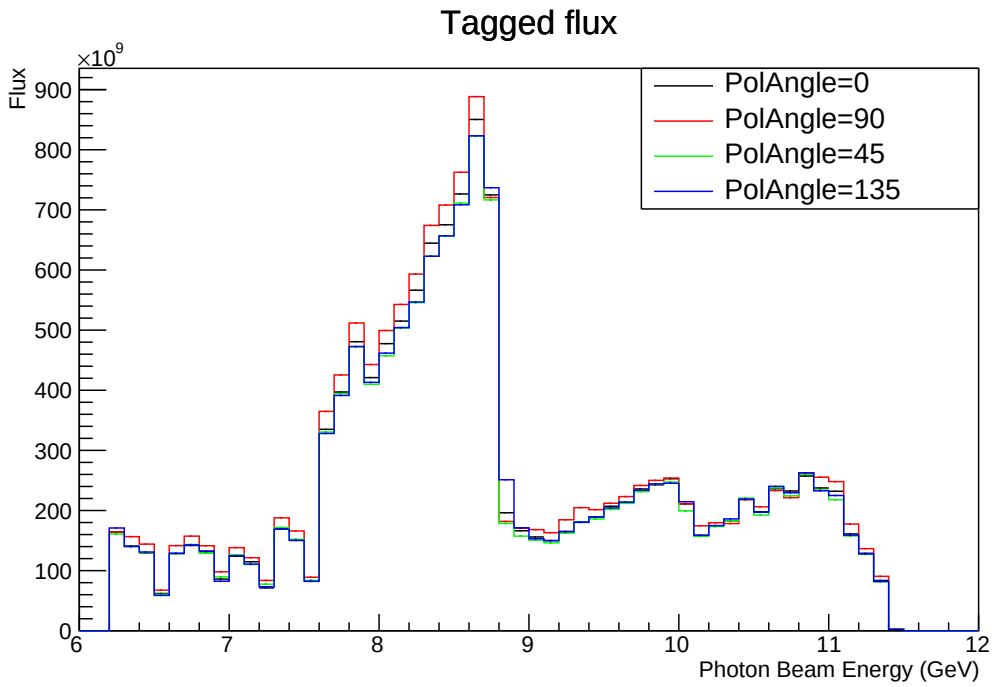

Figure 4.2: The tagger-derived photon-beam energy distribution for PS events in coincidence with a TAGM or TAGH hit for the full run period. A PS acceptance correction has been applied.

expected reaction dependence to extracting ϕ_0 due to kinematics with this method, the same procedure was performed using the sample of π^0 events from this analysis. These two results agreed with each other but the ρ results had an order of magnitude higher precision. The measured value of the phase offset can be seen in Tab. 4.3. The phase offset in the fit to extract Σ will be fixed to these values and discussed more in Sec. 4.5. The values from the ρ analysis are subsequently used by default for all ongoing GlueX analyses.

Polarization Orientation	ϕ_0 (°)	error (°)
0/90	3.1	0.5
45/135	3.2	0.6

Table 4.3: Measured values of the phase offset, ϕ_0 using the sample of ρ events [83].

4.2 Event Selection

The selection of $\gamma p \to \pi^0 p$ and $\gamma p \to \eta p$ events is performed using the standard GlueX analysis software framework [84], using the standard JANA [85] plugin, which produced ROOT TTrees containing the particle combinations of interest. Analysis of the TTrees was performed using the DSelector framework [86]. The plugin requirements, pre-selection and selection of events, as well as the effect of the selection criteria on invariant mass and -t distributions are presented below. The goal of the event selection is to provide clean event samples while maintaining a large enough sample size to perform the

analysis. Background contamination of the signal region is the major concern for measurements of the beam asymmetry, Σ.

4.2.1 Particle Combos

Candidates for the reactions of interest, $\gamma p \to p\gamma\gamma$, $\gamma p \to p\pi^+\pi^-\pi^0, \pi^0 \to \gamma\gamma$ and $\gamma p \to p3\pi^0, \pi^0 \to \gamma\gamma$ were selected inclusively from the data. A requirement that the reconstructed final state topology matched the reaction of interest final state topology was placed. For example, in the $\gamma p \to p\gamma\gamma$ reaction at least one tagged-beam photon, one reconstructed positively-charged track, and two neutral showers in the calorimeters, which together we call a single "combination" or "combo". There was a limitation of 3 extra of tracks in each event but no limitation on the number of showers or beam photons reconstructed in an event. A kinematic fit requires that the charged tracks in the particle combo came from the same production event vertex and that four-momentum is conserved. For the 2 decay modes where η decays to a π^0 the mass of the π^0 is constrained in the kinematic fit. At this stage, the kinematic fit is required to converge. Later in the analysis a tighter cut is placed on the kinematic fit confidence level.

4.2.2 Beam Photon Selection

Charged tracks are matched to hits in the BCAL, FCAL, ST and TOF detectors. The time of these hits are propagated back to the center of the target using the path-length of the track to find a target time associated with each matched hit. The target time for photons use the photon flight time propagated from the position of the photon shower to the target. The target time for each particle is used to vote among different beam bucket times provided by an RF signal from the accelerator to select a primary interaction time associated with each event, referred to as the RF time. The selected RF time is compared to the time of the tagged beam photons. If the RF beam bucket selection is correct then the Δt between the tagged beam photon and the RF signal will be centered at zero as shown in Fig. 4.3. There are sideband peaks that come from accidentally-tagged beam photons. These peaks are separated by 4ns because the accelerator delivers micro-pulses at 249.5MHz. The sideband peaks are usually caused by real electron hits in tagger channels that are near the photon energy associated with the primary interaction. Given the high intensity that CEBAF operates at, it is fairly common for a single beam bunch to radiate 2 or more high energy photons. This will result in accidental hits arriving at the same time as hits associated with the photon involved in the primary interaction. The accidental hits will be in tagger counters spatially nearby the tagger counter that records hits due to the primary interaction photon. Since these two photons arrive at the same time the timing information cannot separate them and there will be an accidental peak contaminating the main RF peak. Therefore a statistical correction due to these accidentals is made by assigning a weight of 1.0 to all combinations that fall inside the main RF peak and a weight equal to the ratio of signal to the number of sideband peaks used, -1/6, for the accidental combinations. The contribution from the accidental background is corrected by performing a sideband subtraction in our analysis using these weights. The systematic effect of over- and under-subtracting the accidentals is studied in Sec. 5.8. All plots shown in this chapter are corrected by subtraction of accidental coincidences (accidental-subtracted).

4.2.3 Combination Pre-selection

Before applying the event selection specific to each reaction, some general pre-selection conditions are applied to remove combinations which may have questionable reconstruction quality for various reasons.

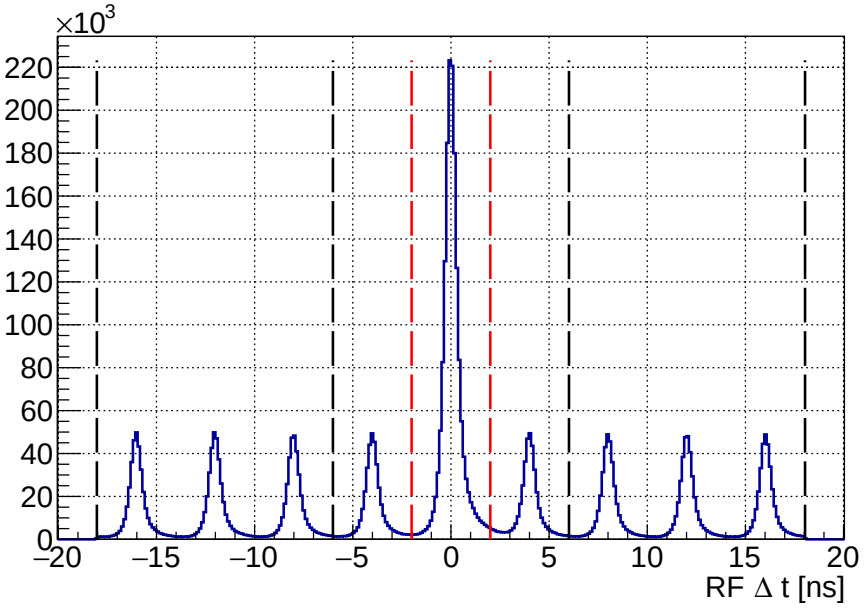

Figure 4.3: Time difference between tagged beam photon and RF time. The dashed red lines indicate the in-time beam photons and the dashed blacks lines indicate the out-of-time beam photons that will be used for accidental subtraction.

The default, loose PID cuts are applied to reject misidentified particles, such as the dE/dx cut on the proton in Fig. 2.15. The remaining pre-selection conditions are explained below,

- Vertex z position allowed: $52 < z < 78$ cm (Fig. 4.4),
- Vertex radial position allowed: $r < 1.0$ cm (Fig. 4.5),
- Proton momentum veto: $p_p < 0.25$ GeV/c. (Fig. 4.6),
- Fiducial gap between the BCAL and FCAL veto: FCAL $\gamma_r > 100$ cm and BCAL $\gamma_z > 380$ cm. (Fig. 4.7),
- Fiducial veto of the BCAL upstream endplate: $\gamma_z < 100$ cm. (Fig. 4.7),
- Fiducial beam background radius veto in the FCAL: $\gamma_r < 25$ cm. The radius is defined in the x-y plane perpendicular to the beam direction with the target set as the origin. (Fig. 4.8).

A systematic study on the placement of these combination pre-selection cuts will be discussed in Sec. 5. A cut is placed on the reconstructed event vertex position to require the vertex to be within the target volume. Figure 4.4 and 4.5 show the vertex z and r positions. The red dashed lines indicate cuts on these quantities to remove any effects from the target windows (z) and cylindrical walls (r). Whenever there is only one charged particle in the final state the reconstructed event vertex is the proton's distance of closest approach to the beam position. Whenever there are multiple charged particles in the final state the reconstructed event vertex is the position of closest approached between the charged particle tracks, this quantity is kinematically fit.

The reconstructed proton momentum is shown in Fig. 4.6. The vast majority of the protons are reconstructed in the CDC, where there is a threshold around 0.25 GeV/c where the protons begin to

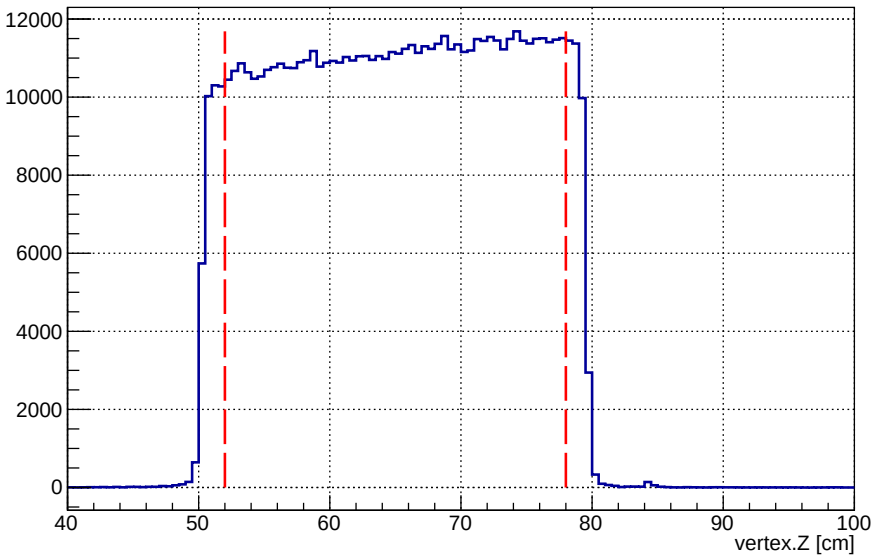

Figure 4.4: Vertex position along the beamline. The vertical red line displays where the cut is placed.

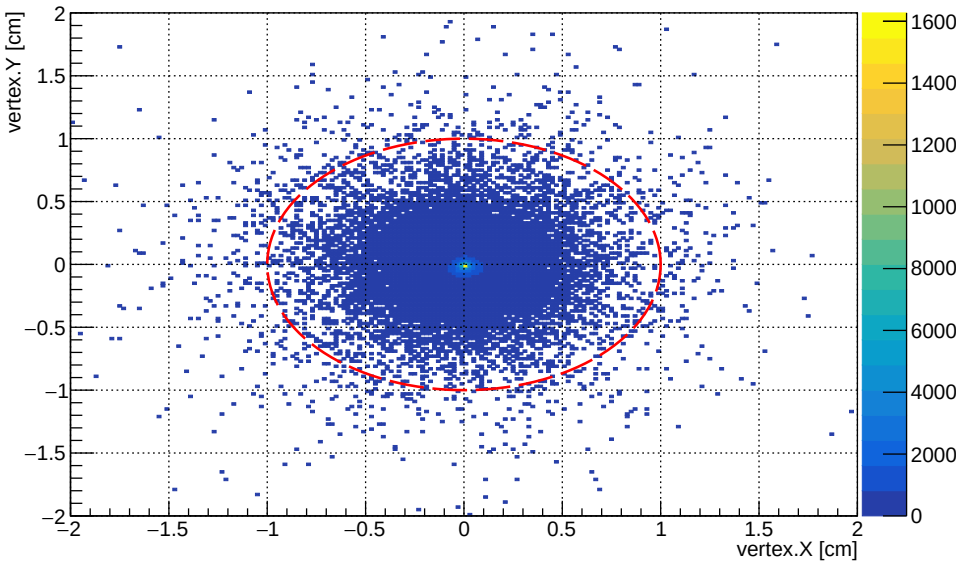

Figure 4.5: Radial vertex position. The circular red line displays where the cut is placed.

have enough hits to be reasonably reconstructed. The momentum threshold indicated by the dashed red line removes the tail of the distribution in the low momentum region.

Fiducial requirements on the reconstructed photon's position in the calorimeters are placed where the reconstruction quality is expected to be poor. The region closest to the beamline in the FCAL is excluded because background from the beam lowers the photon reconstruction quality. The boundary between the FCAL and BCAL is also exluded to reduce any edge and shadowing effects that could result in instrumental asymmetries. Photons that could have some leakage out of the upstream end of the

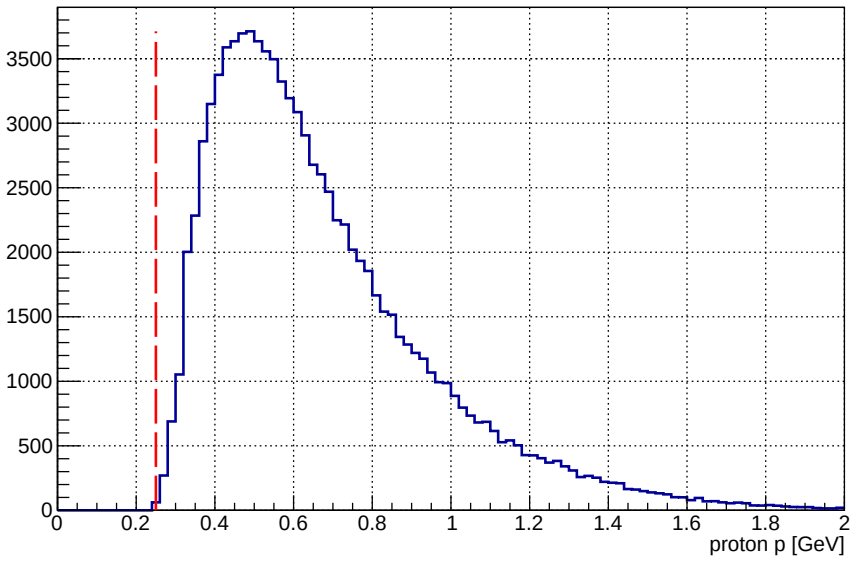

Figure 4.6: Proton momentum distribution. The vertical red line displays where the cut is placed.

BCAL are also vetoed. A single-photon MC was generated and the reconstructed photon energy was compared with the thrown energy as a function of BCAL z-position to place these fiducial cuts. A cut is placed on the BCAL z-position is based on where the MC suggested there was no leakage out of the upstream and downstream faces.

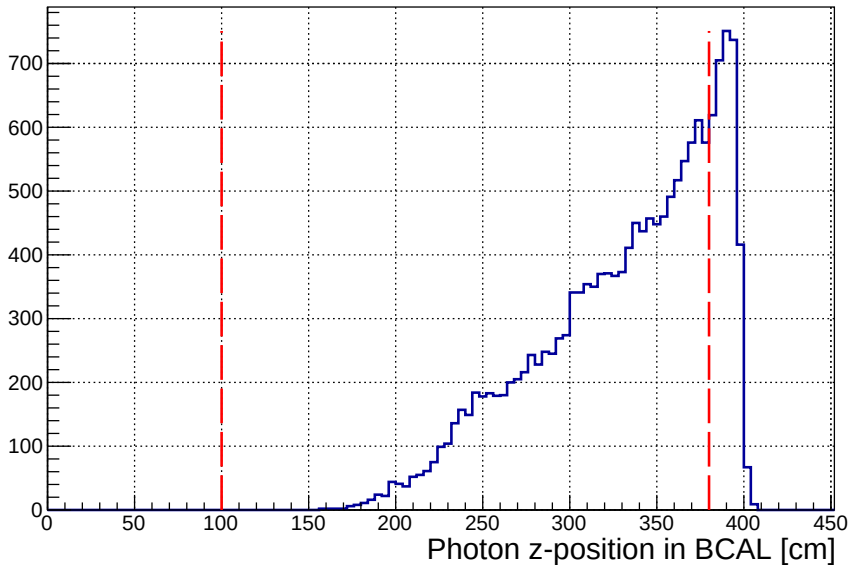

Figure 4.7: photon z-position in the BCAL. The vertical red line displays where the cut is placed.

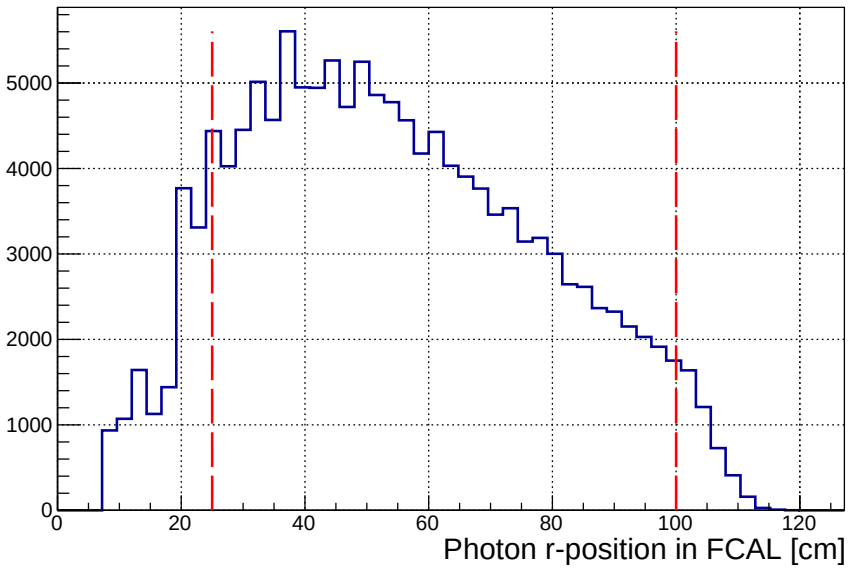

Figure 4.8: photon r-position in the FCAL. The vertical red line displays where the cut is placed.

4.2.4 Combination Selection

The remaining candidate combinations were selected with the following cuts, which are shown graphically and described in more detail below:

- Missing Mass Squared requirement: $|MM^2| < 0.05$ GeV^2. (Fig. 4.9)
- Beam Energy requirement: $8.2 < E_\gamma < 8.8$ GeV (Fig. 2.7)
- No unused energy reconstructed in either the BCAL or FCAL (Fig. 4.10 and 4.11)
- Kinematic fit confidence level rejection: CL $< 10^{-4}$ (Figs. 4.12- 4.14)

The Missing mass squared is defined as $MM^2 = (p_i - p_f)^2$, where

$$p_i - p_f = p_\gamma^{beam} + p_{proton}^{target} - (p_{proton}^{recoil} + \sum_{f=1}^{N_f} p_f). \tag{4.1}$$

The p_γ^{beam}, p_{proton}^{target}, p_{proton}^{recoil} and p_f are the 4-momentum of the tagged beam photon, target proton at rest, measured final state proton track, and measured final-state particles from the meson (π^0 or η) decay, respectively. The missing mass squared and unused energy cuts utilize the exclusive nature of the reactions, which constrain the kinematics of the measured particles in the combo. Figure 4.9 shows the missing-mass-squared distribution which peaks strongly at zero as expected. The magnitude of the missing mass squared is required to be less than 0.05 GeV^2. This is a loose cut to reject events that are obviously background.

As a final constraint on the exclusivity of the reaction, the amount of unused energy in each event is required to be zero. The unused energy is defined as the amount of energy deposited in the BCAL and FCAL calorimeters excluding the energy corresponding to the reconstructed photons from the π^0 or η decay and those matched to charged tracks of the final state particles. This cut is advisable when missing photon backgrounds are involved. Figure 4.10 and Figure 4.11 show the distributions of this Unused Energy, and the cut was applied to reject combos with greater than 100 MeV unused energy effectively requiring no unused showers in the FCAL or BCAL. This is because there is a 100 MeV shower pre-selection cut placed by default. Unused energy could still be deposited in the calorimeters if it is contained in a cluster with energy below 100 MeV. The removal of this default 100 MeV shower energy pre-selection cut was investigated but noticed that it had a very small effect on the event sample. Therefore it was decided to use the default 100 MeV shower energy cut. There is no unused energy cut in the $\eta \to 3\pi^0$ decay mode because it kills a significant portion of the signal and the signal is clean enough without making this cut. The high multiplicity of final state photons in this event ends with many too many events with a significant amount of unused energy.

The kinematic fitting is performed by a χ^2 minimization. The measured quantities of the particle combination are related to various fit hypotheses that come from the underlying physical processes [87],

$$\chi^2 = (\mathbf{y} - \boldsymbol{\eta})^T \mathbf{V}_y^{-1} (\mathbf{y} - \boldsymbol{\eta}). \tag{4.2}$$

In this minimization, $\mathbf{y}$ is defined as the measured quantities, $\boldsymbol{\eta}$ is defined as the estimated fit quantities and $\mathbf{V}_y^{-1}$ is the covariance matrix of the measured quantities. The χ^2 is minimized by imposing constraints using Lagrange multipliers. For each of the reactions one of the constraints is that the energy and momentum are conserved. In exclusive reactions the measured 4-momentum vectors may not appear to conserve energy and momentum due to detector resolutions or misidentified particles, however

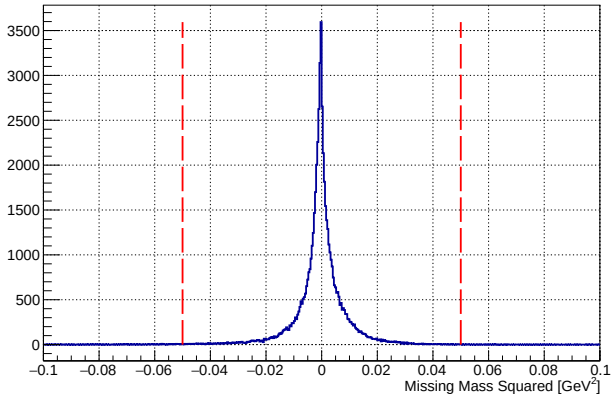

(a) $\eta \to \gamma\gamma$

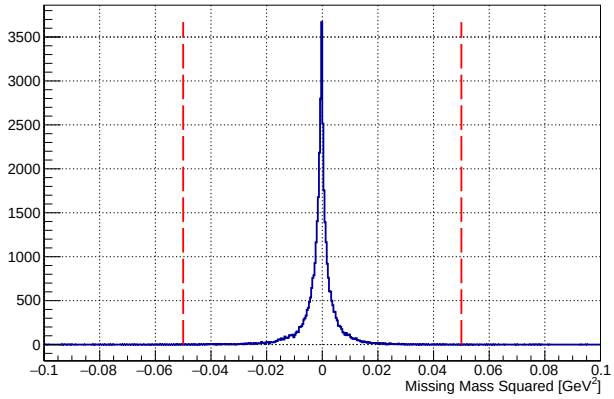

(b) $\eta \to \pi^+\pi^-\pi^0$

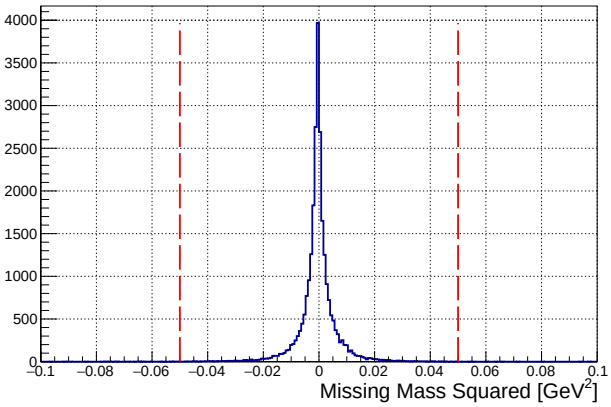

(c) $\eta \to 3\pi^0$

Figure 4.9: Missing-mass-squared distribution. The red dashed-lines display where the cut was applied.

the estimated fit quantities are constrained such that energy and momentum are conserved. Another constraint imposed on each reaction is that each of the photoproduced particles is required to originate from the event vertex. Also, for the two reactions, $\gamma p \to \pi^+\pi^-\pi^0 p$ and $\gamma p \to 3\pi^0 p$, the invariant mass of the 2 photon systems that result from the π^0 decays are constrained to be the π^0 mass literature value. The χ^2 minimization in Eq. 4.2 is performed while satisfying each of these constraints and outputs the kinematically fit 4-vectors and event vertices. These kinematically fit 4-vectors and vertices are used throughout this analysis, unless otherwise stated, to extract the beam asymmetry, Σ.

If the kinematic fit converges then the minimized χ^2 is used to calculate to a confidence level. If the sample was pure signal and the experimental errors were known exactly then the confidence level distribution would be flat, however neither of these conditions is realistic. Background events and poorly determined covariance matrices tend to populate events near 0, a confidence level cut rejecting combinations with low confidence level can be placed to clean up the sample. At higher confidence level values the incorrect covariance matrices would cause the distributions to be unflat indicating the errors need further study. This can also be seen in the kinematic fit χ^2/ndf distributions shown in Fig. 4.12-4.14. Another tool to assess the performance of the kinematic fit is the pull distributions of

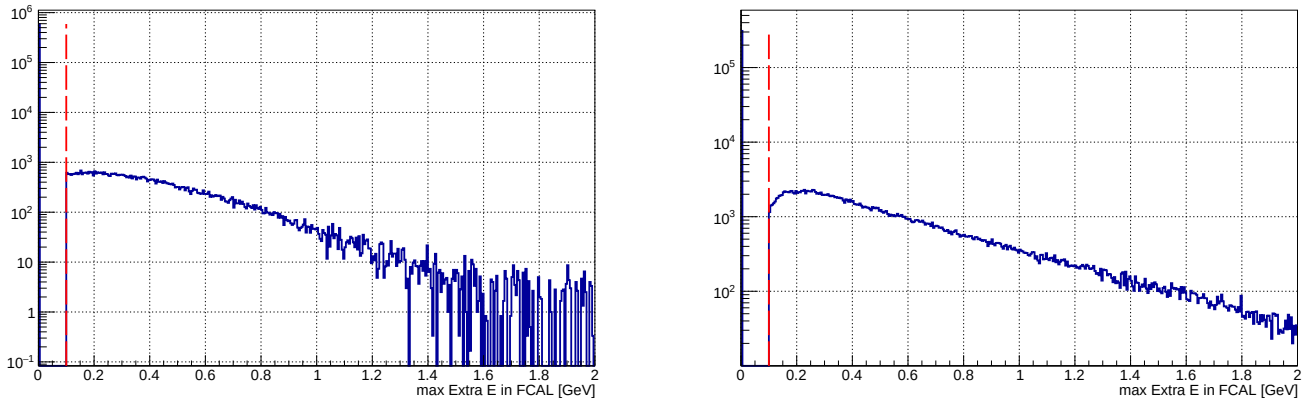

(a) $\eta \to \gamma\gamma$ (b) $\eta \to \pi^+\pi^-\pi^0$

Figure 4.10: Unused energy distribution in the FCAL. The red dashed-line displays where the cut was applied to reject combos with greater than 100 MeV of unused energy. There is no unused energy cut placed on the $\eta \to 3\pi^0$ decay

fits of various quantities. The pull distribution is defined as

$$z_i = \frac{y_i - \eta_i}{\sigma(y_i - \eta_i)} \tag{4.3}$$

and are shown in App. B. If the covariance matrix errors that feed into the kinematic fitter were correctly estimated then the pull distributions would be normally distributed with mean of zero and have a standard deviation equal to unity. If the errors of the measured variables were underestimated, then the corresponding pull distribution would be too wide. If the errors were overestimated then the distribution will be too narrow. In this analysis the pull distributions have a width close to unity and are centered near enough to zero not to cause any major concerns. Understanding the detector errors is an ongoing project for the experiment. The kinematic fit confidence level is a very powerful cut in that it removes a lot of background but it can also remove a lot of signal. The kinematic fitting procedure can also create signal out of background as it tends to converge combos to the signal region that will end up looking like signal events. To balance signal to noise and signal size a confidence level cut was carefully chosen to reject combos with confidence level $< 10^{-4}$. The confidence level of the kinematic fit for the three η decay modes is shown in Figs. 4.12- 4.14. A systematic study is carried out on the placement all of these combination selection cuts in Sec. 5.

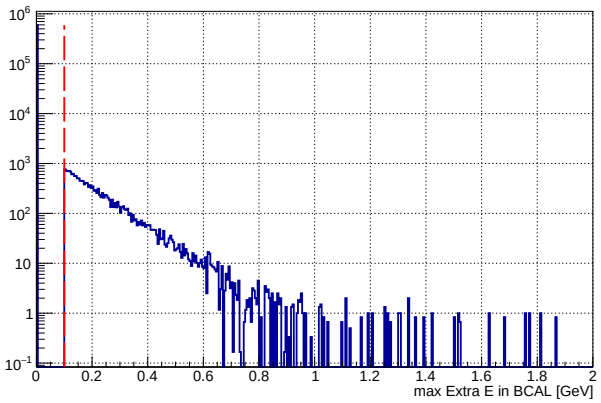

(a) $\eta \to \gamma\gamma$

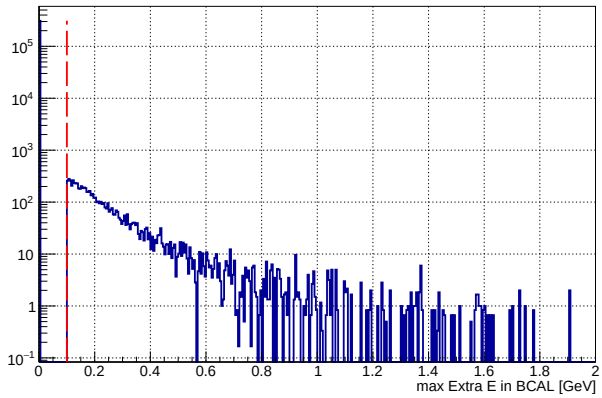

(b) $\eta \to \pi^+\pi^-\pi^0$

Figure 4.11: Unused energy distribution in the BCAL. The red dashed-line displays where the cut was applied to reject combos with greater than 100 MeV of unused energy. There is no unused energy cut placed on the $\eta \to 3\pi^0$ decay.

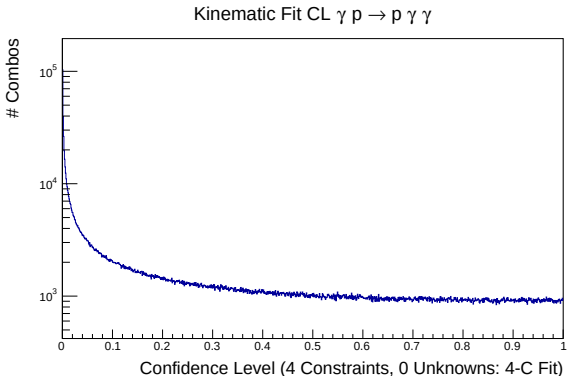

(a) kinematic fit confidence level.

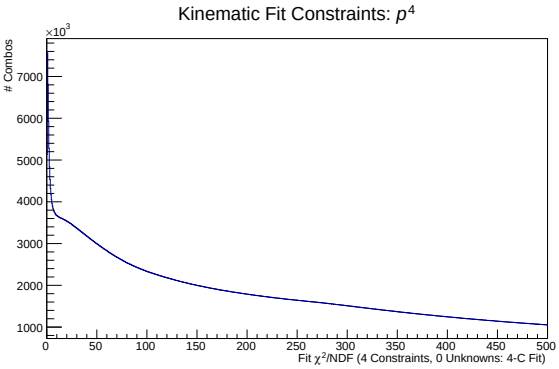

(b) kinematic fit χ^2/ndf.

Figure 4.12: The confidence level and χ^2/ndf of the kinematic fit for $\eta \to \gamma\gamma$.

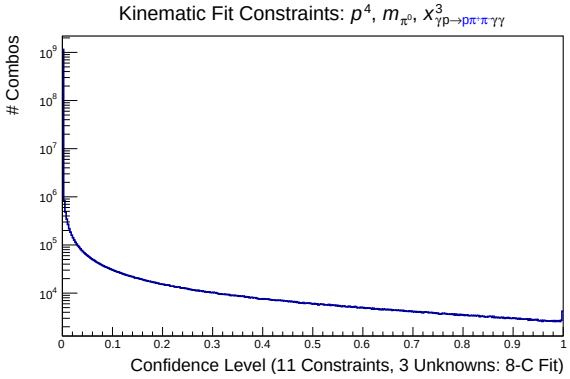

(a) kinematic fit confidence level.

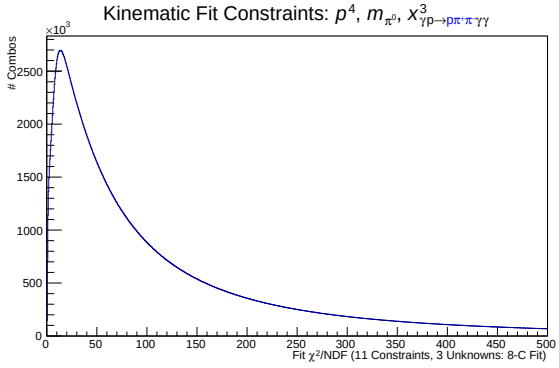

(b) kinematic fit χ^2/ndf.

Figure 4.13: The confidence level and χ^2/ndf of the kinematic fit for $\eta \to \pi^+\pi^-\pi^0$.

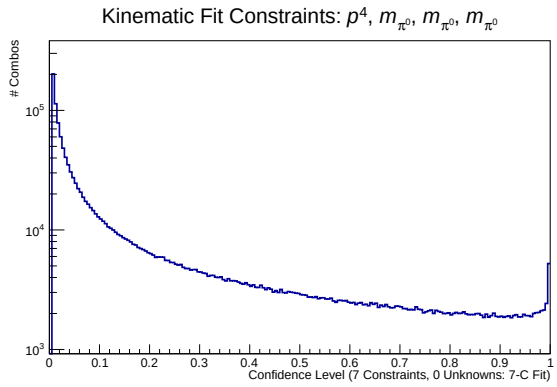

(a) kinematic fit confidence level.

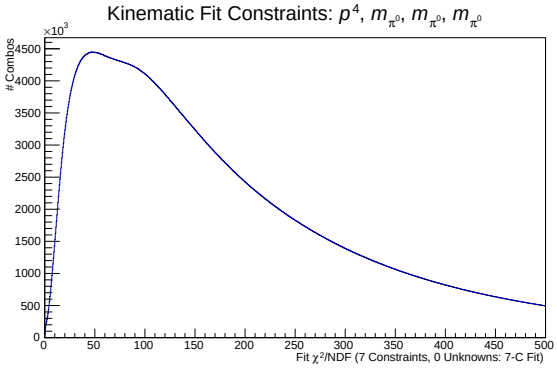

(b) kinematic fit χ^2/ndf.

Figure 4.14: The confidence level and χ^2/ndf of the kinematic fit for $\eta \to 3\pi^0$.

4.3 Event Samples After Applying Cuts

After application of all the above cuts in Sec. 4.2.4 the invariant mass distributions for each decay mode are plotted in Figure 4.15- 4.17. The number of combos that survive each cut in the analysis flow are recorded in Tab. 4.4. The remaining background under the signal regions will be discussed in Sec. 4.4. Each of the mass spectra are fit with

$$f(m) = A_1 e^{-\frac{(m-\mu)^2}{2\sigma_1^2}} + A_2 e^{-\frac{(m-\mu)^2}{2\sigma_2^2}} + e^{B+Cx}. \tag{4.4}$$

The double gaussian accounts for different resolutions between subdetectors, namely FCAL and BCAL, to fit the signal region while the exponential term is a simple estimation of the background. The goal of this fit is to extract the width of the mass distribution and to estimate the contribution from the background in the signal mass region. The width is only used to set limits on the mass cut used to extract the sample for the Σ measurement. The amount of background that is under the signal peak is used to correct the determination of Σ (Sec. 4.4) by extracting a dilution factor, $f = N_{bkgd}/N_{tot}$. The integral of the total fit function Eq 4.4 in the signal region is defined as N_{tot} and the integral of the background exponential function in the same mass range is defined as N_{bkgd}. The background contribution in the $\pi^0 \to 2\gamma$ and $\eta \to 3\pi^0$ modes are small enough to ignore but there is a significant contribution from the background in the η mass region that needs to be corrected for in the other two decay modes. This will be discussed further in Sec. 4.4. A more sophisticated fit could better describe the data but for the purposes of this analysis this is sufficient.

cut	combos survived (2γ)	combos survived ($\pi^+\pi^-\pi^0$)	combos survived ($3\pi^0$)
none	2.17e9	5.57e8	2.84e8
kin. fit CL	6.65e7	1.60e7	8.16e6
Beam Energy	9.89e6	2.38e6	1.69e6
proton momentum	9.86e6	2.37e6	1.67e6
$\|MM\|^2$	9.61e6	2.31e6	9.32e5
photon Fiducial	6.44e6	1.51e6	4.33e5
vertex-z	6.12e6	9.30e5	3.67e5
vertex-r	6.11e6	9.11e5	3.54e5
Unused energy	4.55e6	6.73e5	—
RF	1.60e6	2.23e5	80e4

Table 4.4: Number of combos that survive each cut in the analysis flow.

The mass windows are set at $\pm 3\sigma$ ($|M_{\gamma\gamma} - M_{\pi^0}| < 0.013$ GeV and $|M_{\gamma\gamma} - M_{\eta}| < 0.0297$ GeV) to select the final samples of π^0 and η events for further analysis. When selecting π^0 candidates in the $\eta \to \pi^+\pi^-\pi^0$ and $\eta \to 3\pi^0$ decays, the measured 4-momentum of the decay photons are used instead of the kinematically fit 4-momentum because a mass constraint was applied to the π^0. However, the photon's kinematically fit 4-vectors are used to reconstruct the sample of η candidates. Fig. 4.18 shows the $-t$ distribution utilizing these mass windows, where the π^0 distribution shows the characteristic dip around $-t = 0.5$ GeV^2 due to the Regge vector trajectory going to zero at $-t \approx 0.5$ GeV^2 as discussed in Sec. 1.3.1 and seen in previous measurements [47]. The η distributions, however, do not show any dip in the $-t$ range covered by our data, which is consistent with previous measurements [88].

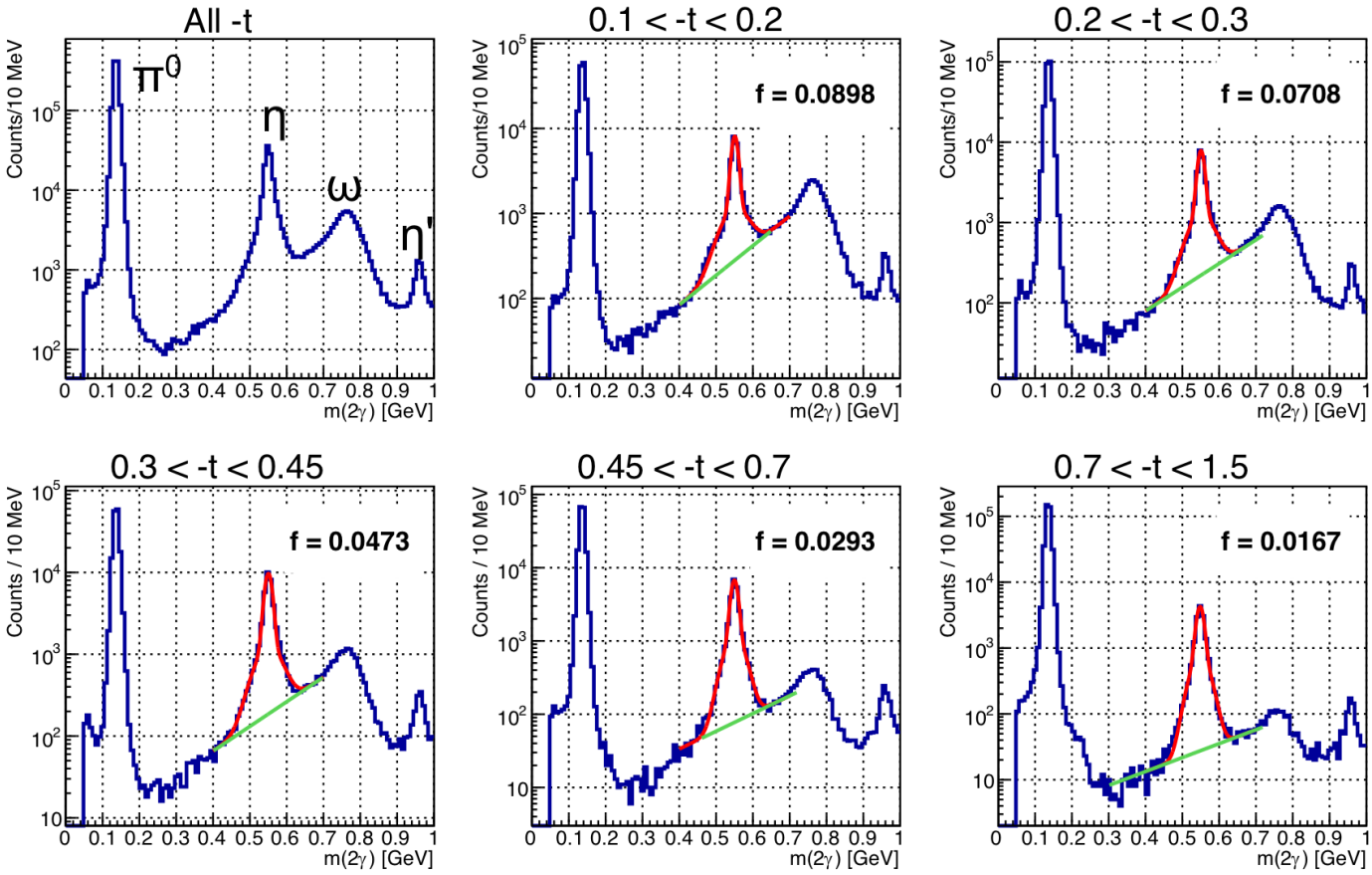

Figure 4.15: Invariant mass of two photons after all cuts are applied in the combo selection. The blue histogram is the plotted 2γ mass distribution, the red curve is a fit to the blue histogram using Eq. 4.4. The green curve is the exponential term from the fit. The value f in these histograms is the dilution factor which is defined as $f = \frac{Background\ Counts}{Signal + Background\ Counts}$ within the signal mass region. The upper left panel shows the mass distribution integrated over the full t-range and the remaining 5 panels are binned in -t.

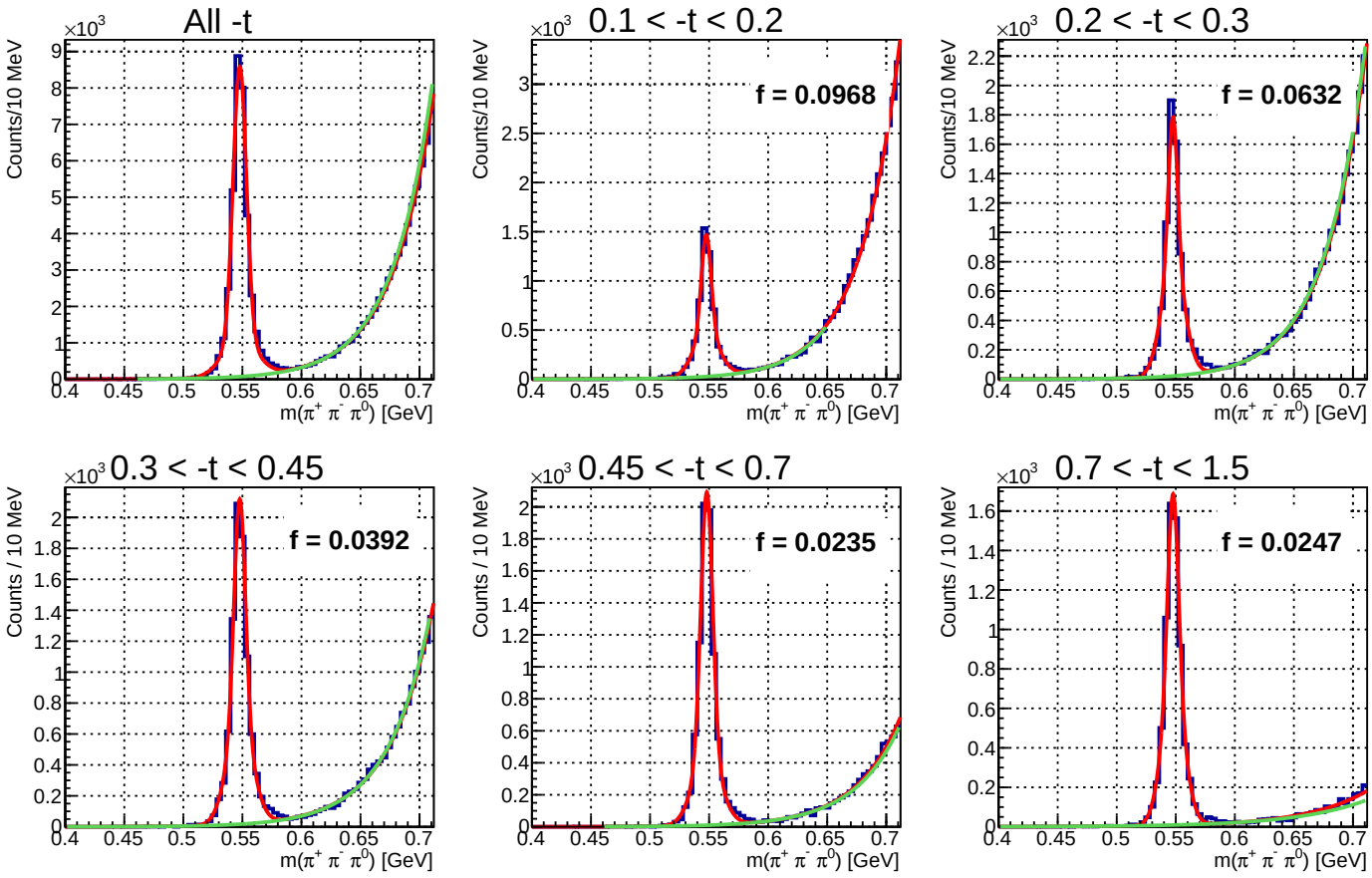

Figure 4.16: Invariant mass of $\pi^+\pi^-2\gamma$ after all cuts are applied in the combo selection. The blue histogram is the plotted mass distribution, the plot is formatted in the same way as in Fig. 4.15. The value f in these histograms is the dilution factor which is defined as $f = \frac{Background\ Counts}{Signal\ +\ Background\ Counts}$ within the signal mass region.

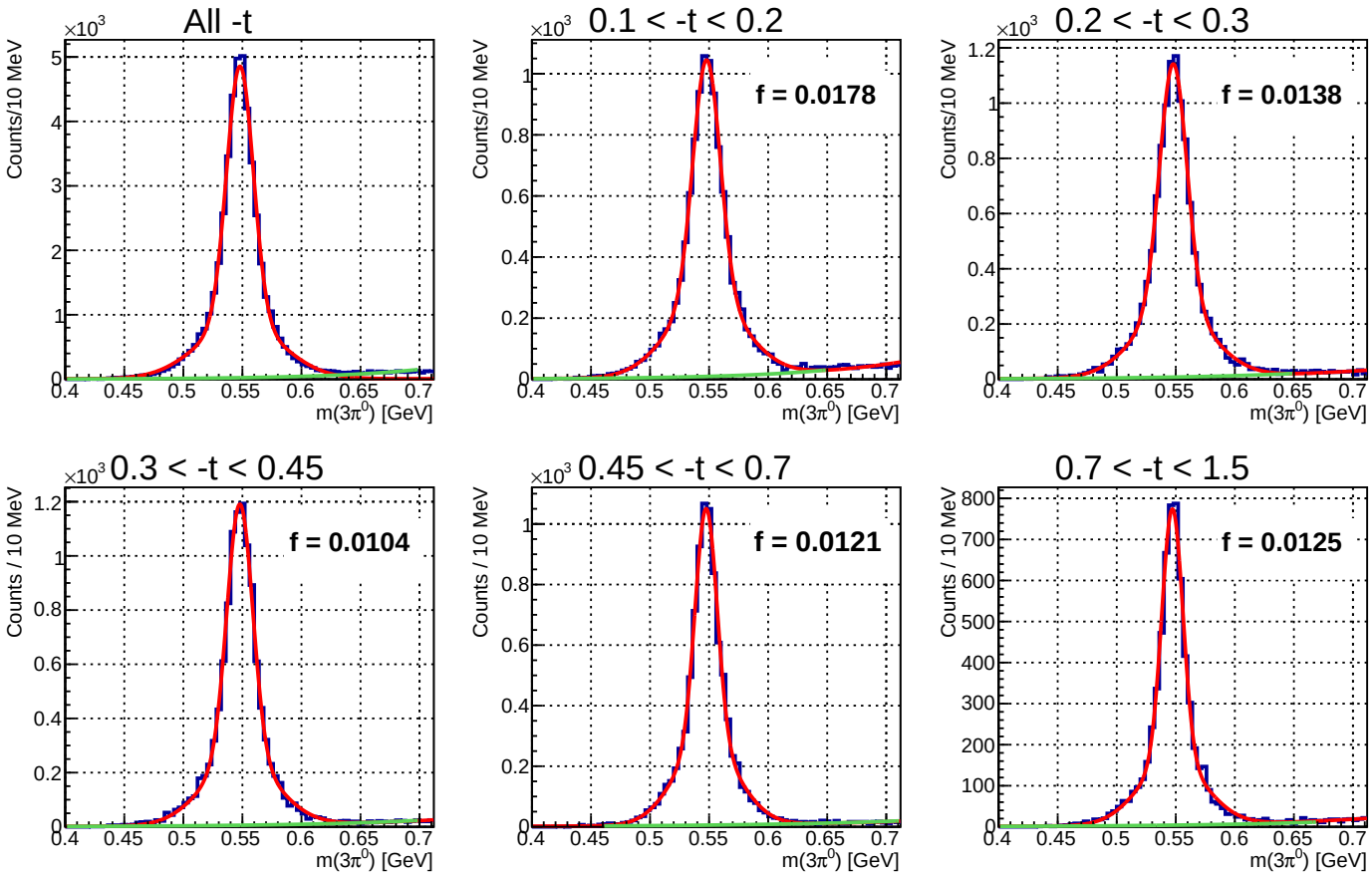

Figure 4.17: Invariant mass of 6γ after all cuts are applied in the combo selection. The blue histogram is the plotted mass distribution, the plot is formatted in the same way as in Fig. 4.15. The value f in these histograms is the dilution factor which is defined as $f = \frac{Background\ Counts}{Signal\ +\ Background\ Counts}$ within the signal mass region.

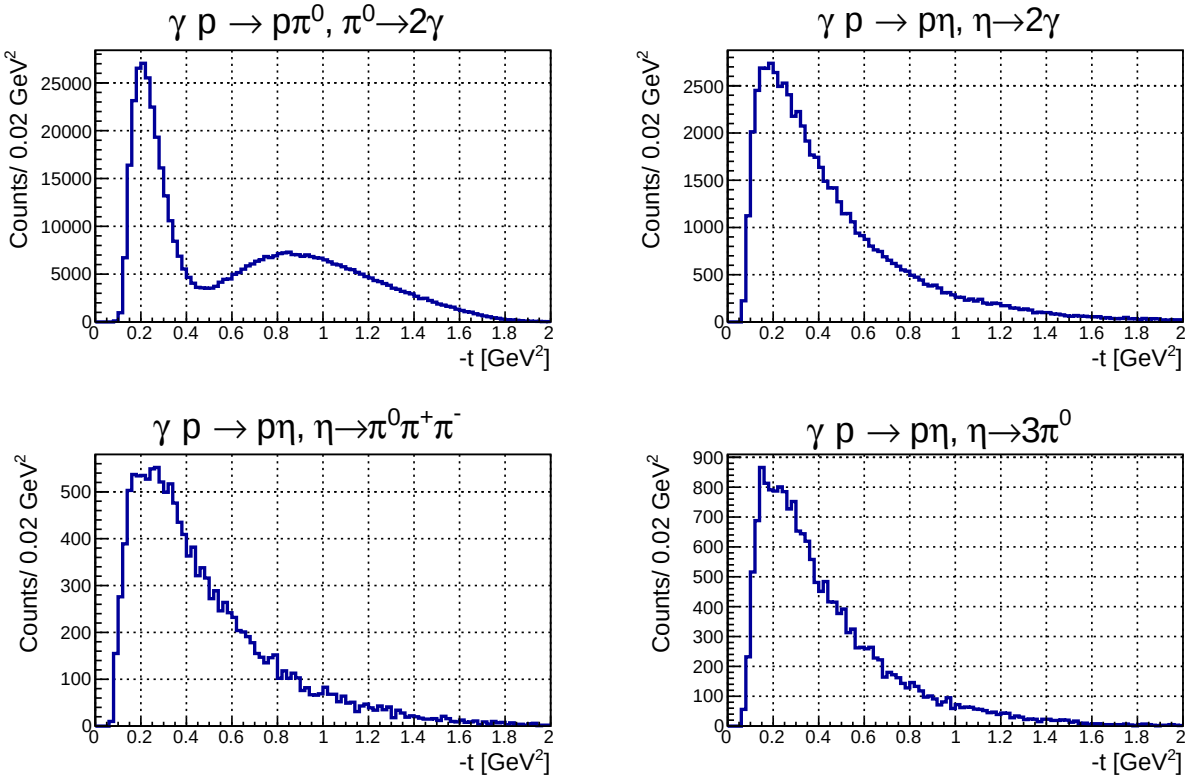

Figure 4.18: $-t$ distribution for events passing the selection criteria discussed in Ch. 4.2, The data have not been corrected for the acceptance functions, but the shapes of the acceptance functions indicate that their application would not introduce additional features in the shape of the data distributions.

4.4 Background estimation

As shown in Fig. 4.15 and 4.16, after all selection cuts are applied some background events remain above the η mass range for the $\eta \to 2\gamma$ and $\eta \to \pi^+\pi^-\pi^0$ decays. These events are largely the result of the much larger cross section of the $\gamma p \to \omega p$ reaction. The background in the $\eta \to 2\gamma$ is due to the ω radiative decay ($\omega \to \pi^0\gamma$) where one of the photons from the $\pi^0 \to \gamma\gamma$ decay is undetected. The background in the $\eta \to \pi^+\pi^-\pi^0$ is due to the hadronic decay ($\omega \to \pi^+\pi^-\pi^0$). The contribution of these events is understood by generating a samples of signal ω MC events for each of these two decay modes. The reconstructed ω MC events are required to pass the same event-selection criteria as the data. The $\omega \to \pi^0\gamma$ decay is passed through the $\eta \to 2\gamma$ analysis chain and so the resulting distribution that survives has an undetected final-state photon. The $\omega \to \pi^+\pi^-\pi^0$ decay has the same final-state topology as the $\eta \to \pi^+\pi^-\pi^0$ decay. Both of the ω MC samples are normalized by the yield of combos in the mass region of $0.7 < M_{\gamma\gamma} < 0.85$ GeV and is shown in Fig. 4.19. This comparison between data and simulation indicates that the background contribution in the η mass window is dominated by ω events. As previously discussed, the η mass peak is fit using Eq. 4.4 to estimate the ω dilution in the η event sample. The amount of dilution was also extracted by counting the data and MC events in the η mass region which agreed with the dilution factor extracted by fitting. The agreement between these two methods builds confidence that the observed background in data really does come from ω events. The effect that the amount of dilution by ω events has on the extraction of Σ due to the $\gamma p \to \eta p$ reaction is discussed in Sec. 4.6.

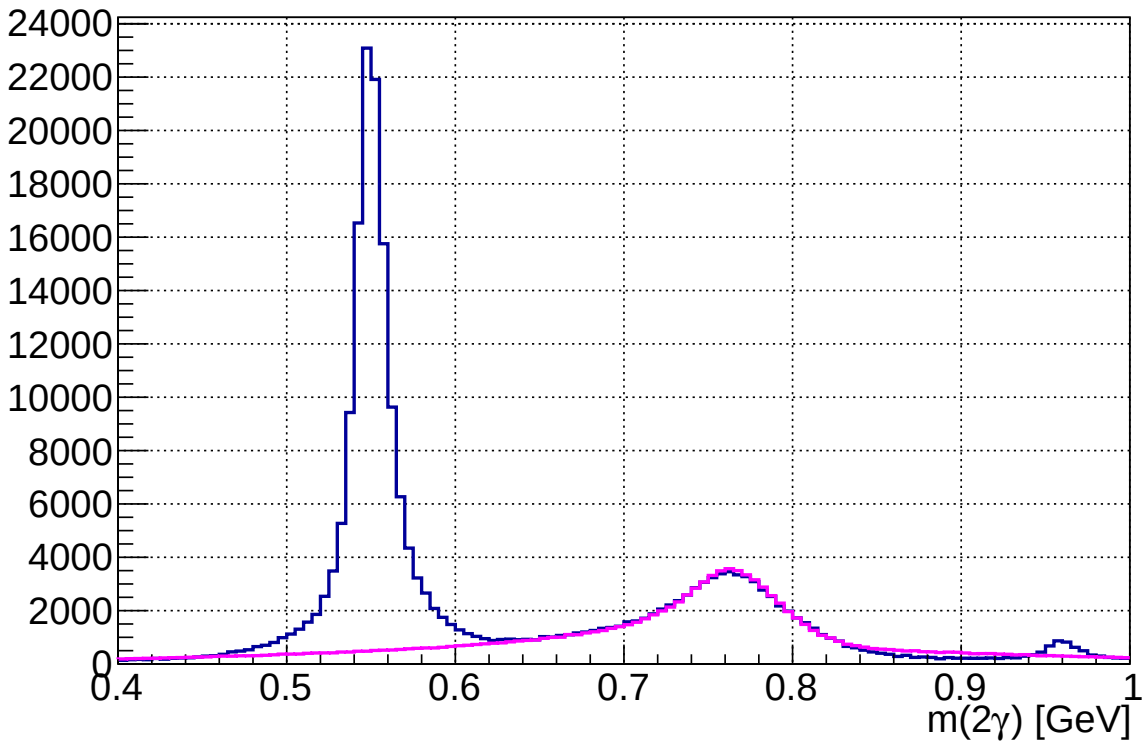

Figure 4.19: The 2γ mass is plotted for data in blue and for the MC in magenta. The MC is scaled to match the data. Both mass distributions are integrated over the full range of -t.

Other background processes that could contribute to a peaking background in the η mass region but

not have a large contribution outside of the η mass region were considered. There were two processes that were determined to be be most likely to contribute, the first being $\gamma p \to \phi p, \phi \to \eta\gamma, \eta \to 2\gamma$ where the γ from the ϕ decay went undetected. This potential background process is expected to be a small contribution by a quick estimation given that $\sigma_\omega = 1.9\mu b/sr$. In the $\pi^+\pi^-\pi^0$ final state the peak in the η mass region is observed to be about 5% of the peak in the ω mass. After accounting for each branching ratio, we estimate that $\sigma_\eta = 0.14\mu b/sr$ and after accounting for the ϕ radiative decay branch, $\sigma_\phi = 0.0028\mu b/sr$. If 100% of the $\phi \to \eta\gamma$ were mis-identified, then the contamination would be 2% of the signal.

A sample of $\gamma p \to \phi p, \phi \to \eta\gamma, \eta \to 2\gamma$ signal MC was generated to study its contribution to the background. This reaction was normalized using MC by making a very rough estimate on the relative cross section of η to ϕ at 9 GeV. This estimated cross-section was used in an attempt to generate about the same number of ϕ events as produced η events. Then, the number of reconstructed MC ϕ events that pass the full analysis chain were compared with the number of reconstructed η events in data that pass the full analysis chain. To obtain the produced number of η events, the η events that were reconstructed were counted and corrected by the MC efficiency (around 20% averaged over -t). Therefore 650k ϕ signal MC events should have been simulated to match the 130k reconstructed $\eta \to 2\gamma$ events. To be conservative the the estimates, 1M events were instead simulated. The *gamma* mass distribution of the 1M generated ϕ signal after passing through the full analysis is shown in Fig. 4.20.

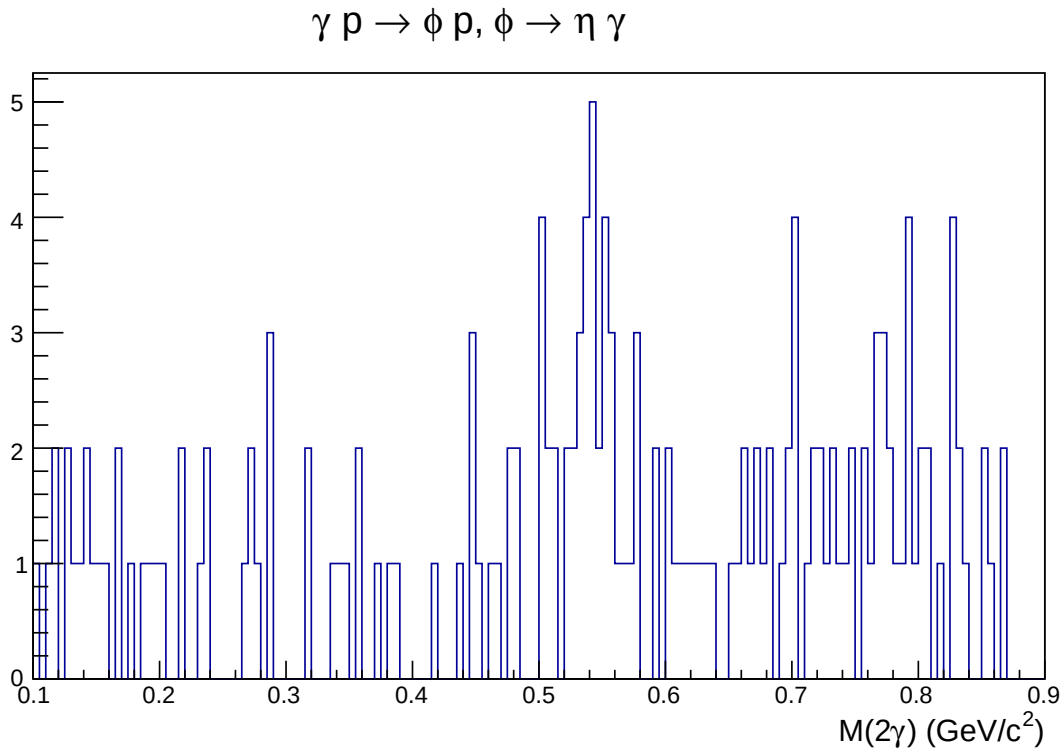

Figure 4.20: The 2γ mass is plotted for the signal MC for the radiative decay of $\phi \to \eta\gamma$.

The second background that was considered to potentially peak in the η mass region was the $\gamma p \to \Delta^+\eta, \Delta^+ \to \pi^0 p$, where both the η and the π^0 decay to 2γ. In this channel 2 of the photons have to go missing and the other two peak at the η mass. For this channel the cross-section was assumed to be approximately the same as η photoproduction and 1M signal MC events were generated again instead of 650k to be conservative. The 2γ mass distribution of the 1M generated signal MC after passing through

the full analysis chain is shown in Fig. 4.21.

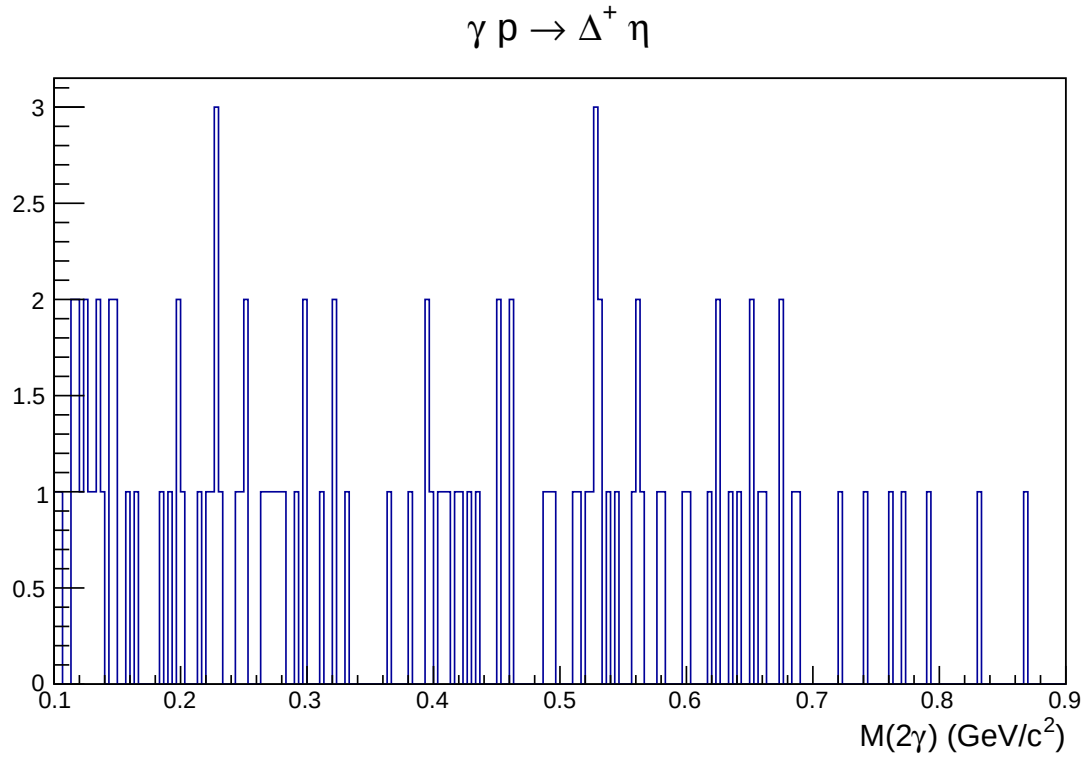

Figure 4.21: The 2γ mass is plotted for the signal MC for the reaction, $\gamma p \to \Delta^+\eta, \Delta^+ \to \pi^0 p$.

About 50 total events from both of these background sources survive the analysis selection criteria. Both of these background contributions are less than 0.01% the size of the sample in the η mass region so their contribution is ignored. This study was performed using the $\eta \to 2\gamma$ branch but it should hold approximately true for the other channels. A smaller number of MC background events would have been generated due to the other decay modes lower efficiencies. Since the observed effect is very small for the $\eta \to 2\gamma$ branch it is reasonable to assume that it will be at least small enough to ignore for the other branches.

4.5 Asymmetry Method and Results

For the photoproduction of pseudoscalar mesons with a linearly polarized photon beam and an unpolarized target, the polarized cross section is given by [89]

$$\sigma_{pol}(\phi, \phi_\gamma^{lin}) = \sigma_{unpol}\left[1 - P_\gamma \Sigma \cos\left(2(\phi - \phi_\gamma^{lin})\right)\right], \tag{4.5}$$

where:

- σ_{unpol} is the unpolarized cross section,
- P_γ is the magnitude of the photon beam polarization,
- ϕ is the azimuthal angle of the production plane,

- ϕ_γ^{lin} is the azimuthal angle of the photon beam linear polarization plane,
- Σ is the beam asymmetry observable of interest.

The coordinate system can be seen in Fig. 4.22 to give a visualization of these different quantities. The photon beam polarization plane is determined by the orientation of the diamond radiator. By setting the orientation of the diamond radiator to produce a beam of linearly polarized photons with polarization plane parallel or perpendicular to the lab floor ($x-z$ plane) the polarized cross-sections can be written as

$$\sigma_\parallel(\phi) = \sigma_{pol}(\phi, \phi_\gamma^{lin} = 0) = \sigma_{unpol}(1 - P_\parallel \Sigma \cos 2\phi), \tag{4.6}$$

$$\sigma_\perp(\phi) = \sigma_{pol}(\phi, \phi_\gamma^{lin} = 90) = \sigma_{unpol}(1 + P_\perp \Sigma \cos 2\phi). \tag{4.7}$$

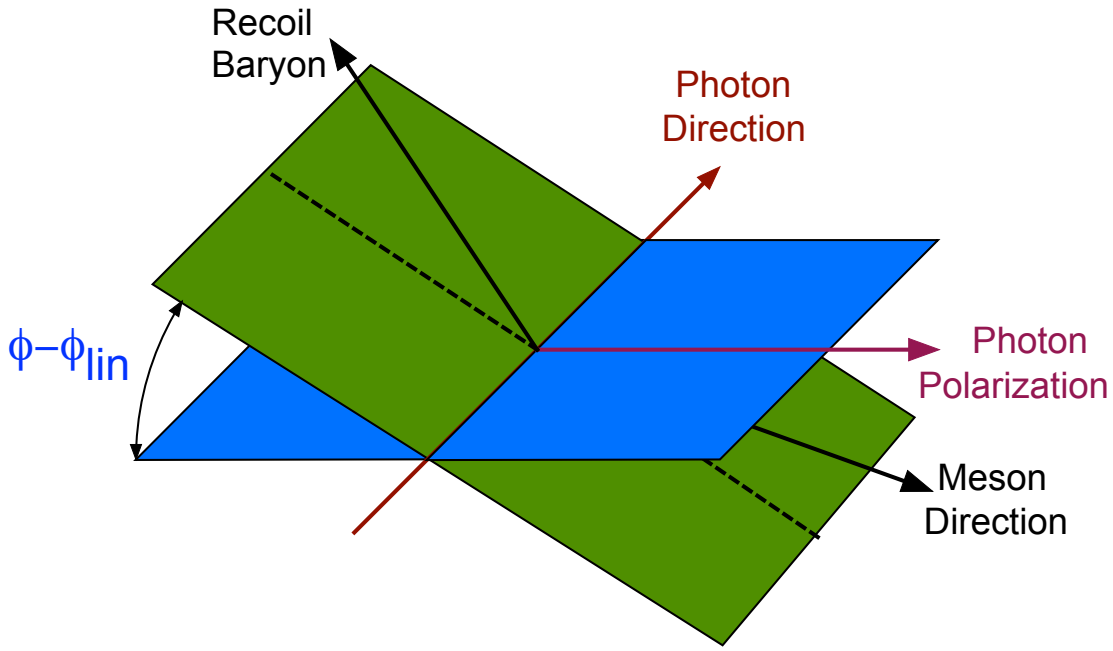

Figure 4.22: Definition of the relevant angules used to extract the Σ beam asymmetry in the LAB frame.

In principle, the experimentally-measured polarized cross-section distribution could be fit to extract Σ if σ_{unpol} and P were known. However, at this stage of GlueX the detector acceptance and efficiency are not understood well-enough to measure σ_{unpol}. The distributions that can be measured are the yields for data taken in each polarization plane as a function of ϕ and $-t$. The yields are the number of π^0 or η candidates as functions of ϕ and $-t$. These are obtained by selecting particle combos in the π^0 or η mass region after event selection for each decay channel and plotting ϕ of the recoil proton as a function of $-t$. The kinematically- fit proton ϕ is chosen because the π^0 or η are produced back-to-back with the recoil proton and the measurement of the single proton is more precise than measuring each of the final state particles to reconstruct the ϕ angle of the π^0 or η. The yields are expected to be given as

$$Y_\parallel(\phi) \sim N_\parallel[\sigma_{unpol} A(\phi)(1 - P_\parallel \Sigma \cos 2\phi)] \tag{4.8}$$

$$Y_\perp(\phi) \sim N_\perp[\sigma_{unpol} A(\phi)(1 + P_\perp \Sigma \cos 2\phi)] \tag{4.9}$$

where

- $A(\phi)$ is an unknown function representing the ϕ-dependent detector acceptance and efficiency,
- $N_{\parallel(\perp)}$ is the integrated flux of the photons in PARA (PERP) orientations.
- $P_{\parallel(\perp)}$ are the magnitude of the photon beam polarization in the PARA (PERP) orientations (Sec. 4.1.1),

The GlueX detector is designed to be symmetric in ϕ and thus have a uniform acceptance and efficiency, but the general case of some arbitrary ϕ-dependent detector acceptance is considered. The method for extracting Σ to cancel this detector acceptance is described in this section. One possibility is to use data with an amorphous radiator to normalize the polarized data, which effectively corrects for any ϕ-dependent acceptance. This procedure, however, requires a significant amount of data taken with an amorphous radiator, which is not desired because it sacrifices taking polarized data. Alternatively, in the absence of background, one can define a polarization-dependent yield asymmetry, $S(\phi)$ as

$$S(\phi) = \frac{Y_\perp(\phi) - F_R Y_\parallel(\phi)}{Y_\perp(\phi) + F_R Y_\parallel(\phi)} = \frac{\sigma_\perp(\phi)A(\phi) - \sigma_\parallel(\phi)A(\phi)}{\sigma_\perp(\phi)A(\phi) + \sigma_\parallel(\phi)A(\phi)}. \tag{4.10}$$

where F_R is the ratio of beam fluxes between PERP and PARA orientations, $N_\perp/N_\parallel$, taken from Sec. 4.1.2. It is clear that the ϕ-dependent acceptance, $A(\phi)$, cancels if it is the same for both PARA and PERP datasets. The measured yield asymmetry $S(\phi)$ can be fit to a function of the following form:

$$f(\phi) = \frac{(P_\perp + P_\parallel)\Sigma \cos 2(\phi - \phi_0)}{2 + (P_\perp - P_\parallel)\Sigma \cos 2(\phi - \phi_0)}. \tag{4.11}$$

The phase offset that was discussed in Sec. 4.1.3, ϕ_0, is introduced into the fit to account for the the PARA (PERP) polarization plane orientations to vary from being parallel to the $x-z$ ($x-y$) plane in the LAB frame. In the limiting case where $P_\perp = P_\parallel = P$ and $\phi_0 = 0°$, Eqns. 4.10 and 4.11 reduce to

$$S(\phi) = \frac{Y(\phi)_\perp - Y(\phi)_\parallel}{Y(\phi)_\perp + Y(\phi)_\parallel} = P\Sigma \cos 2\phi. \tag{4.12}$$

Therefore, with independent measurements of the flux, polarization magnitudes for PARA and PERP running periods and the ϕ_0 offset, Σ is determined independent of any ϕ-dependent detector acceptance effects. In terms of the fit parameters the yield asymmetry distribution is fit using

$$f(\phi) = \frac{(P_\perp + P_\parallel)p_0 \cos 2(\phi - \phi_0)}{2 + (P_\perp - P_\parallel)p_0 \cos 2(\phi - \phi_0)} \tag{4.13}$$

where the Σ asymmetry is the only free parameter, named p_0 in the fit. As a data quality check the individual PARA and PERP yield distributions are also fit to extract $P\Sigma$ using

$$h(\phi) = p_0(1.0 + p_1 cos(2(\phi - p_2))). \tag{4.14}$$

There are three free parameters in the fits for PERP and PARA independently, p_0 gives the normalization, $p_1 = P\Sigma$ and $p_2 = \phi_0$ for the phase constant.

4.5.1 Example fit to the $\eta \to 2\gamma$ sample

Since the relative flux, polarization and ϕ_0 have been measured, the fit of the ϕ-dependent yields to extract the Σ beam asymmetry can be performed. A set of example distributions and fits are shown in Fig. 4.23 for the $\eta \to 2\gamma$ event sample integrated over all $-t$ in the (0/90) diamond orientation. In

this figure , the upper plots are the accidental-subtracted ϕ distributions for the orthogonal polarization directions used to construct the yield asymmetry. Fits to the PERP (left) and PARA (right) ϕ distitrbutions are performed independently using Eq. 4.14. These two distributions are clearly approximately orthogonal to each other and exhibit the expected $\cos(2\phi)$ structure. The lower left plot in Fig. 4.23 is the yield asymmetry distribution given as $S(\phi)$ in Eq. 4.10 and fit using to the fit function Eq. 4.13. The lower right plot shows the polarization cross-weighted sum of the two ϕ distributions plotted in the upper two panels and is relevant for understanding the impact of an instrumental asymmetry. This is discussed in more detail in Sec. 5.3. The fits to the PERP, PARA and yield asymmetry distributions describe the data reasonably well. The fit probabilities are reasonable for all the individual $-t$ bins. These fits for each decay mode in each t-bin performed to extract Σ as a function of $-t$ but aren't shown, they can be found in their respective analysis notes [90, 91, 92].

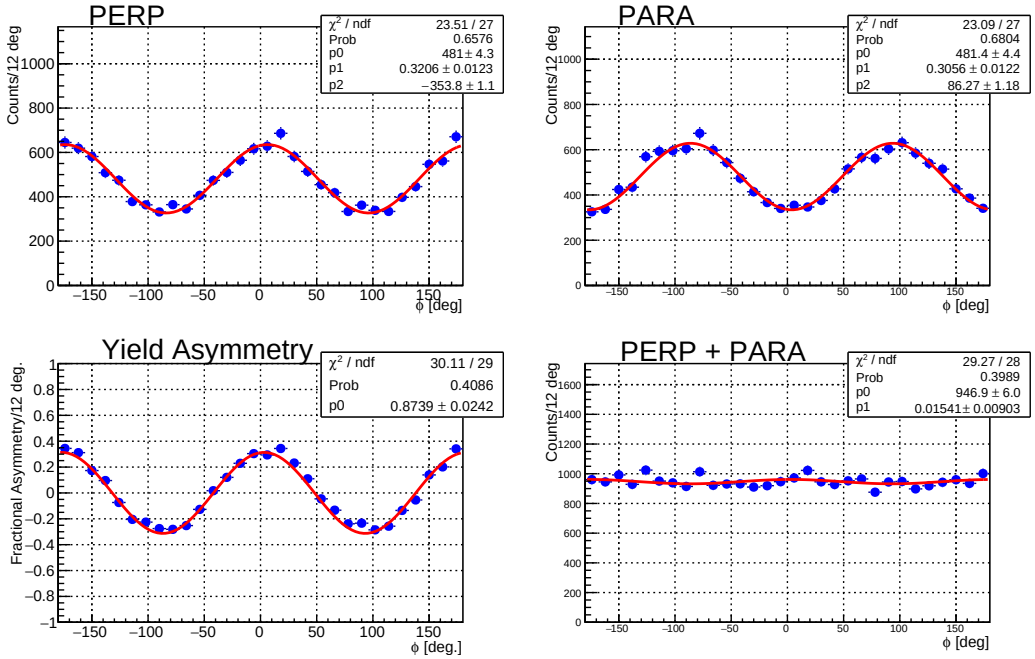

Figure 4.23: $\eta \to 2\gamma$ sample, polarization direction set to 0/90, Low Intensity. Fit to ϕ distributions with beam energy range $8.2 < E_\gamma < 8.8$ GeV, integrated over all $-t$. Upper row: Independent fits to the PERP (left) and PARA (right) distributions. Lower row (left): fits to the asymmetry (Eqn. 4.10). Lower row (right): Fits to the sum $P_\parallel Y_\perp(\phi) + P_\perp F_R Y_\parallel(\phi)$, which is sensitive to instrumental asymmetries.

4.6 Background Correction

Backgrounds to the η signals will generally have a different asymmetry that could affect the extracted value of the beam asymmetry for the processes of interest, as discussed in Sec. 4.4. The observed background in the $\eta \to 2\gamma$ and $\eta \to \pi^+\pi^-\pi^0$ sample are corrected using the following expression

$$\Sigma^{\eta}_{Signal} = \frac{\Sigma^{\eta}_{Measured} - f\Sigma^{\omega}_{Bkgd}}{1 - f} \tag{4.15}$$

where f is the fraction of ω events in the η mass window, $\Sigma^{\eta}_{Measured}$ is the measured asymmetry in the η mass window and Σ^{ω}_{Bkgd} is the background asymmetry from a sample of ω events in the range of $0.72 < M_{\gamma\gamma} < 0.84$ GeV. Σ^{ω}_{Bkgd} is measured by fitting the asymmetry using the same method as for the η sample; an example background fit is shown in Fig. 4.24. The observed background asymmetry from ω events is found to be opposite in sign to the η asymmetry. A set of values of the dilution factor, f, for each t-bin is shown in Table 4.5. The values for Σ^{ω}_{Bkgd} and f are used to correct the measured $\Sigma^{\eta}_{Measured}$ asymmetries.

t-bin range	f	δ_f
$0.1 < -t < 0.2$	0.0898	0.0046
$0.2 < -t < 0.3$	0.0708	0.0041
$0.3 < -t < 0.45$	0.0473	0.0030
$0.45 < -t < 0.7$	0.0293	0.0029
$0.7 < -t < 1.5$	0.0167	0.0027

(a) $\eta \to 2\gamma$

t-bin range	f	δ_f
$0.1 < -t < 0.2$	0.0968	0.0032
$0.2 < -t < 0.3$	0.0632	0.0022
$0.3 < -t < 0.45$	0.0392	0.0014
$0.45 < -t < 0.7$	0.0235	0.0011
$0.7 < -t < 1.5$	0.0247	0.0012

(b) $\eta \to \pi^+\pi^-\pi^0$

Table 4.5: dilution factors for each t-bin.

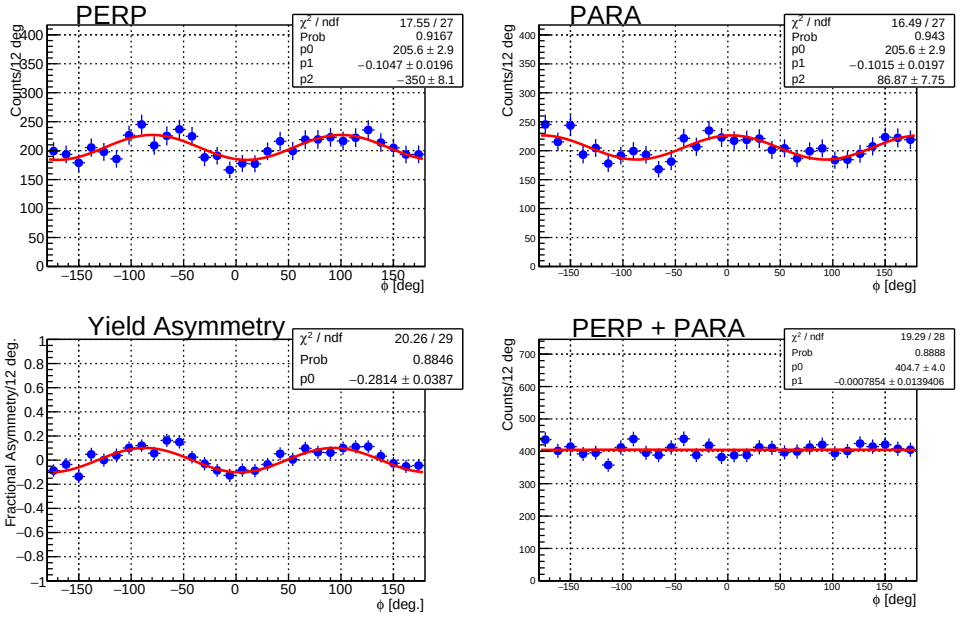

Figure 4.24: Fits to ϕ distribution for ω sample with $0.72 < M_{\gamma\gamma} < 0.84$ GeV, integrated over $-t$, polarization direction set to 0/90 and low intensity beam period. The arrangement of the plots is the same as Fig. 4.23.

Since Σ^{ω}_{Bkgd} is measured at a different mass range than where it is applied as a correction, the mass dependence of Σ^{ω}_{Bkgd} was studied. If there were a mass-dependency on the measured Σ^{ω}_{Bkgd} then an additional correction to the background Σ would need to be applied. This is hard to determine in data because the sideband Σ can't be measured close to the η mass region because the η sigma will dilute the background Σ. The mass-dependency of Σ^{ω}_{Bkgd} was studied in MC, Fig. 4.25 shows the mass bins that were used and the fit results in each bin. For the region that is well-separated from the η peak there is agreement between data and MC. There is no observed mass dependence of Σ^{ω}_{Bkgd}.

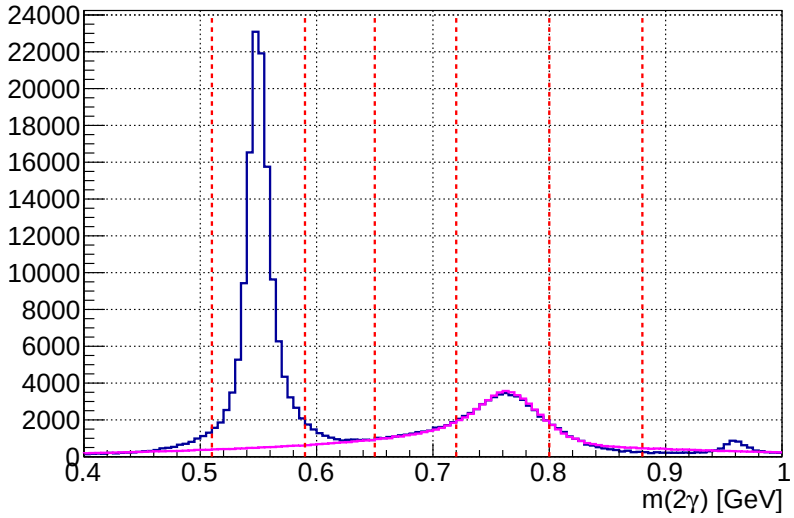

(a) The 2γ mass is plotted for data in blue and for the MC of the ω decay in magenta. The MC is scaled to match the data. Both mass distributions are integrated over the full range of -t. The red lines indicate slices of mass for which the background Σ was measured.

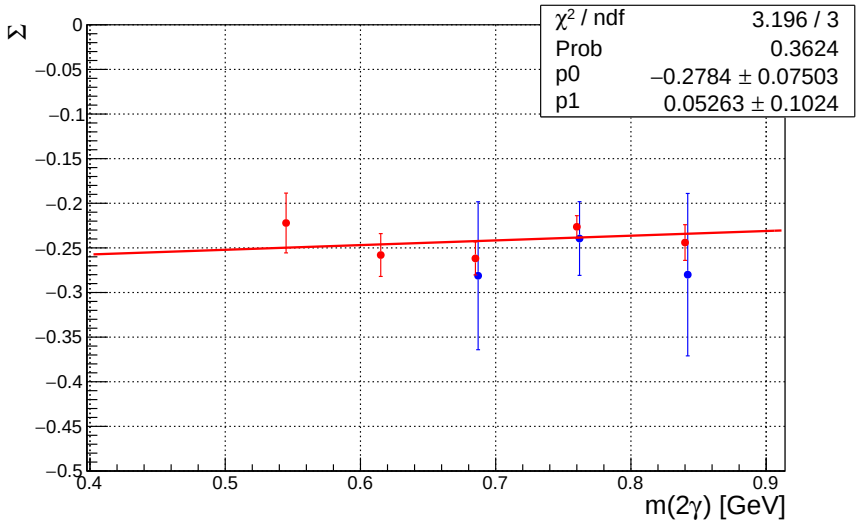

(b) Red points correspond to MC and blue points correspond to data. The red line is a fit to the MC

Figure 4.25: The MC is from generated $\omega \to \pi^0\gamma, \pi^0 \to \gamma$ where one of the photons from the π^0 decay goes undetected.

4.7 Summary of fit results

The results of the η asymmetry extraction based on the fits in the previous section are shown in Figs. 4.26- 4.28 as a function of t bin. Those results are also tabulated in Tables 4.6- 4.11. The results are presented to first show that there is good agreement between the High Intensity and Low Intensity data sets. Then the High and Low Intensity data are combined and good agreement is shown between the (0/90) and (45/135) datasets before they are combined together to give a result for each decay mode.

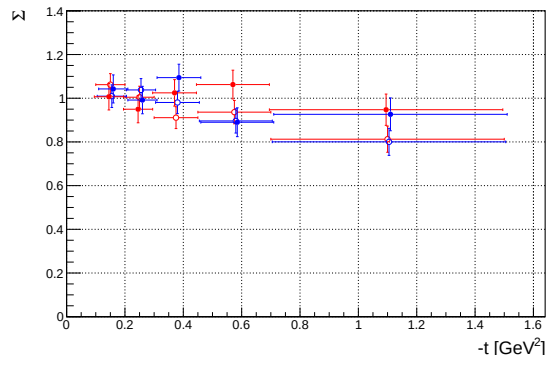

(a) $\eta \to \gamma\gamma$

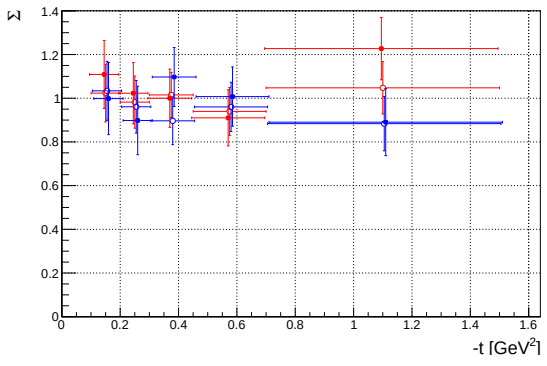

(b) $\eta \to \pi^+\pi^-\pi^0$

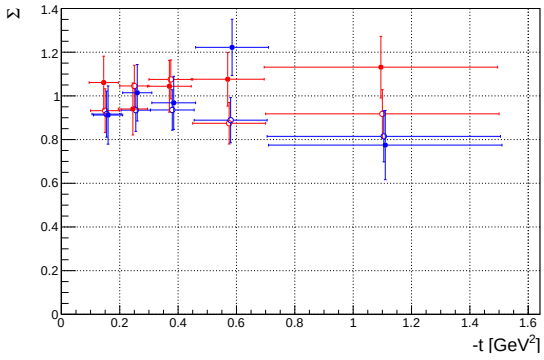

(c) $\eta \to 3\pi^0$

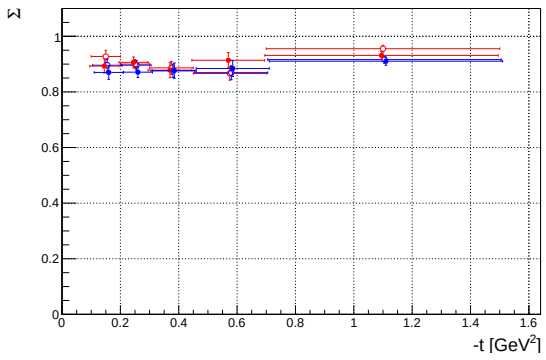

(d) $\pi^0 \to 2\gamma$

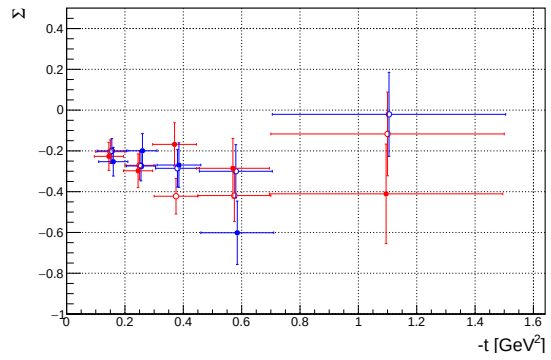

(e) $\omega \to \gamma\gamma$

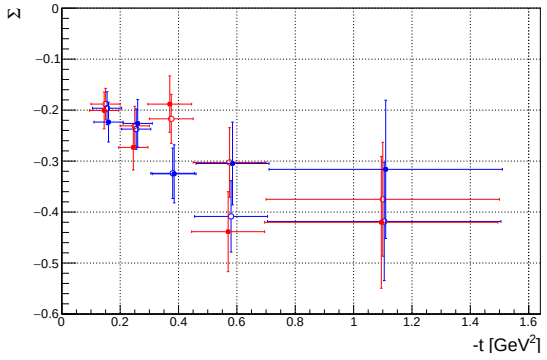

(f) $\omega \to \pi^+\pi^-\pi^0$

Figure 4.26: The open red circles correspond to polarization direction set to 0/90, low intensity beam runs, open blue circles correspond to polarization direction set to 45/135, low intensity runs, close red circles correspond to polarization direction set to 0/90, high intensity runs and the closed blue circles correspond to polarization direction set to 45/135, high intensity running.

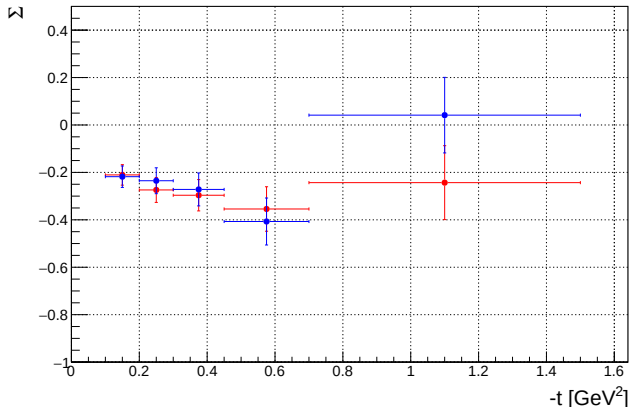

(a) $\omega \to \gamma\gamma$

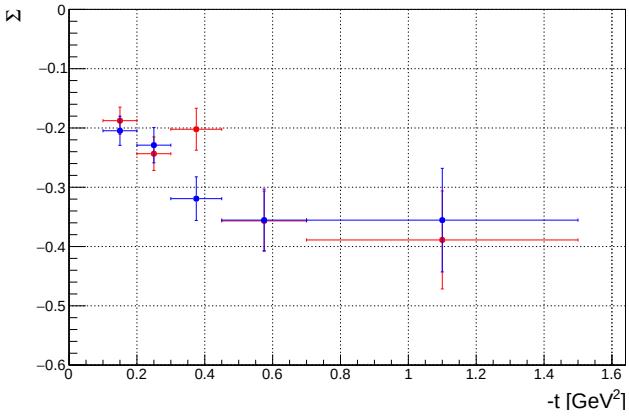

(b) $\omega \to \pi^+\pi^-\pi^0$

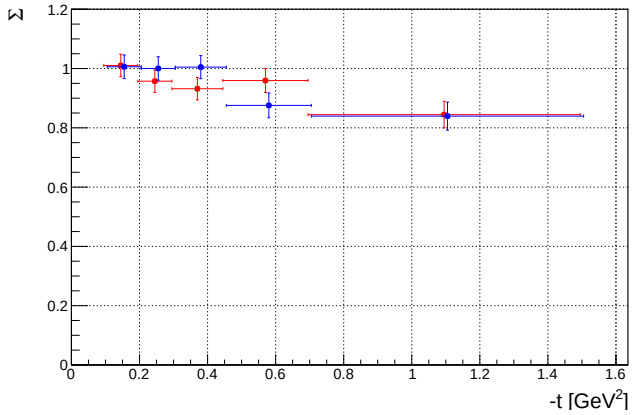

(c) $\eta \to \gamma\gamma$

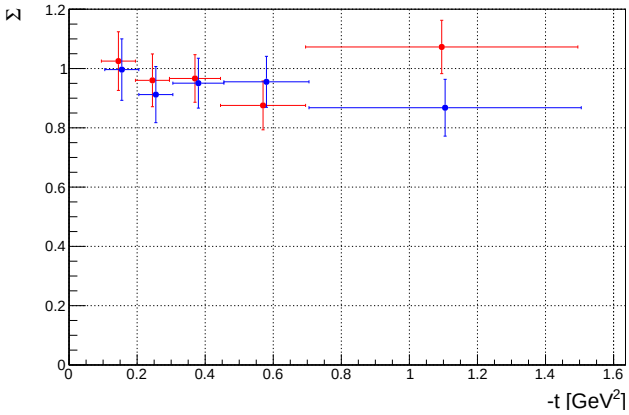

(d) $\eta \to \pi^+\pi^-\pi^0$

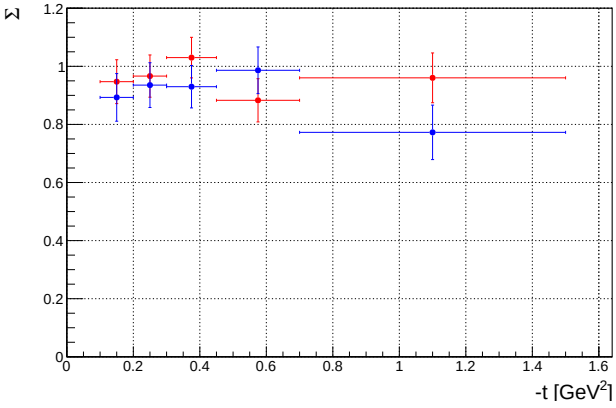

(e) $\eta \to 3\pi^0$

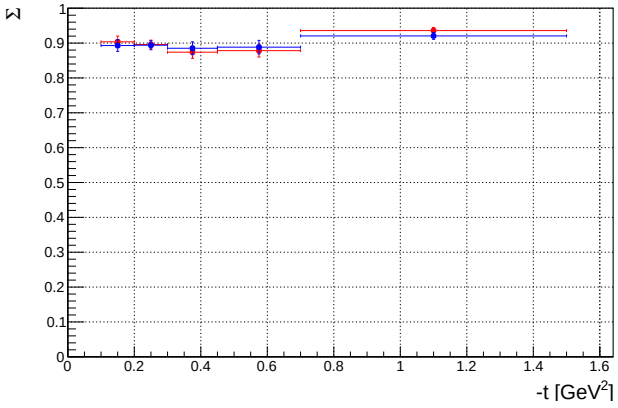

(f) $\pi^0 \to 2\gamma$

Figure 4.27: Beam asymmetry Σ after combining the Low Intensity and High Intensity runs. The red points correspond to polarization direction set to 0/90 and all runs, blue points correspond to polarization direction set to 45/135 and all runs.

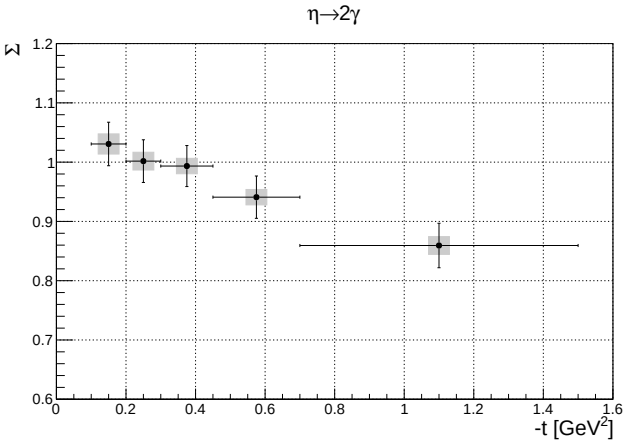

(a) $\eta \to \gamma\gamma$

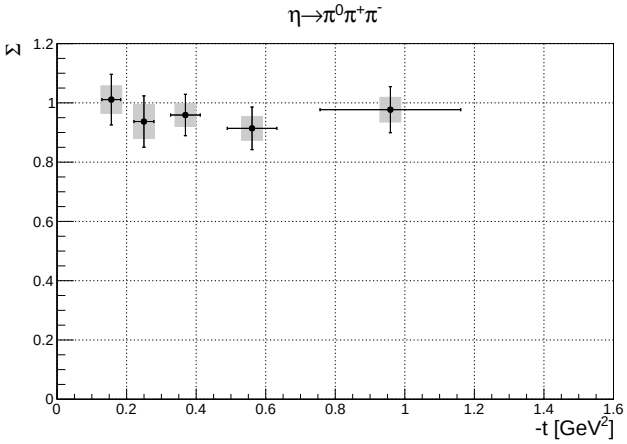

(b) $\eta \to \pi^+\pi^-\pi^0$

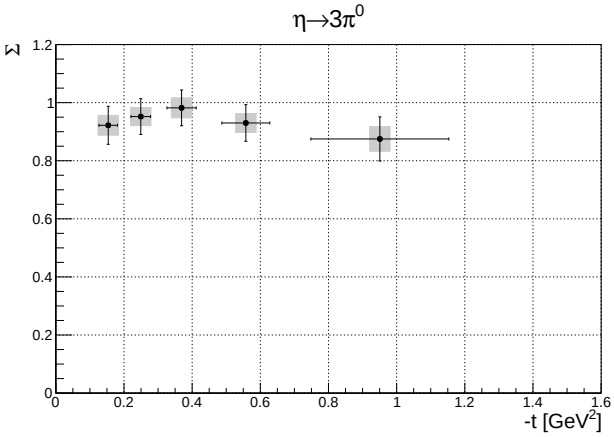

(c) $\eta \to 3\pi^0$

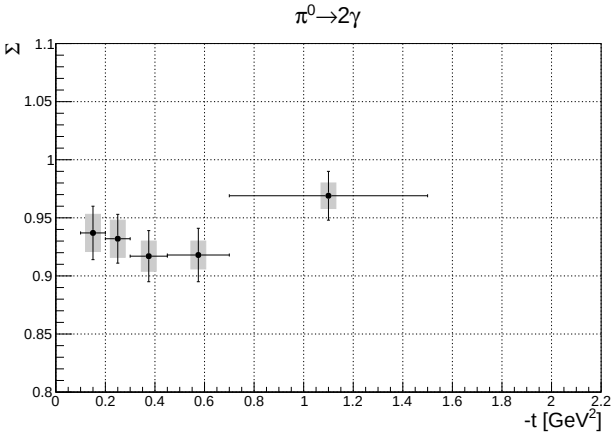

(d) $\pi^0 \to 2\gamma$

Figure 4.28: Beam asymmetry Σ after combining the 0/90 and 45/135 data. The vertical lines are the statistical errors added in quadrature with the systematic errors as discussed in Sec. 5. The grey boxes are the systematic errors, we chose the larger of the two systematic errors from the 0/90 and 45/135 data in each t-bin and assigned that as the systematic error.

-t bin [GeV^2]	Σ_{peak}	δ_{peak}	Σ_{SB}	δ_{SB}	f	δ_f	δ_P	Σ_η	δ_η
0.1 < -t < 0.2	0.901	0.0416	-0.2049	0.0043	0.0898	0.0062	0.028	1.039	0.0414
0.2 < -t < 0.3	0.870	0.0411	-0.2681	0.0040	0.0708	0.0054	0.027	0.983	0.0404
0.3 < -t < 0.45	0.874	0.0396	-0.29	0.0033	0.0473	0.0039	0.026	0.957	0.0389
0.45 < -t < 0.7	0.921	0.0422	-0.344	0.0028	0.0293	0.0039	0.027	0.986	0.0412
0.7 < -t < 1.5	0.8264	0.0457	-0.2357	0.0026	0.0167	0.0030	0.024	0.868	0.0441
0.1 < -t < 1.5	0.8719	0.0193	-0.2461	0.0017	0.0569	0.0046	0.026	0.939	0.0195

Table 4.6: 0/90 All intensity runs. Statistical uncertainties on Σ for individual $-t$ bins in the $\eta \to 2\gamma$ asymmetry. The statistical error on the polarization is not included yet. This table shows the statistical error contributions from each component of the corrected asymmetry measurement as well as their quadrature sum which is quoted as the total statistical error.

-t bin [GeV^2]	Σ_{peak}	δ_{peak}	Σ_{SB}	δ_{SB}	f	δ_f	δ_P	Σ_η	δ_η
0.1 < -t < 0.2	0.896	0.0437	-0.218	0.0045	0.0898	0.0061	0.028	1.022	0.0435
0.2 < -t < 0.3	0.913	0.0426	-0.235	0.0042	0.0708	0.0053	0.028	1.019	0.0422
0.3 < -t < 0.45	0.944	0.0410	-0.272	0.0024	0.0473	0.0040	0.028	1.027	0.0406
0.45 < -t < 0.7	0.840	0.0432	-0.354	0.0030	0.0293	0.0037	0.025	0.894	0.0425
0.7 < -t < 1.5	0.821	0.0480	-0.243	0.0027	0.0167	0.0021	0.024	0.851	0.0464
0.1 < -t < 1.5	0.8771	0.0201	-0.228	0.0018	0.0569	0.0044	0.027	0.944	0.0202

Table 4.7: 45/135 All intensity runs. Statistical uncertainties on Σ for individual $-t$ bins in the $\eta \to 2\gamma$ asymmetry. The statistical error on the polarization is not included yet. This table shows the statistical error contributions from each component of the corrected asymmetry measurement as well as their quadrature sum which is quoted as the total statistical error.

-t bin [GeV^2]	Σ_{peak}	δ_{peak}	Σ_{SB}	δ_{SB}	f	δ_f	Σ_η	δ_η
0.1 < -t < 0.2	0.908	0.0948	-0.188	0.0017	0.0968	0.0042	1.025	0.0948
0.2 < -t < 0.3	0.884	0.0807	-0.243	0.0014	0.0632	0.0027	0.960	0.0808
0.3 < -t < 0.45	0.921	0.0708	-0.202	0.0010	0.0392	0.0018	0.967	0.0708
0.45 < -t < 0.7	0.847	0.0724	-0.357	0.0008	0.0235	0.0013	0.876	0.0724
0.7 < -t < 1.5	0.1.04	0.0797	-0.390	0.00153	0.0247	0.0016	1.073	0.0811
0.1 < -t < 1.5	0.900	0.0358	-0.2103	0.0005	0.0418	0.0004	0.948	0.0358

Table 4.8: 0/90 All intensity runs. Statistical uncertainties on Σ for individual $-t$ bins in the $\eta \to \pi^+\pi^-\pi^0$ asymmetry.

-t bin [GeV^2]	Σ_{peak}	δ_{peak}	Σ_{SB}	δ_{SB}	f	δ_f	Σ_η	δ_η
0.1 < -t < 0.2	0.880	0.0963	-0.205	0.0018	0.0968	0.0042	0.996	0.0964
0.2 < -t < 0.3	0.840	0.0860	-0.229	0.0014	0.0632	0.0027	0.912	0.0861
0.3 < -t < 0.45	0.901	0.0751	-0.319	0.0011	0.0392	0.0018	0.951	0.0752
0.45 < -t < 0.7	0.924	0.0753	-0.355	0.0009	0.0235	0.0013	0.955	0.0753
0.7 < -t < 1.5	0.838	0.0820	-0.355	0.00159	0.0247	0.0016	0.868	0.0821
0.1 < -t < 1.5	0.848	0.0374	-0.2458	0.0005	0.0418	0.0004	0.896	0.0374

Table 4.9: 45/135 All intensity runs. Statistical uncertainties on Σ for individual $-t$ bins in the $\eta \to \pi^+\pi^-\pi^0$ asymmetry.

-t bin [GeV^2]	$\Sigma_\eta^{0/90}$	$\delta_\eta^{0/90}$	$\Sigma_\eta^{45/135}$	$\delta_\eta^{45/135}$
0.1 < -t < 0.2	0.947	0.074	0.893	0.080
0.2 < -t < 0.3	0.968	0.071	0.935	0.075
0.3 < -t < 0.45	1.030	0.068	0.930	0.071
0.45 < -t < 0.7	0.883	0.073	0.986	0.078
0.7 < -t < 1.5	0.960	0.0838	0.773	0.092
0.1 < -t < 1.5	0.952	0.034	0.907	0.036

Table 4.10: All intensity runs. Statistical uncertainties on Σ for individual $-t$ bins in the $\eta \to 3\pi^0$ asymmetry. The statistical error on the polarization is not included yet.

-t bin [GeV^2]	$\Sigma_{\pi^0}^{0/90}$	$\delta_{\pi^0}^{0/90}$	$\Sigma_{\pi^0}^{45/135}$	$\delta_{\pi^0}^{45/135}$
0.1 < -t < 0.2	0.948	0.0173	0.926	0.017
0.2 < -t < 0.3	0.937	0.0131	0.927	0.013
0.3 < -t < 0.45	0.916	0.0183	0.917	0.019
0.45 < -t < 0.7	0.920	0.0191	0.916	0.020
0.7 < -t < 1.5	0.981	0.0098	0.956	0.010
0.1 < -t < 1.5	0.930	0.0063	0.923	0.0066

Table 4.11: All intensity runs. Statistical uncertainties on Σ for individual $-t$ bins in the π^0 asymmetry. The statistical error on the polarization is not included yet. This table shows the total statistical error for the Σ measurement.

Chapter 5

Systematic studies

The value of Σ and the statistical error associated with the measurement can be extracted from fitting the data directly. In order to estimate the systematic uncertainty associated with the measurement several studies are performed. The nature of these studies is to adjust one component of the analysis chain and compare the result with the result obtained from the nominal analysis chain to estimate an uncertainty associated with the varied component.

For each systematic study a Barlow test is also performed to determine if the systematic variation is significant enough to be included in the total error [93]. Since the systematic tests are done on nearly the same data set the statistical errors are dominated by the sampling fraction. Therefore, to determine if the systematic effect is small it cannot be compared to the statistical error of the measurement. The Barlow test provides a method to determine if the systematic effect is significant and should be included in the total error by considering the variance, $\sigma^2 = |\sigma^2_{nom} - \sigma^2_{varied}|$. In order to calculate the number of σ_{Barlow} of separation for each systematic study the following expression is used

$$\sigma_{Barlow} = \frac{|\Sigma_{nom} - \Sigma_{varied}|}{\sqrt{|\sigma^2_{nom} - \sigma^2_{varied}|}}. \tag{5.1}$$

If the size of the discrepancy due to the systematic effect is less than 1σ of separation then it will not included it in the total error. If the size of the discrepancy is greater than 2σ then it will be included in the total error, a discrepancy between 1σ and 2σ should be considered carefully. A systematic effect will only be ignored if the Barlow test suggests that it should be ignored for all decay channels. The Barlow test for each channel can be found in their respective GlueX analysis notes [90, 91, 92] but they won't all be shown here unless necessary. The results of the Barlow test in the $\eta \to 2\gamma$ mode for $\sigma > 2$ are shown in Table. 5.7 and 5.8.

5.1 Event selection

The parameters of the event selection described in Ch. 4.2 were varied to study the systematic dependence of the asymmetry on the selection criteria. Tables 5.1-5.2 contain the list of nominal, upper and lower values of the cuts that were varied. One value was varied at a time, to either only the lower limit cut value or only to the upper limit cut value. For each upper and lower value of the cut parameter the asymmetry was extracted in bins of $-t$ for the π^0 and η event samples. None of the cut variations pruned more than 10% of the signal to avoid any significant statistical effects causing a shift in the asymmetry value.

Figs. 5.1 - 5.6 show the values of the asymmetry as a function of $-t$ for π^0 and η events, where each parameter is represented by an individual color, and the asymmetry for the default cut parameters is

Cut Variable	Lower Bound Values	Nominal Value	Upper Bound Values
Proton momentum (GeV/c)	$p_p > 0.2$, $p_p > 0.3$	$p_p > 0.25$	none
Vertex z position (cm)	$z > 50$, $z > 54$	$52 < z < 78$	$z < 76$, $z < 80$
Vertex radial position (cm)	none	$r < 1.0$	$r < 0.5$, $r < 1.5$
Fiducial r_γ position in FCAL (cm)	$r_\gamma > 20$, $r_\gamma > 30$	$25 < r_\gamma < 100$	$r_\gamma < 95$, $r_\gamma < 105$
Fiducial z_γ position in BCAL (cm)	$z_\gamma > 90$, $z_\gamma > 110$	$100 < z_\gamma < 380$	$z_\gamma < 370$, $z_\gamma < 390$

Table 5.1: Variation of pre-selection cut parameters to study systematic impact on asymmetry.

Cut Variable	Lower Bound Value	Nominal Value	Upper Bound Value
Missing Mass Squared (GeV^2)	$\|MM^2\| < 0.02$	$\|MM^2\| < 0.05$	$\|MM^2\| < 0.1$
Two photon invariant mass	$\|M_{\gamma\gamma} - M_{\pi^0}\| < 0.014$	$\|M_{\gamma\gamma} - M_{\pi^0}\| < 0.021$	$\|M_{\gamma\gamma} - M_{\pi^0}\| < 0.028$
Two photon invariant mass	$\|M_{\gamma\gamma} - M_\eta\| < 0.021$	$\|M_{\gamma\gamma} - M_\eta\| < 0.031$	$\|M_{\gamma\gamma} - M_\eta\| < 0.041$
Kinematic fit confidence level	$CL > 10^{-5}$, $CL > 10^{-3}$	$CL > 10^{-4}$	none

Table 5.2: Variation of event selection cut parameters to study systematic impact on asymmetry.

shown by the open black circles. Almost all of the filled data points are within the 1σ statistical error of the data points, with most of the variations being tightly clustered around the asymmetry with the nominal cuts. Half of the range of the asymmetry values obtained from varying the cut parameters are used as an estimate of the systematic uncertainty, Tables 5.1-5.2. This systematic uncertainty is evaluated in each $-t$ bin individually and the uncertainty values are given in Tables 5.3 - 5.5. The Barlow test was performed and suggests that the cut variation systematic effect should be included in the total uncertainty.

5.2 Cut Variation Results

The following plots are the summary of the effects of varying the cuts on the π^0 and η samples described in Tables 5.1 and 5.2.

The systematic uncertainty is estimated as the range of the asymmetry values obtained from varying the cut parameters, the results for each sample are listed in tables 5.1-5.2. The systematic uncertainty is also compared to the statistical error in each t-bin by taking the ratio of the systematic uncertainty to the statistical error. The systematic errors due to the cut variation are not negligible compared to the statistical error but also don't dominate the result.

$-t$ bin (GeV/c^2)	Sys. Uncert. 0/90	Sys./Stat. Err 0/90	Sys. uncert. 45/135	Sys./Stat. Err 45/135
$0.1 < -t < 0.2$	0.0044	0.14	0.0102	0.32
$0.2 < -t < 0.3$	0.0034	0.11	0.0048	0.16
$0.3 < -t < 0.45$	0.0104	0.33	0.0088	0.28
$0.45 < -t < 0.7$	0.0063	0.19	0.0086	0.29
$0.7 < -t < 1.5$	0.0029	0.09	0.0031	0.31

Table 5.3: Cut-dependence systematic uncertainty on Σ for individual $-t$ bins for the π^0 asymmetry.

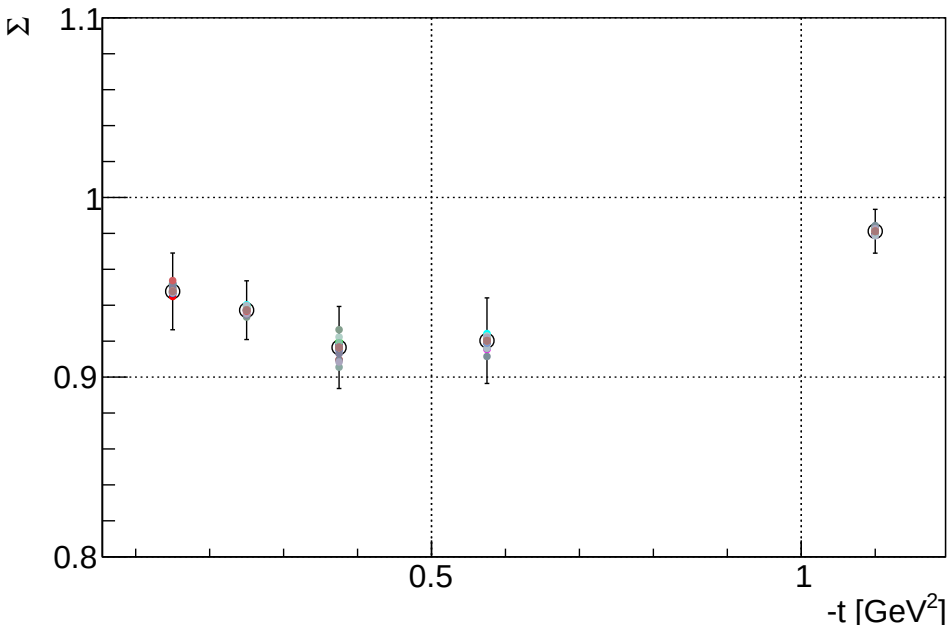

Figure 5.1: Σ asymmetry measured for each of the cut parameter variations, shown as different colored points in each $-t$ bin the $\pi^0 \to 2\gamma$ sample with the diamond radiator in the 0/90 orientation. The open circles and error bars are the asymmetry values and statistical errors using the default cut parameters.

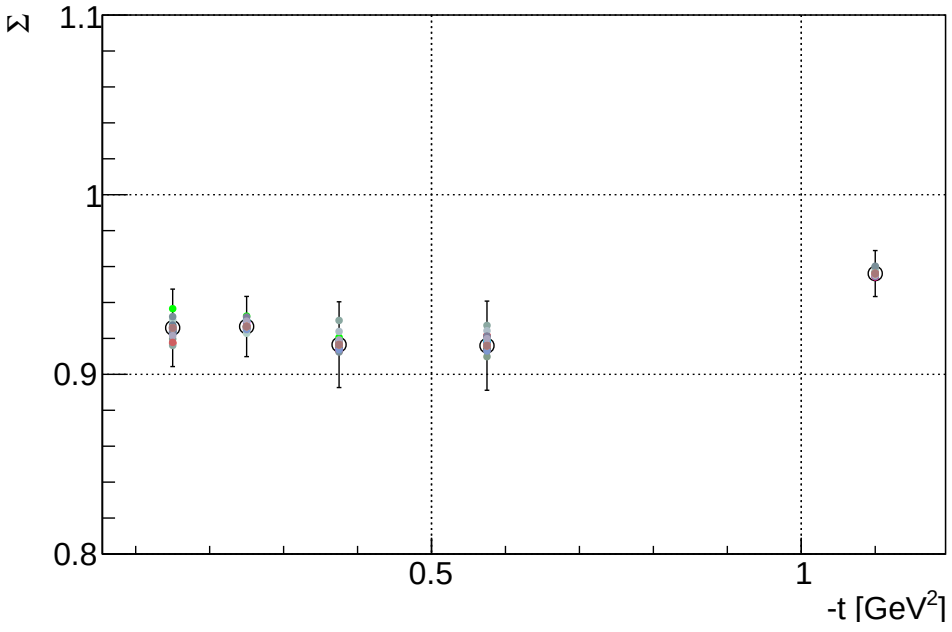

Figure 5.2: Σ asymmetry measured for each of the cut parameter variations, shown as different colored points in each $-t$ bin the $\pi^0 \to 2\gamma$ sample with the diamond radiator in the 45/135 orientation. The open circles and error bars are the asymmetry values and statistical errors using the default cut parameters.

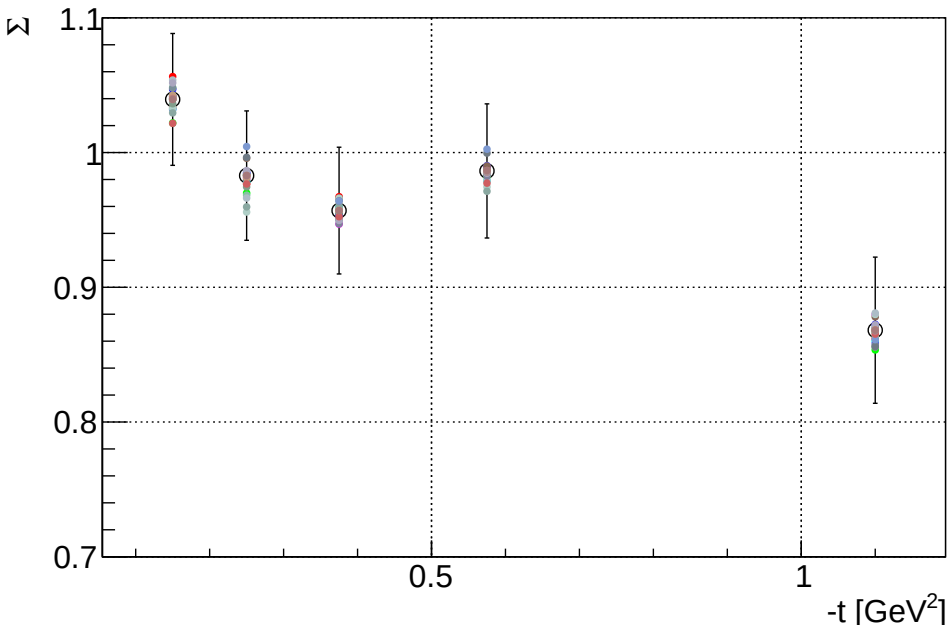

Figure 5.3: Σ asymmetry measured for each of the cut parameter variations, shown as different colored points in each $-t$ bin the $\eta \to 2\gamma$ sample with the diamond radiator in the 0/90 orientation. The open circles and error bars are the asymmetry values and statistical errors using the default cut parameters.

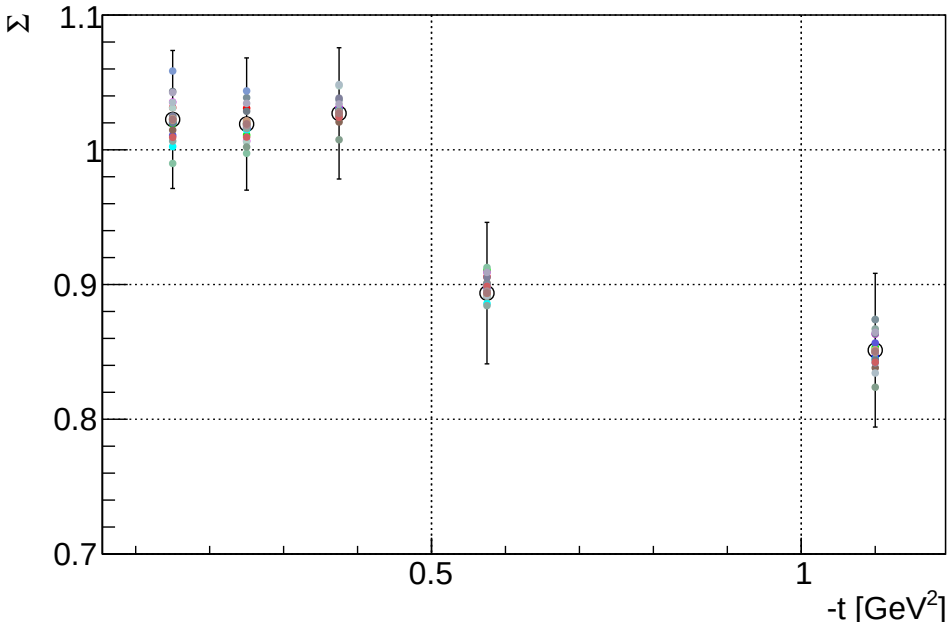

Figure 5.4: Σ asymmetry measured for each of the cut parameter variations, shown as different colored points in each $-t$ bin the $\eta \to 2\gamma$ sample with the diamond radiator in the 45/135 orientation. The open circles and error bars are the asymmetry values and statistical errors using the default cut parameters.

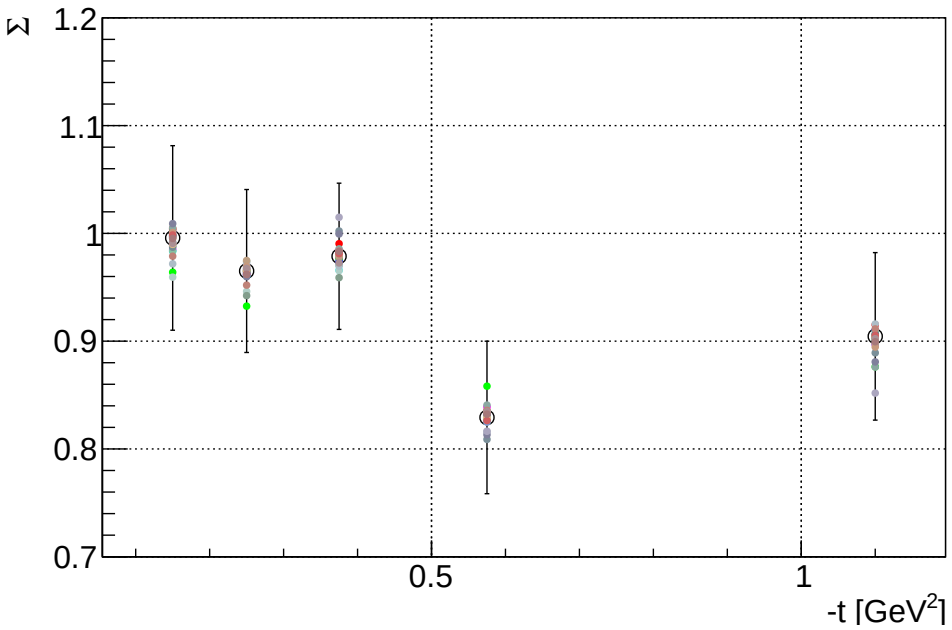

Figure 5.5: Σ asymmetry measured for each of the cut parameter variations, shown as different colored points in each $-t$ bin the $\eta \to \pi^+\pi^-\pi^0$ sample with the diamond radiator in the 0/90 orientation. The open circles and error bars are the asymmetry values and statistical errors using the default cut parameters.

$-t$ bin (GeV/c^2)	Sys. Uncert. 0/90	Sys./Stat. Err 0/90	Sys. Uncert. 45/135	Sys./Stat. Err 45/135
$0.1 < -t < 0.2$	0.0175	0.35	0.0346	0.66
$0.2 < -t < 0.3$	0.0243	0.49	0.0232	0.45
$0.3 < -t < 0.45$	0.0103	0.21	0.0207	0.42
$0.45 < -t < 0.7$	0.0156	0.31	0.0144	0.29
$0.7 < -t < 1.5$	0.0137	0.26	0.0245	0.45

Table 5.4: Cut-dependence systematic uncertainty on Σ for individual $-t$ bins for the $\eta \to 2\gamma$ asymmetry.

$-t$ bin (GeV/c^2)	Sys. Uncert. 0/90	Sys./Stat. Err 0/90	Sys. Uncert. 45/135	Sys./Stat. Err 45/135
$0.1 < -t < 0.2$	0.0261	0.35	0.0306	0.66
$0.2 < -t < 0.3$	0.0212	0.49	0.0312	0.45
$0.3 < -t < 0.45$	0.0289	0.21	0.0289	0.42
$0.45 < -t < 0.7$	0.0256	0.31	0.0310	0.29
$0.7 < -t < 1.5$	0.0327	0.26	0.0305	0.45

Table 5.5: Cut-dependence systematic uncertainty on Σ for individual $-t$ bins for the $\eta \to \pi^+\pi^-\pi^0$ asymmetry.

The results of the Barlow test are shown in Fig. 5.9 and 5.10 for the $\eta \to 2\gamma$ decay mode. Based on these results it is clear that the cut variation effect should be included in the total uncertainty.

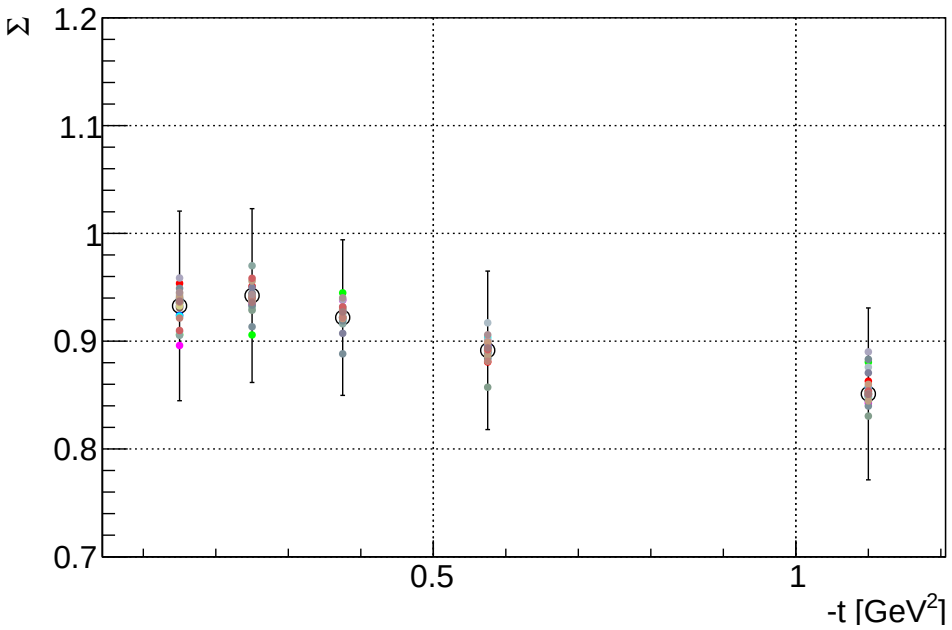

Figure 5.6: Σ asymmetry measured for each of the cut parameter variations, shown as different colored points in each $-t$ bin the $\eta \to \pi^+\pi^-\pi^0$ sample with the diamond radiator in the 45/135 orientation. The open circles and error bars are the asymmetry values and statistical errors using the default cut parameters.

$-t$ bin (GeV/c^2)	Sys. Uncert. 0/90	Sys./Stat. Err 0/90	Sys. Uncert. 45/135	Sys./Stat. Err 45/135
$0.1 < -t < 0.2$	0.0221	0.29	0.0200	0.24
$0.2 < -t < 0.3$	0.0179	0.25	0.0137	0.18
$0.3 < -t < 0.45$	0.0171	0.24	0.0230	0.32
$0.45 < -t < 0.7$	0.0201	0.27	0.0186	0.23
$0.7 < -t < 1.5$	0.0338	0.39	0.0260	0.28

Table 5.6: Cut-dependence systematic uncertainty on Σ for individual $-t$ bins for the $\eta \to 3\pi^0$ asymmetry.

Tables. 5.7 and 5.8 show which cut variation is responsible for a $\sigma_{Barlow} > 2$ to help identify which components of the analysis should be focused on in the future.

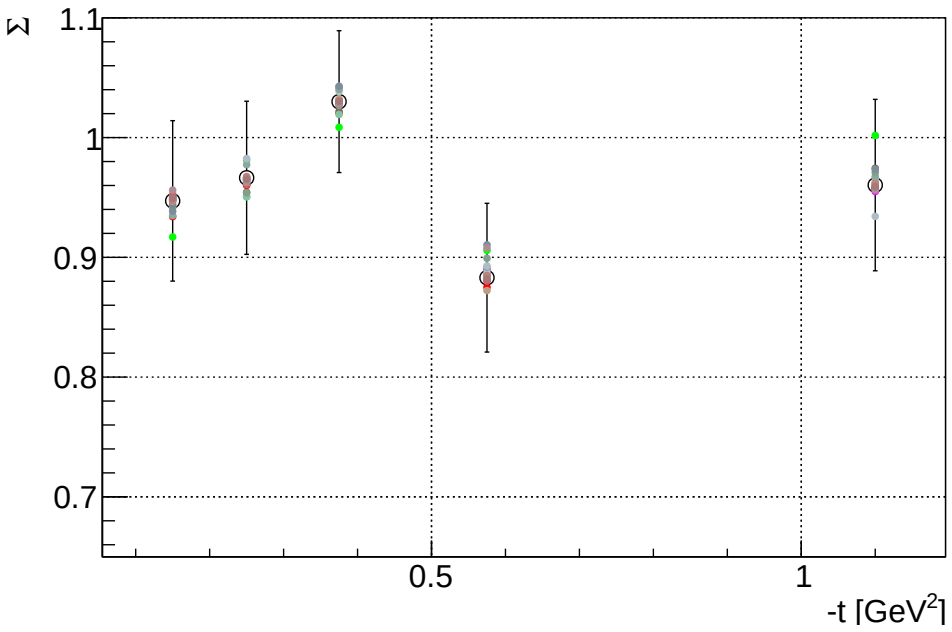

Figure 5.7: Σ asymmetry measured for each of the cut parameter variations, shown as different colored points in each $-t$ bin the $\eta \to 3\pi^0$ sample with the diamond radiator in the 0/90 orientation. The open circles and error bars are the asymmetry values and statistical errors using the default cut parameters.

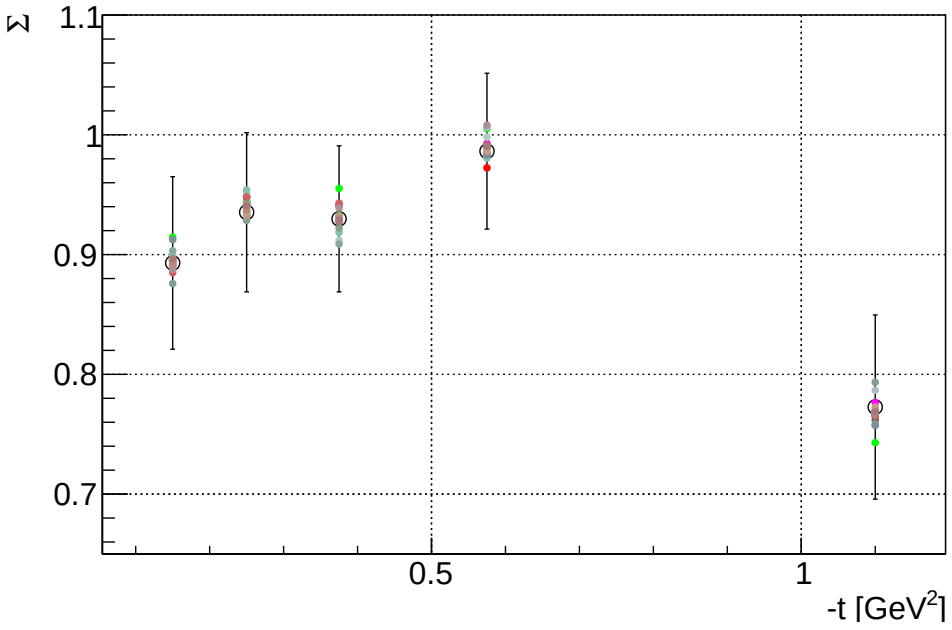

Figure 5.8: Σ asymmetry measured for each of the cut parameter variations, shown as different colored points in each $-t$ bin the $\eta \to 3\pi^0$ sample with the diamond radiator in the 45/135 orientation. The open circles and error bars are the asymmetry values and statistical errors using the default cut parameters.

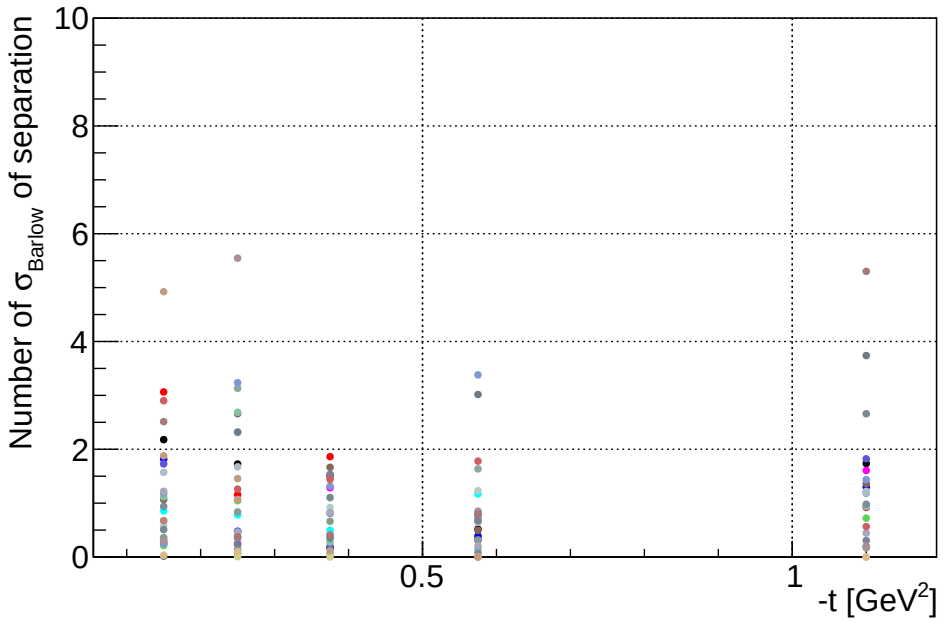

Figure 5.9: Results of the Barlow-test for each of the cut parameter variations, shown as different colored points in each $-t$ bin for the $\eta \to 2\gamma$ sample with the diamond radiator in the 0/90 orientation.

Barlow σ	$-t$ bin (GeV/c^2)	Cut variation
4.923	$0.1 < -t < 0.2$	Fiducial BCAL $z_\gamma < 370$ cm
3.063	$0.1 < -t < 0.2$	kf CL $> 10^{-5}$
2.900	$0.1 < -t < 0.2$	Fiducial Fcal $r_\gamma < 30$cm
2.513	$0.1 < -t < 0.2$	Fiducial Fcal $r_\gamma < 110$ cm
2.179	$0.1 < -t < 0.2$	kf CL $> 10^{-3}$
5.546	$0.2 < -t < 0.3$	Fiducial Fcal $r_\gamma < 0.95$ cm
3.236	$0.2 < -t < 0.3$	Unused E on BCAL > 0.5 GeV
3.131	$0.2 < -t < 0.3$	vertex z > 50 cm
2.690	$0.2 < -t < 0.3$	$M_{\gamma\gamma} - M_\eta < 0.041$ GeV
2.660	$0.2 < -t < 0.3$	$M_{\gamma\gamma} - M_\eta < 0.021$ GeV
2.319	$0.2 < -t < 0.3$	Unused E in BCAL > 0.25 GeV
2.309	$0.2 < -t < 0.3$	$M_{\gamma\gamma} - M_\eta < 0.021$ GeV
3.348	$0.45 < -t < 0.7$	Unused E in BCAL > 0.5 GeV
3.016	$0.45 < -t < 0.7$	Unused E in BCAL > 0.25 GeV
5.301	$0.7 < -t < 1.5$	Fiducial Fcal $r_\gamma < 1.05$ cm
3.739	$0.7 < -t < 1.5$	Unused E in BCAL > 0.25 GeV
2.659	$0.7 < -t < 1.5$	vertex r < 76 cm

Table 5.7: List of cut variations that resulted in a Barlow $\sigma > 2$ for the $\eta \to 2\gamma$ with the diamond radiator in its 0/90 orientation.

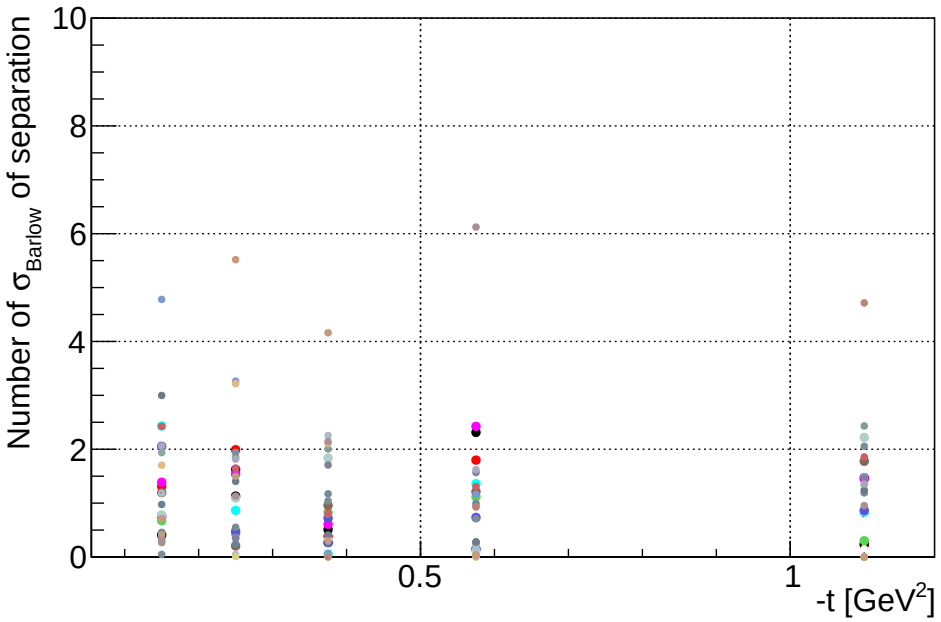

Figure 5.10: Results of the Barlow-test for each of the cut parameter variations, shown as different colored points in each $-t$ bin the $\eta \to 2\gamma$ sample with the diamond in the 45/135 orientation.

Barlow σ	$-t$ bin (GeV/c^2)	Cut variation
4.781	$0.1 < -t < 0.2$	Unused E in BCAL > 0.5 GeV
4.092	$0.1 < -t < 0.2$	$M_{\gamma\gamma} - M_\eta < 0.041$ GeV
2.998	$0.1 < -t < 0.2$	Unused E in BCAL > 0.25 GeV
2.432	$0.1 < -t < 0.2$	MM$^2 < 0.02$ GeV^2
2.423	$0.1 < -t < 0.2$	Fiducial Fcal $r_\gamma > 30.0$ cm
2.060	$0.1 < -t < 0.2$	Unused E in FCAL > 0.5 GeV
2.055	$0.1 < -t < 0.2$	$M_{\gamma\gamma} - M_\eta > -0.041$ GeV
5.518	$0.2 < -t < 0.3$	Fiducial Bcal $z_\gamma < 390$ cm
3.263	$0.2 < -t < 0.3$	Unused E in BCAL > 0.5 GeV
3.217	$0.2 < -t < 0.3$	Fiducial Bcal $z_\gamma > 160$ cm
2.873	$0.2 < -t < 0.3$	$M_{\gamma\gamma} - M_\eta < 0.041$ GeV
4.161	$0.3 < -t < 0.45$	Fiducial Bcal $z_\gamma < 390$ cm
2.255	$0.3 < -t < 0.45$	vertex z < 76.0 cm
2.142	$0.3 < -t < 0.45$	Fiducial Fcal $r_\gamma < 0.95$ cm
2.109	$0.3 < -t < 0.45$	Fiducial Bcal $z_\gamma > 160$ cm
2.004	$0.3 < -t < 0.45$	vertex z < 76.0 cm
6.122	$0.45 < -t < 0.7$	Fiducial Fcal $r_\gamma < 0.95$ cm
2.869	$0.45 < -t < 0.7$	$M_{\gamma\gamma} - M_\eta < 0.041$ GeV
2.424	$0.45 < -t < 0.7$	MMsqLB p1 MM$^2 >$ -0.02 GeV^2
2.312	$0.45 < -t < 0.7$	kf CL $> 10^{-3}$
4.716	$0.7 < -t < 1.5$	Fiducial Fcal $r_\gamma > 0.2$ cm
2.431	$0.7 < -t < 1.5$	vertex z > 54 cm
2.220	$0.7 < -t < 1.5$	$M_{\gamma\gamma} - M_\eta < 0.021$ GeV
2.055	$0.7 < -t < 1.5$	vertex z < 80.0 cm

Table 5.8: List of cut variations that resulted in a Barlow $\sigma > 2$ the $\eta \to 2\gamma$ with the diamond in its 45/135 orientation.

Pol. dir.	Intens.	$A^{\pi^0}_{instr}$	$\sigma^{\pi^0}_A$	$A^{\eta\to 2\gamma}_{instr}$	$\sigma^{\eta\to 2\gamma}_A$	$A^{\eta\to\pi^+\pi^-\pi^0}_{instr}$	$\sigma^{\eta\to\pi^+\pi^-\pi^0}_A$	$A^{\eta\to 3\pi^0}_{instr}$	$\sigma^{\eta\to 3\pi^0}_A$
0/90	LI	0.0107	0.0031	0.016	0.0088	0.0397	0.0172	0.0129	0.0167
45/135	LI	0.0012	0.0031	0.024	0.0088	-0.0200	0.0162	0.0242	0.0170
0/90	HI	0.0111	0.0034	0.018	0.0100	0.0520	0.0191	0.0528	0.0202
45/135	HI	0.0076	0.0036	0.003	0.0104	0.0186	0.020	0.0560	0.0215

Table 5.9: Instrumental asymmetry integrated over all $-t$ bins for the π^0 and η mesons.

5.3 Instrumental asymmetry

Any instrumental asymmetries not canceled by the PERP - PARA subtraction described in Sec. 4.5 would result in a modulation of the sum $Y_\perp(\phi)+F_RY_\parallel(\phi)$, which is in the denominator of the normalized yield asymmetry. If there is a mismatch in the magnitude of the polarization between the PERP and PARA orientation then the physics signal is expected to add to the instrumental asymmetry as shown in Eqn. 5.2

$$Y_\perp(\phi) + F_RY_\parallel(\phi) = 2N_\perp \cdot [1 + ((P_\perp - P_\parallel) \cdot \Sigma_\eta + \Sigma_{inst}) \cdot \cos(2\phi))] \tag{5.2}$$

where Σ_{inst} is an instrumental asymmetry. Assuming that the flux ratio between PERP and PARA is correct then the polarization cross-weighted sum can be plotted to isolate the instrumental asymmetry

$$P_\parallel Y_\perp(\phi) + P_\perp F_R Y_\parallel(\phi) = 2N_\perp P_{avg} \cdot [1 + \Sigma_{inst} \cdot \cos(2\phi)]. \tag{5.3}$$

Fits are performed to Eqn. 5.3 using the following functional form

$$f_{inst}(\phi) = C \cdot (1 + A_{inst} \cos 2(\phi - \phi_0)). \tag{5.4}$$

There are two free parameters, $p_0 = C$ for normalization and $p_1 = A_{inst}$, while the phase constant of the fit ϕ_0 is a free parameter in this fit. The measured instrumental asymmetries are shown in Fig. 5.11 as a function of $-t$ and are consistent with zero for both the π^0 and η samples, thus an additional systematic uncertainty is not assigned to the measured asymmetries.

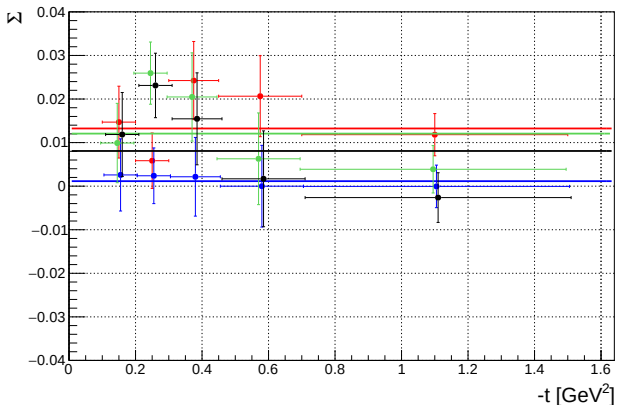

(a) $\pi^0 \to \gamma\gamma$

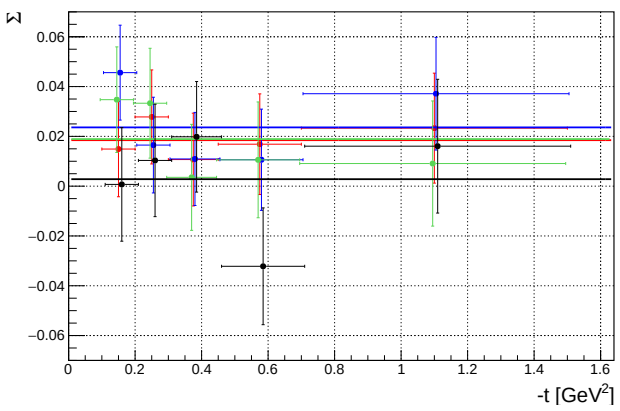

(b) $\eta \to \gamma\gamma$

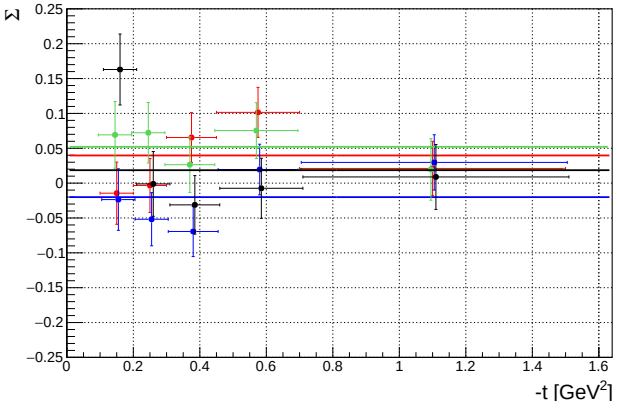

(c) $\eta \to \pi^+\pi^-\pi^0$

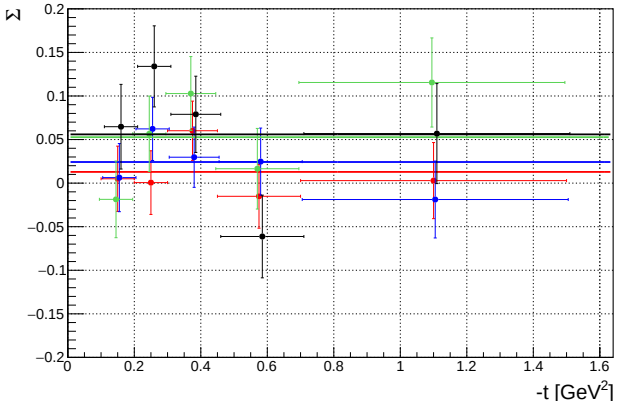

(d) $\eta \to 3\pi^0$

Figure 5.11: Instrumental asymmetry for as a function of $-t$. For both plots the red points correspond to polarization direction set to 0/90 and low intensity beam runs, blue points correspond to polarization direction set to 45/135 and low intensity runs, green points correspond to polarization direction set to 0/90 and high intensity runs and the black points correspond to polarization direction set to 45/135 and high intensity running. The horizontal lines are fits to the data.

5.4 Background Asymmetry Correction

Since the fitted asymmetry is corrected due to the Σ beam asymmetry from the background sideband region for the $\eta \to 2\gamma$ and $\eta \to \pi^+\pi^-\pi^0$ decays, a systematic due to this correction is assigned. The systematic is given by

$$\delta_{bkgd} = \sqrt{\left(\frac{\delta_{SB} \cdot f}{1-f}\right)^2} \tag{5.5}$$

where δ_{SB} is given in Table 4.6 and Table 4.7. The resulting systematics due the background asymmetry are given in Table 5.10.

$-t$ bin (GeV/c^2)	$\eta \to 2\gamma(0/90)$	$\eta \to 2\gamma(45/135)$	$\eta \to \pi^+\pi^-\pi^0$ (0/90)	$\eta \to \pi^+\pi^-\pi^0$ (45/135)
$0.1 < -t < 0.2$	0.0043	0.0045	0.0017	0.0018
$0.2 < -t < 0.3$	0.0040	0.0042	0.0014	0.0014
$0.3 < -t < 0.45$	0.0033	0.0024	0.0010	0.0011
$0.45 < -t < 0.7$	0.0028	0.0030	0.0008	0.0009
$0.7 < -t < 1.5$	0.0026	0.0027	0.0015	0.0016
$0.1 < -t < 1.5$	0.0017	0.0018	0.0005	0.0005

Table 5.10: Background asymmetry systematic uncertainty on Σ for individual $-t$ bins for in the η asymmetry.

5.5 Phase dependence

As described in Sec. 4.5.1, the phase constant ϕ_0 is fixed [83] in the fits to the normalized yield asymmetry distributions to be the same in all the $-t$ bins. Physically, the linear polarization axis cannot change with $-t$, but as a test of the sensitivity to this phase constant fixing, the asymmetries are fit a second time while allowing the phase constant to be a free parameter in the fit. The measured asymmetries are shown in Figs. 5.12- 5.13 and show very little deviation from the nominal results with the fixed phase. The uncertainty due to the variation of allowing the phase offset to be a free parameter in the fit is reported in Tab. 5.11. The uncertainty comes from the rms of the distribution of the difference between the nominal and varied results. The result of the Barlow test is shown in Fig. 5.14 and indicates that this systematic effect should be included in the total uncertainty.

Decay Mode	phase systematic
$\pi^0 \to 2\gamma$	0.0005
$\eta \to 2\gamma$	0.001
$\eta \to \pi^+\pi^-\pi^0$	0.003
$\eta \to 3\pi^0$	0.003

Table 5.11: Phase offset systematic uncertainty on Σ for each decay mode.

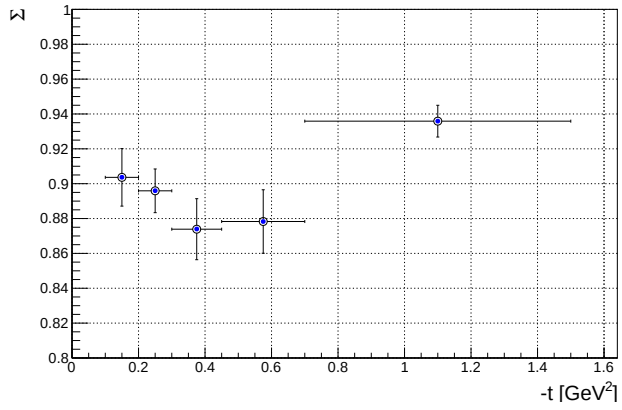

(a) $\pi^0 \to \gamma\gamma$

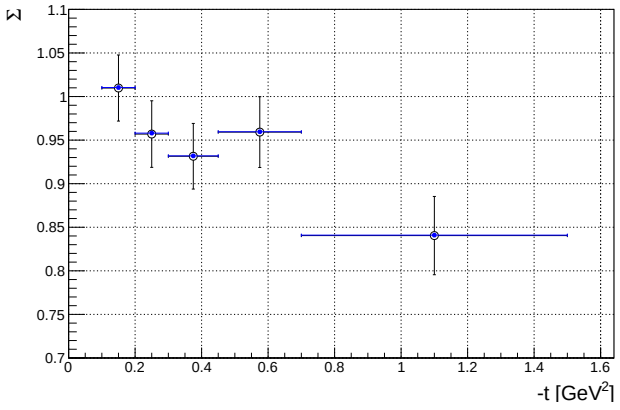

(b) $\eta \to \gamma\gamma$

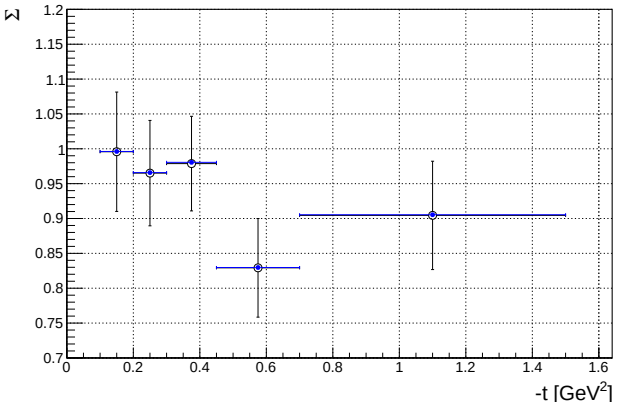

(c) $\eta \to \pi^+\pi^-\pi^0$

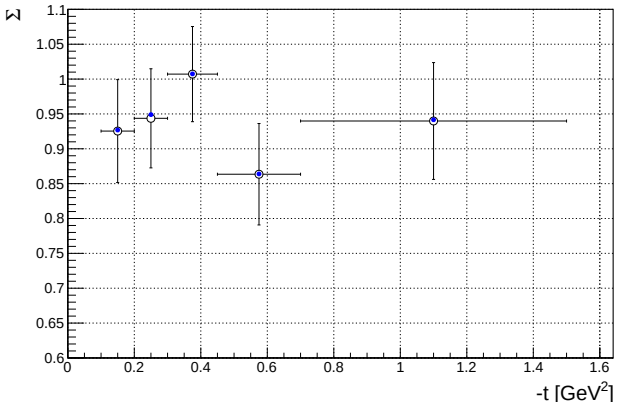

(d) $\eta \to 3\pi^0$

Figure 5.12: Σ asymmetry measured while allowing the phase to be a free parameter in the fit (blue closed point) for the π^0 and η samples in the 0/90 orientation. The open blue circles and error bars are the asymmetry values and statistical errors using the fixed phase.

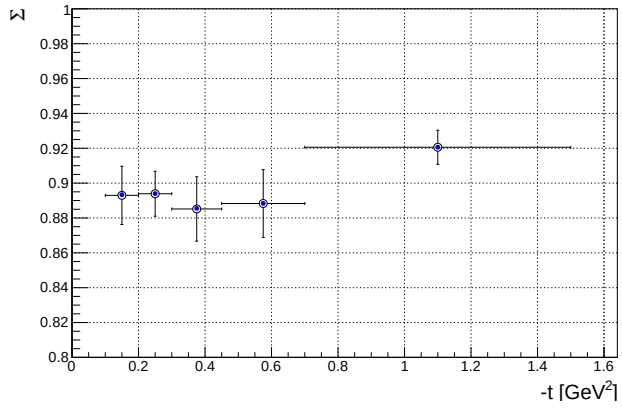

(a) $\pi^0 \to \gamma\gamma$

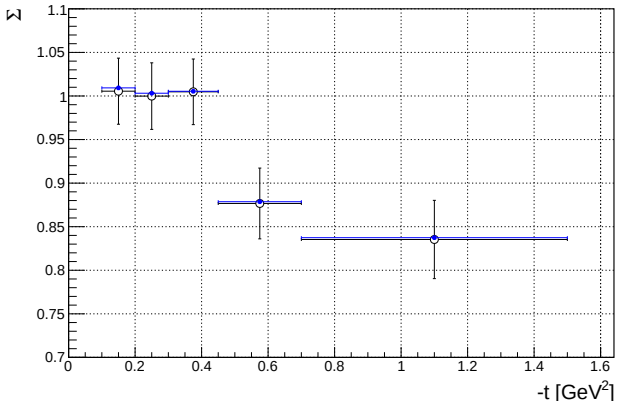

(b) $\eta \to \gamma\gamma$

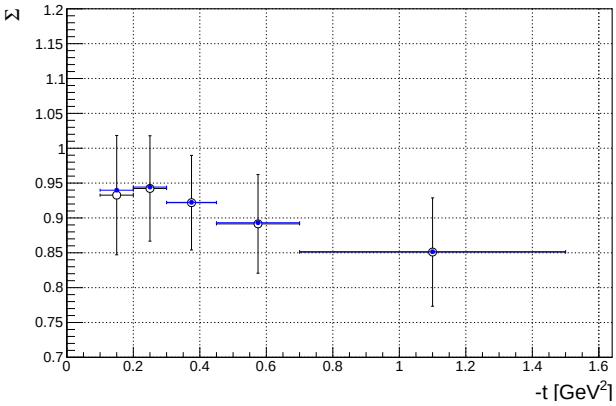

(c) $\eta \to \pi^+\pi^-\pi^0$

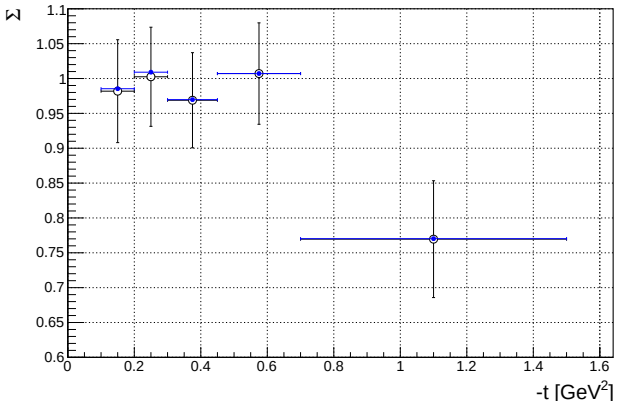

(d) $\eta \to 3\pi^0$

Figure 5.13: Σ asymmetry measured while allowing the phase to be a free parameter in the fit (blue closed point) for the π^0 and η samples in the 45/135 orientation. The open blue circles and error bars are the asymmetry values and statistical errors using the fixed phase.

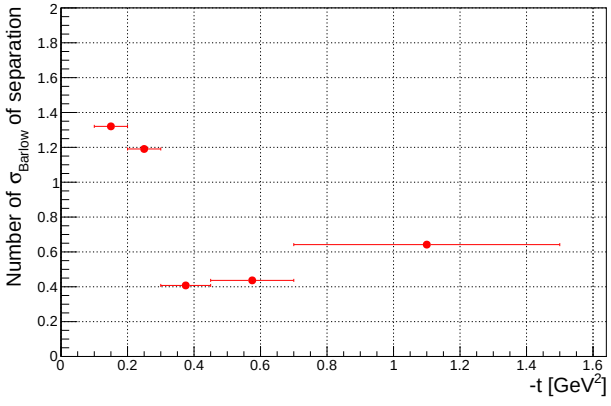

(a) (0/90) dataset

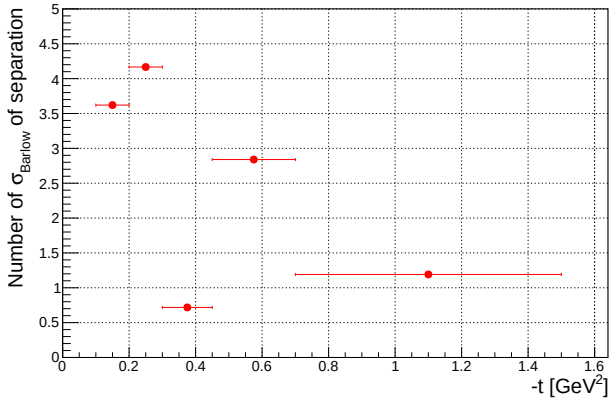

(b) (45/135) dataset

Figure 5.14: Results of the Barlow-test between the Σ asymmetry measured using the nominal fixed phase offset and the Σ asymmetry while allowing the phase to be a free parameter in the fit for the $\eta \to 2\gamma$ sample.

5.6 Flux normalization dependence

The flux normalization determined by the PS yields provides a scaling between the PARA and PERP datasets, necessary to fit the normalized yield distributions. To assess the sensitivity of the measured Σ values to this normalization, the fits were repeated using the nominal flux ratio $\pm 5\%$. This is a conservative estimate on the systematic deviation of the PS yields, as the statistical uncertainty on this quantity is very small. The measured asymmetries with the varied flux normalization are shown in Figs. 5.15 and 5.16 and show very little deviation from the nominal flux ratio value. The deviations from the nominal asymmetry value were computed for all $-t$ bins. Tab. 5.12 displays the assigned systematic uncertainty estimate due to the flux normalization. The uncertainty comes from the rms of the distribution of the difference between the nominal and varied results. The results of the Barlow test suggest that the flux normalization dependence should be included in the total uncertainty.

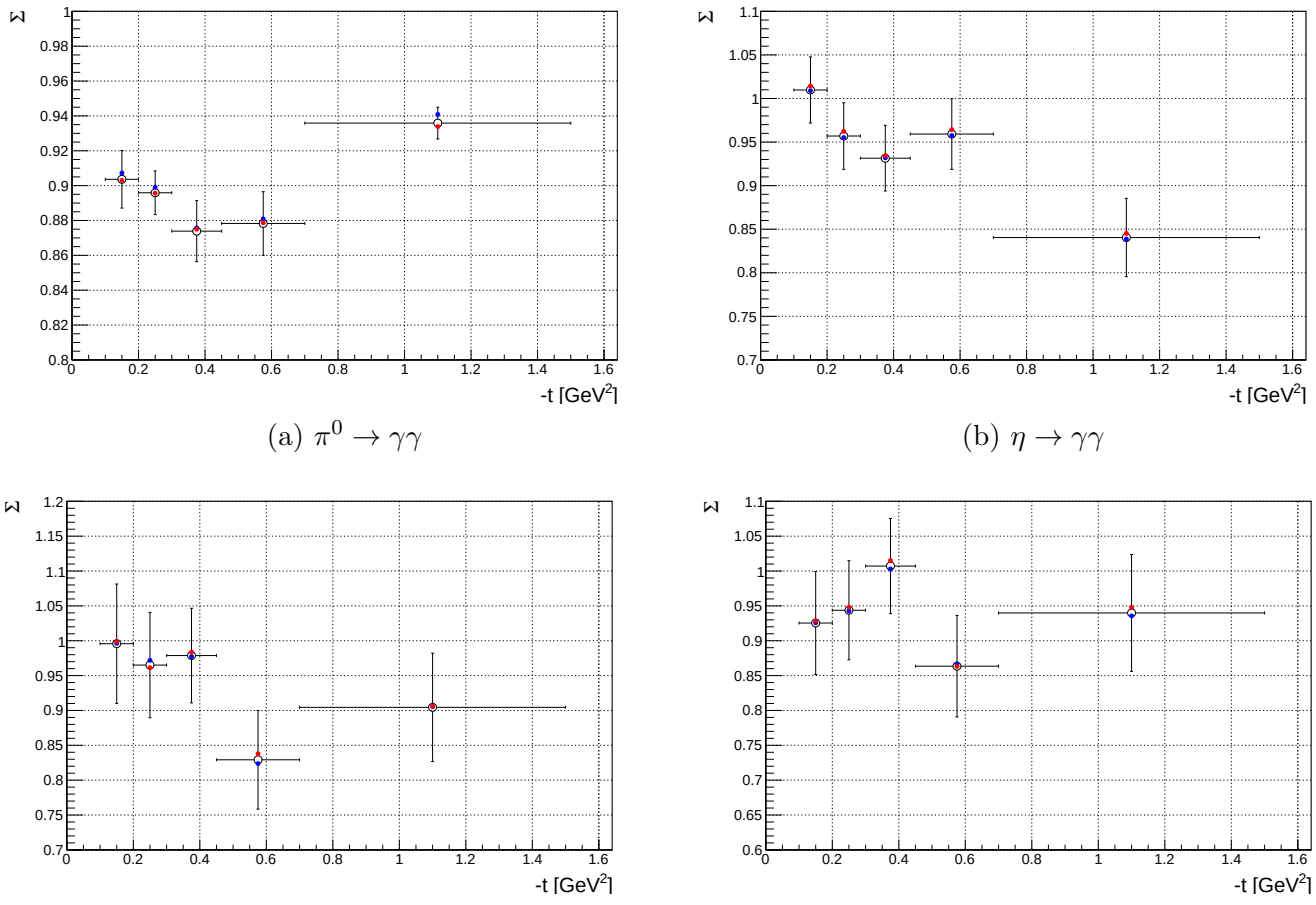

(a) $\pi^0 \to \gamma\gamma$

(b) $\eta \to \gamma\gamma$

(c) $\eta \to \pi^+\pi^-\pi^0$

(d) $\eta \to 3\pi^0$

Figure 5.15: Σ asymmetry measured using a flux normalization altered by $\pm 5\%$ (red and blue closed points) using our π^0 and η samples in the 0/90 orientation. The open circles and error bars are the asymmetry values and statistical errors using the nominal flux normalization.

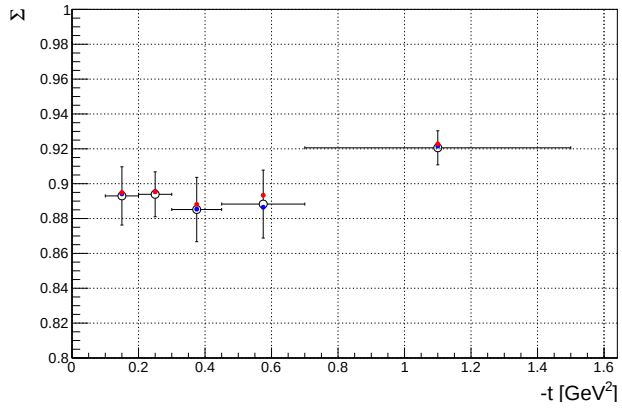

(a) $\pi^0 \to \gamma\gamma$

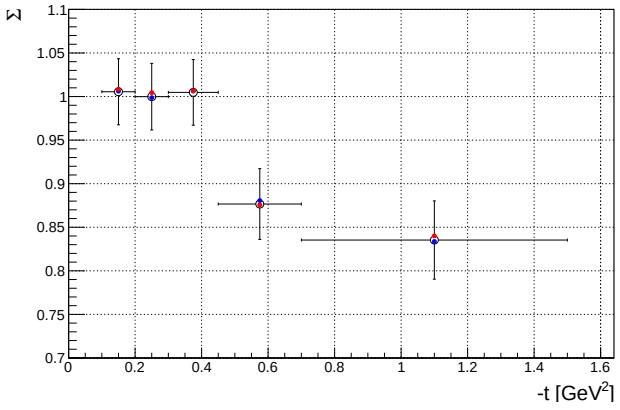

(b) $\eta \to \gamma\gamma$

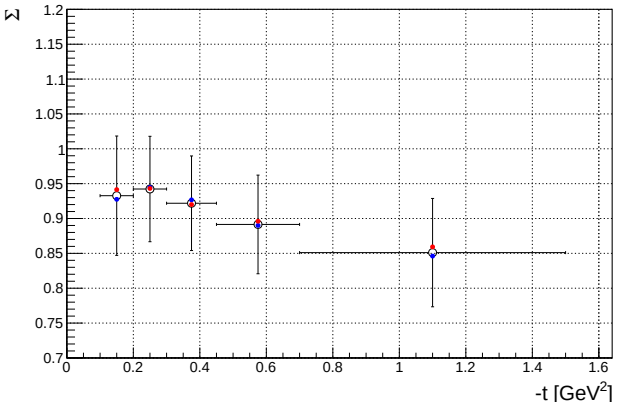

(c) $\eta \to \pi^+\pi^-\pi^0$

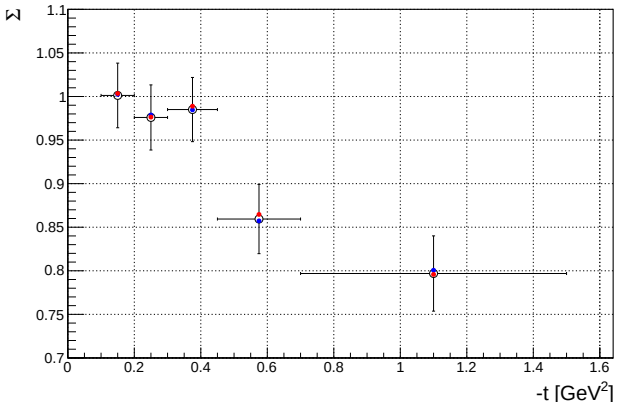

(d) $\eta \to 3\pi^0$

Figure 5.16: Σ asymmetry measured using a flux normalization altered by $\pm 5\%$ (red and blue closed points) using our π^0 and η samples in the 45/135 orientation. The open circles and error bars are the asymmetry values and statistical errors using the nominal flux normalization.

Decay Mode	Flux Ratio Systematic
$\pi^0 \to 2\gamma$	0.002
$\eta \to 2\gamma$	0.002
$\eta \to \pi^+\pi^-\pi^0$	0.005
$\eta \to 3\pi^0$	0.005

Table 5.12: Flux ratio systematic uncertainty on Σ for each decay mode.

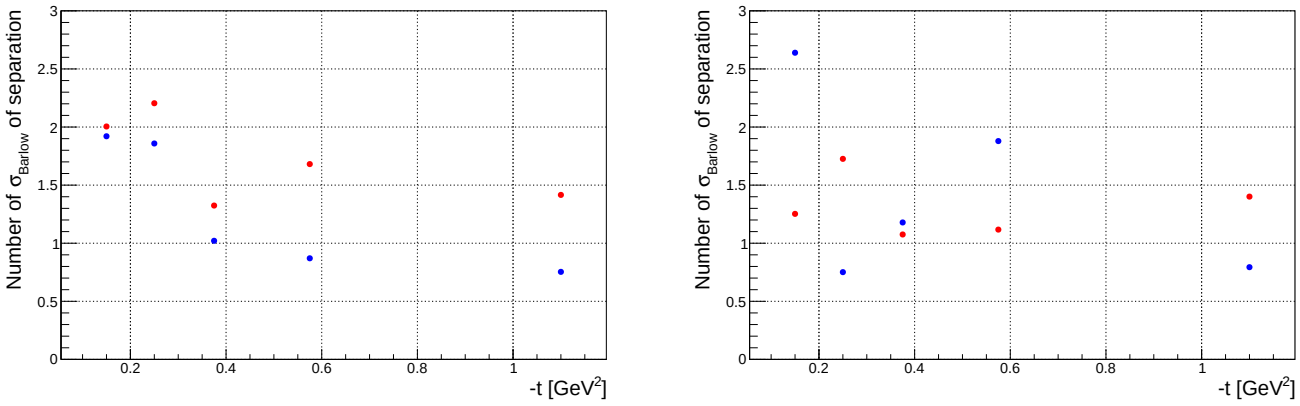

(a) (0/90) dataset

(b) (45/135) dataset

Figure 5.17: Result of the Barlow-test between the Σ asymmetry measured using the nominal flux ratio and the Σ asymmetry while allowing the flux ratio to vary by 5% (red and blue closed points) for the $\eta \to 2\gamma$ sample.

Based on the Barlow test the flux normalization systematic uncertainty will be included in the total uncertainty.

5.7 Finite ϕ bin size

The amount of statistics in each sample determines how many ϕ-bins the yields can be plotted in. If there was a very large dataset then a large number of bins could be used and the fit would have more data points to fit to. It is expected that the result of the fit will be biased when fewer bins are used.

The systematic effect of binning the ϕ distributions with a finite bin width of $2\pi/30$ is determined numerically by simulating an ensemble of 500 samples with a $1 + P\Sigma\cos(2\phi)$ distribution, assuming $P\Sigma = 0.4$. Each sample was fit with a function $p_0(1 + 0.4 \cdot p_1\cos(2\phi - p_2))$, using bin widths of $\Delta = 2\pi/360, 2\pi/180, 2\pi/90$, $2\pi/30$ and $2\pi/20$. Example plots are shown in Fig. 5.18.

The mean and width of the $p1$ parameter distribution obtained from fitting the ensemble are shown in Fig. 5.19 for different number of ϕ bins. This numerical estimation indicates a 0.75% dilution of the extracted asymmetry from the fit due to the use of 30 ϕ bins in the histogram. This dilution is applied as a correction to the beam asymmetry and no systematic uncertainty is associated with this effect.

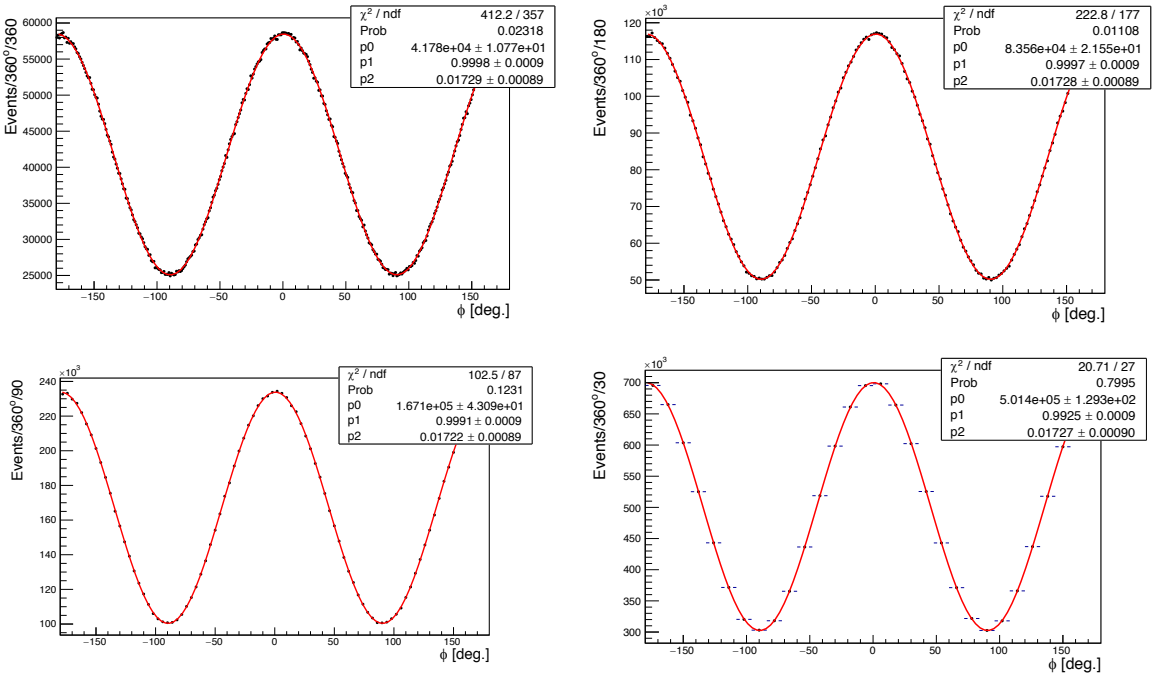

Figure 5.18: Example fits to simulated event samples with different ϕ bin widths $\Delta = 2\pi/360, 2\pi/180, 2\pi/90$, and $2\pi/30$.

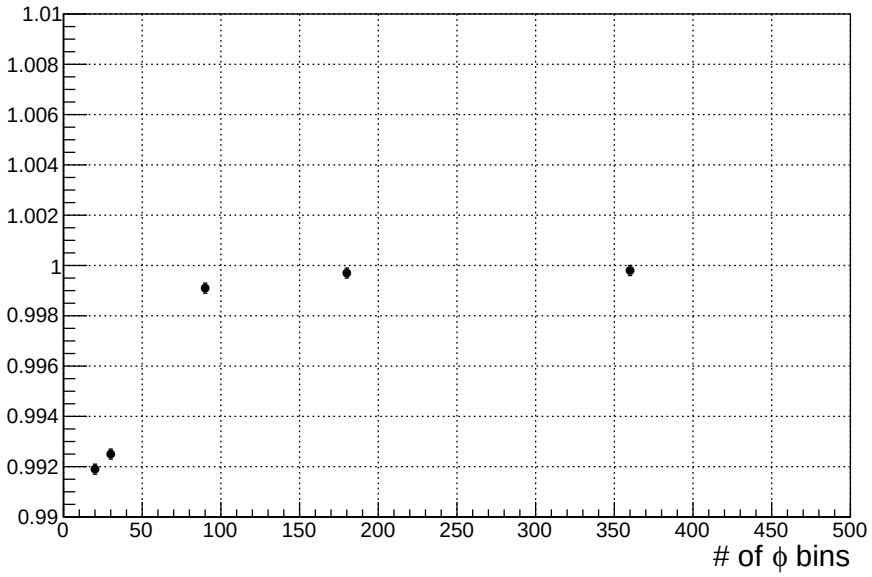

Figure 5.19: Mean and width of the p_1 parameter distributions from fitting the ensemble vs different number of bins.

5.8 Accidental Subtraction

It has been observed [94] that the accidental events in the main RF beam bunch peak do not have the same distribution as those in the six accidental RF peaks as discussed in Sec 4.2.2. The accidentals are being under-subtracted without any correction by around 10% on average and exhibit a run-dependency. At the time of this analysis, the under-subtraction of accidentals is a new observation, and the cause of this effect is under investigation. This gives rise to the possibility that the accidental subtraction may introduce a systematic effect. Nominally, the accidental distributions are scaled by a factor of 1/6, since six accidental RF peaks are used in the sideband subtraction. The sensitivity of the measured Σ to this effect is thus evaluated by repeating the analysis chain while scaling the accidental distributions by a factor of 1/6.5 and by a factor of 1/5.5. Figs. 5.20 and 5.21 show Σ when the analysis is performed using accidental scaling factors of 1/5.5, 1/6.5 and the nominal scaling factor of 1/6. This is a gross over-estimation of the effect observed in data to check if this systematic should be included in the error. A conservative estimation of the effect was chosen because the incorrect accidental subtraction has a run dependence and isn't well-understood. The variation is checked with the Barlow test. Results of the test are shown in Figs. 5.22 and 5.23. Based on the Barlow test no systematic error is assigned to the Σ asymmetry due to the accidental subtraction.

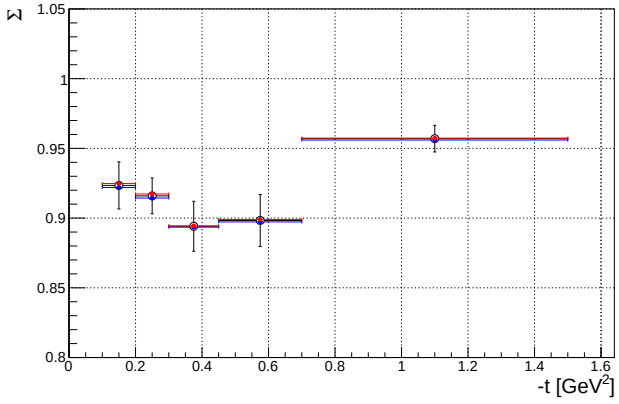

(a) $\pi^0 \to \gamma\gamma$

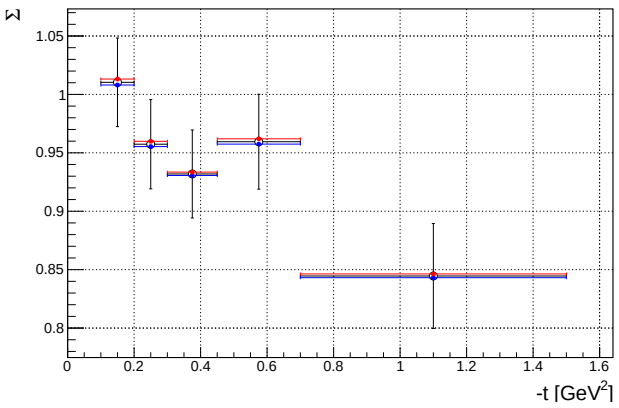

(b) $\eta \to \gamma\gamma$

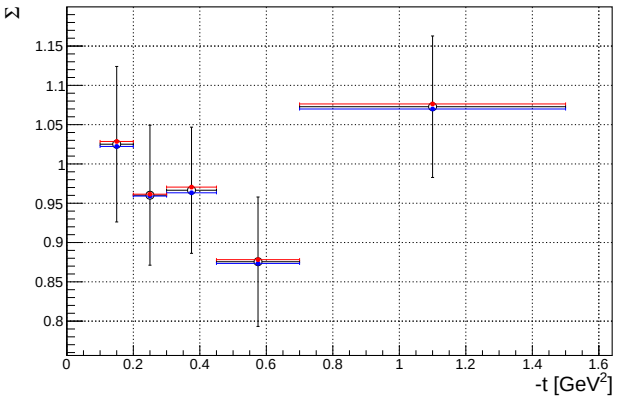

(c) $\eta \to \pi^+\pi^-\pi^0$

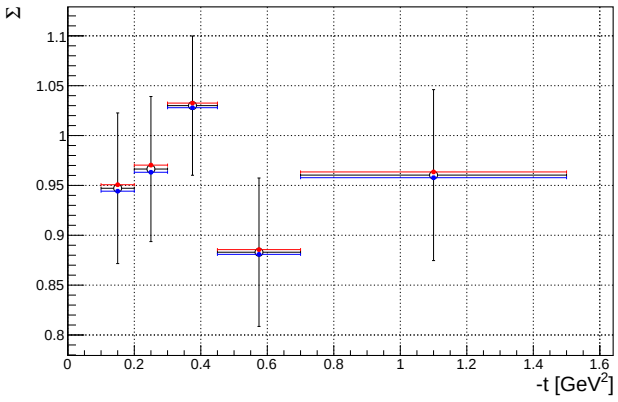

(d) $\eta \to 3\pi^0$

Figure 5.20: Effect of varying the amount of accidentals being subtracted with the diamond in the 0/90 orientation.Open black points correspond to a nominal subtraction of -1/6, blue points correspond to a subtraction of -1/6.5 and red point correspond to a subtraction of -1/5.5.

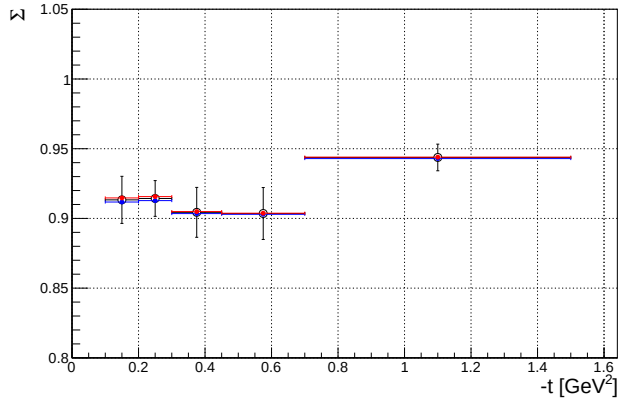

(a) $\pi^0 \to \gamma\gamma$

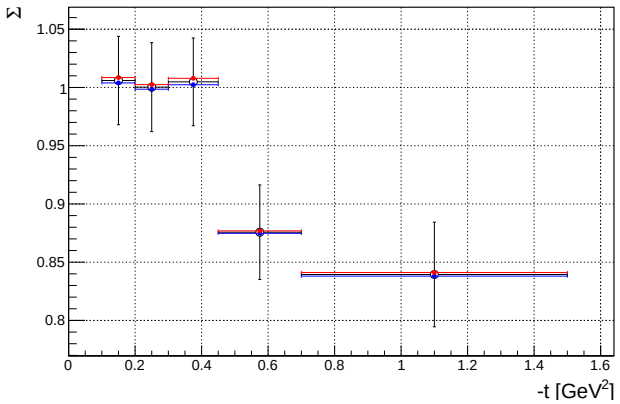

(b) $\eta \to \gamma\gamma$

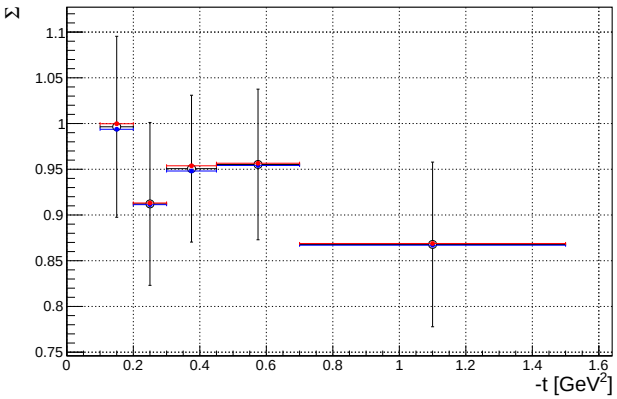

(c) $\eta \to \pi^+\pi^-\pi^0$

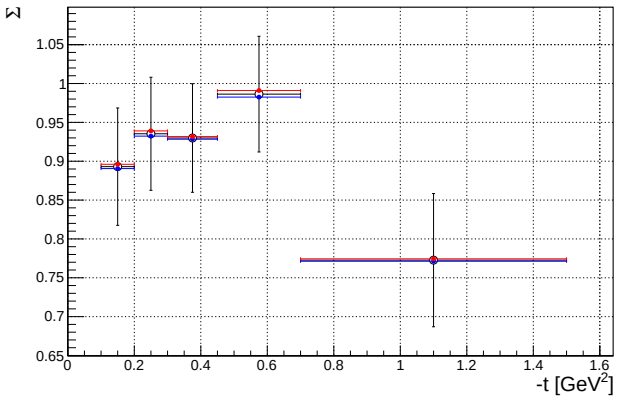

(d) $\eta \to 3\pi^0$

Figure 5.21: Effect of varying the amount of accidentals being subtracted with the diamond in the 45/135 orientation.Open black points correspond to a nominal subtraction of -1/6, blue points correspond to a subtraction of -1/6.5 and red point correspond to a subtraction of -1/5.5.

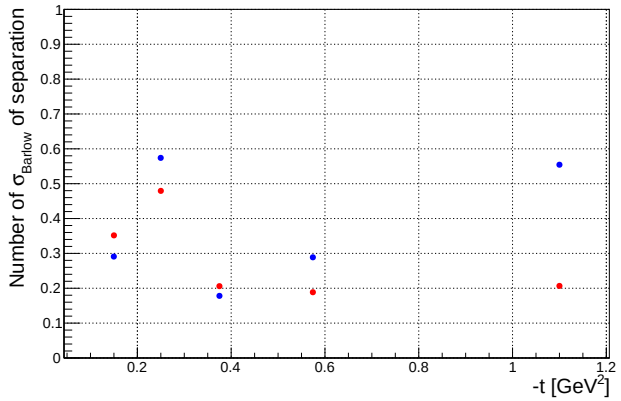

(a) $\pi^0 \to \gamma\gamma$

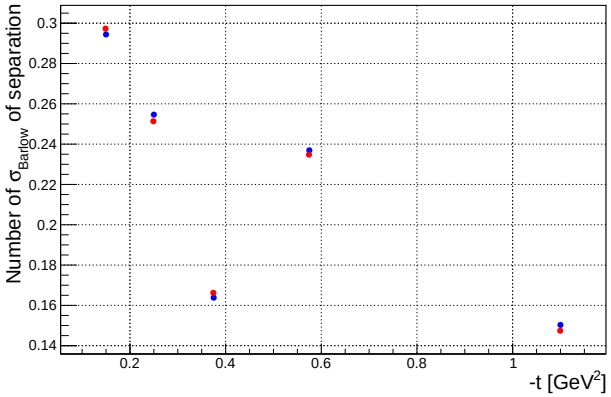

(b) $\eta \to \gamma\gamma$

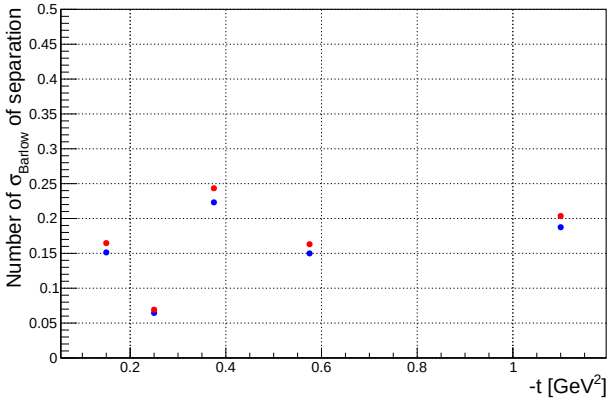

(c) $\eta \to \pi^+\pi^-\pi^0$

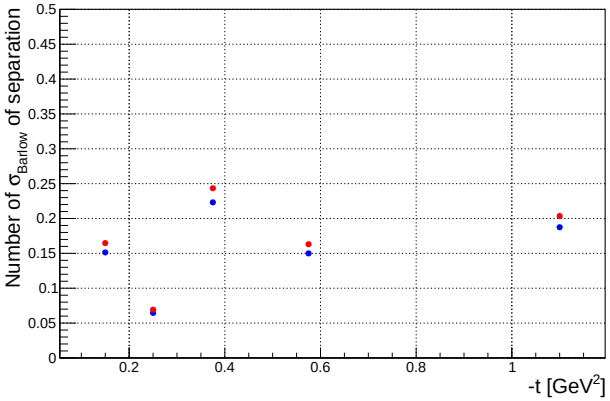

(d) $\eta \to 3\pi^0$

Figure 5.22: Barlow test results of the effect of varying the amount of accidentals being subtracted using the data set with the diamond orientation set to (0/90). Blue points correspond to a subtraction of -1/6.5 and red point correspond to a subtraction of -1/5.5.

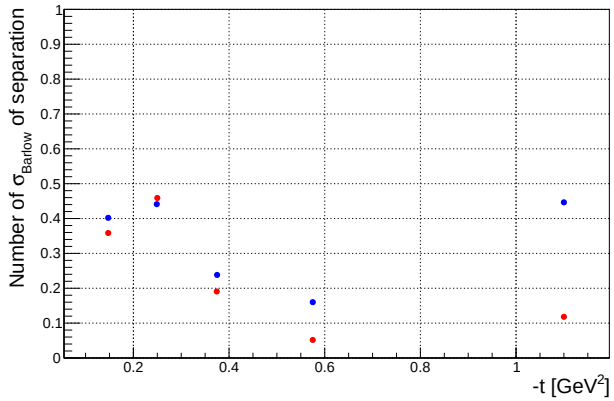

(a) $\pi^0 \to \gamma\gamma$

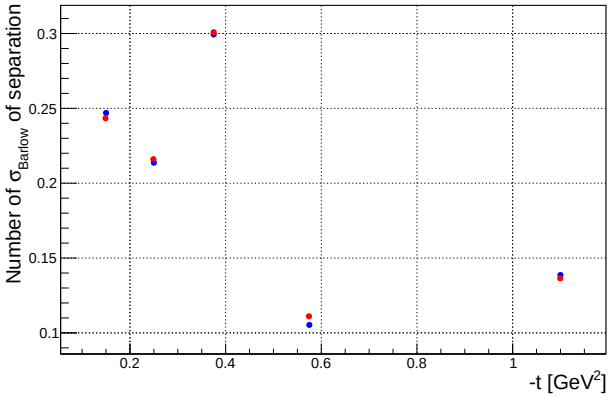

(b) $\eta \to \gamma\gamma$

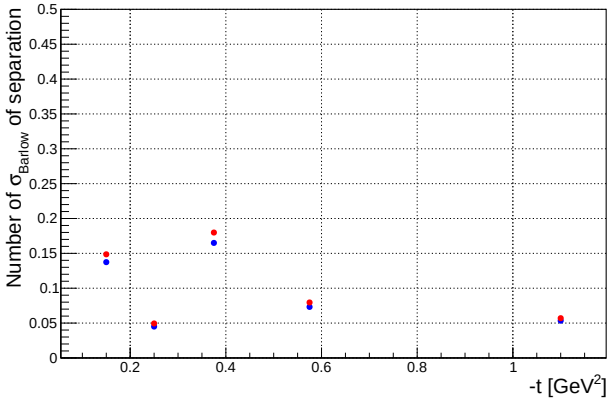

(c) $\eta \to \pi^+\pi^-\pi^0$

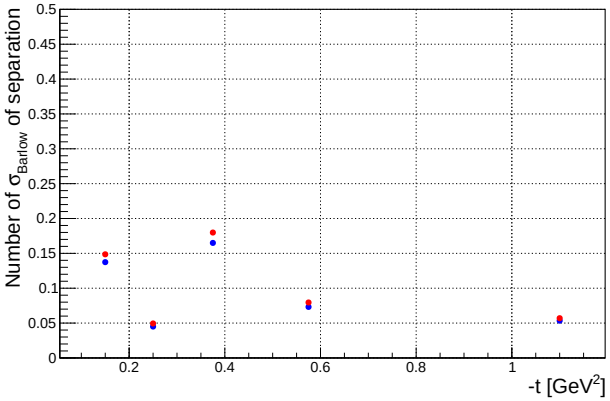

(d) $\eta \to 3\pi^0$

Figure 5.23: Barlow test results of the effect of varying the amount of accidentals being subtracted using the data set with the diamond orientation set to (45/135). Blue points correspond to a subtraction of -1/6.5 and red point correspond to a subtraction of -1/5.5.

5.9 Diamond Orientation Nonorthogonality

When the asymmetry fit function is computed the azimuthal offset that is included is the average offset between the PERP and PARA orientations, ϕ_0, as shown in Eq. 4.11. However, if the two diamond orientations were not orthogonal to each other then the measured Σ would be diluted. Based on a study using a high-statistics sample of ρ candidates, the largest offset between the two diamond orientations is an offset of $2.7^\circ \pm 0.5^\circ$ between PERP and PARA data [83]. Using the independent offsets for the two orientations, the yields would then be

$$Y_\parallel(\phi) \propto (1 - P_\parallel \Sigma \cos 2(\phi - \phi_\parallel)), \tag{5.6}$$

$$Y_\perp(\phi) \propto (1 + P_\perp \Sigma \cos 2(\phi - \phi_\perp)), \tag{5.7}$$

Assuming that $P_\perp = P_\parallel$ for simplicity then

$$\frac{Y_\perp(\phi) - Y_\parallel(\phi)}{Y_\perp(\phi) + Y_\parallel(\phi)} = \frac{1 + P\Sigma\cos(2(\phi - \phi_\perp)) - 1 + P\Sigma\cos(2(\phi - \phi_\parallel))}{1 + P\Sigma\cos(2(\phi - \phi_\perp)) + 1 - P\Sigma\cos(2(\phi - \phi_\parallel))}, \tag{5.8}$$

$$\frac{P\Sigma[\cos(2(\phi - \phi_\perp)) + \cos(2(\phi - \phi_\parallel)]}{2 + P\Sigma[\cos(2(\phi - \phi_\perp)) - \cos(2(\phi - \phi_\parallel)]}, \tag{5.9}$$

$$\frac{2P\Sigma\cos(\phi - \phi_\perp + \phi - \phi_\parallel)\cos(\phi - \phi_\perp - \phi + \phi_\parallel)}{2 - 2P\Sigma\sin(\phi - \phi_\perp + \phi - \phi_\parallel)\sin(\phi - \phi_\perp - \phi + \phi_\parallel)}, \tag{5.10}$$

$$\frac{2P\Sigma\cos(2\phi - \phi_\perp + \phi_\parallel)\cos(\phi_\parallel - \phi_\perp)}{2 - 2P\Sigma\sin(2\phi - \phi_\perp + \phi_\parallel)\sin(\phi_\parallel - \phi_\perp))}. \tag{5.11}$$

If the largest difference of $\phi_\perp - \phi_\parallel = 2.7^\circ$ from the ρ analysis is substituted then

$$\frac{2P\Sigma\cos(2(\phi - \frac{1}{2}(\phi_\perp + \phi_\parallel))) \cdot 0.9989}{2 - 2P\Sigma\sin(2(\phi - \frac{1}{2}(\phi_\perp + \phi_\parallel))) \cdot 0.0471} \tag{5.12}$$

Even though 0.0471 is a large factor it is expected to have a small effect on extracting Σ from the fit because sine has a maximum whenever cosine is at 0. The largest effect on the asymmetry will be a dilution at the zero-crossing which the fit to extract Σ is not very sensitive to. If $\phi_\perp = \phi_\parallel$ then the familiar expression

$$= P\Sigma\cos 2(\phi - \phi_0) \tag{5.13}$$

is recovered.

Additionally toy MC of $\cos(2\phi)$ distributions that are offset from being orthogonal by ϕ_0 were generated with $\Sigma = 1$. The Σ was extracted for varying ϕ_0 values as shown in Tab. 5.13. An example distribution with a $\phi_0 = 2.5^\circ$ is shown in Fig. 5.24. The yield asymmetry distribution using the toy MC generated distributions in Fig. 5.24 with PARA offset by $\phi_0 = 2.5^\circ$ is shown in Fig. 5.25. Within the experimentally measured nonorthogonality between polarization directions the effect is small enough to ignore.

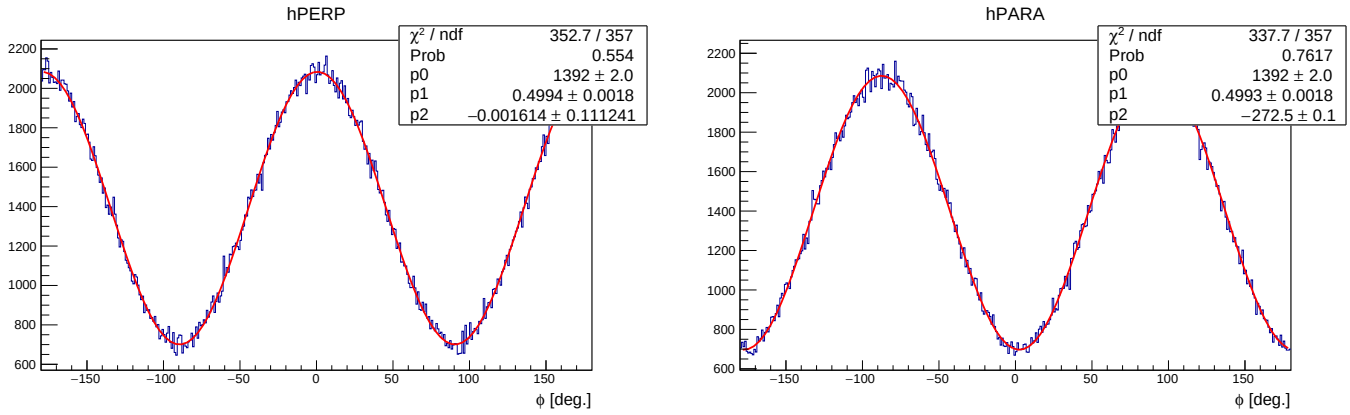

Figure 5.24: Generated $\cos(2\phi)$ distributions. The left plot corresponds to a distribution produced with the diamond in the PERP orientation and no offset. The right plot corresponds to a distribution produced with the diamond in the PARA orientaiton and an offset of $\phi_0 = 2.5°$.

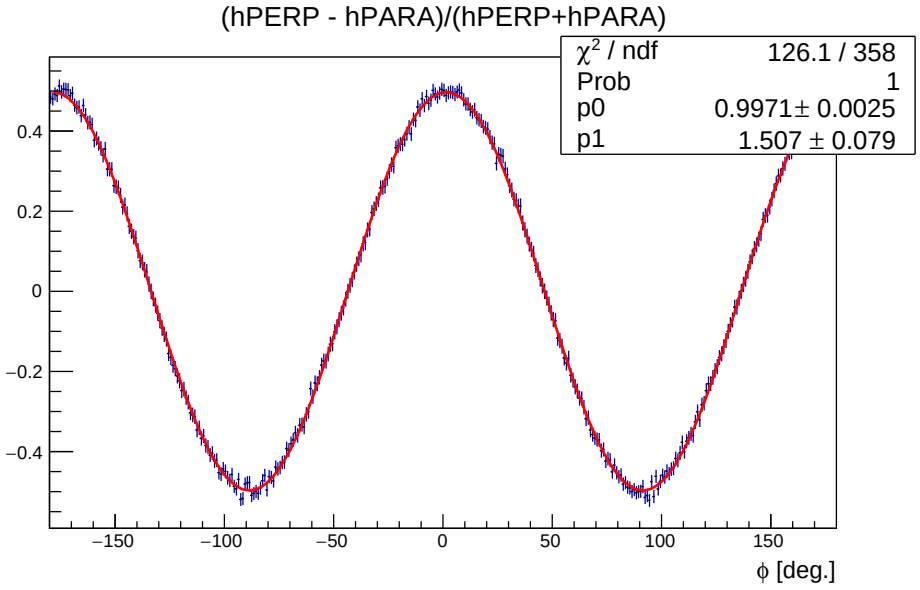

Figure 5.25: The produced asymmetry distribution with a no-offset PERP and 2.5°-offset PARA distribution. No correction was made for the $\phi_0 = 2.5°$offset in the PARA distribution.

PARA offset angle (deg)	Σ	err
0	0.9975	0.0025
2.5	0.9971	0.0025
10	0.984	0.0030

Table 5.13: Σ extracted from the fit for varying PARA offset angles, ϕ_0.

5.10 Polarization

The TPOL measurement has two errors associated with it, a statistical error on each polarization measurement in each energy bin measured during the run period and a systematic error. Since a change in the magnitude of the polarization will directly affect the resulting Σ beam asymmetry by shifting all measured asymmetries to higher or lower values uniformly, the errors on the polarizations contribute to the relative uncertainty on beam asymmetry results. The statistical errors for each t-bin are recorded in Table 5.14.

-t bin [GeV^2]	$\delta_P^{0/90}$	$\delta_P^{45/135}$
$0.1 <$ -t < 0.2	0.027	0.027
$0.2 <$ -t < 0.3	0.027	0.027
$0.3 <$ -t < 0.45	0.026	0.026
$0.45 <$ -t < 0.7	0.026	0.026
$0.7 <$ -t < 1.5	0.028	0.028
$0.1 <$ -t < 1.5	0.027	0.027

Table 5.14: All intensity runs. These are the relative errors that are determined from the statistical errors on the polarization values for each diamond orientation as a function of -t.

To be conservative a 3% relative error for each t-bin is assigned. The TPOL group provides an additional overall systematic uncertainty in the analyzing power of 1.5% [95]. The systematic effects that were studied include the converter thickness, SSD energy threshold, energy calibration uncertainties, detector-to-converter distance, photon beam offset and the simulation statistical precision. Since the polarization is measured for 4 diamond orientations the statistical term of the overall systematic error contribution is weighted by a factor of 1/4 to give the overall uncertainty of

$$\sqrt{\left(\frac{0.03^2}{4}\right) + (0.015)^2}. \tag{5.14}$$

Therefore, the overall systematic relative uncertainty due to the beam polarization is 2.1%.

5.11 Systematics summary

Table 5.15- 5.19 summarize the systematic uncertainties on the Σ beam asymmetries obtained from studies in the previous sections. The common normalization uncertainty on the beam polarization is 2.1% as described in Sec. 4.1.1 is not included in these tables because it applies equally to each measurement.

Study	π^0 Syst. Err	$\eta \to 2\gamma$ Syst. Err	$\eta \to \pi^+\pi^-\pi^0$ Syst. Err	$\eta \to 3\pi^0$ Syst. Err
Event Selection	Table 5.3	Table 5.4	Table 5.5	Table 5.6
Background	—	Table 5.10	Table 5.10	—
Flux normalization	0.002	0.002	0.005	0.005
Phase dependence	0.0005	0.001	0.003	0.003

Table 5.15: Summary of systematic uncertainties from the studies described in Sec. 5.

t-bin $[GeV^2]$	0/90 polarization direction	45/135 polarization direction
$0.1 < -t < 0.2$	0.0049	0.0104
$0.2 < -t < 0.3$	0.0040	0.0052
$0.3 < -t < 0.45$	0.0106	0.0090
$0.45 < -t < 0.7$	0.0066	0.0088
$0.7 < -t < 1.5$	0.0036	0.0037

Table 5.16: Summary of total systematic uncertainties for the π^0 as a function of -t.

t-bin $[GeV^2]$	0/90 polarization direction	45/135 polarization direction
$0.1 < -t < 0.2$	0.0181	0.0350
$0.2 < -t < 0.3$	0.0247	0.0237
$0.3 < -t < 0.45$	0.0109	0.0211
$0.45 < -t < 0.7$	0.0160	0.0149
$0.7 < -t < 1.5$	0.0141	0.0248

Table 5.17: Summary of total systematic uncertainties for the $\eta \to 2\gamma$ as a function of -t.

t-bin $[GeV^2]$	0/90 polarization direction	45/135 polarization direction
$0.1 < -t < 0.2$	0.0268	0.0312
$0.2 < -t < 0.3$	0.022	0.0318
$0.3 < -t < 0.45$	0.0295	0.0295
$0.45 < -t < 0.7$	0.0262	0.0316
$0.7 < -t < 1.5$	0.0333	0.0311

Table 5.18: Summary of total systematic uncertainties for the $\eta \to \pi^+\pi^-\pi^0$ as a function of -t.

t-bin $[GeV^2]$	0/90 polarization direction	45/135 polarization direction
$0.1 < -t < 0.2$	0.0229	0.0208
$0.2 < -t < 0.3$	0.0188	0.0149
$0.3 < -t < 0.45$	0.0181	0.0237
$0.45 < -t < 0.7$	0.0209	0.0195
$0.7 < -t < 1.5$	0.0343	0.0266

Table 5.19: Summary of total systematic uncertainties for the $\eta \to 3\pi^0$ as a function of -t.

Chapter 6

Results and Conclusions

The data points in each plot of this chapter lie at the event-weighted mean value of the t-distribution in each bin. The heights of the error bars correspond to the total error, the quadrature sum of statistical and systematic uncertainties, while the widths of the error bars correspond to the event-weighted rms of the t-distribution. The heights of the boxes correspond to the size of the systematic uncertainty while the width of the boxes is arbitrarily chosen for illustrative purposes. The results from the two different diamond orientation datasets, namely (0/90) and (45/135), are combined using the error-weighted mean to produce final values of Σ and the corresponding statistical error. A conservative approach is taken to obtain the systematic uncertainty for the combined results by assigning the larger of the two systematic uncertainties between the (0/90) and (45/135) data sets as the systematic uncertainty of the combined results. Previously, the π^0 sample was examined in the same binning in -t as the η samples to provide a cross-check, however finer bins of -t are used to make a more precise measurement as shown in Fig. 6.1. The analysis was carried out in exactly the same way with the exception of using more t-bins. The results are compared to a previously published GlueX result [42] that uses an independent dataset and an independent analysis from the results presented in this analysis. The two independent GlueX results are in good agreement with each other. To quantify the agreement between the datasets a χ^2 test was performed. The results in this work were re-binned to match the previous data to compute the χ^2 but that data is not shown here. The χ^2 test metric for comparison of two weighted datasets is given by [96]

$$\chi^2 = \sum_{i=1}^{n} \frac{(W_A \Sigma_i^B - W_B \Sigma_i^A)^2}{W_A^2 \delta_{\Sigma_i^B}^2 + W_B^2 \delta_{\Sigma_i^A}^2} \tag{6.1}$$

where

$$W_A = \sum_{i=1}^{n} \Sigma_i^A \tag{6.2}$$

$$W_B = \sum_{i=1}^{n} \Sigma_i^B. \tag{6.3}$$

The number of data points in $-t$ for each distribution is given by n, i is the particular t-bin, $\Sigma^{A(B)}$ corresponds to a dataset. In this test A corresponds to the current analysis and B corresponds to the previously published result. The more general terms are used because the χ^2 test was also performed to quantify the agreement between different η decay modes in Fig. 6.2. The total errors associated with each measurement are given as δ_{Σ_i}. In order to test if the measurements are consistent or not a p-value

test is performed using the χ^2 as an input. The p-value is defined as the integral over the probability density function ($f_{ndf}(\chi^2)$) of the χ^2 distribution per number of degrees of freedom (ndf) as defined

$$p = \int_{\chi^2}^{\infty} f_{ndf}(x) = \int_{\chi^2}^{\infty} \frac{x^{\frac{ndf}{2}-1} e^{-\frac{x}{2}}}{2^{\frac{ndf}{2}}\Gamma(\frac{ndf}{2})} dx, x > 0. \tag{6.4}$$

For this application the ndf is defined as $ndf = n - 1$. A p-value smaller than a chosen significance level is sufficient to reject the null hypothesis of the test, which in this case is the hypothesis that the two asymmetries from the two different data sets represent the same distributions. The significance is chosen to be 0.05, meaning the test statistic must be extreme enough that there is less than a 5% chance to pull a more extreme test statistic from a χ^2 distribution to claim that the two tested distributions are significantly different from each other. The p-value for the two sets of π^0 data is 0.0958, for a 0.05 significance level the null hypothesis is accepted and the results are consistent with each other.

Four different theory curves are overlayed on top of the data [37, 39, 40, 41]. None of these four theory curves used the GlueX results as inputs.

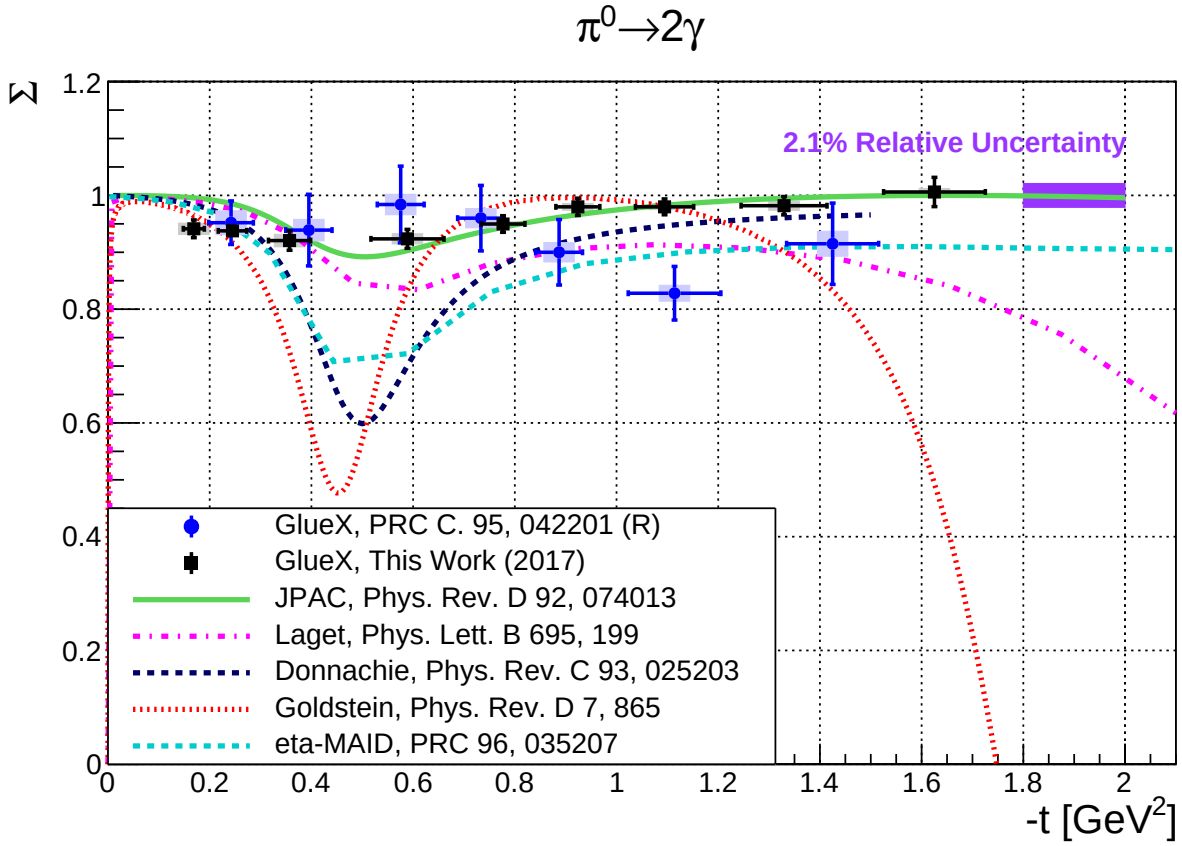

Figure 6.1: Σ asymmetry measured as a function of $-t$. The two independent GlueX measurements are compared to each other and with 5 theory predictions.

The measured Σ for the various η decay modes is compared to the previous GlueX result which comes from an independent data set. The previous GlueX result was extracted via the $\eta \to 2\gamma$ decay mode. Once again, the theory predictions for the η sample does not use the GlueX data as an input. The p-values to test for a 0.05 significance level indicates that the three η decay modes are consistent with each other and can be found in Tab. 6.2.

t-bin $[GeV^2]$	mean of -t	rms of -t	Σ	Sys. Err	Total Err
$0.1 < -t < 0.2$	0.169	0.021	0.941	0.010	0.016
$0.2 < -t < 0.3$	0.245	0.028	0.938	0.005	0.010
$0.3 < -t < 0.45$	0.357	0.042	0.921	0.011	0.017
$0.45 < -t < 0.7$	0.589	0.072	0.924	0.009	0.017
$0.7 < -t < 0.85$	0.777	0.043	0.950	0.004	0.015
$0.85 < -t < 1.0$	0.924	0.043	0.979	0.006	0.015
$1.0 < -t < 1.2$	1.094	0.057	0.980	0.005	0.014
$1.2 < -t < 1.5$	1.329	0.085	0.982	0.008	0.016
$1.5 < -t < 2.0$	1.63	0.100	1.006	0.007	0.026

Table 6.1: Σ and errors for the π^0 sample.

The results for π^0 photoproduction as shown in Fig. 6.1 and Tab. 6.1 show a minimum at $t \approx -0.5$ GeV^2 which qualitatively agrees with the different theory models. At high values of $-t$ the measured values of Σ tend towards unity and only the JPAC [37] and Donnachie [40] models show that behavior. Overall, it is easy to tell by eye that the JPAC model shows the best agreement with the data. However, at low values of -t all the theory models tend towards unity and the data presented here are just slightly below unity. These results go down as low as GlueX can go in -t and a measurement cannot be made at $-t \approx 0$ GeV^2.

The results for η photoproduction as shown in Fig. 6.4 and Tab. 6.6 seem to hint at a falling structure as -t increases however the errors are too large to make a conclusive statement. There is good agreement with both the JPAC [26] and Eta-MAID [44] models and reasonable agreement with Laget [39]. The data is consistent with $\Sigma = 1$ at low-t and agrees with those three models well in that region. The behavior as -t increases is where the models begin to diverge, JPAC appears as though it will recover to unity at high-t and Eta-MAID falls off at high-t. The analysis did not observe any experimental limitations at high-t, there just weren't enough statistics to make a measurement at higher values of -t.

decay modes	p-value
2γ and $\pi^+\pi^-\pi^0$	0.593
2γ and $3\pi^0$	0.8355
$\pi^+\pi^-\pi^0$ and $3\pi^0$	0.7825

Table 6.2: p-values to test for consistency between the three decay modes of η.

t-bin $[GeV^2]$	mean of -t	rms of -t	Σ	Sys. Err	Total Err
$0.1 < -t < 0.2$	0.153	0.028	1.038	0.035	0.051
$0.2 < -t < 0.3$	0.248	0.029	1.009	0.025	0.044
$0.3 < -t < 0.45$	0.369	0.043	1.001	0.021	0.040
$0.45 < -t < 0.7$	0.559	0.071	0.948	0.016	0.039
$0.7 < -t < 1.5$	0.964	0.206	0.866	0.025	0.045

Table 6.3: Σ and errors for the $\eta \to 2\gamma$ sample.

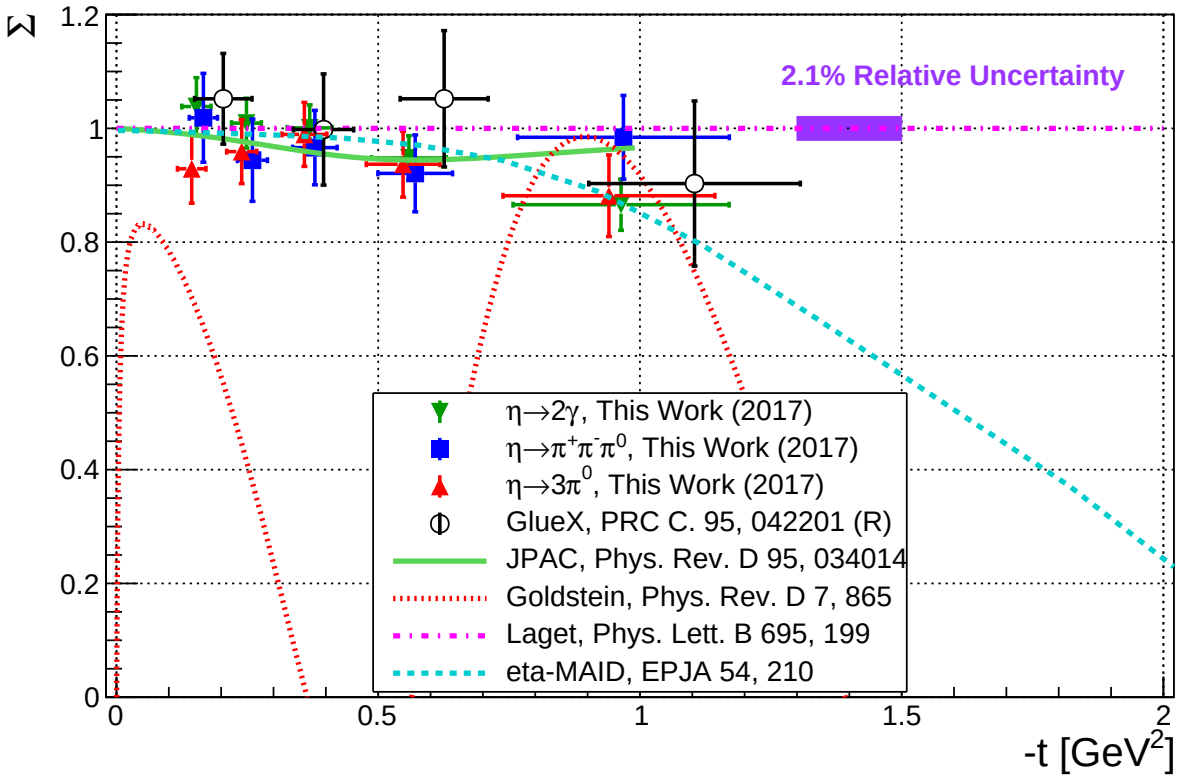

Figure 6.2: Σ asymmetry measured as a function of $-t$ for the 3 dominant decay modes of η. These results are compared with the previous GlueX measurement along with 4 theory predictions.

t-bin $[GeV^2]$	mean of -t	rms of -t	Σ	Sys. Err	Total Err
$0.1 < -t < 0.2$	0.156	0.027	1.019	0.031	0.078
$0.2 < -t < 0.3$	0.250	0.029	0.944	0.032	0.072
$0.3 < -t < 0.45$	0.369	0.043	0.966	0.030	0.065
$0.45 < -t < 0.7$	0.561	0.071	0.921	0.032	0.068
$0.7 < -t < 1.5$	0.958	0.202	0.984	0.033	0.074

Table 6.4: Σ and errors for the $\eta \to \pi^+\pi^-\pi^0$ sample.

t-bin $[GeV^2]$	mean of -t	rms of -t	Σ	Sys. Err	Total Err
$0.1 < -t < 0.2$	0.154	0.027	0.929	0.023	0.061
$0.2 < -t < 0.3$	0.249	0.029	0.959	0.019	0.056
$0.3 < -t < 0.45$	0.369	0.0429	0.989	0.024	0.056
$0.45 < -t < 0.7$	0.558	0.070	0.937	0.021	0.058
$0.7 < -t < 1.5$	0.951	0.202	0.882	0.034	0.072

Table 6.5: Σ and errors for the $\eta \to 3\pi^0$ sample.

The three decay modes of η are averaged to extract a Σ for the $\gamma p \to \eta p$ reaction. The precision of the result is limited by the systematic uncertainty.

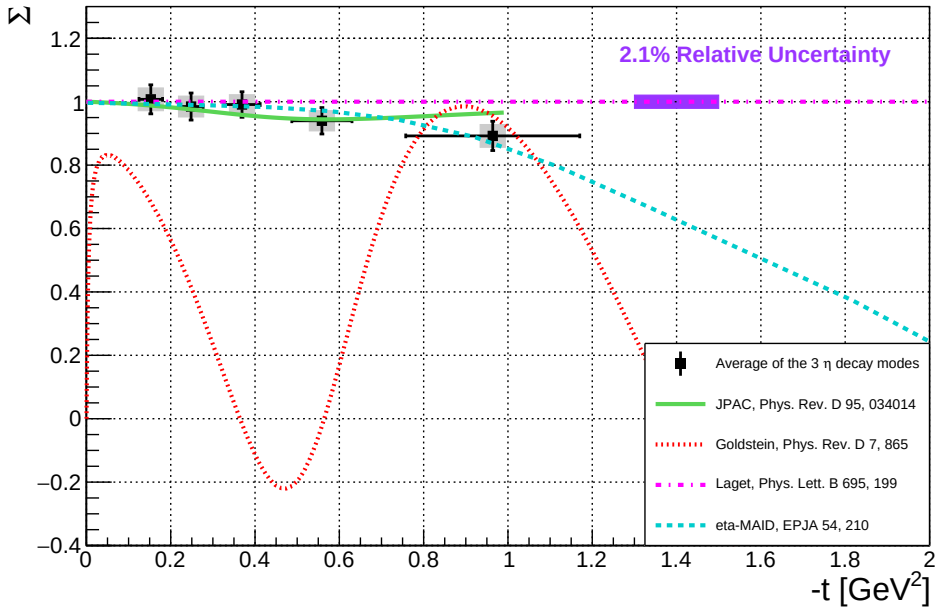

Figure 6.3: Σ asymmetry measured as a function of $-t$. The three decay modes of η are averaged together and compared with 4 theory predictions.

t-bin $[GeV^2]$	mean of -t	rms of -t	Σ	Sys. Err	Total Err
$0.1 < -t < 0.2$	0.153	0.028	1.008	0.035	0.046
$0.2 < -t < 0.3$	0.249	0.0286	0.985	0.032	0.043
$0.3 < -t < 0.45$	0.369	0.043	0.991	0.030	0.040
$0.45 < -t < 0.7$	0.559	0.071	0.940	0.032	0.042
$0.7 < -t < 1.5$	0.961	0.205	0.892	0.034	0.046

Table 6.6: Σ and errors for the average of the 3 η decay modes.

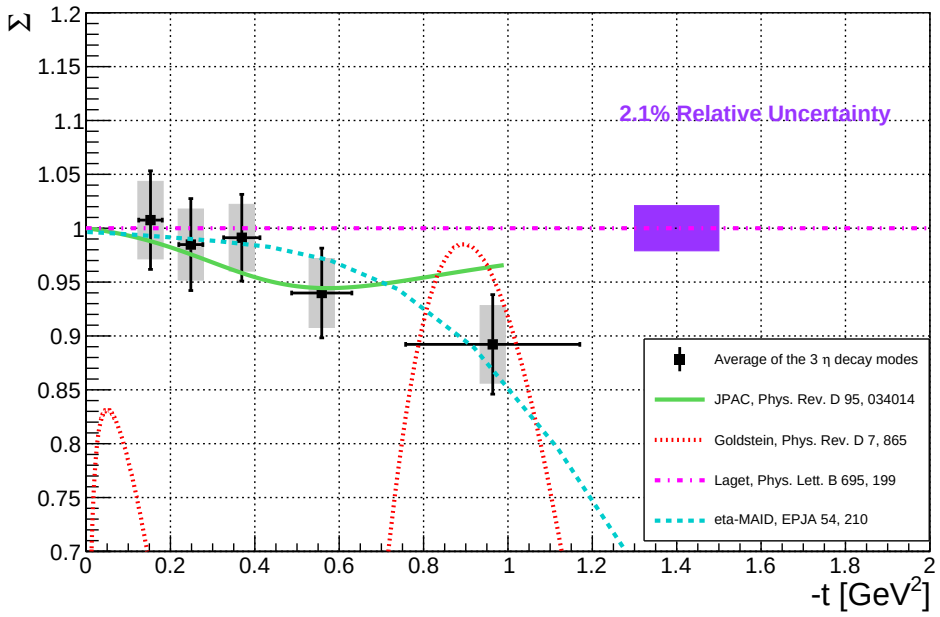

Figure 6.4: The same data as shown in Fig. 6.3 zoomed in on the y-axis. Σ asymmetry measured as a function of $-t$. The three decay modes of η are averaged together and compared with 4 theory predictions.

6.1 Conclusions

With data from the GlueX experiment, the first measurements of the η beam asymmetry at photon beam energies above 6 GeV have been made. In this work the measurement of the beam asymmetry, Σ, has been made for π^0 and η in its three most dominant decay modes. The Σ measurement for $\gamma p \to \pi^0 p$ and $\gamma p \to \eta p$ are both made with higher precision than previous measurements. These results are consistent among one another and with a past measurement by GlueX. The measured asymmetries are statistically consistent with theoretical predictions from the JPAC theory group. This indicates that the production mechanism for both of these mesons is dominated by the exchange of vector mesons with $J^{PC} = 1^{--}$. This result provides insight that the axial-vector contributions to the exchange are not responsible for filling in the dip that is experimentally observed [47] in the π^0 cross-section at $t \approx -0.5$ GeV^2. A variety different models have been introduced to provide at least qualitative agreement to the measured cross-section and Σ beam asymmetry for π^0 and η photoproduction as discussed in Sec. 1.3.1. The most influential developments in these models have come by considering contributions beyond the single Regge pole by including Regge cuts and a different residue in the Regge propagator for the invariant amplitudes of A_1 compared to A_4. Both of these amplitudes contribute to the Regge exchange of $J^{PC} = 1^{--}$. Since the π^0 and η beam asymmetry, Σ, results are measured with higher precision than the previous data for photoproduction the models could use these measurements as inputs to apply tighter constraints to their Regge models.

The measured Σ for the π^0 data seems to agree best with the JPAC model [37] but the other models qualitatively reproduce a similar dipping structure at $t \approx -0.5$ GeV^2 as is seen in the data. The two models [26, 44] that best agree with data for Σ in η photoproduction start to deviate from each other around $t - 1.0$ GeV^2 where the data statistics are low. The data shows a qualitatively slight downward trend as -t increases however the results are not precise enough to make a quantitative statement. There weren't any experimental limitations observed to prevent this measurement extending to higher values of -t aside from a lack of statistics. With the large data sets that GlueX has already taken in 2018 it would be interesting to see how Σ develops at higher-t than what was shown in Fig. 6.4. The measurement of Σ for η photoproduction can also be used as an input to measure a ratio with Σ for η'. The ratio of these two Σ is expected to contain information about possible contributions of hidden strangeness ($s\bar{s}$ states such as ϕ and h_1') and axial-vector meson (b and h) exchange in the production mechanism [58].

The data taken in Spring of 2018 should increase the statistics by a factor of 4, with the inclusion of that dataset it may be possible to extend the $t-$range to determine if the Σ_η decreases at high $-t$ and make more precise measurements. The next steps for the π^0 and η mesons program at GlueX is to shift attention towards the extraction of cross sections at high energy. The models tend to fit both cross-section and beam asymmetry, Σ, data together to extract their parameters. In this high-energy range GlueX expects to make more precise cross-section measurements than what are currently available. Cross-section measurements are the next major milestone, which becomes possible when accurate MC simulation of the detector is achieved. Studies into the acceptance of the GlueX detector for various final state topologies and careful matching of simulation to the measured detector response are needed for cross-section measurements. Work within the collaboration is already underway towards extraction of the cross-section for π^0 and η. Finally, once accurate MC simulations are available that faithfully recreate measured distributions and event selection techniques are developed to cleanly identify the simplest decay products of potential exotic and hybrid mesons, a partial wave analysis can be done. The large body of statistics collected at GlueX, should make possible a comprehensive PWA-based search for evidence of the hybrid mesons claimed by other collaborations and predicted by LQCD. Measuring polarization observables and cross-sections of known particles are the first steps towards this goal. In addition, measurements of cross-sections and polarization observables provide valuable input

to theorists for modelling production and exchange processes. These theoretical models can help guide searches for unexpected and unexplored physics.

Appendix A

List of GlueX Spring 2017 Runs

A.1 PARA 0°Runs (69 total):

31031 31000 30999 30998 30964 30963 30954 30953 30924 30923 30893 30890 30844 30843 30833 30830 30829 30813 30812 30802 30801 30780 30779 30743 30742 30736 30731 30694 30686 30677 30672 30658 30654 30649 30637 30627 30622 30621 30611 30598 30597 30587 30580 30579 30568 30494 30486 30474 30466 30461 30451 30441 30429 30428 30424 30422 30408 30380 30355 30345 30343 30329 30327 30323 30322 30321 30283 30282 30279

A.2 PERP 90°Runs (78 total):

31046 31029 30996 30995 30962 30961 30952 30951 30947 30920 30903 30902 30891 30889 30859 30858 30842 30841 30840 30827 30826 30824 30811 30810 30809 30800 30797 30796 30778 30770 30741 30740 30735 30730 30701 30693 30684 30676 30668 30657 30653 30648 30636 30626 30625 30620 30610 30596 30595 30586 30578 30577 30567 30499 30493 30490 30485 30473 30465 30460 30450 30447 30446 30442 30432 30431 30410 30409 30383 30381 30361 30346 30344 30330 30326 30324 30281 30280

A.3 PARA 135°Runs (74 total):

31032 31002 31001 30966 30965 30956 30955 30927 30926 30896 30895 30848 30847 30835 30834 30816 30815 30804 30803 30784 30783 30745 30744 30737 30733 30732 30696 30695 30688 30687 30679 30678 30673 30659 30655 30650 30638 30630 30629 30623 30612 30607 30602 30600 30590 30589 30582 30581 30570 30496 30495 30487 30480 30477 30468 30467 30463 30462 30453 30452 30448 30433 30420 30411 30404 30403 30385 30384 30349 30347 30331 30299 30285 30284

A.4 PERP 45°Runs (69 total):

31034 31004 31003 30994 30993 30958 30957 30929 30928 30899 30898 30856 30855 30838 30836 30821 30818 30807 30805 30787 30785 30754 30749 30738 30734 30697 30690 30680 30675 30674 30666 30660 30656 30651 30643 30642 30641 30639 30633 30632 30624 30616 30614 30608 30592 30591 30571 30497 30488 30484 30482 30481 30470 30469 30464 30454 30449 30434 30421 30402 30401 30387 30386 30350 30348 30332 30300 30298 30286

Appendix B

Kinematic Fitter Pull distribution

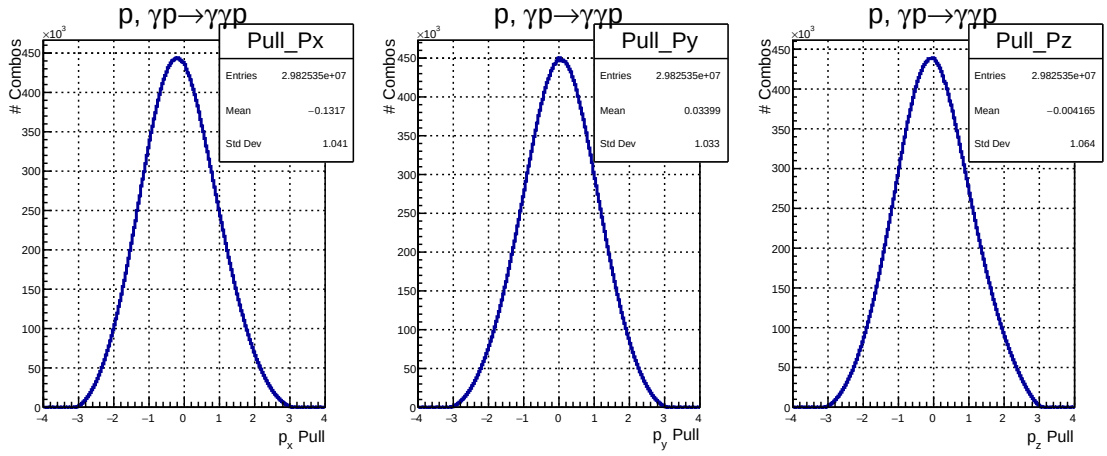

Figure B.1: $\eta \to \gamma\gamma$ Pull quantities from the kinematic fit results for the proton. The pulls have a width close to unity and are centered near zero, which indicates good performance of the kinematic fit.

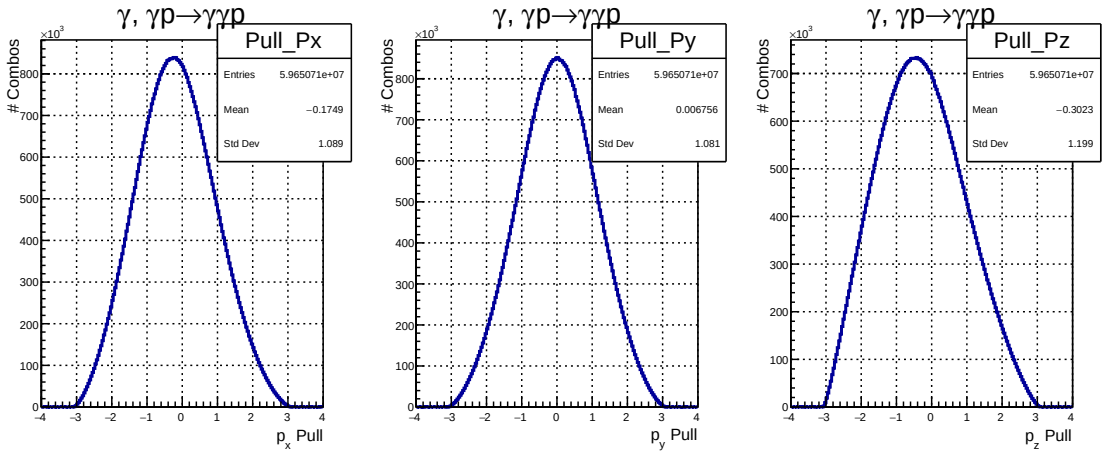

Figure B.2: $\eta \to \gamma\gamma$ Pull quantities from the kinematic fit results for the final state photons. The pulls have a width close to unity and are centered near zero, which indicates good performance of the kinematic fit.

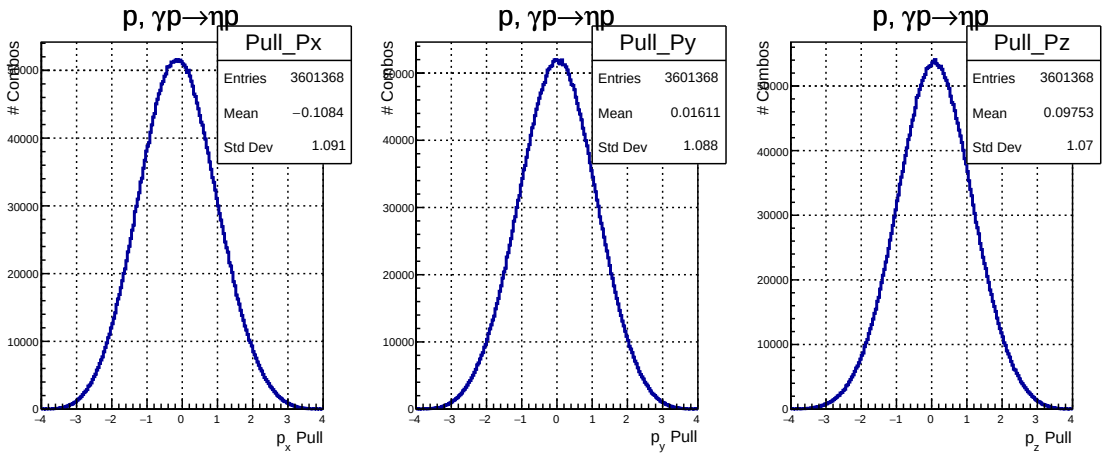

Figure B.3: $\eta \to \pi^+\pi^-\pi^0$ Momentum pull quantities from the kinematic fit results for the proton. The pulls have a width close to unity and are centered near zero, which indicates good performance of the kinematic fit.

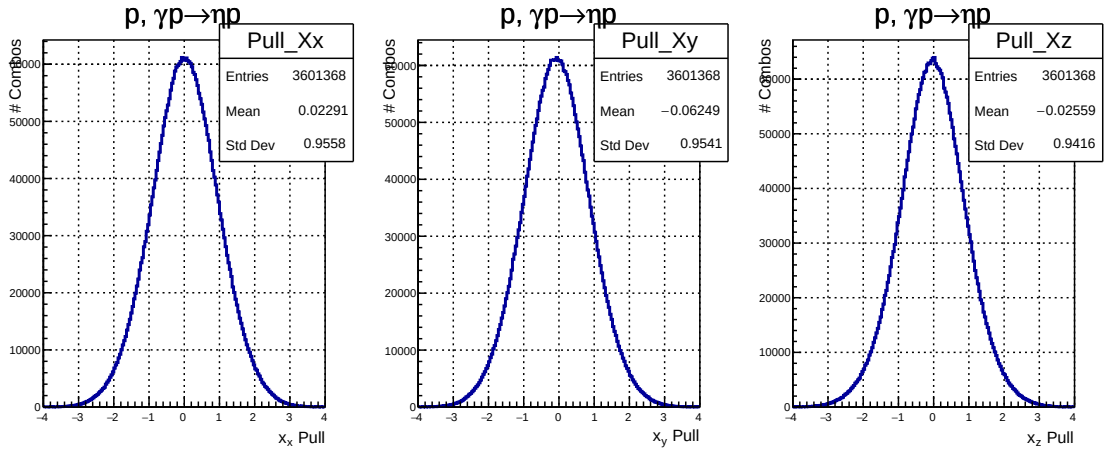

Figure B.4: $\eta \to \pi^+\pi^-\pi^0$ Position pull quantities from the kinematic fit results for the proton. The pulls have a width close to unity and are centered near zero, which indicates good performance of the kinematic fit.

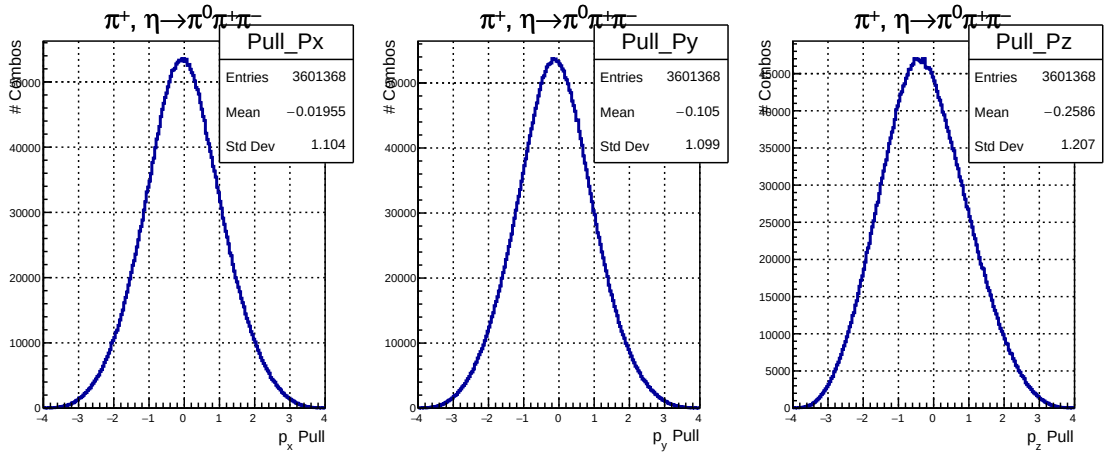

Figure B.5: $\eta \to \pi^+\pi^-\pi^0$ Momentum pull quantities from the kinematic fit results for the π^+. The pulls have a width close to unity and are centered near zero, which indicates good performance of the kinematic fit.

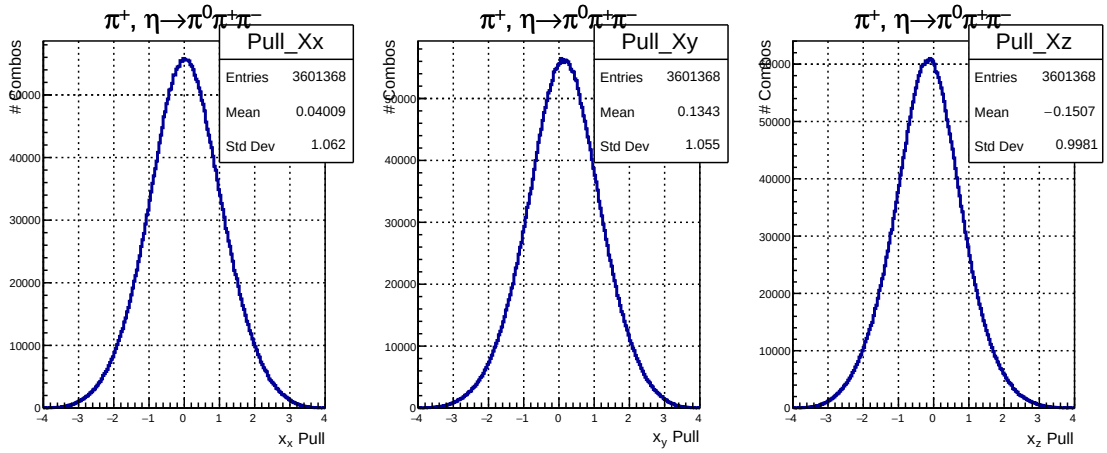

Figure B.6: $\eta \to \pi^+\pi^-\pi^0$ Position pull quantities from the kinematic fit results for the π^+. The pulls have a width close to unity and are centered near zero, which indicates good performance of the kinematic fit.

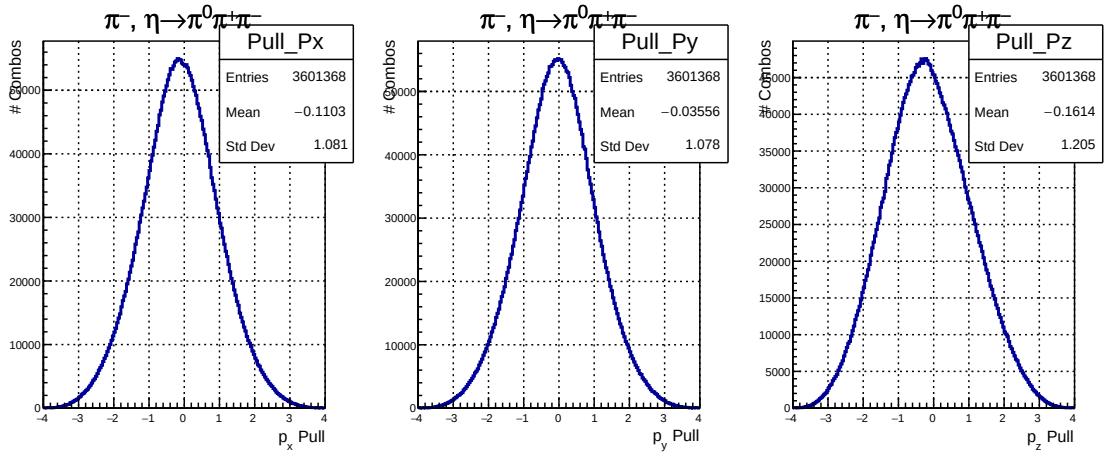

Figure B.7: $\eta \to \pi^+\pi^-\pi^0$ Momentum pull quantities from the kinematic fit results for the π^-. The pulls have a width close to unity and are centered near zero, which indicates good performance of the kinematic fit.

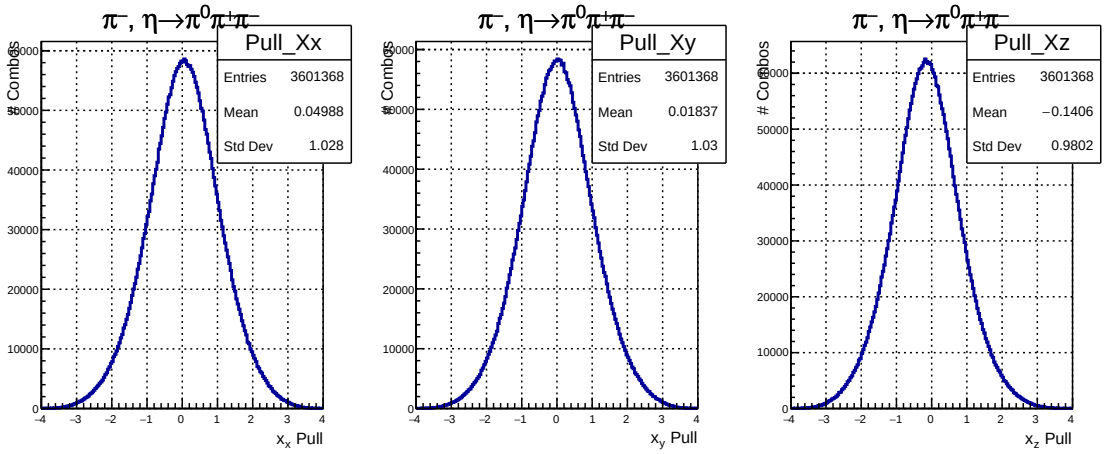

Figure B.8: $\eta \to \pi^+\pi^-\pi^0$ Position pull quantities from the kinematic fit results for the π^-. The pulls have a width close to unity and are centered near zero, which indicates good performance of the kinematic fit.

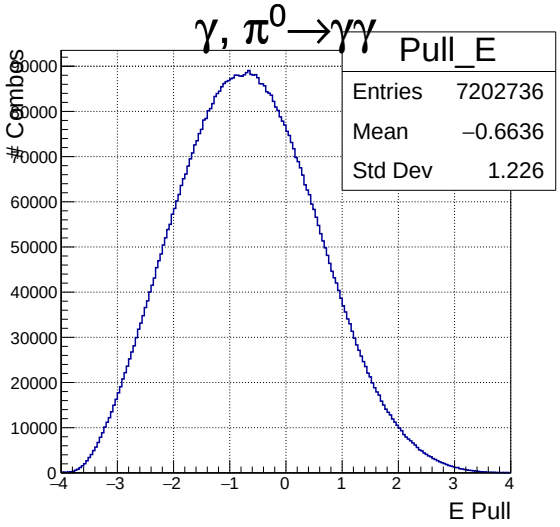

Figure B.9: $\eta \to \pi^+\pi^-\pi^0$ Photon pull energy quantity from the kinematic fit results for the final state photons. The pull has a width close to unity but is not centered near zero.

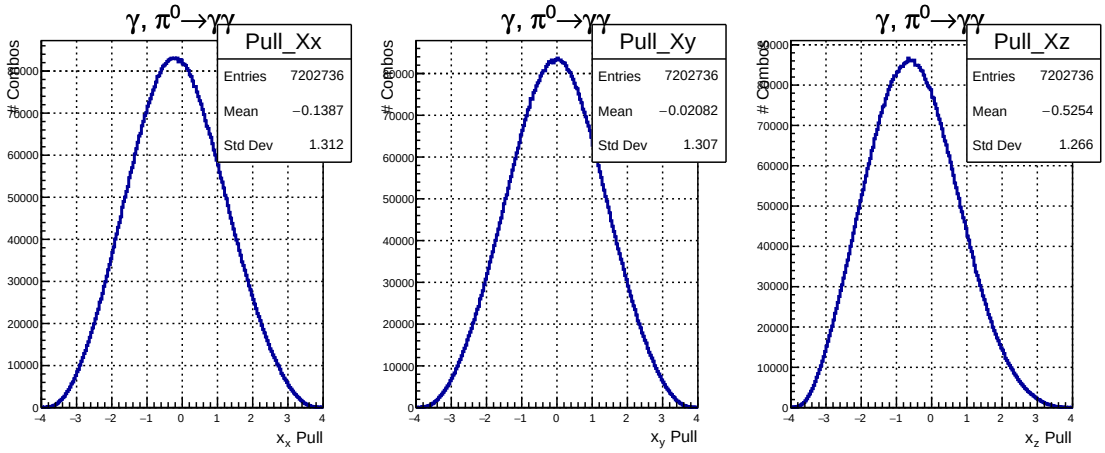

Figure B.10: $\eta \to \pi^+\pi^-\pi^0$ Photon pull position quantities from the kinematic fit results for the final state photons. The pulls have a width close to unity and are centered near zero, which indicates good performance of the kinematic fit.

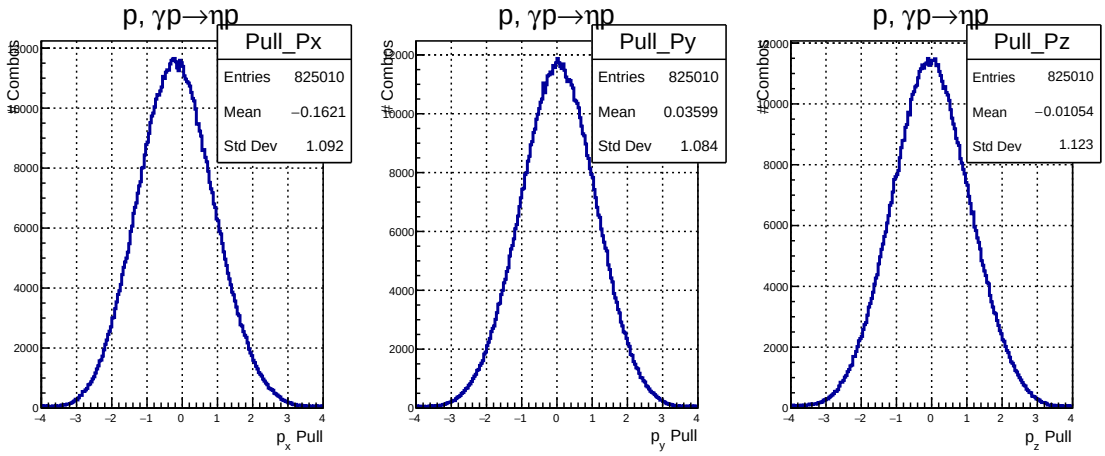

Figure B.11: $\eta \to 3\pi^0$ Pull quantities from the kinematic fit results for the proton. The pulls have a width close to unity and are centered near zero, which indicates good performance of the kinematic fit.

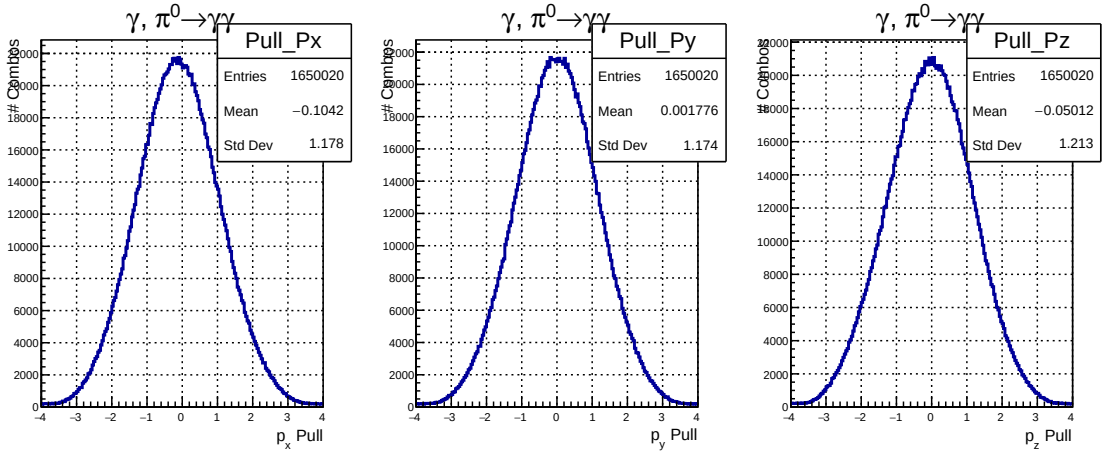

Figure B.12: $\eta \to 3\pi^0$ Pull quantities from the kinematic fit results for the final state photons that decay from 1 of the 3 π^0. The pulls have a width close to unity and are centered near zero, which indicates good performance of the kinematic fit.

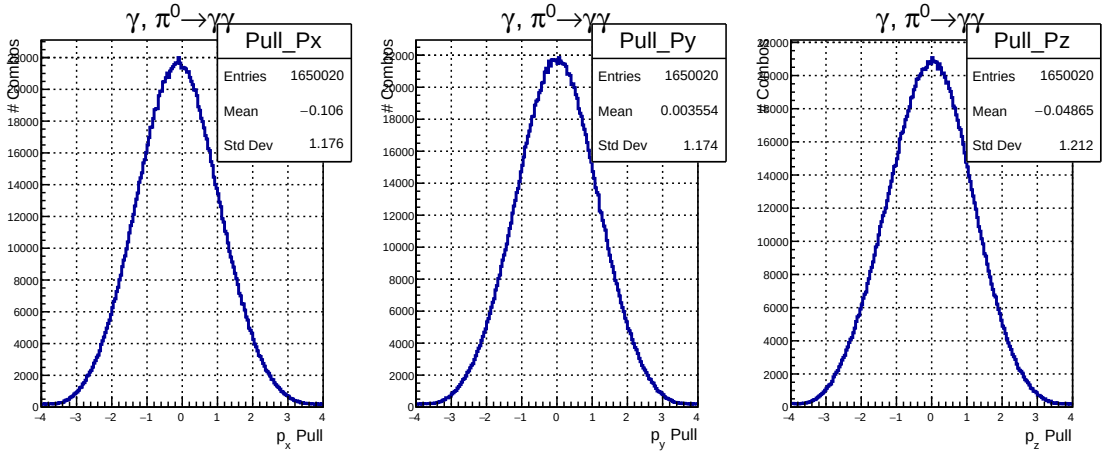

Figure B.13: $\eta \to 3\pi^0$ Pull quantities from the kinematic fit results for the final state photons that decay from 1 of the remaining 2 π^0. The pulls have a width close to unity and are centered near zero, which indicates good performance of the kinematic fit.

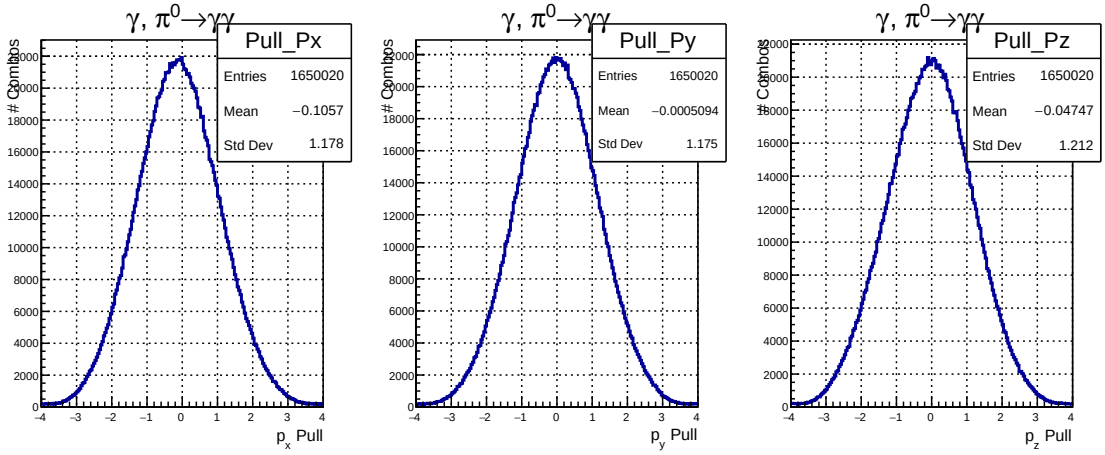

Figure B.14: $\eta \to 3\pi^0$ Pull quantities from the kinematic fit results for the final state photons that decay from the remaining π^0 of the 3. The pulls have a width close to unity and are centered near zero, which indicates good performance of the kinematic fit.

Bibliography

[1] G. Zweig. An SU(3) model for strong interaction symmetry and its breaking. Version 2. In D.B. Lichtenberg and Simon Peter Rosen, editors, *DEVELOPMENTS IN THE QUARK THEORY OF HADRONS. VOL. 1. 1964 - 1978*, pages 22–101. 1964.

[2] M. Gell-Mann. A schematic model of baryons and mesons. *Physics Letters*, 8(3):214 – 215, 1964. ISSN 0031-9163. doi: https://doi.org/10.1016/S0031-9163(64)92001-3. URL `http://www.sciencedirect.com/science/article/pii/S0031916364920013`.

[3] M. Gell-Mann. The eightfold way: A theory of strong interaction symmetry. doi: 10.2172/4008239.

[4] M. Gell Mann and Y. Ne'eman. The eightfold way. *American Journal of Physics*, 33(8):665–665, 1965. doi: 10.1119/1.1972115. URL `https://doi.org/10.1119/1.1972115`.

[5] Jozef J. Dudek, Robert G. Edwards, Peng Guo, and Christopher E. Thomas. Toward the excited isoscalar meson spectrum from lattice qcd. *Phys. Rev. D*, 88:094505, Nov 2013. doi: 10.1103/PhysRevD.88.094505. URL `https://link.aps.org/doi/10.1103/PhysRevD.88.094505`.

[6] Particle Data Group. `http://pdg.lbl.gov/2016/reviews/rpp2016-rev-qcd.pdf`. 2016.

[7] Parikshit Junnarkar, Nilmani Mathur, and M. Padmanath. Study of doubly heavy tetraquarks in Lattice QCD. *Phys. Rev.*, D99(3):034507, 2019. doi: 10.1103/PhysRevD.99.034507.

[8] F. Csikor, Z. Fodor, S. D. Katz, and T. G. Kovacs. Pentaquark hadrons from lattice QCD. *JHEP*, 11:070, 2003. doi: 10.1088/1126-6708/2003/11/070.

[9] Curtis A. Meyer. Light and exotic meons. *Lecture Notes*, 2008. URL `http://www.curtismeyer.com/material/lecture.pdf`.

[10] Klaus J. Peters. A Primer on partial wave analysis. *Int. J. Mod. Phys.*, A21:5618–5624, 2006. doi: 10.1142/S0217751X06034811. [,451(2004)].

[11] M. Lu, G. S. Adams, T. Adams, et al. Exotic meson decay to $\omega\pi^0\pi^-$. *Phys. Rev. Lett.*, 94: 032002, Jan 2005. doi: 10.1103/PhysRevLett.94.032002. URL `https://link.aps.org/doi/10.1103/PhysRevLett.94.032002`.

[12] Tobias Schluter. The Exotic $\eta'\pi^-$ Wave in 190 GeV $\pi^- p - > \pi^-\eta' p$ at COMPASS. *eConf*, C110613: 83, 2011.

[13] A Zaitsev, D Amelin, E Berdnikov, et al. Study of exotic resonances in diffractive reactions. *Nuclear Physics A*, 675:155160, 07 2000. doi: 10.1016/S0375-9474(00)00238-4.

[14] E I Ivanov, D L Stienike, Dmitry Ryabchikov, et al. Observation of exotic meson production in the reaction p p at 18 gev / c. *Physical review letters*, 86:3977–80, 04 2001. doi: 10.1103/PhysRevLett.86.3977.

[15] M. Alekseev et al. Observation of a J**PC = 1-+ exotic resonance in diffractive dissociation of 190-GeV/c pi- into pi- pi- pi+. *Phys. Rev. Lett.*, 104:241803, 2010. doi: 10.1103/PhysRevLett.104.241803.

[16] G. S. Adams, J. Napolitano, K. M. Ecklund, et al. Amplitude analyses of the decays c1 and c1'. *Physical Review. D, Particles, Fields, Gravitation and Cosmology*, 84(11), 12 2011. doi: 10.1103/PhysRevD.84.112009.

[17] C.A. Baker, C.J. Batty, K. Braune, et al. Confirmation of a0(1450) and 1(1600) in pp+0 at rest. *Physics Letters B*, 563(3):140 – 149, 2003. ISSN 0370-2693. doi: https://doi.org/10.1016/S0370-2693(03)00643-9. URL http://www.sciencedirect.com/science/article/pii/S0370269303006439.

[18] A. R. Dzierba et al. A Partial wave analysis of the pi- pi- pi+ and pi- pi0 pi0 systems and the search for a J**PC = 1-+ meson. *Phys. Rev.*, D73:072001, 2006. doi: 10.1103/PhysRevD.73.072001.

[19] D. V. Amelin, Yu. G. Gavrilov, Yu. P. Gouz, et al. Investigation of hybrid states in the ves experiment at the institute for high energy physics (protvino). *Physics of Atomic Nuclei*, 68(3): 359–371, Mar 2005. ISSN 1562-692X. doi: 10.1134/1.1891185. URL https://doi.org/10.1134/1.1891185.

[20] Adam P. Szczepaniak and Maciej Swat. Role of photoproduction in exotic meson searches. *Phys. Lett.*, B516:72–76, 2001. doi: 10.1016/S0370-2693(01)00905-4.

[21] C. A. Meyer and E. S. Swanson. Hybrid Mesons. *Prog. Part. Nucl. Phys.*, 82:21–58, 2015. doi: 10.1016/j.ppnp.2015.03.001.

[22] M. Tanabashi, K. Hagiwara, K. Hikasa, et al. Review of particle physics. *Phys. Rev. D*, 98: 030001, Aug 2018. doi: 10.1103/PhysRevD.98.030001. URL https://link.aps.org/doi/10.1103/PhysRevD.98.030001.

[23] P. Collins et al. Photon beam asymmetry Σ for η and η' photoproduction from the proton. *Phys. Lett.*, B771:213–221, 2017. doi: 10.1016/j.physletb.2017.05.045.

[24] A. Fantini, R. Di Salvo, O. Bartalini, et al. First measurement of the Σ beam asymmetry in η photoproduction on the neutron. *Phys. Rev. C*, 78:015203, Jul 2008. doi: 10.1103/PhysRevC.78.015203. URL https://link.aps.org/doi/10.1103/PhysRevC.78.015203.

[25] I.S. Barker, A. Donnachie, and J.K. Storrow. Complete experiments in pseudoscalar photoproduction. *Nuclear Physics B*, 95(2):347 – 356, 1975. ISSN 0550-3213. doi: https://doi.org/10.1016/0550-3213(75)90049-8. URL http://www.sciencedirect.com/science/article/pii/0550321375900498.

[26] J. Nys, V. Mathieu, C. Fernndez-Ramrez, et al. Finite-energy sum rules in eta photoproduction off a nucleon. *Phys. Rev.*, D95(3):034014, 2017. doi: 10.1103/PhysRevD.95.034014.

[27] The GRAAL Collaboration, O. Bartalini, V. Bellini, J. P. Bocquet, et al. Measurement of η photoproduction on the proton from threshold to 1500 mev. *The European Physical Journal A*, 33 (2):169–184, Aug 2007. ISSN 1434-601X. doi: 10.1140/epja/i2007-10439-9. URL https://doi.org/10.1140/epja/i2007-10439-9.

[28] D. Elsner et al. Measurement of the beam asymmetry in eta-photoproduction off the proton. *Eur. Phys. J.*, A33:147–155, 2007. doi: 10.1140/epja/i2007-10447-9.

[29] G. A. Vartapetian and S. E. Piliposian. Measurements of Cross-section Asymmetry by Polarized Photons and Models of Eta0 Meson Photoproduction in the Energy Range E_γ = 1-GeV to 2-GeV. *Sov. J. Nucl. Phys.*, 32:804, 1980. [Yad. Fiz.32,1553(1980)].

[30] R. L. Workman, R. A. Arndt, W. J. Briscoe, et al. Parameterization dependence of T matrix poles and eigenphases from a fit to πN elastic scattering data. *Phys. Rev.*, C86:035202, 2012. doi: 10.1103/PhysRevC.86.035202.

[31] V. L. Kashevarov, L. Tiator, and M. Ostrick. η MAID-2015: update with new data and new resonances. *Bled Workshops Phys.*, 16(1):9–15, 2015.

[32] D. Rnchen, M. Dring, H. Haberzettl, J. Haidenbauer, et al. Eta photoproduction in a combined analysis of pion- and photon-induced reactions. *Eur. Phys. J.*, A51(6):70, 2015. doi: 10.1140/epja/i2015-15070-7.

[33] V. Mathieu, J. Nys, et al. On the and photoproduction beam asymmetry at high energies. *Physics Letters B*, 774:362 – 367, 2017. ISSN 0370-2693. doi: https://doi.org/10.1016/j.physletb.2017.09.081. URL http://www.sciencedirect.com/science/article/pii/S0370269317307931.

[34] K. Schilling, P. Seyboth, and G. Wolf. On the analysis of vector-meson production by polarized photons. *Nuclear Physics B*, 15:397–412, February 1970. doi: 10.1016/0550-3213(70)90070-2.

[35] Biplab Dey, Michael E. McCracken, David G. Ireland, and Curtis A. Meyer. Polarization observables in the longitudinal basis for pseudo-scalar meson photoproduction using a density matrix approach. *Phys. Rev.*, C83:055208, 2011. doi: 10.1103/PhysRevC.83.055208.

[36] P. D. B. Collins. *An Introduction to Regge Theory and High-Energy Physics*. Cambridge Monographs on Mathematical Physics. Cambridge Univ. Press, Cambridge, UK, 2009. ISBN 9780521110358. doi: 10.1017/CBO9780511897603. URL http://www-spires.fnal.gov/spires/find/books/www?cl=QC793.3.R4C695.

[37] V. Mathieu, G. Fox, and A. P. Szczepaniak. Neutral Pion Photoproduction in a Regge Model. *Phys. Rev.*, D92(7):074013, 2015. doi: 10.1103/PhysRevD.92.074013.

[38] J. M. Laget. The primakoff effect on a proton target. *Phys. Rev. C*, 72:022202, Aug 2005. doi: 10.1103/PhysRevC.72.022202. URL https://link.aps.org/doi/10.1103/PhysRevC.72.022202.

[39] J.M. Laget. Unitarity constraints on neutral pion electroproduction. *Physics Letters B*, 695(1): 199 – 204, 2011. ISSN 0370-2693. doi: https://doi.org/10.1016/j.physletb.2010.11.014. URL http://www.sciencedirect.com/science/article/pii/S0370269310012888.

[40] A. Donnachie and Yu. S. Kalashnikova. Photoproduction of $a_0(980)$ and $f_0(980)$. *Phys. Rev. C*, 93: 025203, Feb 2016. doi: 10.1103/PhysRevC.93.025203. URL https://link.aps.org/doi/10.1103/PhysRevC.93.025203.

[41] Gary R. Goldstein and Joseph F. Owens. π^0 photoproduction in a weak-regge-cut model. *Phys. Rev. D*, 7:865–879, Feb 1973. doi: 10.1103/PhysRevD.7.865. URL https://link.aps.org/doi/10.1103/PhysRevD.7.865.

[42] H. Al Ghoul et al. Measurement of the beam asymmetry Σ for π^0 and η photoproduction on the proton at $E_\gamma = 9$ GeV. *Phys. Rev.*, C95(4):042201, 2017. doi: 10.1103/PhysRevC.95.042201.

[43] G. F. Chew, M. L. Goldberger, F. E. Low, and Y. Nambu. Relativistic dispersion relation approach to photomeson production. *Phys. Rev.*, 106:1345–1355, Jun 1957. doi: 10.1103/PhysRev.106.1345. URL https://link.aps.org/doi/10.1103/PhysRev.106.1345.

[44] L. Tiator, M. Gorchtein, V. L. Kashevarov, and title = others.

[45] Y. L. Dokshitzer V. N. Gribov and J. Nyiri. Strong interactions of hadrons at high energies : Gribov lectures on theoretical physics. 2009.

[46] A. C. Irving and R. P. Worden. Regge Phenomenology. *Phys. Rept.*, 34:117–231, 1977. doi: 10.1016/0370-1573(77)90010-2.

[47] R. L. Anderson, D. B. Gustavson, J. R. Johnson, et al. "high-energy π^0 photoproduction from hydrogen with unpolarized and linearly polarized photons". *Phys. Rev. D*, 4:1937–1946, Oct 1971. doi: 10.1103/PhysRevD.4.1937. URL http://link.aps.org/doi/10.1103/PhysRevD.4.1937.

[48] W. Braunschweig, W. Erlewein, H. Frese, K. Lbelsmeyer, H. Meyer-Wachsmuth, D. Schmitz, A.Schultz von Dratzig, and G. Wessels. Single photoproduction of -mesons of hydrogen in the forward direction at 4 and 6 gev. *Physics Letters B*, 33(3):236 – 240, 1970. ISSN 0370-2693. doi: https://doi.org/10.1016/0370-2693(70)90583-6. URL http://www.sciencedirect.com/science/article/pii/0370269370905836.

[49] V. L. Kashevarov, M. Ostrick, and L. Tiator. Regge phenomenology in π^0 and η photoproduction. *Phys. Rev. C*, 96:035207, Sep 2017. doi: 10.1103/PhysRevC.96.035207. URL https://link.aps.org/doi/10.1103/PhysRevC.96.035207.

[50] B. Barish, R. Gomez, D. Kreinick, C. Peck, J. Pine, F. Sciulli, B. Sherwood, A. Tollestrup, and K. Young. pi0 and rho0 Photoproduction from 6-GeV to 18-GeV. *Phys. Rev.*, D9:566, 1974. doi: 10.1103/PhysRevD.9.566.

[51] R. L. Anderson, D. B. Gustavson, D. M. Ritson, G. A. Weitsch, H. J. Halpern, R. Prepost, D. H. Tompkins, and D. E. Wiser. Measurements of exclusive photoproduction processes at large values of t and u from 4 to 7.5 gev. *Phys. Rev. D*, 14:679–697, Aug 1976. doi: 10.1103/PhysRevD.14.679. URL https://link.aps.org/doi/10.1103/PhysRevD.14.679.

[52] W. Braunschweig, H. Dinter, W. Erlewein, H. Frese, K. Luebelsmeyer, H. Meyer-Wachsmuth, C. C. Morehouse, D. Schmitz, A. Schultz Von Dratzig, and G. Wessels. Single photoproduction of neutral pi mesons on deuterium in the forward direction at 4 gev. *Nucl. Phys.*, B51:157–166, 1973. doi: 10.1016/0550-3213(73)90507-5.

[53] J. Colin, D. Cussol, J. Normand, et al. Dynamical effects in multifragmentation at intermediate energies. *Phys. Rev. C*, 67:064603, Jun 2003. doi: 10.1103/PhysRevC.67.064603. URL https://link.aps.org/doi/10.1103/PhysRevC.67.064603.

[54] Murat M. Kaskulov and Ulrich Mosel. Deep exclusive charged π electroproduction above the resonance region. *Phys. Rev. C*, 81:045202, Apr 2010. doi: 10.1103/PhysRevC.81.045202. URL https://link.aps.org/doi/10.1103/PhysRevC.81.045202.

[55] M. Guidal, J.-M. Laget, and M. Vanderhaeghen. Pion and kaon photoproduction at high energies: forward and intermediate angles. *Nuclear Physics A*, 627(4):645 – 678, 1997. ISSN 0375-9474. doi: https://doi.org/10.1016/S0375-9474(97)00612-X. URL http://www.sciencedirect.com/science/article/pii/S037594749700612X.

[56] Wen-Tai Chiang, Shin-Nan Yang, Lothar Tiator, and Dieter Drechsel. An Isobar model for eta photoproduction and electroproduction on the nucleon. *Nucl. Phys.*, A700:429–453, 2002. doi: 10.1016/S0375-9474(01)01325-2.

[57] J. Dewire, B. Gittelman, R. Loe, et al. Photoproduction of eta mesons from hydrogen. *Phys. Lett.*, 37B:326–328, 1971. doi: 10.1016/0370-2693(71)90030-X.

[58] J. Nys, J. Ryckebusch, D. G. Ireland, and D. I. Glazier. Model discrimination in pseudoscalar-meson photoproduction. *Phys. Lett.*, B759:260–265, 2016. doi: 10.1016/j.physletb.2016.05.069.

[59] Charles E. Reece. Continuous wave superconducting radio frequency electron linac for nuclear physics research. *Phys. Rev. Accel. Beams*, 19:124801, Dec 2016. doi: 10.1103/PhysRevAccelBeams.19.124801. URL https://link.aps.org/doi/10.1103/PhysRevAccelBeams.19.124801.

[60] https://www.jlab.org/physics/gev.

[61] GlueX Collaboration. Gluex photos at https://gluexweb.jlab.org/photos.

[62] The GlueX Collaboration. Hall D / GlueX Technical Design Report. 1997.

[63] Richard Jones. Intense Beams of Polarized and Nearly Monochromatic Photons from Coherent Bremsstrahlung. 1997.

[64] M. Dugger et al. Design and construction of a high-energy photon polarimeter. *Nucl. Instrum. Meth.*, A867:115–127, 2017. doi: 10.1016/j.nima.2017.05.026.

[65] Mike Duggar. script at jlab: makepolvalsv5.

[66] F. Barbosa, C. Hutton, A. Sitnikov, et al. Pair spectrometer hodoscope for hall d at jefferson lab. *Nuclear Instruments and Methods in Physics Research Section A: Accelerators, Spectrometers, Detectors and Associated Equipment*, 795:376 – 380, 2015. ISSN 0168-9002. doi: https://doi.org/10.1016/j.nima.2015.06.012. URL http://www.sciencedirect.com/science/article/pii/S0168900215007573.

[67] Curtis Meyer. Physics and Detector Performance Metrics for the GlueX Experiment. From the GlueX Document Database, Document 1063.

[68] Christopher Keith. Targets for a neutral kaon beam. 02 2016.

[69] Eric Pooser et al. The GlueX Start Counter Detector. *Nucl. Instrum. Meth.*, A927:330–342, 2019. doi: 10.1016/j.nima.2019.02.029.

[70] S. Denisov *et. al.* Characteristics of the TOF Counters for the GlueX Experiment. A**494**:495–499, 2002.

[71] Elton Smith. Time-of-flight measurements with the barrel calorimeter and theforward scintillators. from the gluex document database, document 1001.

[72] L. Pentchev, F. Barbosa, V. Berdnikov, et al. Studies with cathode drift chambers for the gluex experiment at jefferson lab. *Nuclear Instruments and Methods in Physics Research Section A: Accelerators, Spectrometers, Detectors and Associated Equipment*, 845:281 – 284, 2017. ISSN 0168-9002. doi: https://doi.org/10.1016/j.nima.2016.04.076. URL `http://www.sciencedirect.com/science/article/pii/S0168900216302893`. Proceedings of the Vienna Conference on Instrumentation 2016.

[73] Hall d forward drift chamber technical designreport. jefferson lab, va. 2008.

[74] Cristiano Fanelli. `https://halldweb.jlab.org/doc-private/DocDB/ShowDocument?docid=3500`. 2017.

[75] Cristiano Fanelli. Photon energy resolution. URL `https://halldweb.jlab.org/doc-private/DocDB/ShowDocument?docid=3500`.

[76] Tegan D. Beattie et al. Construction and Performance of the Barrel Electromagnetic Calorimeter for the GlueX Experiment. *Nucl. Instrum. Meth.*, A896:24–42, 2018. doi: 10.1016/j.nima.2018.04.006.

[77] F. Barbosa et al. A VME64x, 16-Channel, Pipelined 250 MSPS Flash ADC With Switched Serial (VXS) Extension. Technical report, Jefferson Lab, April 2008. Technical Report GlueX-doc-1022 (hyperlink).

[78] R.T. Jones, T Bogue, B.E. Evans, et al. Performance of the radphi detector and trigger in a high rate tagged photon beam. *Nuclear Instruments and Methods in Physics Research Section A: Accelerators, Spectrometers, Detectors and Associated Equipment*, 570:384–398, 01 2007. doi: 10.1016/j.nima.2006.09.039.

[79] Justin Stevens. `https://halldweb.jlab.org/wiki-private/index.php/Spring_2017_Dataset_Summary`. 2017.

[80] Justin Stevens. `https://halldweb.jlab.org/wiki/index.php/Spring_2017_Trigger_Summary`. 2017.

[81] Mike Dugger, Nathan Sparks, and Barry Richie. "Photon beam polarization by analysis of data from the Hall D Triplet Polarimeter" (GlueX DocDB 3181): `http://argus.phys.uregina.ca/cgi-bin/private/DocDB/ShowDocument?docid=3181` . 2016.

[82] Justin Stevens. `https://halldweb.jlab.org/wiki/index.php/PS_acceptance_and_luminosity_determination#Instructions_for_obtaining_measured_fluxes_from_CCDB`. 2017.

[83] Alexander Austregesilo. `https://halldweb.jlab.org/doc-private/DocDB/ShowDocument?docid=3977`. 2019.

[84] Paul Mattione. `https://halldweb.jlab.org/wiki/index.php/GlueX_Analysis_Software`. 2013.

[85] David Lawrence. Jana framework.

[86] Paul Mattione. https://halldweb.jlab.org/wiki/index.php/DSelector. 2016.

[87] https://halldweb.jlab.org/doc-private/DocDB/ShowDocument.

[88] R. Anderson, D. Gustavson, J. Johnson, et al. "neutral-boson photoproduction on hydrogen at high energies". *Phys. Rev. D*, 1:27–47, Jan 1970. doi: 10.1103/PhysRevD.1.27. URL http://link.aps.org/doi/10.1103/PhysRevD.1.27.

[89] I. S. Barker, A. Donnachie, and J. K. Storrow. "Complete Experiments in Pseudoscalar Photoproduction". *Nucl. Phys.*, B95:347–356, 1975. doi: 10.1016/0550-3213(75)90049-8.

[90] William McGinley. https://v2.overleaf.com/2448997318msfdtdyvdnft. .

[91] William McGinley. https://v2.overleaf.com/project/5bfc130574b27d5e8529101b. .

[92] William McGinley. https://v2.overleaf.com/project/5c93d98b7d330b111036de20. .

[93] Roger Barlow. "Systematic Errors: facts and fictions". *arXiv*, 2002.

[94] Justin Stevens. Docdb 4074. 2019.

[95] M. Dugger, B. G. Ritchie, N. Sparks, et al. "Design and construction of a high-energy photon polarimeter" Submitted to Nucl. Instrum. Meth. (GlueX DocDB 3248): https://halldweb.jlab.org/doc-private/DocDB/ShowDocument?docid=3248 . 2017.

[96] N. D. Gagunashvili. Comparison of weighted and unweighted histograms. *arXiv e-prints*, art. physics/0605123, May 2006.